Fibre Reinforced Polymer (FRP) Stay-in-Place (SIP) participating formwork for new construction

Gai, Xian

Award date:
2012

Awarding institution:
University of Bath

Fibre Reinforced Polymer (FRP) Stay-in-Place (SIP) Participating Formwork for New Construction

submitted by

Xian Gai

for the degree of Doctor of Philosophy

University of Bath

Department of Architecture and Civil Engineering

2012

COPYRIGHT

Acknowledgement

Firstly I would like to thank Antony Darby, Tim Ibell and Mark Evernden for their supervision, advice and friendship throughout this study. For their financial support and enthusiasm, I would like to express my gratitude to Fibreline Composites, Exel Composites and BRE Trust. All the experimental work in this thesis was completed in the structures laboratory at the University of Bath and I would like to thank all of the laboratory staff for their assistance. Finally I would like to thank all of my friends and family for their support throughout. I would like to extend my particular gratitude to Yuli, Kunal, Phil, Pete, Chris, Andy, John, Mum, Dad and my grandparents.

List of Publications

Conference papers

1. Gai, X., Darby, A., Ibell, T. and Evernden, M., 2009. Development of a robust mechanical shear connector between FRP and concrete for FRP stay-in-place participating formwork. *In: 9th International Symposium on Fibre Reinforced Polymer Reinforcement for Concrete Structures (FRPRCS-9),* 13-15 July 2009, Sydney, Australia.

2. Gai, X., Darby, A., Ibell, T., Evernden, M. and Matthews, S., 2009. FRP stay-in-place formwork – design considerations and preliminary testing. *In: Advanced Composites in Construction 2009 (ACIC),* 1-3 September 2009, Edinburgh, Scotland.

3. Gai, X., Ibell, T., Darby, A., Evernden, M. and Orr, J., 2011. Permanent participating FRP formwork for concrete floor slabs. *In: 10th International Symposium on Fibre Reinforced Polymer Reinforcement for Concrete Structures (FRPRCS-10),* 2-4 April 2011, Tampa, Florida. Paper No. SP-275-55. American Concrete Institute, pp.981-987.

4. Gai, X., Darby, A., Ibell, T. and Evernden, M., 2011. Experimental investigation of a novel FRP-concrete composite floor slab. In: Advanced Composites in Construction (ACIC 2011), 6-8 September 2011, Warwick, UK.

Abstract

The concept of stay-in-place (SIP) structural formwork has the potential to simplify and accelerate the construction process to a great extent. Fibre-reinforced polymer (FRP) SIP structural formwork offers further potential benefits over existing formwork systems in terms of ease and speed of construction, improved site safety and reduced long-term maintenance in corrosive environments. However, it is not without its limitations, including primarily the possibility of a lack of ductility, which is a key concern regarding the use of FRP structural formwork in practice.

This thesis presents the findings of an experimental and analytical investigation into a novel FRP SIP structural formwork system for a concrete slab with a particular emphasis on its ability to achieve a ductile behaviour. The proposed composite system consists of a moulded glass fibre-reinforced polymer (GFRP) grating adhesively bonded to square pultruded GFRP box sections. The grating is subsequently filled with concrete to form a concrete-FRP composite floor slab. Holes cut into the top flange of the box sections allow concrete studs to form at the grating/box-section interface. During casting, GFRP dowels are inserted into the holes to further mechanically connect the grating and box sections.

An initial experimental investigation into using GFRP grating as confinement for concrete showed that a significant increase in ultimate strength and strain capacity could be achieved compared to unconfined concrete. This enhanced strain capacity in compression allows greater use of the FRP capacity in tension when used in a floor slab system. Further experimental investigation into developing ductility at the grating/box-section interface showed that the proposed shear connection exhibited elastic-‘plastic’ behaviour. This indicated the feasibility of achieving ductility through progressive and controlled longitudinal shear failure. Following these component tests on the concrete-filled grating and the shear connectors, a total of six (300 x 150 x 3000) mm slab specimens were designed and tested under five-point bending. It was found that the behaviour of all specimens was ductile in nature, demonstrating that the proposed progressive longitudinal shear failure was effective. A three-stage analytical model was developed to predict the load at which the onset of longitudinal shear failure occurred, the stiffness achieved during the post elastic

behaviour and, finally, the deflection at which ultimate failure occurred. Close agreement was found between experimental results and the theory.

Contents

List of Figures

List of Tables

List of Notations

a	Length of shear span
A_{bond}	Surface area of GFRP dowels embedded in the concrete
A_c	Cross sectional area of the concrete-filled grating
A_f	Cross sectional area of each component of box section
A_m	Area of the moment diagram
A_{sh}	Area of longitudinal thrust diagram
b_f	Width of box section
C	Cohesion of the concrete
C_1 , C_2	Sectional geometry coefficient of the composite section
d_w	Depth of box section
D	Diameter of the GFRP dowels
D_L , D_T , D_{LT} , D_s	Longitudinal, transverse, coupling and shear flexural rigidities of a orthotropic plate
e	Strain difference at the grating/box-section interface
E_L , E_T	Longitudinal, transverse modulus of elasticity of a orthotropic plate
$(EA)_c$	Axial rigidity of the concrete-filled grating
$(EA)_f$	Axial rigidity of GFRP box sections
EI	Flexural rigidity of the GFRP section
$(EI)_c$	Flexural stiffness of concrete-filled grating
$(EI)_f$	Flexural stiffness of GFRP box sections
f_{cube}	Cube strength of concrete
f_{ck}	Characteristic compressive strength of concrete

f_{ctm}	Mean tensile strength of concrete
$f_{ctk\,0.05}$	Lower characteristic tensile strength
F_f	Compressive or tensile force in each component of box section
F_{sh}	Residual strength determined from push-out tests
G_{LT}	Shear modulus of elasticity of a orthotropic plate
h_c	Distance from centroid of the concrete-filled grating to the grating/box-section interface
h_f	Distance from centroid of the GFRP box section to the grating/box-section interface
I	Second moment of area of the transformed composite section
k	Rotational stiffness of the flange/web junction of a box section
K_1, K_2	Anisotropy factor which depends on the elastic moduli of the wall material
l	Span of GFRP section
L	Embedded length of GFRP dowels in concrete
M	The sum of the moments generated by all forces from each component of FRP-concrete composite slab
M_c	Moment in the concrete-filled grating
M_f	Moment in the GFRP box sections
M_i	Moment experienced within each of region with a length of 100 mm
$M_{cr}^{local,box-flange}$	Critical bending moment for compression flange buckling for a homogeneous box section
$M_{cr}^{local,box-web}$	Critical bending moment for local web buckling for a homogeneous box section
$M_{\max}$	Applied moment due to either Type A or Type B loading
N	Normal force acting on the shear interface
N_{sh}	Total number of shear connectors

P	Point load acting on each quarter span of slabs
P_B	Ultimate load in the box section corresponding to failure in bending
P_S	Ultimate load in the box section corresponding to failure in shear
$P_{quarter}$	Longitudinal shear thrust between the end support and the quarter span
P_{sh}	Overall longitudinal shear thrust between the end support and the mid-span
P_u	Peak strength of a single shear connector
q	Longitudinal shear flow
$q_{resistance}$	Resistance to shear flow
Q	First moment of area of the region above the elevation of interest
S	Displacement in the horizontal direction of a point at the grating soffit relative to the top flange of the box section
S_i	Slip when shear connector reaches its full plastic capacity
S_u	Ultimate slip at which fracture of shear connectors occurs
t_f , t_w	Thickness of flange, web
V	Vertical shear force experienced by slabs
V_L	Maximum shear force being transferred at the longitudinal shear interface
V_s	Shear resistance of each dowel crossing the shear plane
V_u	Frictional resistance to shear along the crack
w	Self weight of the glued GFRP section
$\bar{y}$	Distance between the centroid of the concrete-filled grating and the centroid of the transformed composite section.
τ_{bond}	Maximum bond strength of GFRP dowels embedded in the concrete
$\tau_{\max}$	Shear strength of the wall material for a box section
τ_{Rd}	Shear strength of concrete

τ_s	Maximum shear strength of GFRP dowels
ε_c	Longitudinal strain of the concrete-filled grating
ε_f	Mean strain in each component of box section
ψ	Corresponding curvature of the member
ψ_i	Curvature of the member in each region
ϕ	Angle of friction
$\Delta\theta_i$	Change of slope of the member in each region
Δv_i	Deflection of the member in each region
ν_L , ν_T	Major, minor Poisson's ratio
$\sigma_{\max}$	Material failure stress in either tension or compression of a box section
$\left(\sigma_{ss}^{ss}\right)_f$, $\left(\sigma_{ss}^{ss}\right)_w$	Critical stress in the flange, web of a box section (simply supported)
$\sigma_{cr}^{local,box-flange}$	Local buckling stress for the rotationally restrained compression flange for a homogeneous box section
$\sigma_{cr}^{local,box-web}$	Local buckling stress for the rotationally restrained web for a homogeneous box section
ζ	Coefficient of edge restraint
δ	Theoretical immediate deflection of the glued GFRP section
δ_A	Mid-span vertical deflection for Type A loading at local buckling failure
δ_B	Mid-span vertical deflection for Type B loading at local buckling failure
φ	Thin-walled compression flange buckling coefficient
γ	Thin-walled shear buckling coefficient

Chapter 1 Introduction

1.1 General

Conventional reinforced concrete structures are fabricated by casting concrete in temporary formworks that are usually made from timber or steel. These formworks are often held in place by temporary scaffoldings. Upon curing of the concrete, the formwork and temporary support are removed, revealing the concrete structure. Permanent participating formwork, also referred to as a stay-in-place (SIP) system, remains structurally integrated with the concrete and provides structural strength to the overall system. The formwork not only acts as a self-supporting formwork during construction, but also acts as external, durable, structural reinforcement throughout the lifetime of the structure. The system has the benefit of simplifying the construction process and can improve the speed and ease of construction.

Erection and striking of conventional formwork and its associated falsework is often costly, potentially hazardous and in some instants presents significant technical challenges. In some circumstances, the use of permanent formwork might significantly reduce these costs and risks. In addition, the elimination of conventional rebar cages can significantly simplify the engineering and detailing process (Ralph and Denton, 2004).

FRP materials have numerous potential advantages over the more traditional materials, such as steel and timber, particularly in terms of better strength-to-weight ratio and increased durability (Bank, 2006). Within the new-build sector, there has been a significant interest in the use of FRP-hybrid systems in concrete decks and slabs. A number of hybrid systems have been developed, where FRP materials are used as a structurally integrated stay-in-place formwork for concrete (Hall and Mottram, 1998; Dieter *et al.* 2002; Ringlestter *et al.* 2007; Bank *et al.* 2007; Keller *et al.* 2007; Fam and Skutezky, 2006; Honickman *et al.* 2009). Since this type of formwork is typically mass produced using FRP pultrusion in factories, it is ready to be used immediately when it arrives on site. It is also relatively light-weight, so formworks can be shipped and installed by a few workers without the aid of heavy machinery. Since this formwork has excellent stiffness and dimensional stability, the need

for temporary support is greatly reduced or eliminated completely. In this case, the FRP formwork can simply be rested on supports at either end of the span, and then the concrete can be cast onto the formwork. This hybrid FRP-concrete system makes appropriate use of the FRP in tension and the concrete in compression. While the initial cost of FRP stay-in-place formwork is currently greater than that of conventional concrete members fabricated from timber or steel, this additional cost could be offset by improved ease and speed of erection, and reduced life-cycle costs of the overall structure due to superior durability.

This project will investigate the development of an innovative structural formwork system which has practical application within the construction industry. The prime motivation for the development of such a system is to provide ease of construction. FRP materials are lightweight in comparison to steel reinforcement and formwork systems. This speeds up and simplifies construction, due to reduced need for heavy plant and labour. There is also no need for the use of welding or heavy cutting tools (adhesive is used to connect sections), as well as no need for fixing of any internal reinforcement since all reinforcement is built into the formwork itself. In relation to these advantages, health and safety concerns are also likely to be reduced. Secondly, FRP materials are very durable, particularly in exposed conditions. Where structures may be exposed to aggressive environments, concern about corrosion of steel reinforcement could be reduced or eliminated. In such situations the lifespan of structures with exposed FRP reinforcement could be increased dramatically. This project represents a feasibility study to investigate how such a durable system with significant construction advantages can be designed for optimum structural integrity.

1.2 Objectives

The primary objective of this study is to assess the feasibility of a proposed hybrid FRP-concrete composite floor system, consisting of two layers of different materials: moulded Glass FRP (GFRP) grating filled with concrete to carry the compression forces and pultruded hollow GFRP box sections to carry the tension forces. The project also investigates the most appropriate method to achieve a robust shear connection between the concrete and FRP.

The main topics addressed by this study are:

1. To investigate the performance of the proposed shear connectors, which are GFRP dowels combined with concrete studs formed along the grating/box section interface.

2. To study the behaviour of the concrete-filled GFRP grating and its suitability for confining the concrete, with the aim of creating a progressive failure due to the controlled crushing of the concrete.

3. To develop an all-GFRP box girder by adhering the moulded GFRP grating to the square GFRP box sections. The hybrid section is then to be used as a stay-in-place structural formwork for concrete.

4. To examine the failure modes of the proposed FRP-concrete slabs in two different loading conditions, representing key-load envelope situations。

5. To assess the effect of changing the number of shear connectors to achieve the most appropriate layout for demonstrating ductile failure behaviour.

6. To solve construction issues of this hybrid system which could arise during concrete casting, including improving the flow and penetrating ability of the concrete into the formwork.

7. To develop analytical models to help understand the structural behaviour of the slabs, with an emphasis on bond behaviour at the GFRP/concrete interface. This model will lead to a robust design approach for such systems.

1.3 Scope

The scope of this study includes experimental investigations and analytical models associated with the proposed hybrid GFRP-concrete floor system.

The experimental investigation was intended to assess the feasibility of using commercially available GFRP materials in combination with concrete to produce a durable, easy-to-construct, strong, stiff and ductile structural flooring system. Six one-way spanning slabs were constructed and tested in five-point bending.

These tests were used to quantify the performance of the GFRP-concrete hybrid system, and to investigate the performance of bond at the GFRP/concrete

interface. The tests were also used to optimise the shear connectors by assessing the effects of varying their number and locations.

Analytical models have been developed to test theories and concepts pertaining to the complex mechanical behaviour of the proposed hybrid system. The first model uses linear elastic analysis, using load-slip characteristics of the shear connectors to predict the initial peak load. The second model applies a elastic-plastic analysis, assuming all the shear connectors are fully 'plastic' throughout the length of the slab, with a failure criterion applied to fracture of the shear connectors due to excessive slip. The third model is a local buckling analysis of the main structural GFRP box section, used to help predict the final failure point. Once the whole model was fully developed and verified, it was used in order to inform design methodologies for this form of structural system.

1.4 Outline of Thesis

The contents of this thesis are listed below:

Chapter 2: A review of literature pertaining to the topics studied in this investigation, demonstrating clearly why the present research is required.

Chapter 3: A review of how the prototype system was developed, with how the ductility can be potentially achieved.

Chapter 4: Material characterisation of each component in the proposed hybrid FRP-concrete floor system.

Chapter 5: Details of experimental and analytical investigations into the development of a mechanical shear connector – GFRP dowels embedded in concrete and its potential to achieve a ductile failure.

Chapter 6: Presentation of the experimental investigation of using GFRP grating as confinement for concrete in the compression zone to provide ductility.

Chapter 7: Presentation of the main experimental investigation involving concrete slabs cast on the GFRP stay-in-place structural formwork composed of a moulded GFRP grating and pultruded GFRP box sections. Different number of shear connectors and two different loading configurations are assessed.

Chapter 8: Discussion of experimental results of six slab specimens S_1-S_6 in terms of their overall flexural behaviour, failure mode, effects of different loading conditions on its performance and ductility.

Chapter 9: Derivation and validation of an analytical model for the slabs discussed in Chapter 7.

Chapter 10: The conclusions that were drawn from this investigation are presented, as well as recommendations for further work in this area of research.

References

Chapter 2 Literature Review

2.1 Introduction

In the past few decades the use of fibre reinforced polymer (FRP) material for the retrofitting and strengthening of existing structures has been widely used in the construction industry (Ralph and Denton, 2004). Whilst FRP materials have been widely used for structural retrofit, their use in new construction has been largely limited to demonstration projects and niche markets where electromagnetic transparency, for instance, is required (Honickman, 2008). However, in the last few years, a number of FRP SIP formwork systems have been developed. In particular, concrete-filled FRP tubes (CFFTs) have been investigated for use as piles in corrosive marine environments and as bridge piers and columns (Mirmiran and Shahawy, 1996; Fam and Rizkalla, 2001; and Seible, 1996). The FRP provides confinement and shear strength to the concrete, and helps prevent corrosion of any additional steel reinforcement. The idea has been extended to rectangular sections for beam applications (Fam *et al.* 2003 and Mirmiran *et al.* 1999). This is perhaps structurally more efficient than the FRP U-sections filled with concrete, proposed by Fardis and Khalili (1981) but is more difficult to construct. Fardis and Khalili's research has revealed many of the inherent advantages of FRP SIP structural formwork, and has subsequently triggered interest in other types of FRP SIP structural formwork systems. In order to make better use of materials, Deskovic *et al.* (1995) proposed a beam system that consisted of a GFRP box beam with a stronger and stiffer Carbon FRP (CFRP) laminate bonded to its tension side to carry the tension forces, and a concrete layer cast on the compression side. Hall and Mottram (1998) proposed a slab system that consisted of a concrete slab cast onto a pultruded FRP panel with a flat continuous base and two 'T' up-stands as shear studs.

This chapter gives a general review of research that has been performed on stay-in-place structural formwork for reinforced concrete flexural members. In particular, this chapter addresses FRP profiles that have potential as structural formworks, various bond mechanisms, and flexural members that have been developed and studied. Firstly, two conventional formwork systems using steel and concrete materials are introduced.

2.2 Conventional Structural Formwork Systems

2.2.1 Profiled steel decking

In the UK, Profiled steel decking is the most common stay-in-place formwork for concrete slab applications, especially for multi-storey steel framed building constructions, because it is light and easy to install. Once in place, it requires very little additional connection to the frame and only small amounts of additional bar reinforcement (Kim *et al.* 2008). The corrugated shape of the steel provides adequate flexural stiffness to support the weight of the concrete before it cures. Many steel decking systems also incorporate surface deformations like indents or grooves so that a mechanical interlock may occur between the concrete and the steel decking, thus resulting in composite action, which contributes to the flexural strength and stiffness of the concrete slab. Figure 2.1 shows a typical composite steel decking concrete floor.

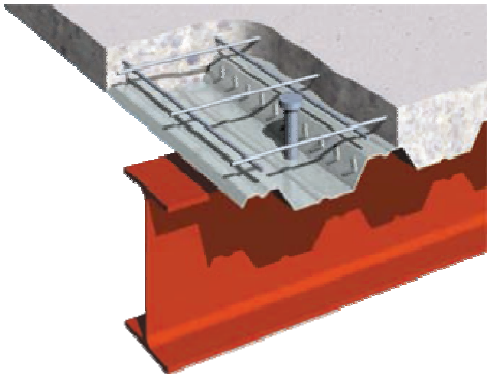

Figure 2.1– Conventional composite slab-on-girder construction using profiled steel decking (TATA steel, 2008)

Figure 2.2– The Slimdek system (TATA steel, 2008)

TATA steel (previously Corus Ltd) has developed a steel stay-in-place profiled decking that is essentially an enlarged version of the aforementioned corrugated steel deck section. The product (Slimdek system) is essentially a cold-formed

stamped galvanized steel sheet that is trapezoidal in section, as shown in Figure 2.2. Multiple sections can be joined together in a tongue-and-groove fashion in order to create a large corrugated sheet of any size. The corrugations in this product feature a larger amplitude and wavelength than conventional profiled steel decking. The sheet metal of these sections is also stamped with ribs running transversely on all surfaces (webs and flanges). The primary purpose of these ribs is to provide mechanical interlock between the steel formworks and the concrete overlay in order to ensure that full composite action can be achieved. Upon completion, the system essentially takes the form of many reinforced concrete T-beams running parallel to one-another, as shown in Figure 2.2. It is designed for flooring, roofing, and decking applications. The profiled steel section itself is stiff enough that it can serve as stable working platform prior to pouring concrete, and is capable of supporting the self-weight of fresh concrete without the aid of shoring (Honickman, 2008).

This system performs well in building works but additional attention is needed in respect of fire resistance and potential corrosion in car park applications where road salts can be introduced by the traffic (Wrigley, 2001). The corrosive nature of steel can become the major concern during design. It has been well established that the use of stay-in-place formwork traps moisture within the concrete, which can cause harmful chloride attack leading to accelerated corrosion (Kuennen, 2006). Corrosion of conventional steel reinforcing bars can be structurally detrimental due to the loss of cross-sectional area, and spalling of concrete cover. Similarly, corrosion of steel structural formwork, if not protected or galvanized, would cause a reduction in the cross-sectional area of the formwork, as well as loss of crucial bond between steel formwork and concrete overlay.

2.2.2 Pre-cast concrete planks

Precast concrete systems often offer an attractive and economic alternative to profiled steel decking by eliminating the need for fireproofing and any additional finishes for durability. Nevertheless, due to the weight of such units, mechanised handling is generally required. In addition, a topping layer of concrete is needed to tie the concrete planks together. These issues can complicate and add cost to the installation (Kim *et al.* 2008).

Pre-cast concrete planks incorporating a welded lattice have been used as participating formwork in both floor panels and bridge decks in recent years (Ralph and Denton, 2004). The lattice girder projects into, and provides shear connection to, overlying in-situ concrete to form a composite slab. A typical example, the OMNIDEC panel designed by Hanson Heidelberg Cement Group, is shown in Figure 2.3. This system allows large areas to be placed quickly, but does require mechanical handling which adds to the installation costs. Concerns have been raised regarding the long-term fatigue performance of the welded lattice (Beales and Ives, 1990)

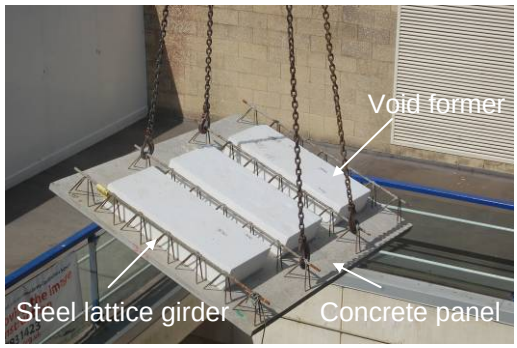

Figure 2.3 – OMNIDEC panels (Hanson Ltd, 2010)

The triangular steel lattice girder, as shown in Figure 2.4, ensures a mechanical bond between pre-cast and in-situ concrete and provides the pre-cast concrete panel with its stiffness during the temporary condition. It also facilitates support of the top layer of reinforcement provided by the contractor (Hanson Ltd, 2010).

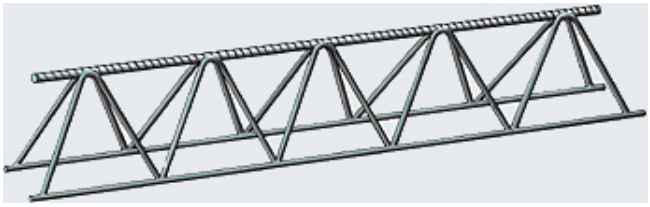

Figure 2.4 – Typical steel lattice girder (Hanson Ltd, 2010)

This type of permanent formwork has potential economic advantages by providing rapid unpropped construction and excellent controlled surface finishes. However, due to the development of tensile strains induced in the precast concrete at the construction stage, the quality of the surface can be affected by unsightly cracking. Strong connections are also required between the top and bottom chords because shear strength is critical at the supports. Additional

compressive reinforcements are still required (Kim *et al.* 2008). Finally, the presence of steel renders this system susceptible to corrosion. Therefore, the use of FRP materials for these stay-in-place structural formworks could be a suitable alternative.

2.3 Advanced Composites

2.3.1 General

'Advanced composites' refer to the family of fibre-reinforced polymers (FRPs) which are used for structural purposes. These materials consist of fibres encased in a resin matrix. The fibres bring the strength to the composite, while the matrix binds the fibres together, transfers loads between them and the rest of the structure, and protects the fibres from the environment (Ibell and Darby, 2007).

One of the best-known FRP composite materials is glass-fibre-reinforced polymer (GFRP). The commonly used term 'fibreglass' is generally used to refer to the glass fibre reinforced polymer composite material. When referring to the fibrous reinforcement alone, the term 'glass fibre' is preferred. Glass fibres are used in a multitude of FRP products for structural engineering, from FRP reinforcing bars to FRP structural profile shapes. A borosilicate glass known as E-glass (electrical glass) because of its high electrical resistivity is used to produce the vast majority of glass fibre used in FRP products for structural engineering. E-glass normally has a longitudinal tensile modulus of 72.5 GPa and a longitudinal tensile strength of 3400 MPa as approximate properties (Bank, 2006).

2.3.2 Manufacturing process

Pultrusion

Pultrusion is a process for continual production of composite profiles with constant cross sections and material properties which are manufactured for specific purposes. Pultrusion is done by continual reinforced material being pulled through a guide where the fibres are placed precisely in relation to the profile cross section. The fibres are then led through processing equipment where the fibres are impregnated with the matrix material. The combined mixture of fibres and matrix is pulled on through the heated equipment where the profile

is cured in its final geometry. The fully cured profile is then pulled forward to a floating suspended saw which cuts the profiles into defined length as shown in Figure 2.5 (Fiberline Composites, 2003).

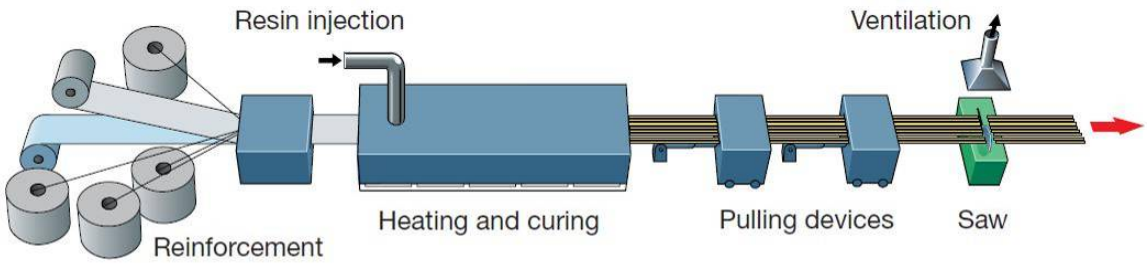

Figure 2.5 – Pultrustion Line (Fiberline Composites, 2003)

Pultrusion is a continuous and highly cost-effective manufacturing technology for producing constant-cross-section fibre-reinforced polymer (FRP) structural profiles. Pultruded profiles are made of pultruded materials. Pultruded materials consist of fibre reinforcement (typically, glass fibre or carbon fibre) and thermosetting resins (typically, polyester, vinylester, and epoxy polymers). The fibre architecture within a thin panel or plate (such as a web or a flange) in a pultruded profile typically consists of longitudinal continuous fibre bundles (called roving or tows) and continuous filament mats (CFMs). Pultruded profiles (such as beams, columns, and panels) are produced for use in building and bridge structures. Most structural product profiles are produced in conventional profile shapes similar in geometry to those of metallic materials (e.g., steel and aluminum) such as the I-beam, angle, square, and channel profiles as shown in Figure 2.6 (Bank, 2006).

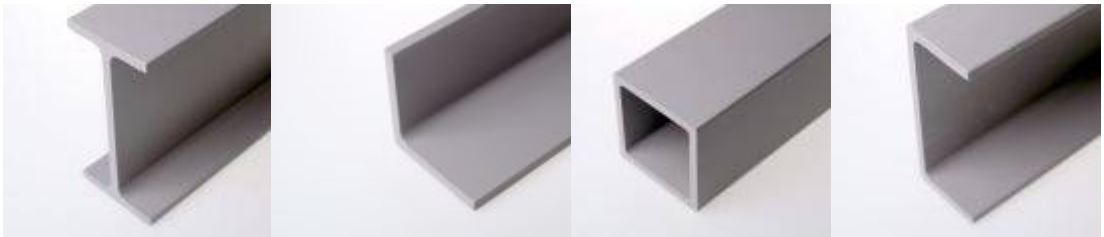

Figure 2.6 – Conventional pultruded profiles: I-beam, angle, square, and channel section (Fiberline Composites, 2003)

The shapes formed have high fibre content, up to 70% by weight is achievable, and good alignment and therefore good mechanical properties can be achieved.

The minimum longitudinal tensile modulus and tensile strength for pultruded profile grade E23 are 23 GPa and 240 MPa respectively, according to the European Standard EN13706 (2002). These properties are higher than can generally achieved by any other FRP manufacturing process.

Moulded GFRP grating process

Moulded grating is manufactured in an open, heated mould that resembles a large waffle iron. Continuous glass fibres are placed in the mould in alternating layers and thoroughly wetted out with resin. This continuous process produces an integral, one-piece construction, which offers excellent corrosion resistance as well as bi-directional strength. When the weaving process is completed, the mould is heated to cure the panel. If the grating is to have embedded grit, the mould will receive the grit at this time before the part is cured. After curing, the part is extracted from the mould. The standard part would have meniscus (concave) top surface for slip resistance. A typical moulded GFRP grating is shown in Figure 2.7. According to the manufacturer's data sheet (Fiberline Composites, 2003), the grating has a compressive modulus and compressive strength of 14 GPa and 172 MPa respectively in both longitudinal and transverse directions. The covered grating is a long-lasting, moulded one-piece GFRP floor product that combines a slip-resistant floor plate with moulded grating panel. The top plate can be integrally-moulded to the supporting bars for a flat surface which provides approximately 50% higher stiffness values than open mesh grating (Fiberline Composites, 2003).

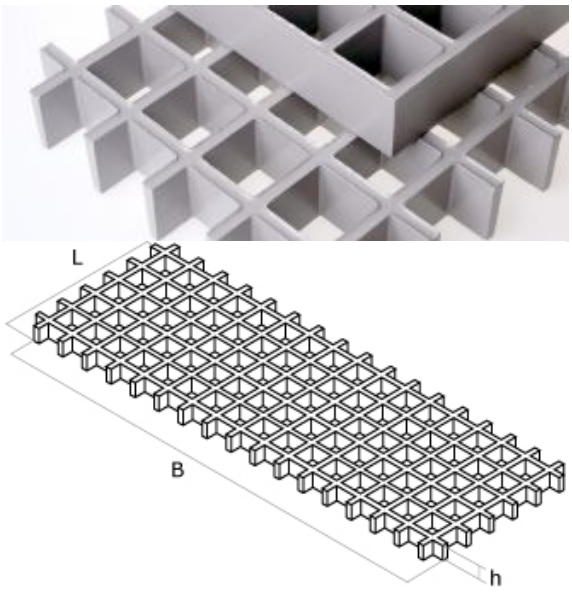

Figure 2.7 – Moulded GFRP grating (Fiberline Composites, 2003)

2.4 Hybrid FRP-Concrete Flexural Systems

2.4.1 Introduction

Based on published research and discussion with research establishments, it appears that there has been limited work carried out into the use of FRP for permanent participating formwork systems, particularly in the UK. Notable exceptions include Hall and Mottram, 1998; Dieter *et al.* 2002; Ringlestter *et al.* 2007; Bank *et al.* 2007; Keller *et al.* 2007; Fam and Skutezky, 2006; Honickman *et al.* 2008. Before such a system is widely adopted, a number of design issues need to be fully investigated. These include serviceability, in terms of deflection control under construction load, longitudinal shear transfer between FRP and concrete, robustness, ductility and strength. However, it appears from the review of the work carried out to date that FRP permanent participating formwork systems may be viable and have a number of significant potential benefits over existing products in the construction market including:

Durability

It was estimated by Engineering Consultants Parsons Brinckerhoff (Ralph and Denton, 2004) that the annual cost for repair of concrete structures with steel corrosion in the United Kingdom is in excess of 500 million sterling pounds. Using FRP panels as formwork and longitudinal reinforcement may reduce the quantity of steel required and protection which is used, giving potential benefits in terms of durability.

Practicality

As the formwork is designed to be permanent the need for striking is eliminated which might lead to benefits in construction time, expense and safety. The panels themselves could be relatively light-weight compared to the most common fully participating formwork system currently used, pre-cast concrete slabs, and might prove more practical to handle, potentially reducing the need for mechanical plant (Ralph and Denton, 2004).

2.4.2 Bond mechanisms between concrete and structural formwork

Several FRP sections are now commercially available and have the potential to be used as stay-in-place structural formwork for concrete structures. Figure 2.8 shows some of these off-the-self sections of different configurations. Of

particular interest is the moulded GFRP grating as shown in Figure 2.9(a), as well as the pultruded box section shown in Figure 2.9(b), which is used in this study to fabricate the stay-in-place structural formwork for the concrete.

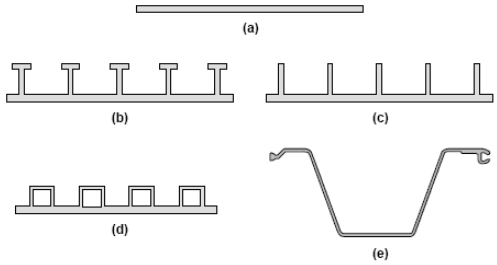

Figure 2.8 – A selection of commercially available GFRP sections (Honickman, 2008)

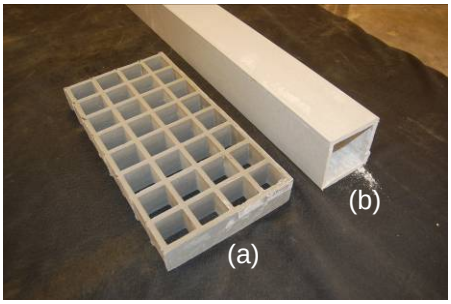

Figure 2.9 – Moulded GFRP grating and pultruded GFRP box sections

In order to ensure that stay-in-place structural formwork acts as tension reinforcement in flexure, it is crucial that an adequate shear connection exists between the concrete and the formwork. A study was carried out by Hall and Mottram, 1998, on a hybrid GFRP-concrete section incorporating FRP stay-in-place structural formwork. Pultruded GFRP walkway panels (T-upstands fixed to a continuous flat sheet) produced as floor panels, as shown in Figure 2.8(b), provided tensile reinforcement, and behaved as permanent stay-in-place structural formwork for the concrete slab overlay, as shown in Figure 2.10. The resultant GFRP-concrete hybrid beams were tested in four-point bending. Initially, it was found that a significant amount of horizontal shear slippage occurred between the concrete and the FRP formwork. This severely limited the flexural capacity of the member since a large strain lag existed between the concrete and the GFRP section. In an attempt to combat this problem, adhesive bonding was used. This adhesive was specially formulated for bonding to fresh, wet concrete. The resultant system behaved monolithically under bending. The

observed mode of failure was diagonal tensile shear cracking in the concrete, which can be attributed to the absence of shear reinforcement within the concrete, and the fact that the beams were over-reinforced in flexure. Tension cracking of concrete was severe in the vicinity of the longitudinal stiffening T-upstands of the GFRP sections. Overall, the concept of applying adhesive to the formwork prior to casting the concrete improved the performance of the beams, but resulted in brittle failure.

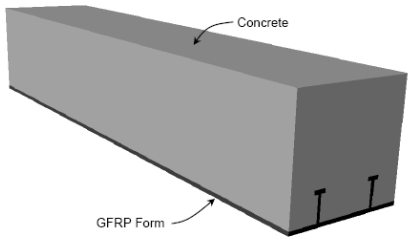

Figure 2.10 – Pultruded GFRP panels with T-upstand ribs combined with the concrete (Hall and Mottram, 1998)

Another study was carried out (Dieter *et al.* 2002) on a hybrid GFRP-concrete stay-in-place structural formwork and GFRP grid reinforcement for bridge deck applications. A pultruded GFRP sheet stiffened using hollow GFRP box sections, similar to that shown in Figure 2.8(d), provided tensile reinforcement, and functioned as stay-in-place structural formwork for the concrete slab overlay. A bi-directional grid composed of pultruded GFRP elements provided the upper longitudinal and transverse reinforcement in regions of hogging moments. A cut-away photograph of this system is shown in Figure 2.11. In order to generate sufficient shear transfer between the GFRP stay-in-place formwork and the concrete overlay, the surface of the GFRP formwork was roughened prior to pouring the concrete by coating it with a mixture of epoxy and gravel. The panels demonstrated the capacity to maintain relatively high loads under significant deflections. However, cracking patterns and ultimate capacities that were significantly lower than analytical predicted values indicated that the FRP reinforcement system did not act fully compositely. This was attributed to the lack of uniform shear transfer between the FRP and the concrete. Due to the complex geometry of the formwork, roughening was only applied to horizontal surfaces. This was found to have a detrimental effect on the bond performance.

In regions where bond-enhancing roughening was absent, severe slippage occurred between the formwork and the concrete overlay. As a result, the flexural crack pattern in the concrete over unbonded regions was considerably more pronounced than it was in bonded regions.

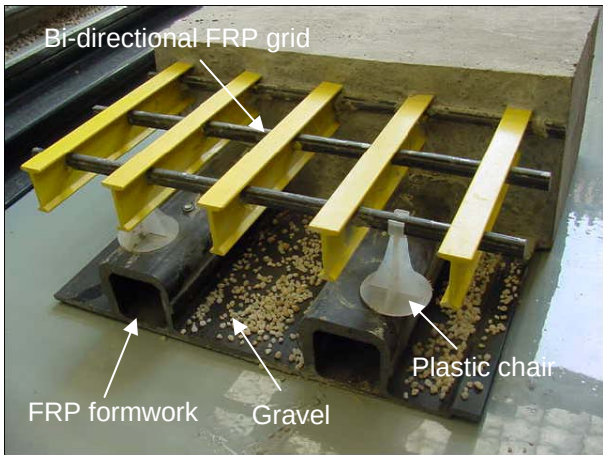

Figure 2.11 – GFRP SIP formwork and GFRP grid reinforcement (Dieter *et al.* 2002)

A similar study (Bank *et al.* 2007) was carried out on concrete slabs cast on pultruded FRP planks having integral T-upstand ribs resembling the section shown in Figure 2.12, which provided tensile reinforcement and acted as stay-in-place structural formwork. In order to achieve sufficient bond between the FRP plank and the concrete, three possible options were investigated. The first was to apply a sand or gravel coating to the surface of the FRP plank. The second was to apply epoxy adhesive to the FRP plank before pouring the concrete, but this option was felt to be unrealistic for on-site application as there is insufficient time to coat formwork with epoxy during casting and finishing operations and further, workers would inevitably stand on the sticky formwork during casting. The last method considered to develop bond between the FRP and concrete was to use pultruded GFRP bars inserted through the longitudinal webs of the FRP plank in the transverse direction, as shown in Figure 2.13. This option was attempted in a previous study by Ringlestter *et al.* (2007); however, it was discovered to be difficult and costly. The labour costs of the fabrication activities associated with the drilling of the holes through the webs of the plank were uneconomical. Therefore, bonding the aggregate to the surface of the FRP plank prior to pouring the concrete was selected as the preferred option. The size of aggregate was varied (both gravel and sand were used) in order to study the effect that this had on the flexural performance of the system. It was shown

that the finer sand coating led to a higher initial cracking moment than was achieved when the gravel coating was used. Five 230 mm wide by 178 mm deep beams with different lengths (three beams with a 1.09 m span, referred to as specimen 1-3 and two beams with a 1.83 m span, referred to as specimen 4-5) were fabricated using the aggregate coated FRP plank as the bottom formwork for the concrete. These specimens were tested under three point bending. Specimen 1-3 failed in shear with evidence of diagonal shear cracks forming as the load approached the maximum. Partial debonding between the FRP plank and the concrete was observed at the mid-span during the tests for all the beams. However, there was no evidence of any slip of the FRP plank from the concrete at the ends of the beam following shear failure of the specimens. Specimen 4-5 failed in a hybrid mode of shear and flexure at the failure load, after the occurrence of distributed flexural cracking. This study illustrated the feasibility of using the aforementioned FRP planks as stay-in-place open structural formwork for concrete slabs, and showed that the plank functioned as flexural reinforcement when the aggregate coating was employed.

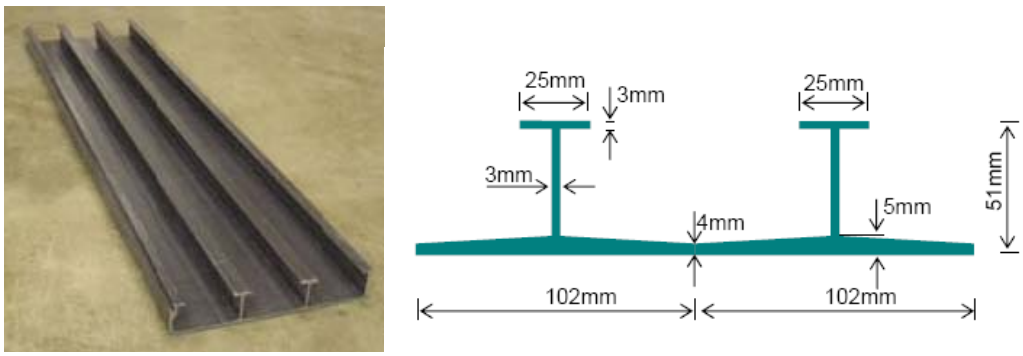

Figure 2.12 – Pultruded FRP Plank having T-upstand ribs (Bank *et al.* 2007)

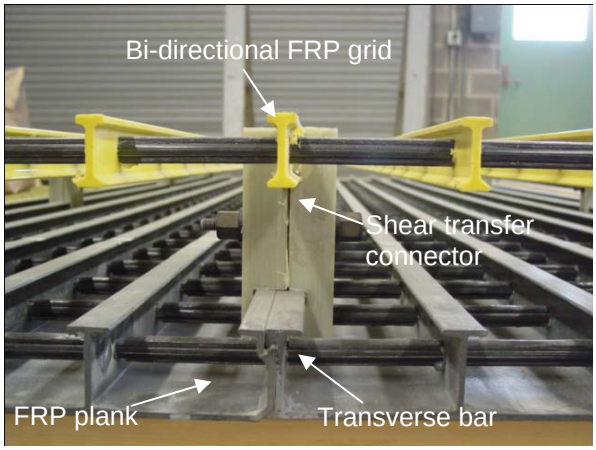

Figure 2.13 – Pultruded FRP planks with transverse bars inserted through the T-upstand ribs (Ringlestter *et al.* 2007)

2.4.3 Other stay-in-place structural formwork systems

A number of FRP-concrete hybrid systems have been developed, where FRP materials are used as a structurally integrated SIP formwork for concrete (Keller *et al.* 2007; Li *et al.* 2006; Descovic *et al.* 1995; Canning *et al.* 1999; Huallat *et al.* 2003; Larralde, 1992; Fam and Skutezky, 2006). The details of these FRP SIP systems are discussed below.

Hybrid FRP-Concrete sandwich panels

A sandwich panel is a flexural member consisting of a light-weight core that is sandwiched between two relatively stiff skins. The concept behind sandwich panels is that the skins are responsible for the longitudinal (tensile and compressive) stresses associated with flexure, whereas the light-weight core is responsible for carrying the shear forces. The core also acts as a spacer that separates the skins in order to increase the depth of the sections, thereby increasing the moment of inertia. This dramatically increases flexural stiffness and strength with only a minimal increase in the mass of the specimen.

Research in this field by Keller *et al.* (2007) utilised pultruded FRP planks with T-upstands as formwork for concrete. These T-shape longitudinal ribs not only increased the section stiffness when compared to a flat sheet, but also served as an embedded mechanical anchor at the GFRP/concrete interface. This research appears to be the first case of utilising lightweight concrete in a hybrid FRP-concrete system in order to reduce the dead weight. This study presents a new concept for a lightweight hybrid FRP-concrete sandwich bridge deck panel. The sandwich construction consists of three layers: a fibre-reinforced polymer composite (FRP) sheet with T-upstands for the tensile skin, lightweight concrete (LC) for the core and a thin layer of normal concrete as a compression skin, as shown in Figure 2.14 and Figure 2.15. Mechanical tests on eight hybrid beams were performed with two types of lightweight concrete (low and high density) and two types of FRP/LC interface: unbonded (only mechanical interlocking of LC between T-upstands) and bonded with an epoxy adhesive. These sandwich panels were tested in flexure using a three-point bending set-up. For those panels with an unbonded FRP/concrete interface, mechanical interlock between the concrete and the ribs of the pultruded FRP decking panels was relied upon in order to provide shear connection. However, because the ribs of the FRP panels

were oriented longitudinally, this shear connection proved to be insufficient due to lack of transverse interlocking. As a result, significant slippage was observed between the lightweight core and the FRP formwork, thus reducing composite action between the two components. Consequently, tensile stresses within the light concrete core increased, leading to flexural failure by tensile cracking of the concrete. Those panels with an adhesive bond between the lightweight concrete core and the FRP decking panels failed by longitudinal shear within the light concrete core itself prior to any bond failure occurring in the vicinity of the FRP/concrete interface. However, the failure behaviour changed from progressive, for the unbonded FRP/concrete interface, to brittle, for the bonded FRP/concrete interface, which is undesirable.

The idea of using lightweight materials in regions of low flexural stress (near the neutral axis) is attractive as it can significantly reduce the self-weight of a member without an excessive loss of flexural stiffness or strength. However, it is important to recognize that the implementation of such a technology could shift the design to one that is limited by its shear strength (Honickman, 2008).

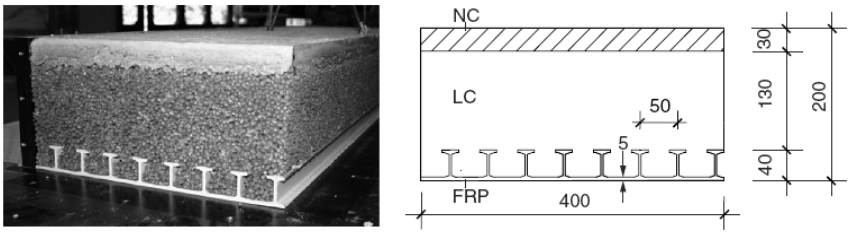

Figure 2.14 – Cross-section of hybrid sandwich beams [NC = normal concrete, LC = lightweight concrete, FRP = fibre-reinforced polymer plank with T-upstands] (Keller *et al.* 2007)

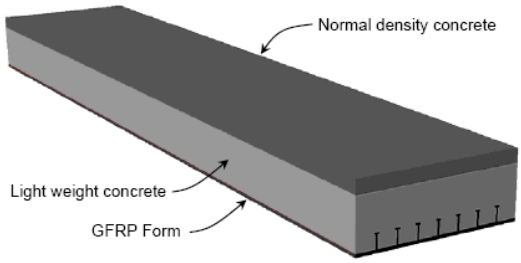

Figure 2.15 – Sandwich panel comprising a GFRP SIP formwork and concrete (Keller *et al.* 2007)

Concrete slab cast on FRP I-beam

Typical composite slab-on-girder construction involves steel I-beams and profiled steel floor decks that are overlaid with a concrete slab. A similar system was investigated (Li *et al.* 2006) in which both the steel I-beam and formwork were replaced with GFRP sections of comparable dimensions. The system consisted of a pultruded GFRP I-beam (with unidirectional longitudinal fibres) overlaid by pultruded GFRP ribbed sheets (E-shaped sections) oriented horizontally. These ribbed sheets (Figure 2.8(c)) acted as permanent stay-in-place formwork for the concrete slab which was cast on top of the sheets, as shown in Figure 2.16. The ribs on these E-shaped sections could bear the weight of the wet concrete. This could also potentially aid in providing the completed system with improved flexural strength and stiffness in the transverse direction; however, this characteristic was not studied. FRP bolts were used to connect the E-shaped sections to the I-beams. These bolts also behaved as shear studs in order to ensure monolithic composite action between the concrete slab and the FRP sections. The resultant composite girders were tested in four-point bending. Concrete strength and slab thickness were the primary test parameters varied; however, some specimens also included a laminate of CFRP bonded to the bottom flange of the I-beam to improve flexural stiffness and strength. The general mode of failure observed was longitudinal shear splitting of the web of the GFRP I-beam. This proved to be a brittle mode of failure. The specimens with thicker concrete slabs gave some warning of failure when the bottom of the concrete slab began to crack. This, however, was unrelated to the shear failure mode. It simply illustrated that the neutral axis in the specimens was located within the concrete slab. These cracks served as an indication that significant deflections were occurring. The stiffness of the members was largely dictated by the thickness of the concrete slab. A relatively large percentage of the deflection was caused by shear deformations occurring within the web of the beam. As a result, the CFRP layers provided very little contribution to stiffness. Also, since the specimens ultimately failed in shear, the addition of the CFRP layers yielded no increase in ultimate strength (Honickman, 2008).

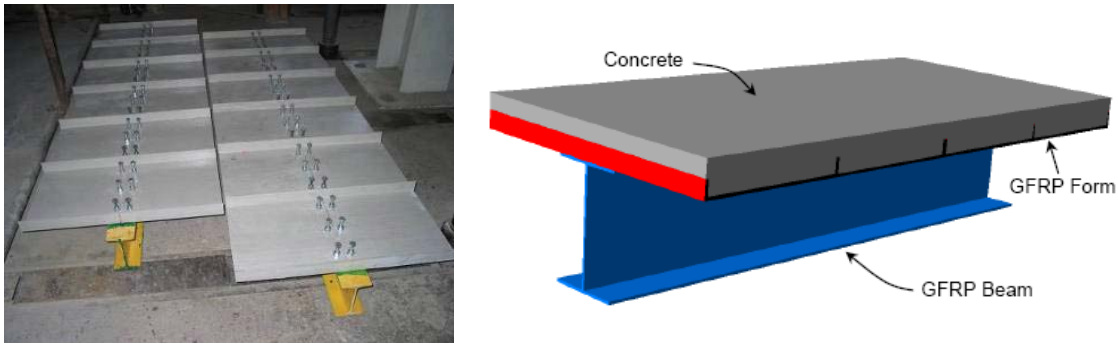

Figure 2.16 – FRP composite slab-on-girder design (Li *et al.* 2006)

FRP box beam with concrete in the compression zone

One of the first hybrid concepts to make use of shear connection systems, as proposed by Descovic *et al.* (1995), consists of a rectangular GFRP filament wound box section with an upper layer of concrete and a thin layer of CFRP bonded to the lower flange (Figure 2.17). Note that the top concrete layer is encased in a GFRP channel with wall thickness just equal to that required to carry the wet concrete and to transfer the GFRP/concrete interface shear stress. The concrete slab behaves as the compression flange of the member. The upper flange of the GFRP box section behaves as a SIP formwork for the concrete slab, which simplifies the construction process considerably. Bond between the concrete and the GFRP section is facilitated by the application of a two-part epoxy adhesive prior to pouring the wet concrete. The hybrid member also included a CFRP laminate bonded to the bottom surface of the bottom (tension) flange of the GFRP box section, to increase flexural stiffness. Also, because CFRP has a lower failure strain than that of GFRP, the CFRP layer would fail prior to the tension flange of the GFRP section, thus providing warning signs of imminent flexural failure (pseudoductility). This is important since FRP and concrete are both brittle materials that do not provide obvious warning signs prior to failure.

A number of potential failure mechanisms have been studied analytically for this hybrid member. The webs may buckle or fracture, resulting in shear failure; one of the beam's elements could exhibit a flexural failure; the bond between the GFRP section and the concrete slab could fail; and the concrete slab could fail in diagonal shear. The most common mode of failure observed experimentally was debonding between the GFRP section and the concrete slab. Despite this

unfortunate premature failure mode, the flexural response of the specimens showed good pseudoductility as a result of the CFRP fracture. This study, like the other ones presented earlier, highlighted the potential of hybrid members composed of hollow GFRP sections overlain with concrete slabs, but it also illustrated that such hybrid systems are highly dependent upon the quality of the shear bond between the concrete and the GFRP section. However, the beam shown in Figure 2.17 is rectangular beam, which in reality is seldom used. In building and bridge construction, there is always a T-section beam or a slab, so the tests of this prototype system in this study did not represent the real case in building construction. Further research on hollow FRP box sections with a thin concrete top layer, similar to those originally proposed by Descovic *et al*. (1995), were performed by Canning *et al*. (1999) and Huallat *et al*. (2003). The investigation of different configurations of hybrid beams showed that the best method of ensuring fully composite action between the FRP and the concrete was to apply fresh concrete onto a water-based adhesive. The failure mechanism in this case was concrete crushing and local buckling of the FRP component. However, it was realised that this bonding technique is impractical on site. Therefore, investigation into providing a practical, robust mechanical shear bond between concrete and GFRP formwork seems to be the key element for such a hybrid system.

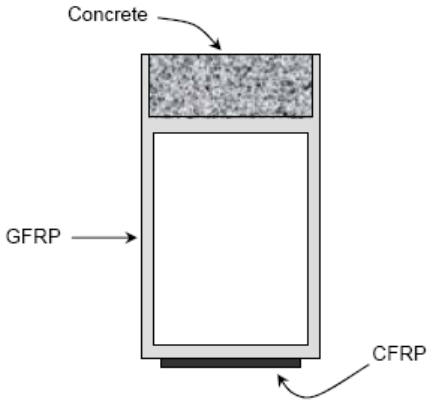

Figure 2.17 – GFRP-concrete hybrid flexural member (Deskovic *et al.* 1995)

FRP moulded grating with concrete in the compression zone

A study of the behaviour of one-way concrete slabs reinforced with FRP moulded grating were carried out by Larralde (1992). Commercially available

FRP moulded grating is mainly used as walkway panels for use in highly corrosive environments. The covered grating, which has an integrated flat plate moulded on top, as shown in Figure 2.18, can be turned upside down to use as a formwork for concrete, combining the FRP moulded grating with concrete, thereby forming a composite deck, can significantly increase the stiffness and serviceability characteristics of the system. As a result, the allowable load for a given maximum deflection is considerably increased (Larralde, 1992). A total of eight specimens, as shown in Figure 2.19, were fabricated with variable concrete depths and were tested in four-point bending under various shear-span to depth ratios. Unsurprisingly the stiffness of the grating-concrete composite was found to be considerably greater than that of the FRP grating alone. The increase in stiffness was found to depend on the thickness of the concrete layer added to the grating. For specimens 1 and 2 with shear-span to depth ratios of 7.7 or higher, failure occurred as crushing of concrete in the compression zone. For specimens 3 and 4 with shear-span to depth ratios of 5 or lower, failure occurred due to diagonal tension cracking. Based on these experimental results, Larralde (1992) concluded that the FRP moulded grating-concrete composite has to fail in shear when the shear-span to depth ratio is lower than 5. The shear failure in the specimens presented here started as diagonal tensile cracking and extended as longitudinal shear cracking at the grating/concrete interface. Four of eight beams were also reinforced with vertical studs consisting of either FRP bars or steel bolts attached to the grating, in order to increase the shear capacity. However, shear studs used in the tests did not seem to be sufficient to prevent failure due to cracking caused by diagonal tension or by shear at the grating/concrete interface.

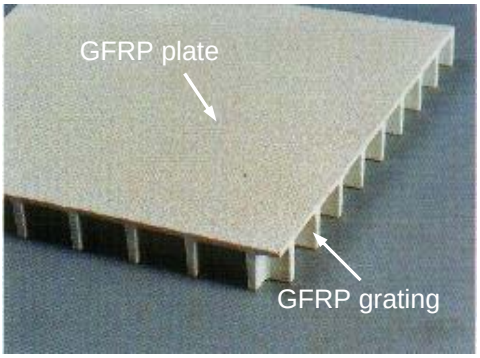

Figure 2.18 – Hollow grating with a flat plate (Exel Composites, 2008)

As part of Larralde's experimentation, it was found that due to vertical shear studs, the load capacity after failure did not drop completely to zero but rather down to approximately 55% of the maximum load. However, the drop in load capacity after the specimens reached its peak load was still sudden. Because only a small number of FRP dowels (3, 4 or 6) were introduced in a limited number of tests (four tests only), definite conclusions from these tests cannot be made. These dowels were spaced evenly along the span, not particularly installed in high-shear zones. In order to verify whether the vertical shear studs are sufficient to prevent shear failure, optimum numbers of shear studs and embedded positions should have been investigated.

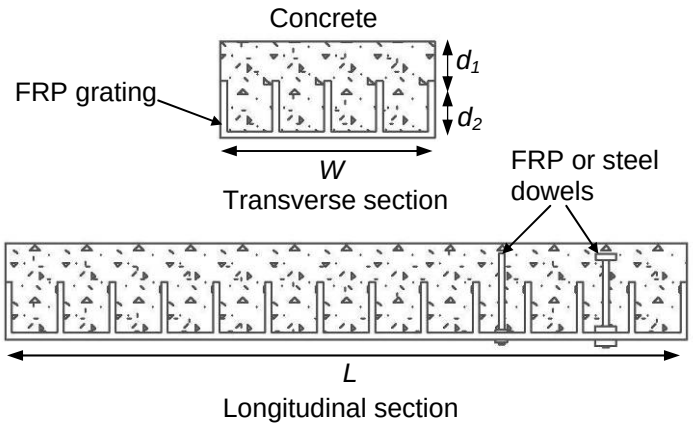

Figure 2.19 – Transverse and longitudinal cut-through views of beam specimens (Larralde, 1992)

Table 2.1 – Dimensions of the FRP grating-concrete beam specimens (Larralde, 1992)

Specimen	W (mm)	d_1 (mm)	d_2 (mm)	L (mm)	Shear studs
1	152	44.5	44.5	1828	None
2	152	50.8	44.5	1828	None
3	152	101	44.5	1828	None
4	152	140	44.5	1828	None
5	152	70.0	44.5	914	3 FRP dowels
6	152	70.0	44.5	914	4 FRP dowels
7	152	70.0	44.5	914	6 FRP dowels
8	152	70.0	44.5	914	6 steel dowels

Concrete-filled FRP tubes (CFFTs) with a concrete slab on top

CFFTs have been proposed and have been used as bridge girders, using CFRP circular tubes (Seible *et al.* 1997) and were also tested in composite action with GFRP and concrete deck, using steel rebars as shear connectors. Rectangular CFFTs made of GFRP tubes with inner ribs have been tested by Mirmiran *et al*. (1999) and have shown excellent composite action. Fam *et al*. (2005) developed and tested rectangular concrete-filled filament-wound GFRP tubes in flexure, where GFRP tubes were either totally filled with concrete or partially filled to

reduce self-weight, by having an inner hole placed eccentrically toward the tension side such that the concrete fill was optimally used in compression and shear. Later Fam and Skutezky (2006) added a thin concrete layer on the top of the concrete-filled pultruded rectangular GFRP tubes, mechanically bonded using GFRP dowels embedded into the tubes, as shown in Figure 2.20. The research studied the effects of concrete filling of the tubes, length of shear span, and CFRP lamination of the GFRP tension flange. Seven beams were tested in four-point bending in this study in order to assess the aforementioned parameters. In rectangular GFRP tubes without a thin layer of concrete overlay, concrete fill in the tubes was found to have a substantial effect on flexural strength but a small effect on stiffness, whereas in tubes with slabs, concrete fill in the tubes was found to have a substantial effect on stiffness but a small effect on strength. It is clear that the concrete in the tension zone could not contribute to any increase in strength once the concrete had cracked, as the tubes were used entirely in tension. The experiments also demonstrated that dowels used in the concrete-filled GFRP tube-slab system provide more slip resistance and more composite action than those used in the hollow GFRP tube-slab system. In the former, dowels are embedded in concrete from both sides and subjected mainly to shear. In the latter, the GFRP flange does not provide sufficient fixity and the dowels deflect and become subjected to bending in addition to shear. The tests also demonstrated that adding a concrete slab to a concrete-filled GFRP rectangular tube enhances its flexural strength and stiffness. However, this changes the failure mode from shear failure of GFRP dowels to rupture of GFRP tension flange, which is sudden and brittle.

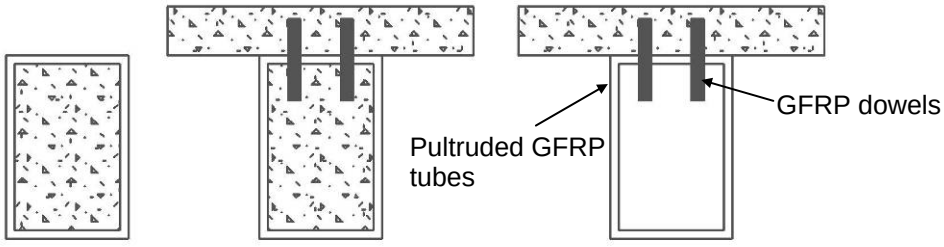

Figure 2.20 – Concrete-filled FRP tubes with a concrete slab on top (Fam and Skutezky, 2006)

2.5 Cost of FRP SIP Structural Formwork

The initial cost of using FRP stay-in-place (SIP) structural formwork is likely to be higher than conventional steel formwork; however, the overall cost will be

compromised by the saving on construction and long-term maintenance costs. Bank (2002) conducted a cost comparison between FRP bridge decks and conventional reinforced concrete bridge decks. In terms of rough cost, the lower bound for current FRP decks appears to be \$ 700/m^2 (£ 453/m^2, 1 U.S.dollar = 0.647 British pounds, 2012), which corresponds to about \$ 7/kg (£ 4.52/kg, 2012) of material. This cost is greater than the roughly \$ 322/m^2 (£ 208/m^2, 2012) typically quoted for the construction of a new bridge or a deck replacement with conventional materials (Lopez-Anido, 2001). However, the higher costs of FRP decks can be absorbed in certain conditions, particularly when a complete reconstruction is necessary in the absence of a lightweight deck alternative. It remains to be determined if the higher initial cost of FRP decks can be justified based on other economic considerations, such as cost saving due to reduction in construction time and labours, closure for road traffics and maintenances.

Berg *et al.* (2006) conducted a cost analysis of concrete highway bridge constructed using FRP materials as reinforcements and SIP structural formwork. Three forms of FRP reinforcing were combined to reinforce the concrete deck: FRP SIP structural formwork, deformed FRP reinforcing bars, and a special prefabricated pultruded FRP reinforcing grid. The construction of this FRP reinforced concrete bridge deck using conventional construction technology and labour was accomplished with a 57% savings in concrete labour over a nominally identical steel rebar reinforced deck. Material costs for the FRP reinforced deck bridge were 60% higher than that of the steel reinforced deck bridge. Based on the analysis of the short-term material and labour costs it appears that given the savings in construction time and their potential long-term durability and maintenance benefits, FRP reinforcements for bridge decks should be cost-effective notwithstanding their currently high initial costs. Future optimisation of the design of FRP SIP formwork and competitive biding between FRP manufacturers is recommended to decrease the cost of the FRP reinforcement system.

2.6 Ductility in FRP-Reinforced Concrete Structures

In practice it is necessary for concrete structures to exhibit a ductile failure and forms a crucial part of the design process. Steel-reinforced concrete members are under-reinforced in order to achieve a ductile response as the steel yields

prior to concrete crushing. However, FRPs exhibit linear elastic behaviour up to ultimate tensile rupture, so failure of FRP-reinforced concrete members is brittle, with either the concrete crushing or the FRP rupturing. Therefore, ductility in FRP-reinforced concrete structures can not be provided in the conventional way.

Burgoyne (2001) suggests that since the failure of FRP reinforcement is sudden and catastrophic, then structures should be designed so that the concrete fails first, rather than for the FRP to rupture. The reason for this is that while FRP behaves virtually linear-elastically to material rupture (for actions aligned with continuous fibre reinforcement), concrete crushes in a moderately non-linear way, so that at least some ductility is displayed during crushing. Thus it is desirable to over-reinforce FRP-reinforced concrete members, forcing concrete crushing before FRP rupture. If the structures are to be over-reinforced then it is necessary to increase the strain capacity of the concrete in the compression zone by the use of confinement reinforcement, as concrete still crushes in a rather brittle fashion. The investigation of seeking an appropriate method to confine the concrete will be discussed in the subsequent chapters.

2.7 Fire Protection of FRP

The performance of FRP-strengthened structures in fire is of great concern for application of FRP in buildings. In many situations, concerns about fire resistance can severely restrict potential applications of FRP. The fundamental problem is that FRPs are inherently combustible. Furthermore, typical polymer resins for FRPs for civil engineering applications typically have glass transition temperatures between 60°C and 80°C (Bisby *et al*. 2005). At temperatures above the glass transition temperature, the polymer softens and degrades. Thus, the load-sharing function of the polymer resins suffers and individual fibres may become overstressed and break (fib, Bulletin 14, 2001). This will lead to eventual failure of the FRP structure at a reduced load capacity. In principle, some fibres themselves are inherently resistant to high temperature. Unfortunately, when combined with the resin as a composite, the high temperature resistance drops considerably. At temperatures between 250°C and 400°C, most composites lose half of their original tensile strength (Green *et al*. 2007). Current information about design requirements for applying FRP as external reinforcement in buildings is either not available or misunderstood. More knowledge and

understanding of the behaviour of FRP strengthened and reinforced concrete structures is still required before detailed design requirements can be established but some preliminary proposals for design procedures are made by Green (2007).

FRPs need to be designed with some type of fire protection to restrict the evolution of smoke and prevent excessive flame spread. The specific requirements will depend on the classification of the buildings. It should be noted that most commercial FRP systems have formulations or coatings that meet the requirements of most building codes. FRP-strengthened concrete structures can have adequate performance in fire, and can achieve fire endurance ratings of more than four hours if suitable insulating fire protection is provided (Bisby, 2005). The best potential design approach for FRP-strengthened concrete structures is to apply performance-based design procedures, such procedures are already recommended by fib Bulletin 14 (2001). Therefore, although FRPs have definite fire issues, with thought they can be designed appropriately to resist fire.

2.8 Local Buckling of Thin-Walled FRP Profile

Conventional pultruded GFRP profiles are especially susceptible to local buckling under transverse loads due to the low in-plane modulus and the slenderness (width-to-thickness ratio) of the plate elements, referred as walls, which make up the thin-walled profile. Local buckling in compression flanges of beams has been demonstrated in numerous tests (Barbero *et al*. 1991; Bank *et al*. 1994; 1996; 1999).

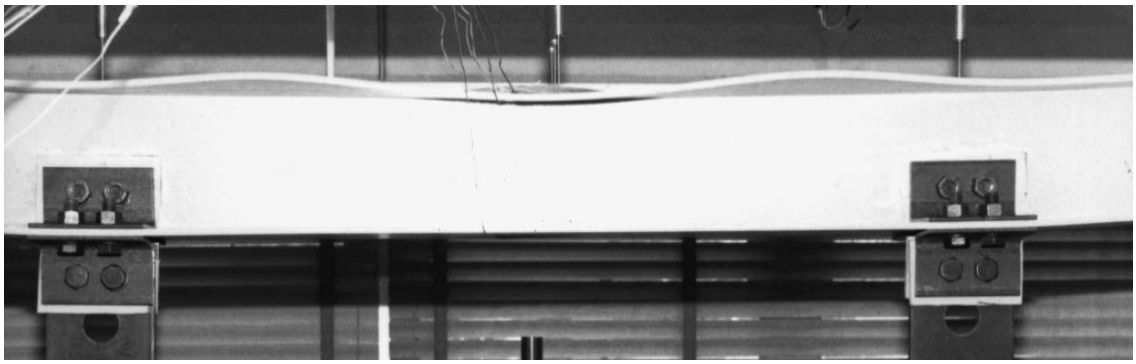

Figure 2.21 – Postbuckled compression flange in pultruded beam tested in pure bending (Bank *et al*. 1999)

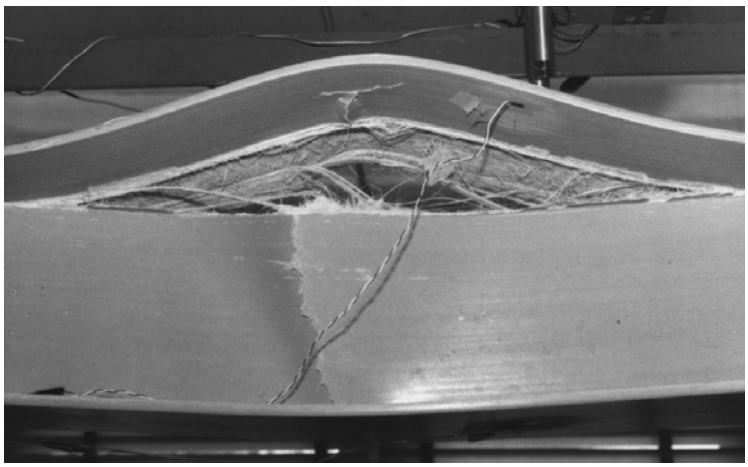

Figure 2.22 – Separation between flange and web in pultruded beam tested in pure bending (Bank *et al*. 1999)

The failure mode of thin-walled profiles is caused by the separation of the compression flange of the profile from the web after the compression flange has buckled elastically and is in its postbuckled deformation. This type of failure mode has been observed by a number of authors (Bank *et al*. 1994; Palmer *et al*. 1998 and Charoenphan *et al*. 2003). It has been observed experimentally in these researches that a unique mode of progress failure, termed ‘local buckling failure’, can occur in pultruded I-beams and box sections in which the walls of I-beams and box sections separate from each other at their junctions as loading progresses. Figure 2.21 shows the local buckling of the compression flange in the constant moment region of a transversely loaded wide-flange pultruded profile. If the load is increased in the post buckled regime (beyond the elastic buckling load), the amplitude of the flange deformation increases and separation failure occurs at the junction between the flange and the web. This failure propagates rapidly along the junction, leading eventually to a large region of separation between the flange and web. This is followed immediately by in-plane buckling of then-unsupported webs as shown in Figure 2.22 (Bank and Yin, 1999). As the instant of initial separation, load capacity drops and continues to decreases as the separation continues. By definition the profile has collapsed at this point because the load-carrying capacity has decreased and the geometrical configuration of the section has changed dramatically.

This type of failure mode has also been observed by Mottram (1991). Twenty-three tests have been used to evaluate a simplified design analysis developed by Johnson (1985) for the ultimate resistance of pultruded GFRP box

beams. Johnson's buckling analysis assume failure in any one of five distinct modes of elastic failure – compression flange buckling, tension material failure, compression material failure, shear material failure and shear buckling in the side wall. This analysis assumes there is no interaction between bending and shear failure, thus the ultimate load for a beam is the lower of the two. Four different hollow box section profiles in a total number of 23 pultruded box sections have been tested under three-point bending with a number of different spans, varied from 300 mm to 1600 mm. For each beam, initiation of longitudinal cracks were observed with acoustic emission in the form of 'snap' at a load below the maximum attained, as illustrated in Figure 2.23. These cracks beneath the central load nose are very important as they can affect the final mode of failure.

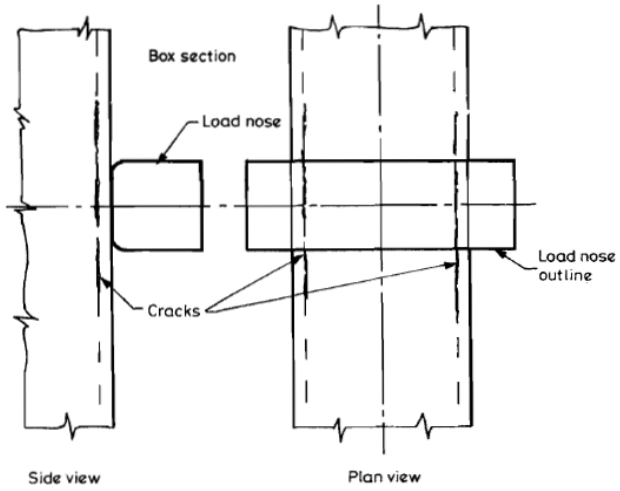

Figure 2.23 – Longitudinal cracks under the central load nose (Mottram, 1991)

The short term strengths and modes of failures were used to establish the limitations of the Johnson's analysis. The test data can be divided into two categories: long span and short span. When the span was long, which span-to-depths is above 17.7, the failure mode appeared to be one of the five assumed in the analysis. In all the long-span specimens, ultimate failure was found to have occurred in the top compression flange beneath the load nose. For the beam specimens with thick walls (6 mm) the ultimate resistance was found to be controlled by compression strength of materials. The predicted ultimate bending load for the beams with thin walls (2 and 3 mm) was close to that given by assuming the mode of failure to be compression flange buckling.

Figure 2.24 gives a schematic illustration of the observed local deformation beneath the load nose. It was found that the Johnson's analysis gave good estimates of the bending load at ultimate failure when comparing with the experimental data, proving that a modification is made for thick walls (Mottram, 1991).

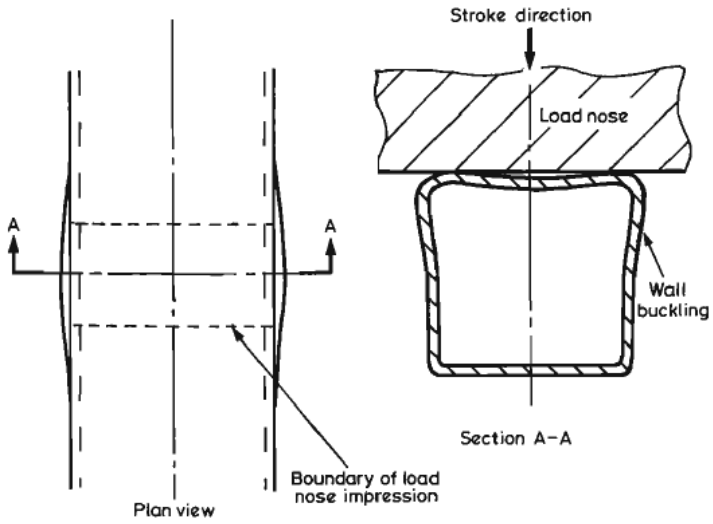

Figure 2.24 – Schematic illustration of local wall buckling (Mottram, 1991)

When the span was short, for span-to-depth below 11.9, the failure was not one of the five distinct modes assumed in the analysis. Here failure was found to be progressive. The longitudinal cracks, first appearing after the audible acoustic emission, were seen to control the complex failure mode in the specimens with side walls 2 and 3 mm thick. A schematic representation of this mode of failure is given in Figure 2.25. The experimental evidence indicated the resistance and mode of failure of short-span box beams depended on the bearing area of the nose distributing load into the non-yielding fibre-reinforced composite material. In view of this evidence, the simplified design analysis was found to be inappropriate when the span was short (Mottram, 1991).

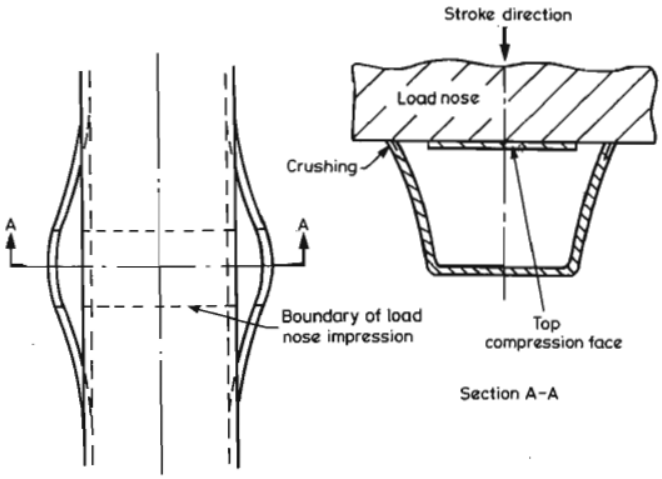

Figure 2.25 – Failure mode of box section when span is short and wall thickness is 'thin' (Mottram, 1991)

2.9 Summary

The reviewed research shows a high potential for hybrid FRP-concrete construction where the FRP is utilised in tension and the concrete is utilised in compression. Each developed system shows distinct advantages and disadvantages. The main structural issues highlighted in previous research are local buckling of FRP hollow sections, lack of ductility of the overall system, insufficient shear transfer between the FRP and concrete to maintain full composite action, and complicated manufacturing processes which are impractical for most applications. The novel hybrid FRP-concrete floor system proposed in this research provides a potential solution to at least most of these problems.

Chapter 3 Composite GFRP-Concrete Floor System

3.1 Introduction

The previous chapter highlighted various structural issues surrounding the effective use of an FRP-concrete hybrid SIP formwork system, one of which was how bond is generated and maintained effectively between FRP and concrete. This chapter describes how the concept of the FRP-concrete hybrid SIP formwork system is developed and how ductility can be potentially achieved either at the FRP/concrete interface, through progressive longitudinal shear failure, or within the compression zone, through the controlled concrete crushing.

3.2 Rationale

In general, structures are designed to give reasonable warning before collapse. Building structures that are subjected to sudden failure mechanisms with little or no warning are highly undesirable. FRP composites and concrete typically exhibit little or no ductility, thus failure modes involving FRP fracture and concrete crushing will be brittle. The design of a composite FRP-concrete system must take account of this behaviour, preferably by ensuring that the failure of the structure is governed by a less brittle potential failure mechanism, and also preferably by giving forewarning of collapse, perhaps through ensuring that some serviceability limit state is reached prior to the ultimate limit state.

As lack of ductility is a key concern regarding the use of FRP SIP formwork in practice, investigating the means to achieve a robust bond between the FRP and concrete, leading to a ductile failure, is crucial. A potential solution is to extract ductility from the FRP/concrete bond interface through controlled longitudinal shear failure. In considering the design of the interface between the concrete and FRP, it is important to recognise the brittle failure behaviour of bond techniques attempted by others in this field (Hall and Mottram, 1998; Bank *et al*. 2007; Keller *et al*. 2007). Therefore, the fundamental behaviour of the FRP-concrete interface needs to be investigated.

Experimental work has shown that the performance of the interface between the concrete and FRP can be enhanced through the use of adhesives, roughening

of the FRP surface and the use of mechanical shear connector as discussed in Chapter 2. The first option, which is referred to as ‘Chemical bond’, involves application of epoxy adhesive at the FRP/concrete interface before the concrete is cast. It has been shown that this technique significantly improved the bond strength compared to an unbonded interface (Hall and Mottram, 1998; Canning *et al*. 1999; Keller *et al*. 2007). However, this option is deemed to be unrealistic for on-site construction and its associated debonding failure is brittle in nature. The second method is to roughen the FRP surface with coarse sand or gravel coating (Dieter *et al*. 2002; Bank *et al*. 2007). This technique relies on the mechanical interlock generated at the interface to enhance the bond, which is the most common method in FRP reinforcing for concrete structures, referred to as ‘Friction bond’. Nevertheless, brittle debonding failure remains a drawback for this technique.

As discussed in Chapter 2, several embedded mechanical shear connectors were introduced to achieve composite action between FRP and concrete: GFRP dowels (Larralde, 1992; Fam and Skutezky, 2006) and built-in T-upstand ribs in FRP planks (Hall and Mottram, 1998; Bank *et al*. 2007; Keller *et al*. 2007). It has been well established by these authors that the use of mechanical shear connectors provides better overall bond performance than that of adhesives or roughening of the FRP surface.

In the design of conventional reinforced concrete structures, efforts are made to ensure that the reinforcement yields before the concrete crushes. This is done to introduce ductility into the behaviour of the member. Conversely, however, for FRP-concrete systems it is possible that concrete crushing will be a more ductile, and therefore more desirable, failure mode than FRP fracture or a breakdown in composite action. In fact, if the strain capacity of the concrete in compression is enhanced, for example, by confining it, it is quite possible that concrete crushing could be associated with substantial non-linear deformation capacity (Ralph and Denton, 2004).

Experimental work by Burgoyne et al, 2001 has shown that by placing a circular FRP helix in the compression zone, the helix confines the concrete extraordinarily well. Tests by Burgoyne (2001) with aramid helical FRP reinforcement found that the strain capacity of the plain concrete (typically

0.0035) can be significantly increased with the introduction of confining reinforcement up to approximately 1%. The presence of aramid helix increases the concrete failure strain in compression zone so that the concrete is used to a greater extent, introducing real ductility into the systems. Therefore, it is feasible to use FRP reinforcement to confine the concrete, not necessary to be a helix, such as the moulded GFRP grating mentioned in Figure 2.7 in Chapter 2, to achieve extra strain capacity from the concrete. It is possible that the controlled concrete crushing, by confining the concrete with FRP grating, can introduce ductility to the FRP-concrete composite system.

3.3 FRP-Concrete Composite Floor Slab Assembly

The first prototype system was developed as a 300 mm wide, 100 mm deep and 3000 mm long double-layer grating system, as shown in Figure 3.1. The material used in this system is a moulded GFRP grating with an integrated flat plate, as seen in Figure 2.18 in Chapter 2. It consisted of two layers of the concrete-filled grating: The top grating (50 mm deep) in the compression zone acts compositely with the concrete to resist the compression, and the bottom grating (50 mm deep) in the tension acts as a tensile reinforcement. The moulded GFRP grating was selected as a SIP formwork for concrete as its lattice structure (42 x 42 mm square) allows the wet concrete to flow into the grating and forms a number of concrete studs which acts as mechanical shear connectors. Both layers are glued together with epoxy adhesive before the concrete is cast, and further connected with GFRP dowels embedded in the concrete afterwards. However, due to the relatively low longitudinal tensile modulus of 14 GPa and longitudinal tensile strength of 172 MPa of the grating, the bottom grating failed both the serviceability and ultimate limit state checks as a tensile reinforcement. Availability has prevented consideration of a deeper grating. Therefore, in order to fulfill the requirements of the stiffness in the serviceability limit state and strength in the ultimate limit state, pultruded GFRP box sections were introduced as a substitute for the bottom GFRP grating. This is because the pultruded profile has better tensile properties with a minimum longitudinal tensile modulus of 23 GPa and longitudinal tensile strength of 240 MPa and deeper sections (up to 300 mm depth) are available (Fiberline Composite, 2003).

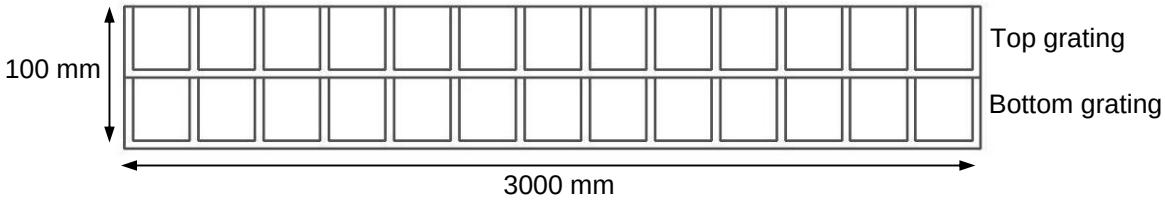

Figure 3.1 – Initial design of a double GFRP grating formwork system

Figure 3.2 presents the key sectional elements that constitute the proposed 300 mm wide, 150 mm deep and 3000 mm long FRP-concrete composite assembly. The proposed FRP-concrete composite floor slab consist of two layers of different materials: two pultruded hollow GFRP box sections (100 x 100 x 8 mm) to resist the tensile forces and a moulded GFRP grating filled with concrete (300 x 50 mm) to resist the compressive forces, as shown in Figure 3.3. FRP materials are inherently non-ductile, so other means of providing progressive failure of the system are required. Thus, to provide ductility, the concrete in compression is utilised. Mass concrete has minimal ductility, but by utilising a moulded GFRP grating filled with concrete in the compression zone, the concrete is confined, allowing at least 100% greater strain capacity to be developed and hence increasing overall ductility. This design was selected since the neutral axis of the section is located along the FRP/concrete interface, therefore the box sections are fully utilised in tension and the concrete filled grating are fully utilised in compression, both materials are in their optimum positions.

Figure 3.2 – GFRP dowels, moulded GFRP gratings, foam blocks, and GFRP box sections.

(From left to right)

Figure 3.3 – The proposed FRP formwork

The requirement to provide a robust connection between the GFRP box section and the concrete is addressed by using 10 mm GFRP dowels embedded into the concrete through the pre-cut holes at the top flange of box sections, as shown in Figure 3.4. Foam block was introduced in the box section, leaving a 40 mm gap which will be filled with concrete later. The purpose for inserting the foam block is to remove unnecessary concrete mass in the tension zone. More importantly, it holds the dowel in place before the concrete is cast, which benefit from the construction point of view. After the concrete is cured, the GFRP dowels are embedded into the concrete and acts compositely with concrete studs to resist the longitudinal shear at the grating/box-section interface. The function of GFRP dowels is to provide additional connection at both sides of the grating/box-section interface, preventing a brittle failure.

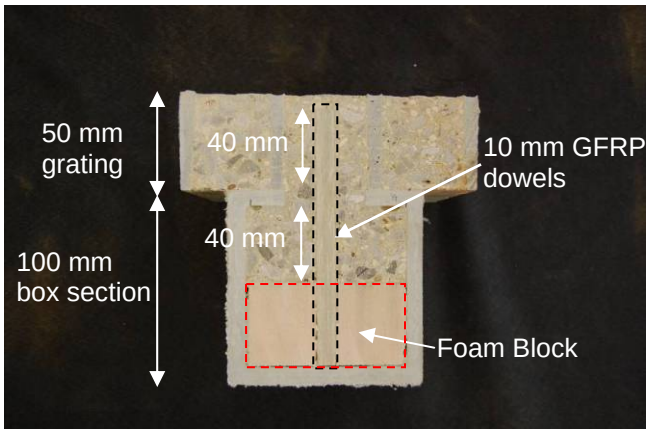

Figure 3.4 – GFRP dowels embedded in to the concrete

3.4 Summary

This chapter describes the design concept and key components of the proposed FRP-concrete composite system, consisting of two distinct layers – the concrete-filled grating and GFRP box sections. The layers are connected using

GFRP dowels through embedment in the concrete. In the next chapter, components in this system are investigated through coupon tests in order to obtain the material properties for designing of composite section.

Chapter 4 Characterisation of Materials

4.1 Introduction

The previous chapter described the design concept of the composite FRP-concrete hybrid formwork system. This chapter presents the test methodologies, rationales and experimental results for characterisation of the components of the proposed FRP-concrete hybrid formwork system. The European Standard EN 13706 (CEN 2002b) is currently the only published standards document that specifies minimum properties for pultruded materials. Property data provided in pultrusion manufacturer design guides are obtained from tests on coupons of pultruded materials taken from pultruded profiles. The properties given by manufacturers can be assumed to be lower bounds for the class of profiles indicated in the manuals (Bank *et al*, 2006). Therefore, coupon testing is recommended for obtaining the strength and modulus of elastic properties for design of composite slab sections.

4.2 Material Characterisation Tests

4.2.1 Moulded GFRP grating

Commercially available panels of moulded GFRP grating, fabricated by Fiberline Composites Ltd, were received in standard units of 1220 x 3658 mm, as shown in Figure 4.1. The moulded grating is fabricated using a square mesh pattern of glass fibres in bidirectional bundles which is laid down and then submerged in resin contained in a mould. The grating is 50 mm in depth with a fibre volume fraction of 35 - 40% and has a tensile strength and elastic modulus of 172 MPa and 14 Gpa, respectively, in both longitudinal and transverse direction. These values are obtained from the manufacturer with reference to EN 13706. The individual grid elements have a trapezoidal cross section with a nominal top width of 4.6 mm and a bottom width of 7.1 mm.

Figure 4.1 – Commercial available moulded GFRP grating

Rather than rely on the manufacturers data, the compressive elastic modulus and compressive strength of moulded GFRP grating in this study were determined from the coupons extracted and tested using the method outlined within BS EN ISO 14126 (1999). The test set-up is shown in Figure 4.2.

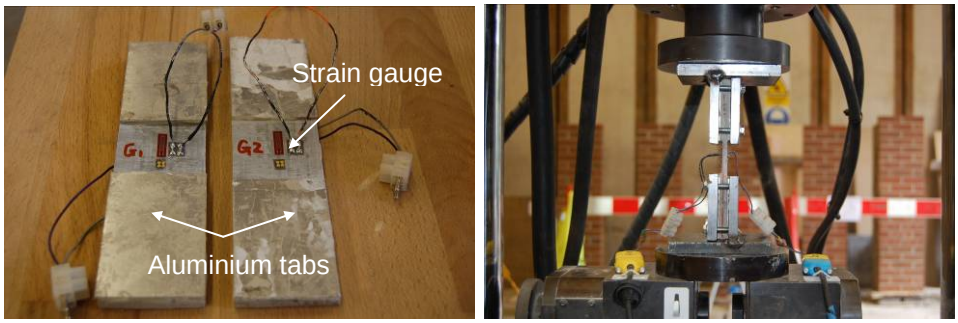

Figure 4.2 – The grating coupon specimens and compression test set-up

Two compressive coupon tests (G_1 and G_2) were carried out on 48.8 x 175 mm (width x length) coupons, to establish the compressive elastic modulus of the grating, as it was intended to be used in compression, acting compositely with the concrete, in the full slab specimens. It should be noted that only a limited number of coupons were tested due to the difficult manufacturing process of coupons.

The compressive load was applied by direct end loading of the specimens. Specimens G_1 and G_2 were tested in a universal 200 kN Dartec machine at a displacement rate of 1 mm/min. Failure was defined as the point at which maximum load resistance was reached. Aluminium tabs of 65 mm length were glued on both ends of the specimen to maintain a 40 mm gap between tabs. The tabs were glued on both sides of the coupon specimens using epoxy adhesive Araldite 2015 (Huntsman Advanced Materials, 2010). 10 mm electrical resistance strain gauges FLA-10-11 (Tokyo Sokki Kenkyujo, 2010) were glued on both sides at the central-region of the specimen back-to-back in order to capture the strain measurements.

The compression test results of the grating are summarised in Table 4.1. The mean values were calculated in accordance with BS EN ISO 14126. The modulus of elasticity was calculated by:

$$E = \frac{\sigma_2 - \sigma_1}{\varepsilon_2 - \varepsilon_1} \tag{4.1}$$

where ε_1 = 0.0005, ε_2 = 0.0025, σ_1 is the corresponding stress at ε_1 and σ_2 is the corresponding stress at ε_2.

The ultimate stress, σ_{ult}, is defined as the peak load resistance divided by the cross section area of the specimens, using:

$$\sigma_{ult} = \frac{P}{A} \tag{4.2}$$

where P is the peak load and the cross section area A, is given by: $A = \frac{1}{2}(T_{top} + T_{bottom})d$, T_{top} is thickness of the top surface, T_{bottom} is thickness of the bottom surface, d is depth of the component specimen.

Failure strain, ε_{ult}, is calculated by using the ultimate stress divided by the modulus of elasticity determined in Eq. (4.1), assuming there is a linear-elastic stress versus strain relationship as shown in Eq. (4.3):

$$\varepsilon_{ult} = \frac{\sigma_{ult}}{E} \tag{4.3}$$

Table 4.1 – Summary of grating coupon test results

Coupons	T_{top} (mm)	T_{bottom} (mm)	d (mm)	L (mm)	L_o (mm)	Failure mode	E_1 (GPa)	E_2 (GPa)	σ_{ult} (MPa)	ε_{ult} (%)
G_1	7.2	4.8	48.7	175	40	Splitting of fibres	24.3	23.1	243	1.03
G_2	7.1	4.6	48.9	176	42	Splitting of fibres	24.2	25.7	329	1.32

The average compressive modulus of the grating calculated from the coupon tests is 24.3 GPa, as determined from Eq. (4.1), which is higher than the manufacturer's specified elastic modulus value (14 GPa) by 73.6%. These compressive coupons failed by splitting of the fibres in the central regions, as shown in Figure 4.3. The stress versus strain plots of specimens G_1 and G_2 are presented in Figures 4.4 and 4.5. It should be noted that the stress reading in Figure 4.5 for specimen G_2 on side A stopped at 280 MPa prior to reaching its ultimate stress due to failure of strain gauges.

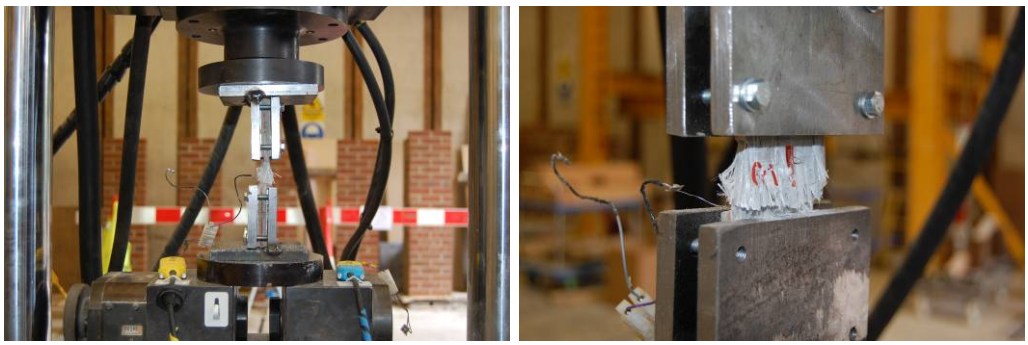

Figure 4.3 – Fibre delaminating and crushing of the GFRP grating coupons

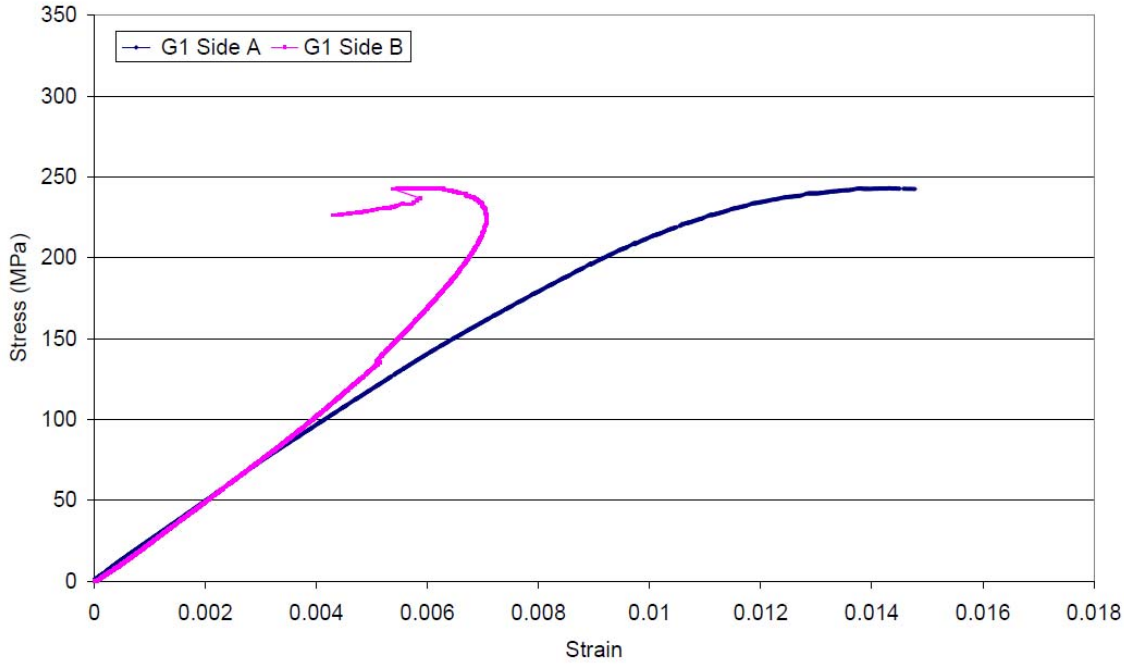

Figure 4.4 – Stress vs. strain plot of the grating coupon specimen G_1

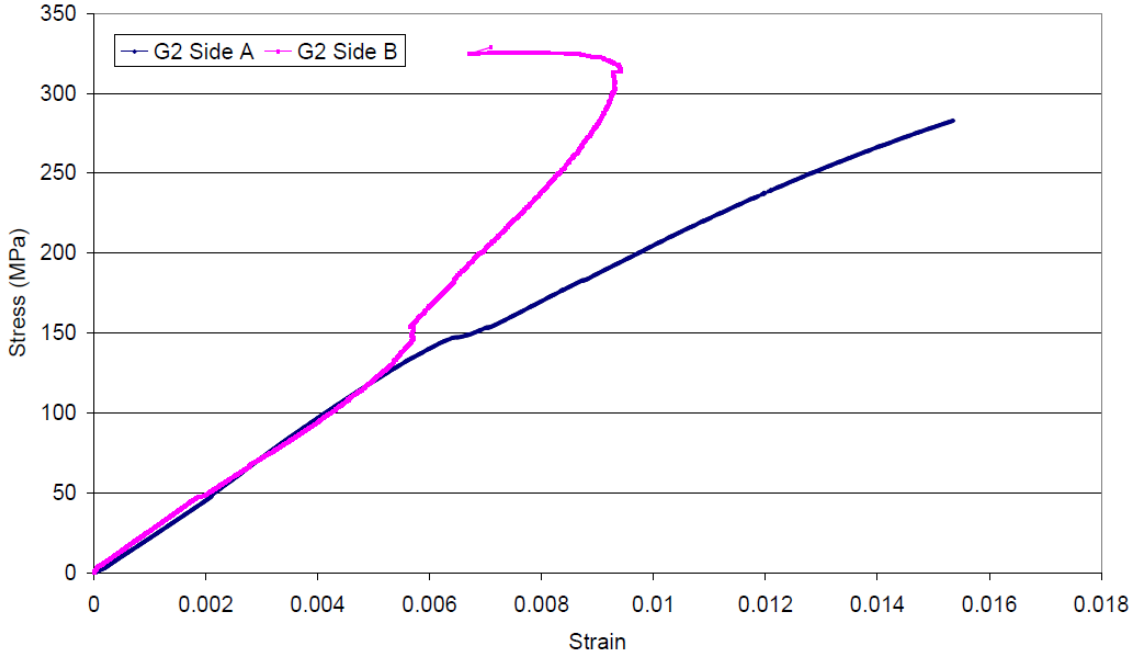

Figure 4.5 – Stress vs. strain plot of the grating coupon specimen G_2

As shown in Figures 4.4 and 4.5, there was a discrepancy in stress versus strain plots at both sides when strain reading exceeds 0.004. This difference was the result of the specimen buckling, when the strain on the opposite faces increased and decreased rapidly. Specimen G_1 buckled at 80 MPa and specimen G_2 buckled at 130 MPa. However, it is quite clear from the Eq. (4.1) that the stress reading was taken at strain reading equals 0.0005 and 0.0025. Therefore, this discrepancy has no effect on the calculation of elastic modulus. The failure strength of specimens G_1 and G_2 were 243 MPa and 329 MPa respectively. The discrepancy in strength might be caused by the buckling of both specimens during the tests. It is apparent from visual inspection during the test that the coupons buckled before the ultimate failure when fibre delaminating occurred at 60 to 67% lower stress compared with their ultimate stress.

4.2.2 GFRP box section

Commercially available 6 m long GFRP pultruded box sections manufactured by Fiberline Composites, Denmark, were used as the tension component. The section is 100 mm square with a nominal wall thickness of 8 mm. The manufacturer reported data indicates the box section had a tensile and compressive strength of 240 MPa and a tensile and compressive elastic modulus of 23 GPa in longitudinal direction. These values were obtained by the manufacturer according to European Standard EN 13706, which can be taken as the characteristic material properties (Fiberline Composites, 2003).

For the purpose of the design, the longitudinal (fibre direction) tensile and compressive properties of GFRP box section (strength and elastic modulus) were determined from the coupons extracted from the box section and tested using the method outlined within BS EN ISO 527-5 (2009). The coupon specimens and tensile test set-up is shown in Figure 4.6.

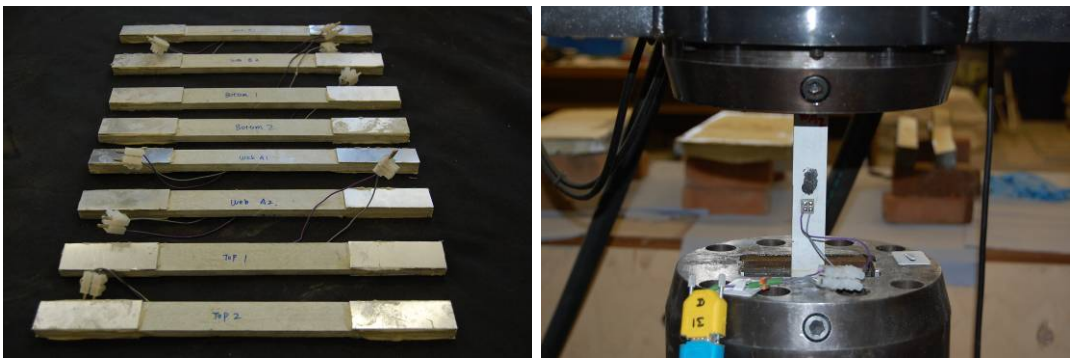

Figure 4.6 – Box section coupon specimens and tensile test set-up

Eight specimens were prepared and tested in a universal 200 kN Dartec machine at a displacement rate of 2 mm/min. The final failure was defined as the point at which maximum load resistance was reached. Coupons were cut from top flange, bottom flange and both webs, referred to as specimen ‘Top’, ‘Bot’, ‘WA’ and ‘WB’. The length of the specimens ranged from 300-302 mm, the thickness from 7.8-8.5 mm and the width from 25.1-25.7 mm. The variation in specimen dimensions was due to both the pultrusion and cutting processes. All specimens were strain-gauged with 10 mm electric resistance strain gauges in the central regions on one side. Aluminium tabs of 75 mm length were bonded on both ends of these coupons to avoid slip between coupons and jaws of the machine, preventing local failure of coupons at the jaws due to high grip pressure required.

Figure 4.7 shows the stress versus strain plots of the eight coupon specimens tested in tension. These coupon specimens failed due to the snapping of the outer mat layers at the jaws and splitting of the fibres, as shown in Figure 4.8. It should be noted that half of these coupons did not reach ultimate failure strength, as the aluminium tabs failed prematurely. This undesired tab failure is shown in Figure 4.9. The tensile modulus of elasticity was calculated from Eq. (4.1). A summary of test results is shown in Table 4.2.

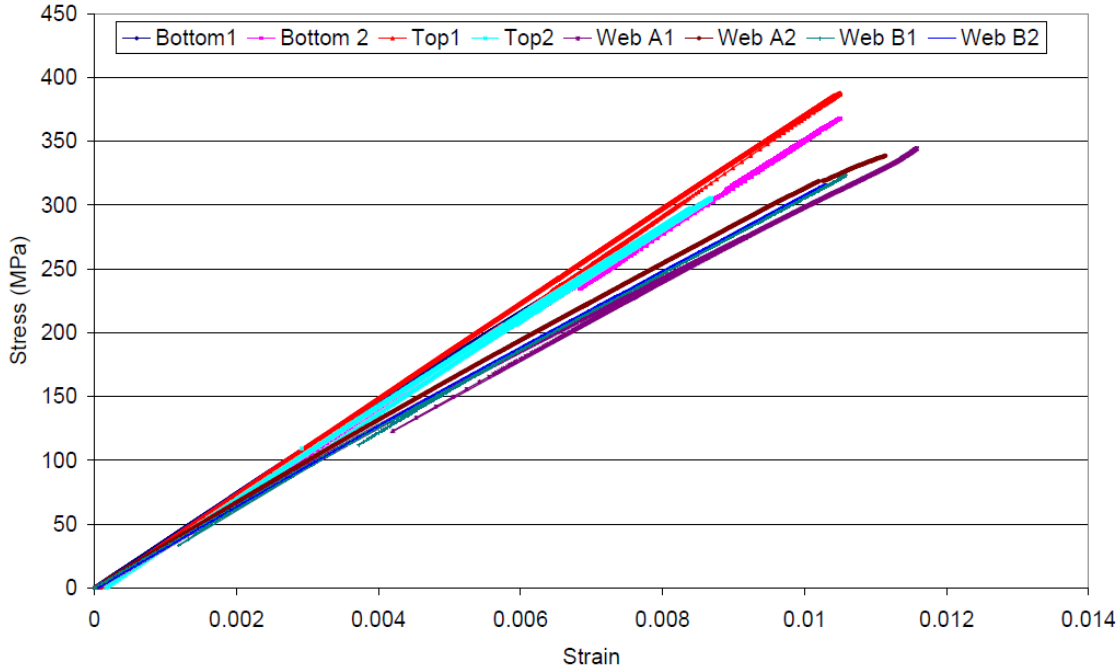

Figure 4.7 – Stress vs. strain plot of coupon specimens tested in tension

Figure 4.8 – Splitting of the fibres and fibre outlayer snapping adjacent to the tabs

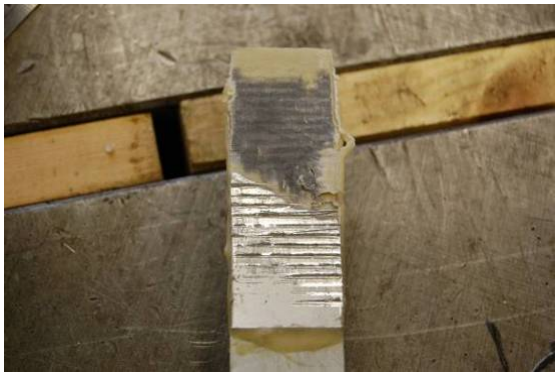

Figure 4.9 – Premature rupture of tabs in the jaws of the machine

As shown in Figure 4.8, in most cases, fibre snapping occurred in the jaws of the machine, rather than the central region where the strain gauges were located. Based on these coupon test results, the average longitudinal tensile modulus was founded to be 32.1 GPa, which is 40% higher than the manufacturer's

specified elastic modulus (23 GPa). The average tensile strength, determined by specimens 'WA_1', 'WA_2', 'WB_1', and 'WB_2', was 355 MPa, 48% higher than the manufacturer's specified tensile strength (240 MPa). Keller (2004) carried out material characterisation tests on similar profiles with different plate thickness. In his tests, the coupons were also cut from standard structural profiles manufactured by Fiberline Composites. The mechanical properties of the profiles were determined through full-scale tensile tests and listed in Table 4.3 for the 5 and 10 mm thick profiles. It was also found by Keller that the 3, 4, 6, 8 and 12 mm thick profiles showed similar results. Table 4.3 shows the comparison of coupon test results from the author, Keller and manufacturer's design manual.

Table 4.2 – Summary of coupon tensile test results

Tensile properties	*T*- thickness (mm)	*W*- width (mm)	*L*- total length (mm)	L_o- distance between grips (mm)	*E*- elastic modulus (GPa)	Failure mode	σ - Failure stress (MPa)	ε - Failure strain (%)
Top_1	7.8	25.1	302	150	31.3	Tab failure	N/a	N/a
Top_2	7.9	25.4	301	151	32.1	Tab failure	N/a	N/a
Bot_1	8.5	25.5	301	150	33.2	Tab failure	N/a	N/a
Bot_2	8.5	25.4	301	151	32.6	Tab failure	N/a	N/a
WA_1	8.2	25.2	300	150	32.4	Splitting of fibres	357	1.10
WA_2	8.2	25.2	301	151	31.5	Splitting of fibres	345	1.09
WB_1	8.0	25.4	301	151	31.8	Splitting of fibres	351	1.10
WB_2	7.9	25.7	300	150	32.2	Splitting of fibres	368	1.13
Average					32.1		355	1.10

Table 4.3 – Comparisons of coupon tensile test results

Profiles	Failure stress (MPa)	Failure strain (%)	Longitudinal elastic modulus (GPa)
100 x 8 mm (8 specimens)	355	1.10	32.1
100 x 5 mm (8 specimens)*	434	1.38	34.4
100 x 10 mm (8 specimens)*	332	1.03	32.5
Manufacturer's design data	240	-	23
* shows the full-scale tensile tests by Keller, 2004			

As can be seen from Table 4.3, close agreement between coupons test results conducted by the author and Keller was found, in terms of the failure stress, failure strain and the modulus of elasticity.

The longitudinal compressive modulus was also measured by compression tests using the same test rig as described previously in Section 4.2.1. The coupon specimens and compression test set-up are shown in Figure 4.10. The dimensions and test results of the specimens are summarised in Table 4.4. It should be noted that there was no tab glued on coupon specimens tested in compression.

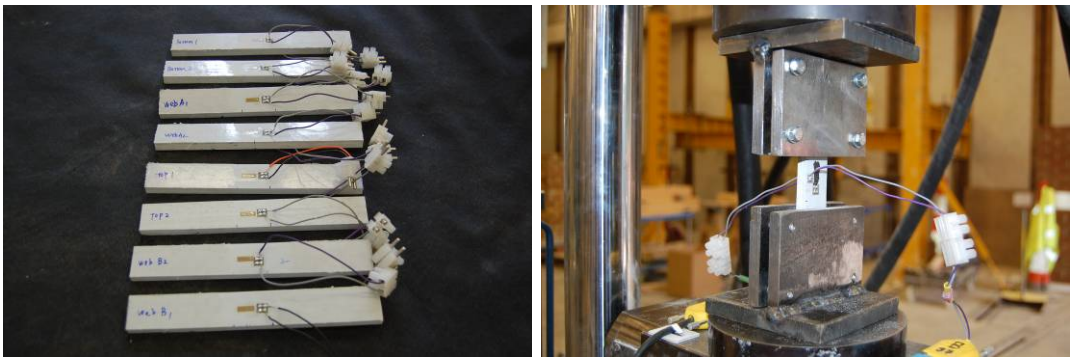

Figure 4.10 – Box section coupon specimens and compression test set-up

Table 4.4 – Summary of coupon compressive test results

Compressive properties	*T*- thickness (mm)	*W*- width (mm)	*L*- total length (mm)	L_o- distance between grips (mm)	E_a- elastic modulus (GPa)	E_b- elastic modulus (GPa)	Failure mode	$E_{average}$ (GPa)	Failure stress (MPa)	Failure strain (%)
Top_1	8.0	25.0	177	37	32.5	29.7	End crushing	31.1	346	1.12
Top_2	7.9	25.0	177	37	35.9	33.5	End crushing	34.7	360	1.05
Bot_1	8.1	25.3	179	39	32.5	33.1	End crushing	32.8	343	1.05
Bot_2	8.1	24.9	179	39	33.8	37.9	End crushing	35.9	391	1.29
WA_1	8.2	25.3	180	40	37.1	38.8	Splitting of fibres	39.0	416	1.01
WA_2	8.2	25.2	178	38	42.9	37.5	End crushing	40.2	432	1.08
WB_1	7.7	25.2	177	37	39.9	41.5	End crushing	40.7	461	1.16
WB_2	7.7	25.0	177	37	42.0	40.9	End crushing	41.4	456	1.08
Average								37.0	401	1.10

As can be seen from Table 4.4, most of the specimens failed due to crushing or 'brooming' either from the top or the bottom end, where the loading was actually applied, as shown in Figure 4.11(a). Only one specimen (specimen WA_1) failed due to the splitting of fibres in the central region where the strain gauges were located, as shown in Figure 4.11(b). It should be noted that the modulus of elasticity $E_{average}$ was calculated by taking the average value of E_a and E_b, failure strain was calculated by using the failure stress divided by the average modulus of elasticity $E_{average}$. Figure 4.12 shows a typical stress versus strain plot of coupon specimen Top_1 in compression. The average longitudinal compressive modulus obtained from these coupon tests calculated using Eq. (4.1), was 37.0 GPa, 15% higher when compared with its longitudinal tensile modulus of 32.1 GPa. This value is still 61% higher than the manufacturer's specified elastic modulus (23 GPa). The average longitudinal compressive strength derived from coupon tests was 401 MPa, 67% higher than the manufacturer's specified compressive strength (240 MPa). There were still evidences of buckling of these specimens in compression, as shown in Figure 4.11(b).

(a) End crushing (b) Fibre breaking in the central region

Figure 4.11 – Failure mode of coupon specimens tested in compression

It should be noted that the transverse and shear properties of box section and grating were not characterised due to unavailability of manufacturing and testing equipment. Manufacturer's data was, therefore, used for transverse and shear properties in the analysis presented in Chapter 9.

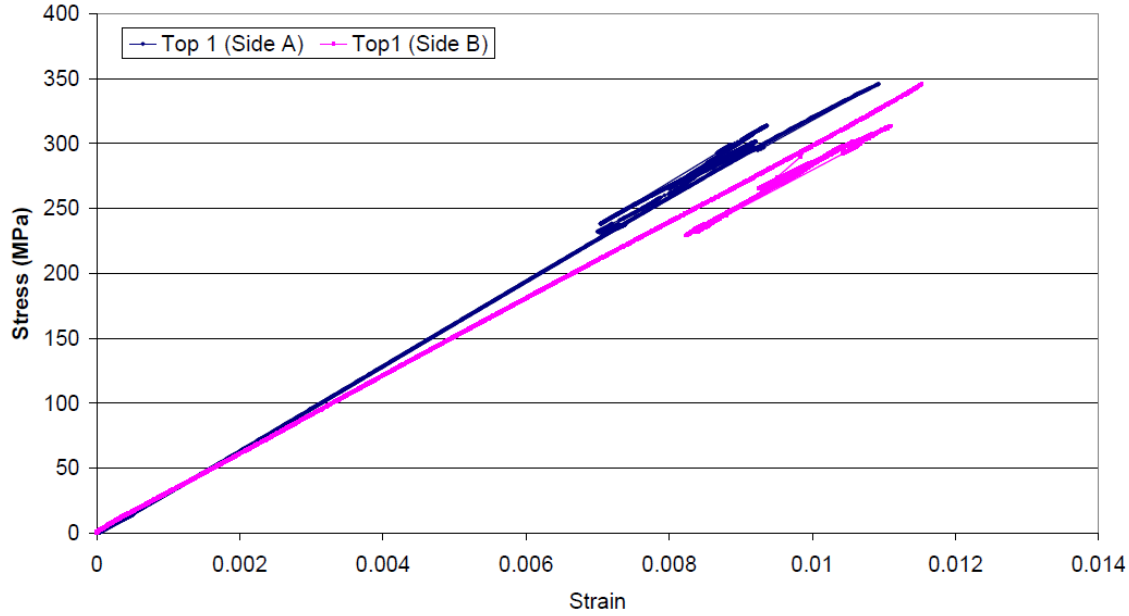

Figure 4.12 – Typical stress vs. strain plot of coupon specimen in compression (specimen Top_1)

4.3 Summary

This chapter presents the material characterisation of component elements used in the FRP-concrete hybrid formwork system. The reported material properties obtained from coupon tests are used for design of the composite slab section and prediction of ultimate strength of slab specimens.

As discussed in Chapter 3, the feasibility of using GFRP dowels embedded into the concrete to provide a robust shear connection between FRP and concrete with ductile failure behaviour will be examined experimentally in the next chapter.

Chapter 5 Investigation of Robustness and Ductility at the FRP/Concrete Interface

5.1 Introduction

Chapter 3 described the design concept of the composite FRP-concrete hybrid formwork system. This chapter provides details of experimental investigation into the mechanical bond fabricated using pultruded GFRP dowels embedded into the concrete at the FRP/concrete interface. The investigation has been divided into two stages: preliminary tests and subsequent tests. In the preliminary tests, four push-out specimens were fabricated and tested in double shear to determine whether the failure of the proposed mechanical shear connectors provides a ductile behaviour. Later, three Hofbeck style specimens were fabricated and tested in single shear to determine load versus slip characteristics of the shear connectors. The development of this proposed shear connection and its potential to contribute to the ductility of the overall system are discussed. Based on the findings from these preliminary tests, the improvement in terms of displaying progressive failure behaviour has been made and verified in the subsequent tests. Four push-out specimens were fabricated and tested in double shear to investigate the load versus slip characteristics of the improved shear connectors and their failure behaviour. Based on the experimental results from subsequent push-out tests, a modified shear friction model is developed to predict the shear resistance of a single connector, and was successfully verified.

5.2 Preliminary Experimental Investigation

5.2.1 Push-out tests

Push-out specimens D_1 and D_2 were fabricated by bonding two 300 x 500 mm moulded GFRP gratings (50 x 50 mm square mesh, depth is 50 mm) back-to-back using epoxy adhesive Araldite 2015, with a 3.3 mm thick pultruded GFRP sheet in between to contain the concrete in the cells. This is shown in Figure 5.1. Push-out specimens D_3 and D_4 were fabricated using two 300 x 200 mm moulded GFRP gratings. The size of the grating and the thickness of sheet were chosen because they were the biggest sample sizes available from the manufacturers. 100 mm thick concrete was cast on both sides with the concrete filling the cells in the gratings. The concrete strength was chosen to be 40 MPa

as C40 is a moderate concrete strength. The details of the four push-out specimens and concrete strength are shown in Table 5.1. The concrete strength was determined from six (100 x 100 x100 mm) cube tests at the time of push-out testing (28 days). It should be noted that there was a difference in concrete strength between both sides. This difference was caused by the construction procedure in which the concrete was cast on one side initially and cured for 48 hours, then turned over and cast on the other side. The concrete strength of specimens D_3 and D_4 were identical, as they were cast and tested on the same day.

Table 5.1 – Push-out specimens A_1-A_4

Specimen	Bond area (mm^2)	Cube strength (MPa) Side A at testing	Cube strength (MPa) Side B at testing	Mean Cube strength (MPa) Side A/Side B at testing	No. of concrete studs per grating	No. of GFRP dowels per grating	Ratio of GFRP dowels/cell
D_1	300 x 400	47.6	40.9	47.6/41.4	48	Nil	0:1
		47.4	39.1				
		50.3	39.3				
		46.7	42.1				
		45.3	42.8				
		48.4	44.1				
D_2	300 x 400	43.1	37.1	47.4/38.7	48	48	1:1
		47.9	38.7				
		48.2	36.0				
		45.6	38.6				
		48.9	41.1				
		50.7	40.6				
D_3	300 x 200	41.8	39.1	42.1/38.3	24	12	1:2
		43.5	37.1				
		42.6	36.8				
D_4		40.7	37.9		24	6	1:4
		42.3	40.8				
		41.9	38.1				

Figure 5.1 – Plan and elevation view of push-out specimens A_1 before concrete was cast

All specimens were loaded at a displacement rate of 0.3 mm/min. Relative slip was measured by tracking the displacement between the concrete and the grating using transducers. The bond area was 300 x 400 mm for specimens D_1 and D_2, and 300 x 200 mm for specimens D_3 and D_4, leaving 100 mm of the gratings protruding for applying the load. The push-out test set-up is shown in Figure 5.2.

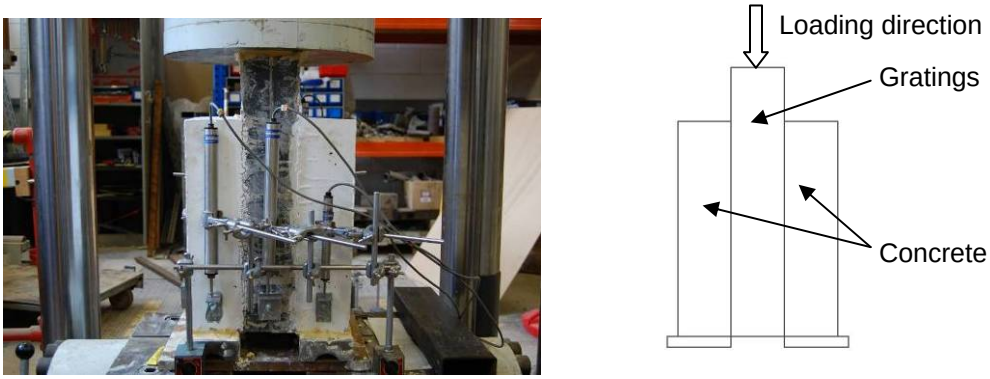

Figure 5.2 – Push-out test set-up

A preliminary test was carried out on specimen D_1 showed a brittle response with failure occurring due to the shearing of the concrete across the grating/concrete interface as shown in Figure 5.3, achieving a maximum failure capacity of 1204 kN.

Figure 5.3 – Shear failure of concrete at the grating/concrete interface in specimen D_1

In order to add ductility into this predetermined failure plane by causing a more progressive failure, GFRP dowels were introduced providing an additional connection at both sides of the grating/concrete interface. This concept was investigated through three push-out specimens D_2, D_3, and D_4. Specimen D_2 contained 48 GFRP dowels (one dowel in each square hole of the grating) embedded at the grating/concrete interface, as shown in Figure 5.4. These

dowels were held in place inside the grid cells of the grating, using a circular plastic spacer before the concrete was cast. The GFRP dowels were 10 mm in diameter and 100 mm in length, embedded within concrete with 50 mm above and below the grating/concrete interface.

Figure 5.4 – Push-out specimen D_2

Specimen D_2 failed at 1736 kN (see Figure 5.7) due to crushing of protruding part of the grating, which was directly underneath the loading rig, rather than the expected shear failure at the grating/concrete interface, as shown in Figure 5.5. This is because the shear capacity at the grating/concrete interface was over-strengthened by the addition of the GFRP dowels, exceeding the material capacity of the grating, causing a crushing failure.

Figure 5.5 – Crushing of protruding part of the grating in specimen D_2

In order to reduce the shear capacity at the grating/concrete interface, specimens D_3 and D_4 were tested in a smaller scale by reducing the bond area of both specimens to 300 x 200 mm. The number of embedded shear connectors was reduced to 12 dowels (one dowel in every second hole) in specimen D_3 and 6 dowels (one dowel in every fourth hole) in specimen D_4, as

shown in Figure 5.6. The dowels in both specimens were arranged in a ‘zig-zag’ pattern to ensure the uniform shear transfer between the grating and concrete.

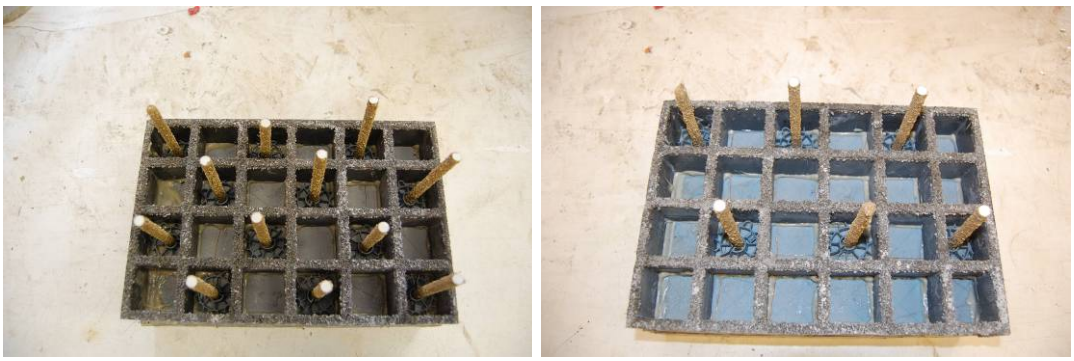

Figure 5.6 – Push-out specimens D_3 and D_4

The results of the tests are summarised in Table 5.2 with a load versus relative slip plot as shown in Figure 5.7.

Table 5.2 – Results of push-out specimens A_1-A_4

Specimen	No. of GFRP dowels in (300 x 200) mm^2 bond area	Peak load (kN)	Peak average shear stress across the interface (MPa)	Post peak residual load (kN)	Failure mode
D_1	Nil	1204	7.11	N/A	Sudden debonding failure at the grating/concrete interface
D_2	24	1736	10.3	N/A	Crushing of protruding part of the gratings in a brittle manner
D_3	12	731	8.63	300	Progressive debonding failure at the grating/concrete interface
D_4	6	505	5.96	172	Progressive debonding failure at the grating/concrete interface

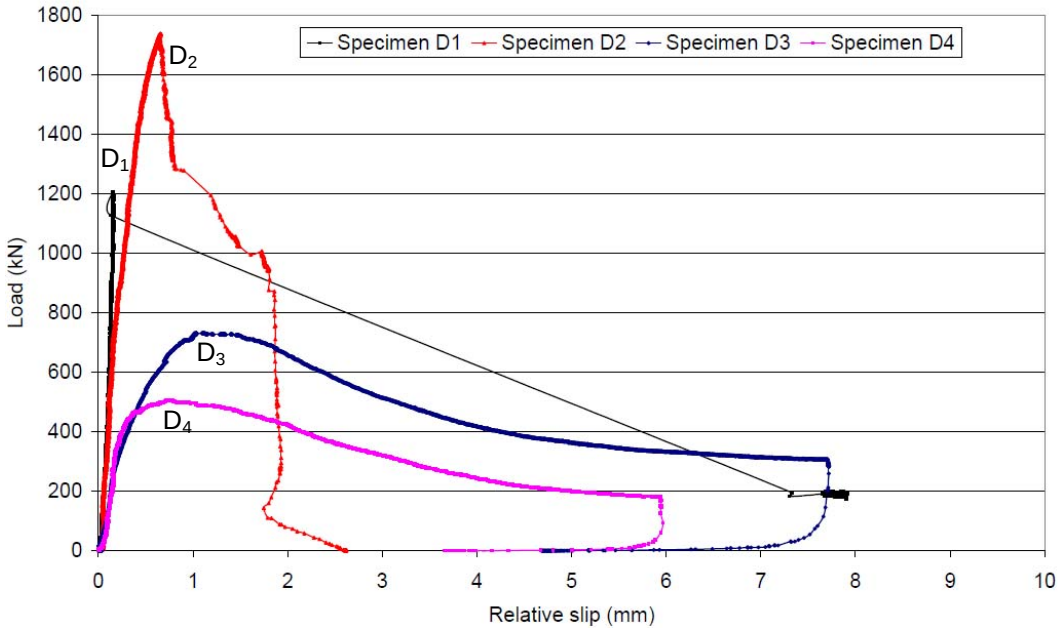

Figure 5.7 – Load vs. relative slip plot of push-out specimens D_1-D_4

To summarise, as shown in Figure 5.7, Specimen D_1 failed in a sudden manner at the grating/concrete interface due to shear failure of concrete with no ductility. Specimen D_2 exhibits little ductility, although it achieved a higher peak strength of 1736 kN, this is because failure occurred due to crushing of the protruding part of the gratings under the applied load. Clearly, this indicated that the capacity had been significantly enhanced by additional GFRP dowels since shear failure was precluded, but strength was increased beyond the capacity of the grating, preventing a ductile failure being observed. Specimen D_3 failed in shear at the grating/concrete interface in a more gradual manner. It had a high initial stiffness until concrete shear cracking occurred followed by a gradual reduction in capacity as the embedded GFRP dowels began resisting the shear. The post peak residual strength gradually decreased to 40% of the peak strength until the concrete components failed in compression due to the propagation of cracks. The failure behaviour of specimen D_4 was similar to specimen D_3, with a reduction of the peak load of 30%, and a 40% decrease in post peak residual strength compared to specimen D_3.

These key findings from the push-out tests demonstrated the potential to achieve ductility from the grating/concrete interface by adding GFRP dowels perpendicular to that interface. However, tests of specimens D_3 and D_4 were

stopped when the loads were starting to drop; therefore, the final failure mode of both specimens was not clear. Hence, the load versus slip response of this shear connector was further investigated through a series of Hofbeck tests, which are discussed in the following section.

As can be seen in Table 5.2, it is logical that the peak average shear stress at the grating/concrete interface reduced as the number of GFRP dowels decreased. However, it was found that that the peak average shear stress of specimen D_4 was lower than that of specimen D_1. This was probably due to the size effect, as the bond area between the gratings and concrete components in specimens D_3 and D_4 was only half the size of that in specimen D_1 and D_2. In the subsequent tests, as specimens D_3 and D_4 exhibited a progressive failure behaviour, three more specimens were fabricated by following the design of specimens D_3 and D_4, and tested in Hofbeck tests.

5.2.2 Hofbeck tests

Details of Hofbeck specimens

The Hofbeck test is designed for the investigation of shear strength cross a specific plane. A typical test set-up is shown in Figure 5.8.

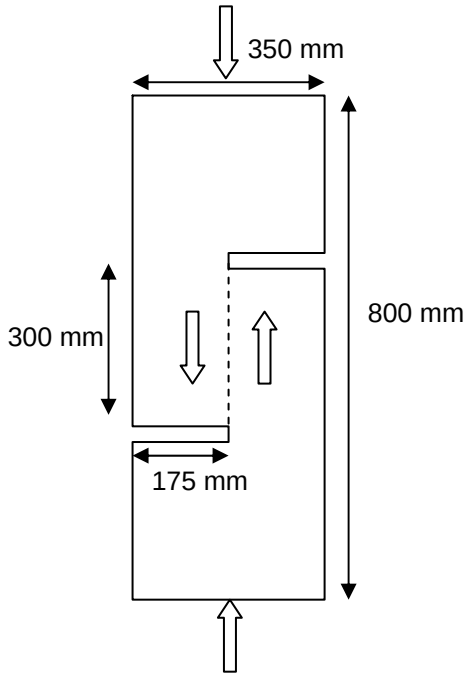

Figure 5.8 – Hofbeck shear test set-up

Three concrete ‘Hofbeck’ specimens were designed and tested to further investigate failure behaviour of GFRP dowels embedded in the concrete along either concrete/grating interface or grating/grating interface. The described dimension of the Hofbeck test specimens is to allow space for sufficient steel reinforcement to prevent flexural failure of the specimen. The purpose for this is to ensure the shear failure only occurred along the predetermined shear plane. Three specimens were prepared using the same mix proportions C50 and arrangement of steel reinforcement. Each specimen has a length of 800 mm, a width of 350 mm, and a depth of 200 mm. This is the smallest sample size which gives the representative behaviour of the proposed shear interface.

A summary of the details for Hofbeck specimens are presented in Table 5.3. The concrete strength was determined from three (100 x 100 x100 mm) cube tests for each specimen at the time of Hofbeck testing. Figure 5.9 shows the different layouts of the GFRP dowels at the grating/concrete interface in specimens H_1, H_2 and H_3. 100 mm long GFRP dowels were arranged in a ‘zig-zag’ pattern and held in place with circular plastic spacers inside the grid cells. The diameter, number, embedment length and arrangement of dowels in Hofbeck specimens H_1-H_3, as well as the size of the grating, was identical to the push-out specimens D_3 (12 dowels) and D_4 (6 dowels) allowing for direct comparison of both test results. A 200 x 300 x 50 mm (width x length x depth) moulded GFRP grating was introduced on one or both side of the predetermined failure plane in the central region of specimens, which is represented by the dashed line in Figure 5.10. This test arrangement was designed to define the shear bond interface behaviour between the concrete and the grating in the subsequent slab tests. Gaps of 25 mm were created above and below the grating using plywood, as shown in Figure 5.10, in order to give sufficient space for vertical slip. Steel hooks were welded on right-angle reinforcing bars in order to ensure that shear failure occurred only along the predetermined failure plane. The purpose of specimen H_2 is to investigate the feasibility of using previous mentioned double-layer grating system in Chapter 3.

Table 5.3 – Summary of details of Hofbeck specimens

Specimens	No. of GFRP dowels	No. of concrete studs	No. of the grating at the shear plane	Cube strength(MPa) at testing	Average Cube strength (MPa) at testing	Ratio of GFRP dowels/cell
H_1	6	24	Single	45.3 48.8 46.5	46.9	1:4
H_2	6	24	Double	49.8 51.5 51.2	50.8	1:4
H_3	12	24	Single	45.0 45.9 48.0	46.3	1:2

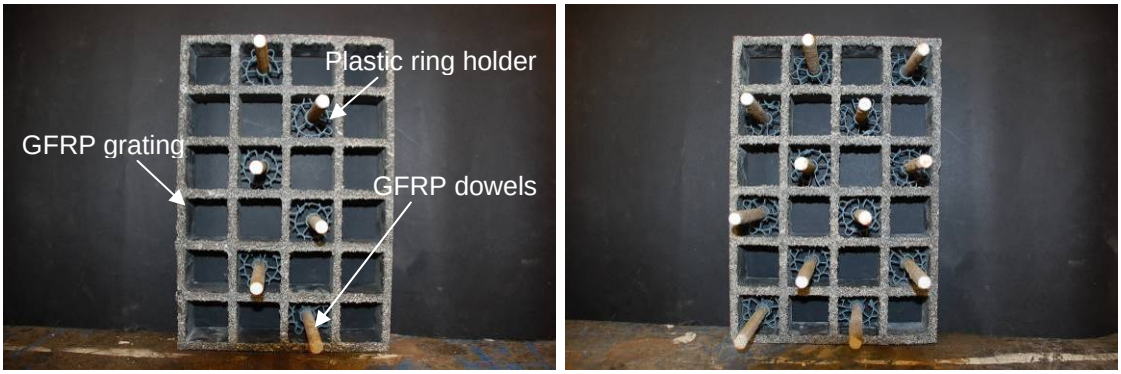

(a) Specimens H_1 and H_2 (6 dowels) (b) Specimen H_3 (12 dowels)

Figure 5.9 – Dowel arrangements in specimens H_1, H_2 and H_3

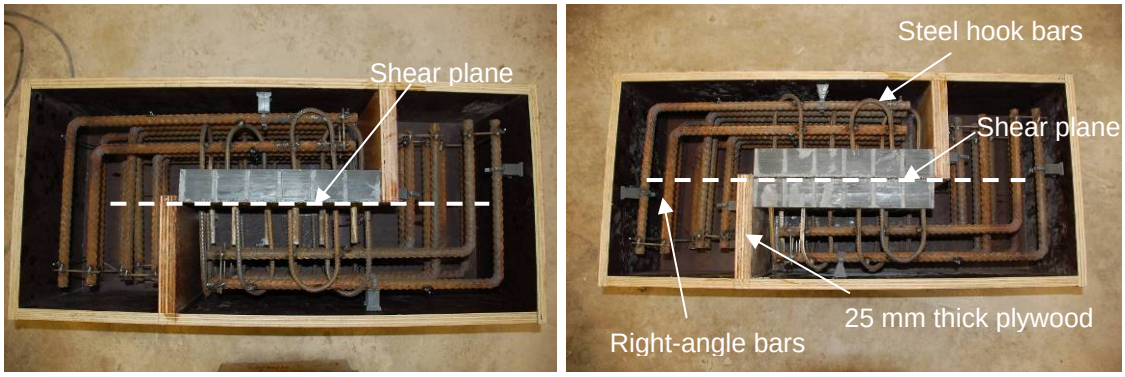

Figure 5.10 – Specimen H_1 (single grating) and H_2 (double gratings)

Test set-up and instrumentation

Vertical displacement and crack widths were measured by two pairs of LVDTs (linear variable differential transducers), as shown in Figure 5.11. The specimens were loaded using a 2000 kN Dartec machine at a displacement rate of 0.01 mm/s.

(a) (b)

Figure 5.11 – Hofbeck shear test set-up and shear failure in vertical plane

Experimental results and discussions

Figure 5.11(b) shows the failure mode typical of all three specimens. It is clear from visual inspection of the failed specimens that the failure was indeed through shear at the grating/concrete interface in specimens H_1 and H_3 and grating/grating interface in specimen H_2 as would be expected from such a test arrangement. As can be seen from Figure 5.12, the three specimens exhibited an extremely high initial stiffness until concrete shear cracking occurred. After cracking occurred on the vertical predetermined plane, there was a sudden drop in load capacity as the concrete studs failed in shear, as shown in Figure 5.13. After this, the embedded GFRP dowels began carrying the load, and the shear resistance was maintained at approximately 29%-33% (for specimen H_1 and H_2) and 41% (for specimen H_3) of the peak load during 6 to 8 mm relative slip prior to the onset of fracture of the dowels. This is represented in Figure 5.12 by a plateau after the initial load drop, as the dowels were mobilised to carry the shear. After a further slip of 2 mm, the shear capacity of the three specimens diminished in a number of small drops, representing the ultimate failure of the dowels. Final failure is indicated by fracture of all the dowels after approximately 10 mm of slip, as seen in Figure 5.12.

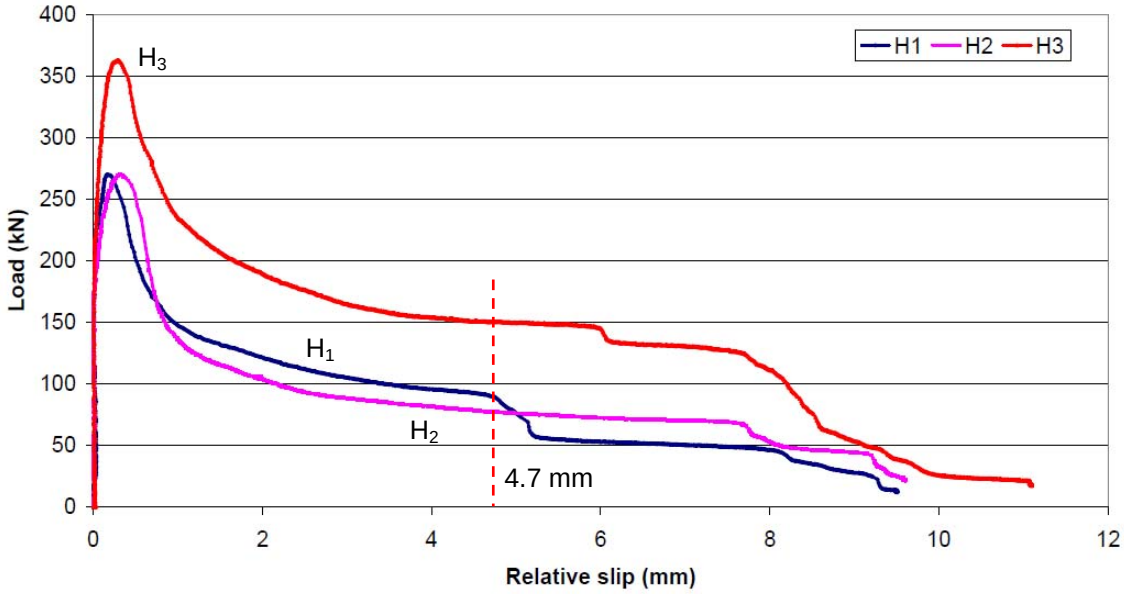

Figure 5.12 – Load vs. relative slip plot of the proposed shear connector system

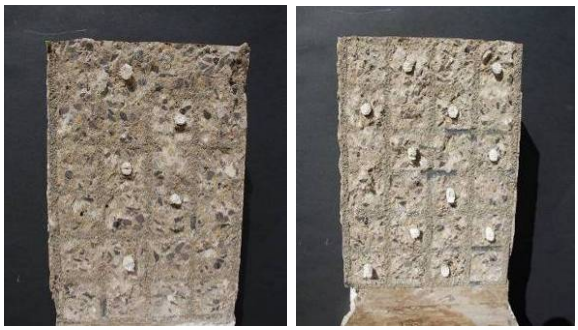

Figure 5.13 – Shear off of concrete studs and GFRP dowels at the vertical failure plane

Table 5.4 summarises the results from this test series. The table provides average cube strength values for the specimens on the day of testing, the peak strength of each specimen in kN, and the residual post peak strength in kN, of the central shear plane prior to the failure of all dowels. As can be seen from Table 5.4, for an identical number of concrete studs (same bond area), there is a 34% increase in the peak strength by doubling the number of dowels. This demonstrates that the peak load is determined by both the concrete studs and GFRP dowels, with the concrete studs providing the majority of the resistance to shear prior to their failure. Table 5.4 also illustrates that there is between 67% and 95% increase in the residual post peak strength by doubling the number of dowels. The shear resistance provided by individual dowels is 15.0 kN for specimen H_1, 12.8 kN for specimen H_2 and 12.5 kN for specimen H_3. The

feasibility of using double grating prototype system mentioned earlier in Chapter 3 was investigated by specimen H_2. It was found that the peak load of specimens H_1 and H_2 were identical at 270 kN, and their residual strength after the peak showed good agreement. The cracking opening width of all three specimens is within a narrow range from 2.8 to 3.0 mm.

Table 5.4 – Summary of Hofbeck test results

Specimens	No. of GFRP dowels	No. of grating	Average Cube strength (MPa)	Peak strength (kN)	Residual strength at 4.7 mm slip (kN)	Ultimate shear resistance per dowel (kN)	Crack opening width (mm)
H_1	6	Single	46.9	270	90	15.0	3.0
H_2	6	Double	50.8	270	77	12.8	2.9
H_3	12	Single	46.3	363	150	12.5	2.8

The Hofbeck test results have established that the peak strength is determined by the shear strength of concrete and GFRP dowels, and the residual post peak strength is determined primarily by the presence of the GFRP dowels. In the tests presented above, all the grid cells in the grating were concrete-filled, resulting in a significantly high peak shear resistance. This is because the shear was carried by both concrete studs and GFRP dowels, though the shear strength of concrete dominated. However, once the concrete studs failed in shear, only the GFRP dowels were carrying the shear, leading to a dramatic drop in shear resistance following the peak strength being reached.

5.2.3 Conclusions from preliminary tests

This section described the experimental investigation of using GFRP dowels through embedment of concrete at the grating/concrete interface. Two types of test methods were used in this study: Push-out test and Hofbeck test. Load versus slip responses determined from both test results demonstrated that the post peak behaviour is quite progressive due to the presence of GFRP dowels across the failure plane, although there is a significant drop in load capacity after the peak load. These preliminary tests indicate that using GFRP dowels embedded in the concrete as mechanical shear connectors provides ductility at the grating/concrete interface. An obvious improvement would be to seek a way to reduce the difference between the peak strength and the post peak residual strength. The peak strength is mainly dependent on the concrete studs, while,

the post peak residual strength is dependent on GFRP dowels. This difference might be reduced by having a single concrete stud for each GFRP dowel at the grating/concrete interface. The investigation into improving the failure behaviour of this bond mechanism is discussed in the following section.

5.3 Subsequent Experimental Investigation

5.3.1 Introduction

The previous section demonstrated the potential of using GFRP dowels embedded within the concrete to provide ductility at the grating/concrete interface. In the aforementioned FRP-concrete hybrid formwork system in Chapter 3, the bond between the concrete-filled grating and box sections is achieved by GFRP dowels embedded within the concrete through the pre-cut holes at the top flange of box sections. The improvement in ductile failure behaviour might be achieved by having fewer concrete studs per dowel, thereby reducing the peak strength. It was found in Section 5.2 that the peak strength primarily relied on the shear strength of concrete. Therefore, having fewer concrete studs per dowel might result in a reduction in the peak strength, leading to a more progressive failure. This section provides details on experimental and analytical investigations into the behaviour of GFRP dowels embedded within the concrete at the grating/box-section interface. Four push-out test specimens were fabricated and tested in double shear to investigate the robustness of the proposed shear connectors and their load versus slip behaviour. Based on the experimental data from push-out tests, a modified shear friction model was developed to predict the shear resistance of a single connector, and was successfully verified.

5.3.2 Description and fabrication of specimens

Two push-out test specimens (A_1 and A_2) were initially tested to compare the load versus slip response of GFRP dowels embedded in a partially concrete-filled GFRP box section (A_1) with those embedded in a fully concrete-filled GFRP box section (A_2). Both specimens consisted of two 450 mm long GFRP box sections bonded back-to-back using a two component epoxy adhesive (Araldite 2015). These were then connected on both sides to a 150 x 50 x 400 mm moulded GFRP grating (grid size = 50 x 50 mm, thickness of

individual bars = 8 mm) using the same epoxy adhesive. Four 42 mm diameter holes were drilled into the top flange of the GFRP box sections to allow the concrete studs to form at the grating/box-section interface. In specimen A_1, a foam block of 84 x 44 mm (width x depth) was inserted into the hollow GFRP box sections in order to hold the GFRP dowels in place, as shown in Figure 5.14(a). This reduced the concrete-filled depth in the box section to only 40 mm. In specimen A_2, although no foam block was used and the whole box section was filled with concrete as shown in Figure 5.14(b), the same lengths of GFRP dowel (40 mm) were inserted into the concrete in the box sections as found in specimen A_1. Four sand-coated GFRP dowels (diameter 10 mm) were manually pushed into the foam block with an upstand of 88 mm and longitudinal spacing of 100 mm centre-to-centre, as shown in Figure 5.14(c). The cross section, plan and side view of the push-out specimens are shown in Figure 5.14(d).

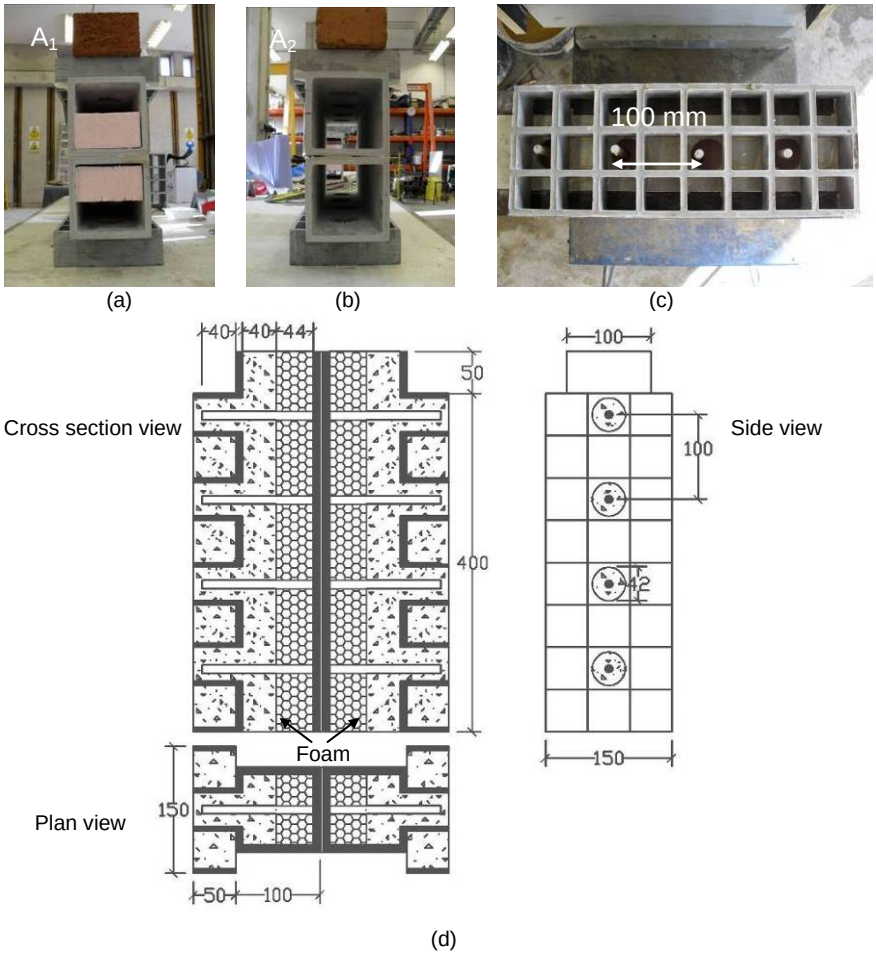

Figure 5.14 – Push-out specimens A_1 and A_2

Following the initial testing, push-out specimens A_3 and A_4 were designed and tested to compare the load versus slip response of eight GFRP dowels (A_3) with

four GFRP dowels (A_4) embedded in a partially concrete-filled GFRP box section. The fabrication procedure was exactly the same as for specimen A_1, although the distribution of shear connectors in specimens A_3 and A_4 was in a 'zig-zag' pattern rather than the straight line seen in specimen A_1, as illustrated in Figure 5.15(a) and (b). This is because only a 'zig-zag' arrangement of GFRP dowels can allow a sufficient number of holes to be drilled into the box section with at least 40 mm distance between the edges of adjacent circular holes. This spacing between two adjacent holes permits sufficient strength within the top flange to resist the shear stud loading. Shear connectors were longitudinally spaced at 100 mm centre-to-centre in specimen A_3 and 200 mm centre-to-centre in specimen A_4, with a transverse spacing of 46 mm used in both, as shown in Figure 5.15(c). The diameter of the hole was reduced from 42 mm in specimen A_1 to 38 mm in specimens A_3 and A_4 due to space limitations dictated by the width of the flange, as shown in Figure 5.15(d).

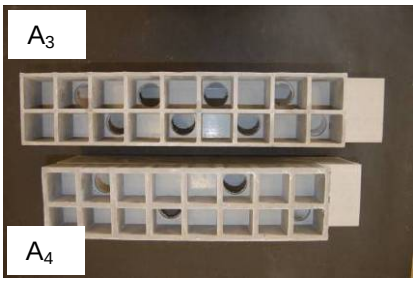

(a) 'zig-zag' pattern of holes

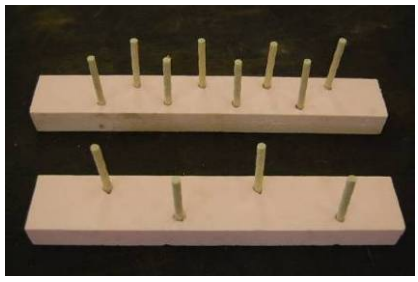

(b) Distribution of GFRP dowels

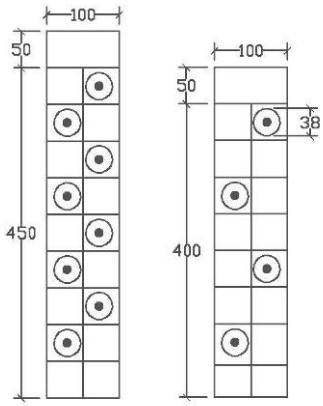

(c) Details of specimens A_3 and A_4, unit in mm

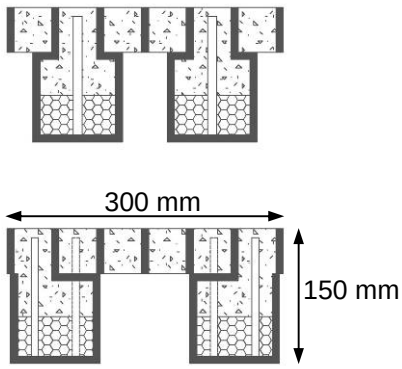

(d) Cross section view of original and new design

Figure 5.15 – Push-out specimens A_3 and A_4

5.3.3 Test set-up and instrumentation

Push-out specimens were loaded using a 2000 kN Dartec machine at a constant displacement rate of 0.3 mm/min. The schematic test arrangement for investigating the load versus slip behaviour of the proposed shear connectors is presented in Figure 5.16. Three pairs of LVDTs were used to measure the relative slip between the concrete-filled grating and the GFRP box section, as shown in Figure 5.16. The average concrete cube strength in specimens A_1 and A_2 is 43 MPa on one side and 52 MPa on the other side at the time of testing. The average concrete cube strength in specimens A_3 and A_4 is 35 MPa on both sides at the time of testing. The concrete strength was determined from four (100 x 100 x100 mm) cube tests at the time of push-out testing.

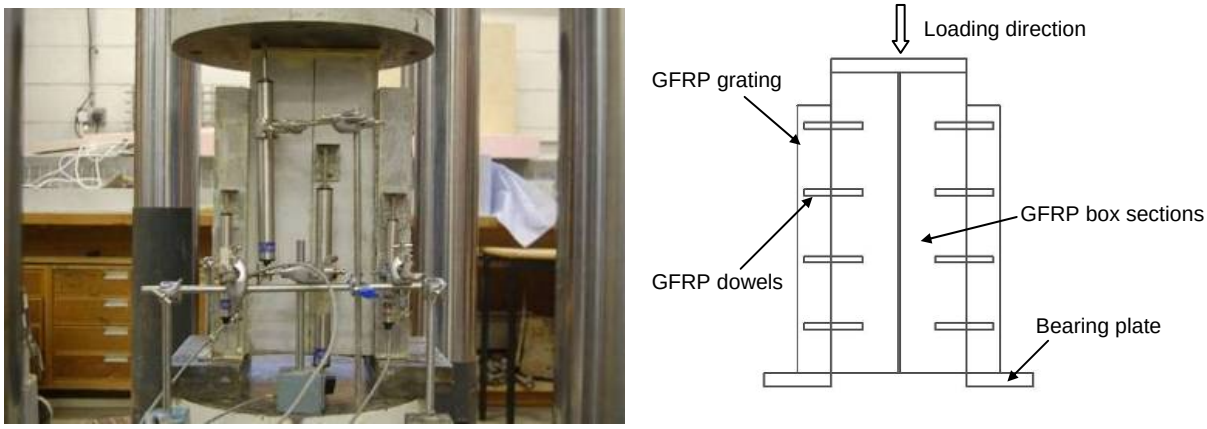

Figure 5.16 – Push-out test set-up

5.3.4 Experimental results

Push-out specimens A_1 and A_2

Figure 5.17 shows that the load versus slip response was quite similar in both specimens A_1 (partially-filled) and A_2 (fully-filled) at any given load. Both specimens had an extremely high initial stiffness of 1.52 x10^6 kN/m, the shear force reached a maximum of approximately 240 kN in specimen A_1 and 213 kN in specimen A_2, provided by the concrete studs combines with GFRP dowels at the grating/box-section interface, followed by a 'plastic' plateau as the embedded GFRP dowels began to resist the shear. As illustrated in Figure 5.17, at a slip of approximate 10 mm in specimen A_1 and 7 mm in specimen A_2, the resistance of shear diminished in a number of drops, representing the ultimate failure of individual dowels. Visual inspection after the tests reveals all the GFRP dowels failed in shear.

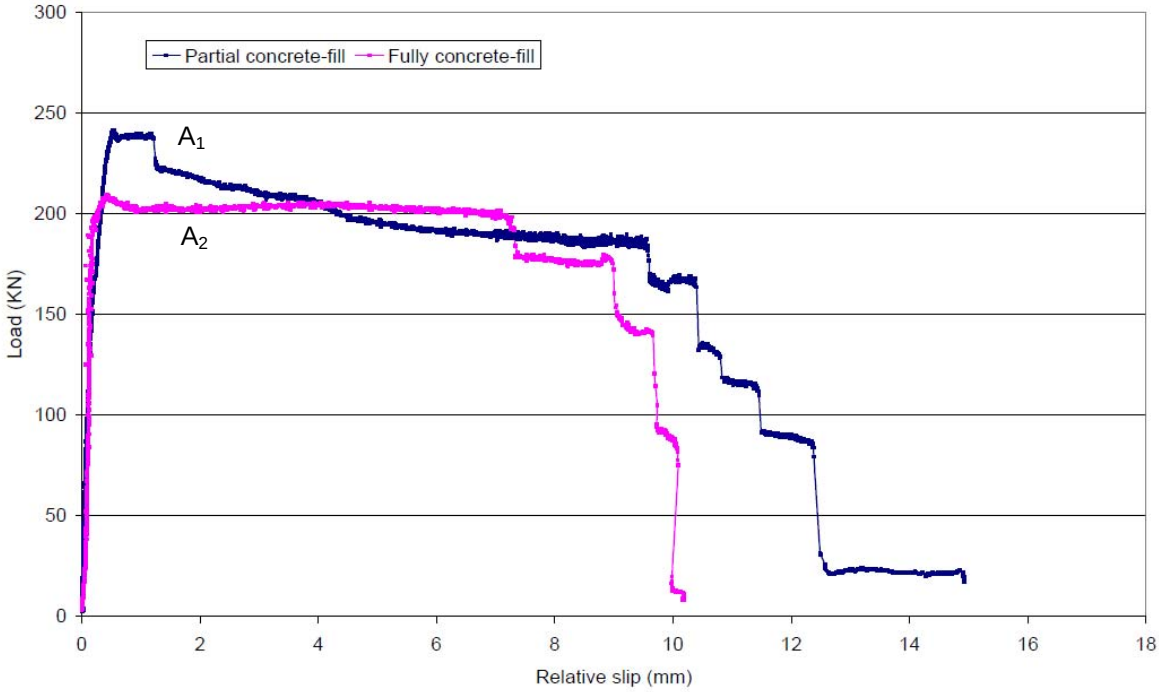

Figure 5.17 – Load versus relative slip plot of push-out specimens A_1 and A_2

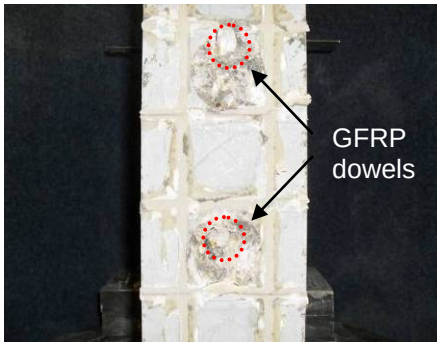

Figure 5.18 – Typical ultimate failure of the concrete studs and GFRP dowels (specimen A_1)

The experimental results demonstrated that there was no significant difference between specimens A_1 and A_2 with identical embedded length of GFRP dowels (40 mm) in terms of load versus slip response and ultimate shear capacity. It was then clear that the main function of the concrete fill in the box section was to provide support and anchorage for the GFRP dowels through embedment within the concrete fill. Partially-filled concrete sections can also reduce the immediate deflection in the construction stage as unnecessary concrete mass in the box sections is removed. More importantly, the foam block provided a holder for the GFRP dowels, thus simplifying the construction process. For these reasons the

partially-filled construction method was adopted for subsequent push-out tests and slab tests.

Push-out specimens A_3 and A_4

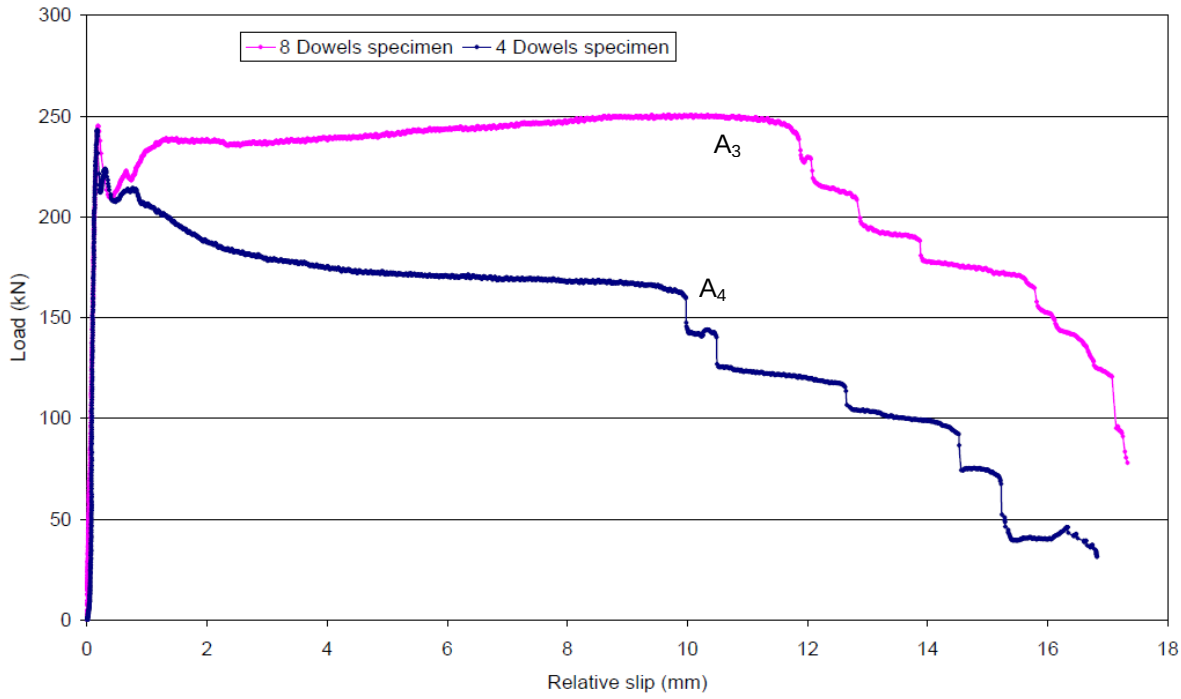

Figure 5.19 – Load versus relative slip plot of push-out specimens A_3 and A_4

Figure 5.19 shows that both specimens A_3 (8 dowels) and A_4 (4 dowels) had a high initial stiffness of 1.68 x10^6 kN/m and the shear resistance of both reached a maximum of 240 kN. Following this, the shear force of specimen A_3 gradually dropped to 170 kN and maintained this level. Conversely, the shear force of specimen A_4 dropped initially by 30 kN before quickly recovering its original peak of 240 kN at 1 mm relative slip. The initial load drop signified a failure of the adhesive bond and cracking of the concrete along the grating/box-section interface. The GFRP dowels began to fail at approximately 12 mm for specimens A_3 and 10 mm for specimen A_4. The initial load is provided by the combination of concrete studs and GFRP dowels across the concrete-filled grating/box-section interface, followed by a residual load provided by the GFRP dowels acting in tension and shear along the concrete failure plane.

Comparisons of push-out test results

Table 5.5 – A summary of results for push-out specimens A_1, A_2, A_3 and A_4.

Specimen	No. of shear connectors	Average Cube strength (MPa) Left/Right side	Diameter of concrete studs (mm)	Pattern of shear connectors	Concrete fill	Peak load (kN)	Residual load (kN)	Ultimate Slip (mm)
A_1	4	43/52	42	Straight	Partial	240	190	10
A_2	4	43/52	42	Straight	Full	213	200	7
A_3	8	35/35	38	Zig-zag	Partial	245	240	12
A_4	4	35/35	38	Zig-zag	Partial	241	170	10

Table 5.5 shows that there was a small drop of 10% in residual load (20 kN) by changing the pattern of the GFRP dowels from a straight line (A_1) to a zig-zag (A_4). However, the ultimate slip at fracture of the GFRP dowels was identical in both specimens A_1 and A_4. It can also be seen that in the zig-zag arrangement doubling the number of GFRP dowels results in a 40% increase in post damage load capacity (A_3 and A_4). However, it seems that there is a negligible difference in the peak strength caused by changing the number of GFRP dowels combined with concrete studs, even though the number of shear connectors decreased. This suggests that the glued FRP-FRP interface has a significant impact on the peak load. When comparing specimens A_1 and A_4, the strength of concrete, size of concrete studs and pattern of shear connectors has no effect on the peak load and residual load, it further indicates that the adhesive bond plays an important role in the peak load. Furthermore, the residual load is shown to be mainly dependent on the shear resistance and tensile resistance of GFRP dowels, this allows a progressive failure mechanism to be achieved.

5.3.5 Shear friction model

Introduction

A modified shear friction model has been developed to predict the shear resistance provided by individual GFRP dowel after concrete studs failed in shear. The model has been successfully verified against the experimental results. Shear friction models allow the actual physical behaviour of the longitudinal shear interface to be reasonably predicted. It is based on a friction coefficient (equal to $\tan\phi$, where ϕ is the angle of friction), and represents the

nature of the two surfaces in contact. The amount of shear that can be transferred between two interfaces clamped together with reinforcement is determined by the equation

$$V_L = C + N \tan \phi \qquad (5.1)$$

where V_L is the maximum shear force being transferred and N is the normal force acting on the interface, C is cohesion of the concrete, which equals to zero when cracking of concrete and failure of adhesive bond occurs.

Shear transfer behaviour of initially cracked concrete with reinforcement perpendicular to the shear plane

When an initially cracked specimen is loaded in shear, slip will occur along the shear plane. The faces of the crack are rough and hence when slip occurs, the crack faces are forced to separate. This separation causes tensile strains in the reinforcement crossing the shear plane. The tension force induced in the reinforcement is balanced by an equal compression force across the crack. This compression force produces a frictional resistance to sliding between the faces of the crack, thus opposing the applied shear. The relative movement of the concrete on opposite sides of the crack also subjects the individual reinforcing bars to shearing action. The resistance of the bars to this shearing action, sometimes referred to as dowel action, also contributes to the shearing resistance. Therefore, the applied shear is then resisted by friction between the crack faces and by dowel action of the reinforcement crossing the crack. Both mechanisms are illustrated in Figure 5.20.

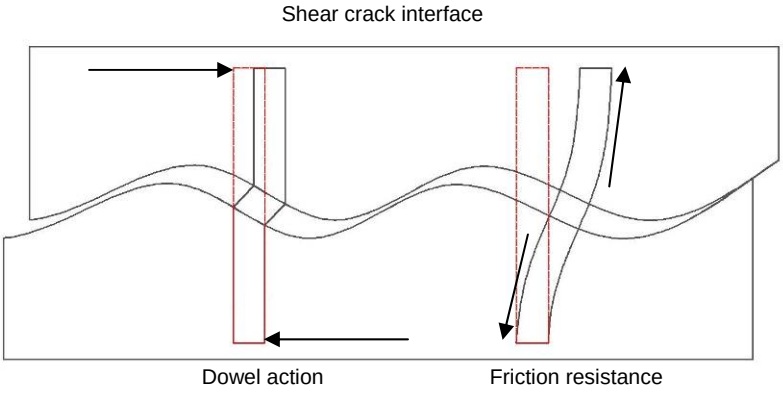

Figure 5.20 – Shear friction mechanism showing behaviour at crack interface

For the GFRP dowel shear plane discussed previously, the separation of the crack faces is eventually sufficient to strain the GFRP dowels to their maximum embedded bond strength. At ultimate strength therefore, the compression force perpendicular to the crack is equal to the maximum bond strength of the GFRP dowels

$$N = \tau_{bond} A_{bond} \tag{5.2}$$

where N is the clamping force acting on both sides of the shear crack, τ_{bond} is maximum bond strength of GFRP dowel embedded in concrete, and A_{bond} is the surface area of GFRP dowel embedded in concrete, which is equal

$$A_{bond} = \pi DL \tag{5.3}$$

where D is the diameter of the GFRP dowel and L is embedded length of GFRP dowel in concrete.

By substituting Eq. (5.2) and Eq. (5.3) in to Eq. (5.1), the frictional resistance to shear along the crack is then equal to:

$$V_u = \tau_{bond} \pi DL \tan\phi \tag{5.4}$$

where V_u is the frictional resistance, the product $\tau_{bond} \pi DL$ is the normal force acting on the interface N, the angle of friction ϕ is 37 degrees for concrete.

This model assumes that the crack separates enough to generate a clamping force exceeding the maximum bond strength of the embedded dowels, causing the dowels to be pulled-out of the concrete.

In addition to this frictional resistance to shear, there is an accompanying shear resistance due to the dowel action of the GFRP dowels crossing the crack in the shear plane. Shear resistance of each dowel crossing the shear plane is equal to:

$$V_s = \tau_s \cdot \pi (\tfrac{D}{2})^2 \tag{5.5}$$

where τ_s is shear strength of GFRP dowel.

The total shear resistance V_T lies within a range between V_s and $V_u + V_s$.

where V_s is the lower bound, corresponding to shear resistance across the plane when the dowels are not strained in tension whilst $V_s + V_u$ is the upper bound where the dowels are fully strained in tension and reach the ultimate bond strength limit.

Comparisons between push-out tests and shear friction model

Table 5.6 – Shear resistance of each dowel in specimens A_1-A_4

Specimen	No. of GFRP dowels	Mean Cube strength of concrete (MPa) Left/Right side	Diameter of concrete studs (mm)	Pattern of shear connectors	Concrete fill	Residual strength (kN)	Shear resistance per dowel (kN)
A_1	4	43/52	42	Straight	Partial	190	23.8
A_2	4	43/52	42	Straight	Full	200	25.0
A_3	8	35/35	38	Zig-zag	Partial	240	15.0
A_4	4	35/35	38	Zig-zag	Partial	170	21.3

Based on the shear friction model described above, the maximum bond strength τ_{bond} and the maximum shear strength τ_s of GFRP dowel are two main parameters in the calculation of the shear resistance of each dowel. As specified from manufacturer's design data, the maximum bond strength (τ_{bond}) of GFRP dowels, Aslan 100 GFRP rebars, used in this study is 11.6 MPa. This value was determined from pull-out tests using test methods proposed in ACI 440.3R-04 Method B.3 by manufacturer (Hughes Brothers Inc, 2010). The testing method is illustrated in Figure 5.21.

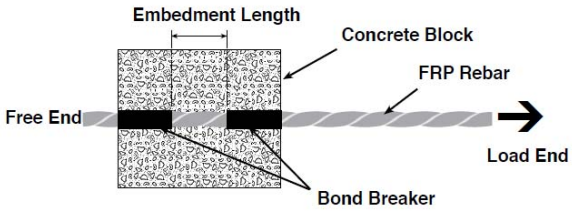

Figure 5.21 – Testing method for obtaining the bond stress of GFRP dowels (Hughes Brothers Inc, 2010)

The shear strength (τ_s) of Aslan 100 GFRP rebars is 152 MPa, which is also determined according to the ACI 440.3R-04 Method B.3 by manufacturer

(Hughes Brothers Inc, 2010). *D* is 10 mm and the embedded length (*L*) is 40 mm. Using Eqs. (5.4) and (5.5), the shear resistance of single GFRP dowel is calculated to be in the range 12 kN (dowel resistance only) to 23 kN (dowel resistance plus friction resistance). As can be seen from Table 5.6, the shear resistance per dowel for the three four dowel specimens (A_1, A_2 and A_4) is close to the upper bound (23 kN), which indicates the dowel action and friction resistance are fully mobilised. This suggests the efficient use of dowels. However, the shear resistance per dowel in eight dowels specimen A_3 is much lower and just above the lower bound of 12 kN. The system therefore appears to be less efficient if too many dowels are used. In all cases, it is evident that all the dowels fractured after 7-12 mm slip, indicating that the dowel action is fully mobilised.

5.4 Summary

This chapter demonstrates that the combination of concrete studs formed at the FRP/concrete interface and GFRP dowels anchored either side of the grating/box-section interface provide a robust shear connection in the joint, resulting in a progressive longitudinal shear failure. The peak load is governed by the mechanical bond at the FRP/concrete interface and the adhesive bond at the glued FRP/FRP interface, while the post peak residual strength is provided by GFRP dowels through dowel action and friction resistance at the concrete failure plane.

As previously discussed in Chapter 3, FRP can be potentially used as confinement for concrete in compression to add ductility to the overall system. The feasibility of using FRP grating to confine concrete in compression to provide ductility will be investigated in the Chapter 6.

Chapter 6 Experimental Investigation of using GFRP Grating as Confinement for Concrete

6.1 Introduction

The previous chapter demonstrated a means of providing ductility for the FRP-concrete hybrid formwork system, through progressive longitudinal shear failure at the grating/box-section interface. This chapter presents an experimental investigation into using GFRP grating as confinement for concrete in compression to provide ductility. This concept was investigated by comparing the stress versus strain response of a concrete-filled grating block with an unconfined concrete block in compression, as shown in Figure 6.1. Another objective was to obtain the stress-strain response for the concrete-filled grating, allowing design calculations of the composite section to be performed.

The concrete-filled grating block was fabricated by bonding two pieces of 50 x 100 x 210 mm grating back-to-back, using epoxy adhesive Araldite 2015, in order to achieve a 100 x 100 mm square loading cross section, which is identical to the unconfined concrete block dimensions. The bonded gratings were filled up to their top surface with concrete.

6.2 Preliminary Test of the Concrete-Filled Grating Block

(a) The unconfined concrete block (b) The concrete-filled grating block

Figure 6.1 – Block specimens and compression test set-up

The block specimens were loaded using a 2000 kN Dartec machine at a displacement rate of 0.3 mm/min. As shown in Figure 6.1, a pair of displacement transducers on two opposite sides was used to measure the axial compressive

displacement at a point 150 mm above the bottom surface of the specimens, referred to as transducer reading ‘Dis/150’. An additional transducer was used to measure the overall deformation of specimens, referred to as transducer reading ‘Dis/210’. The concrete strength was determined by six 100 x 100 x 100 mm cube tests. The average cube strength was 52 MPa at the time of block testing.

As can be seen in Figure 6.2, the concrete-filled grating block specimen behaved linear-elastically before it reached a stress of 38 MPa. Following that, it behaved non-linearly until reaching a peak stress of 68 MPa. As the load increases, the concrete around the cells of the grating began crushing and vertical cracks in the grating were observed, resulting in a gradual drop in load capacity after the peak strength. The concrete-filled grating block failed due to concrete crushing around the grating cells and longitudinal splitting of the fibres, as shown in Figure 6.4(a). As illustrated in Figure 6.3, the unconfined concrete block exhibited a similar elastic behaviour before 30 MPa, followed by a non-elastic behaviour until reaching peak strength of 36 MPa. After that, it failed due to concrete crushing with little ductility, as shown in Figure 6.4(b).

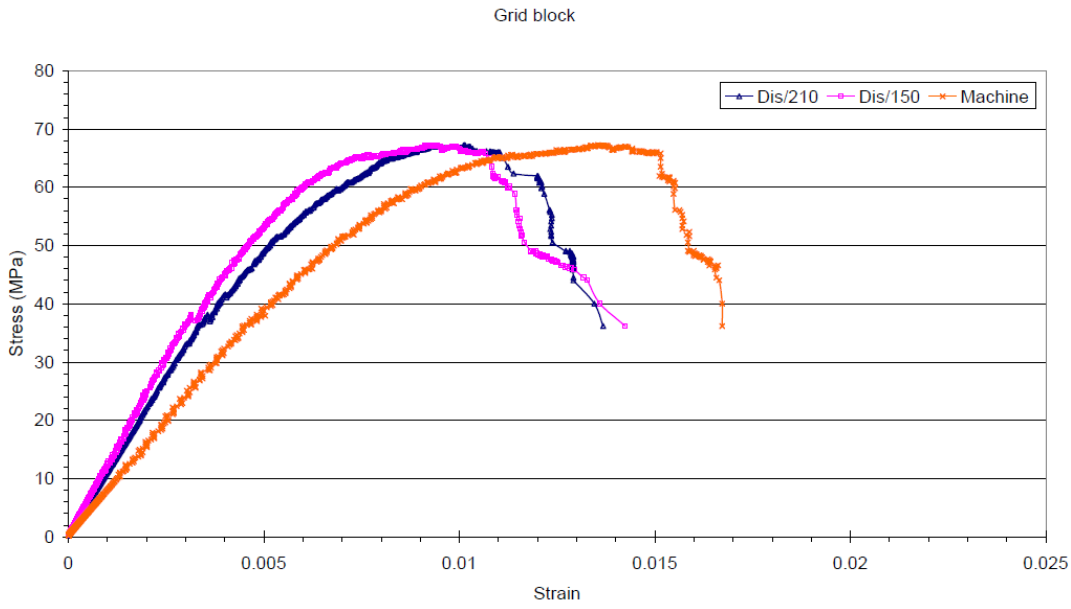

Figure 6.2 – Compressive stress vs. strain plot of the concrete-filled grating block specimen

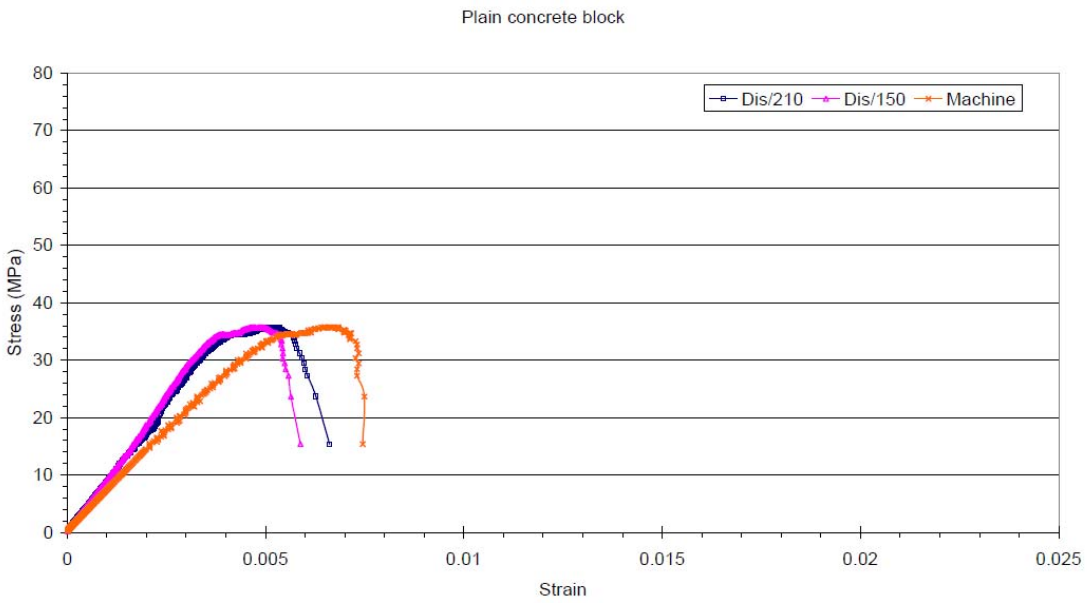

Figure 6.3 – Compressive stress vs. strain plot of unconfined concrete block specimen

(a) The concrete-filled grating block (b) Unconfined concrete block

Figure 6.4 – Failure modes of block specimens

Figures 6.2 and 6.3 show the stress versus strain plots for the concrete-filled grating block and unconfined concrete block specimens respectively, the strain reading ‘Dis/210’ was calculated as the displacement measured from the top of the specimens divided by the overall length of the specimens (210 mm). The strain reading ‘Dis/150’ was calculated as the displacement measured from a point, 150 mm from the bottom surface, divided by the original distance (150 mm). There is a close agreement between both of these strain readings. However, there is a discrepancy between the transducer readings and the load-testing machine readings. This required validation through subsequent tests. The compressive moduli of the concrete-filled grating block and

unconfined concrete block were calculated to be 11.7 GPa and 10.3 GPa respectively, determined by the initial slope of the elastic phase. It is clear from both figures that the addition of the grating led to an 88% increase in ultimate compressive strength, and a 115% increase in strain capacity compared to the unconfined concrete block.

Due to the discrepancy in readings, in order to establish the stress versus strain response of the concrete-filled grating block, an additional test was designed adopting three different strain measurement techniques, as described in next section.

6.3 Additional Compression Test of Concrete-Filled Grating Block

As present in section 6.2, the strain value measured in the preliminary test by the transducers showed a dramatic difference compared with that measured by the load-testing machine. To measure strain precisely, two pairs of same sized specimens, of different concrete strengths, were manufactured and loaded using a 2000 kN Dartec machine at a displacement rate of 0.3 mm/min. The average cube strength was 22 MPa for the concrete-filled grating block 1 and unconfined concrete block 1; and 34 MPa for the concrete-filled grating block 2 and unconfined concrete block 2 at the time of testing. The relative displacement of two points, 100 mm apart in the central region of the specimen, was measured with two pairs of LVDTs on the opposite sides. An additional LVDT was used to measure the deformation of the whole specimen, as shown in Figure 6.5. Strain was then calculated by using the relative displacement of two points (point A and B) divided by the gauge length (100 mm), referred to as ‘transducer reading 1’. Strain was also calculated by using the displacement of the whole specimen divided by the original length (210 mm), and is referred to as ‘transducer reading 2’. In order to verify the readings measured with transducers, DeMec gauges were installed on two opposite sides of the grating with a gauge length of 100 mm. The DeMec gauge readings were taken at 25 kN increment. For the concrete-filled grating specimens, 10 mm FLA-10-11 electrical resistance strain gauges (Tokyo Sokki Kenkyujo Co.Ltd) were installed on four sides of the grating in the central region, as shown in Figure 6.6.

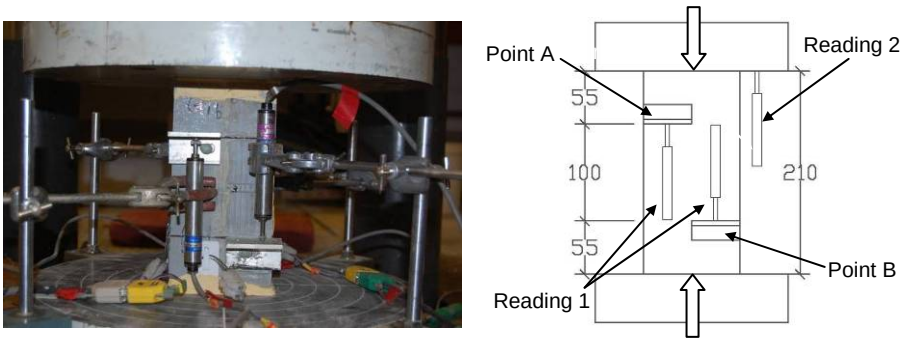

Figure 6.5 – Subsequent compression test set-up

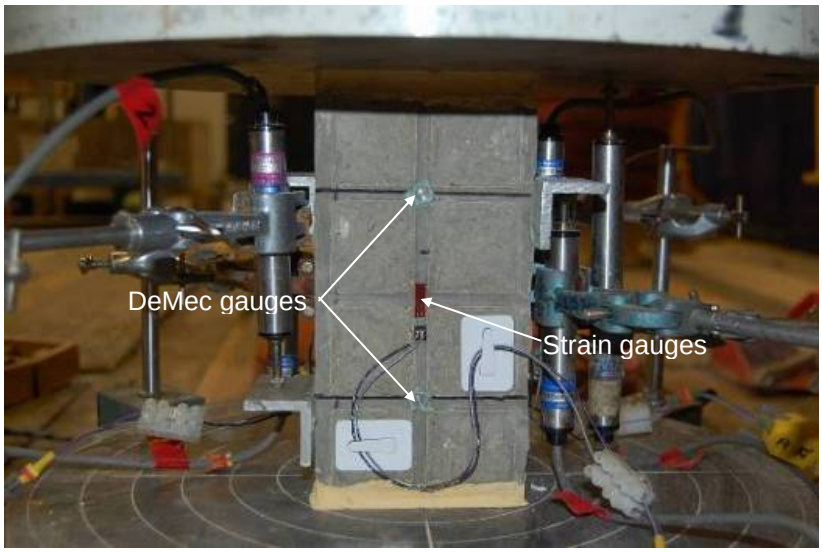

Figure 6.6 – Installation of DeMec gauges and strain gauges

As seen in Figure 6.7(a), the unconfined concrete block specimens failed in a brittle manner due to concrete crushing. The concrete-filled grating block specimens failed in a progressive manner due to longitudinal fibres buckling with fibres splitting apart perpendicular to the loading direction, and crushing of the concrete around the grid cells in the grating directly under the loading head or close to the bottom as shown in Figure 6.7(b).

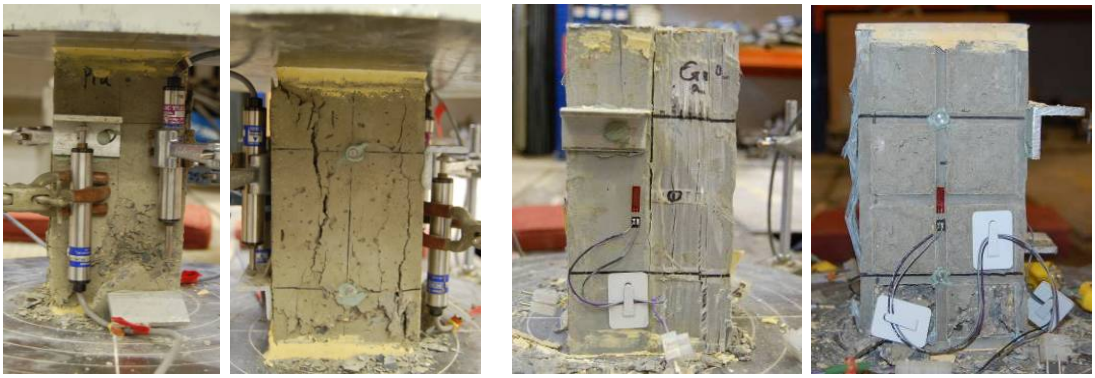

(a) Unconfined concrete block (b) Concrete-filled grating block

Figure 6.7 – Failure modes of block specimens

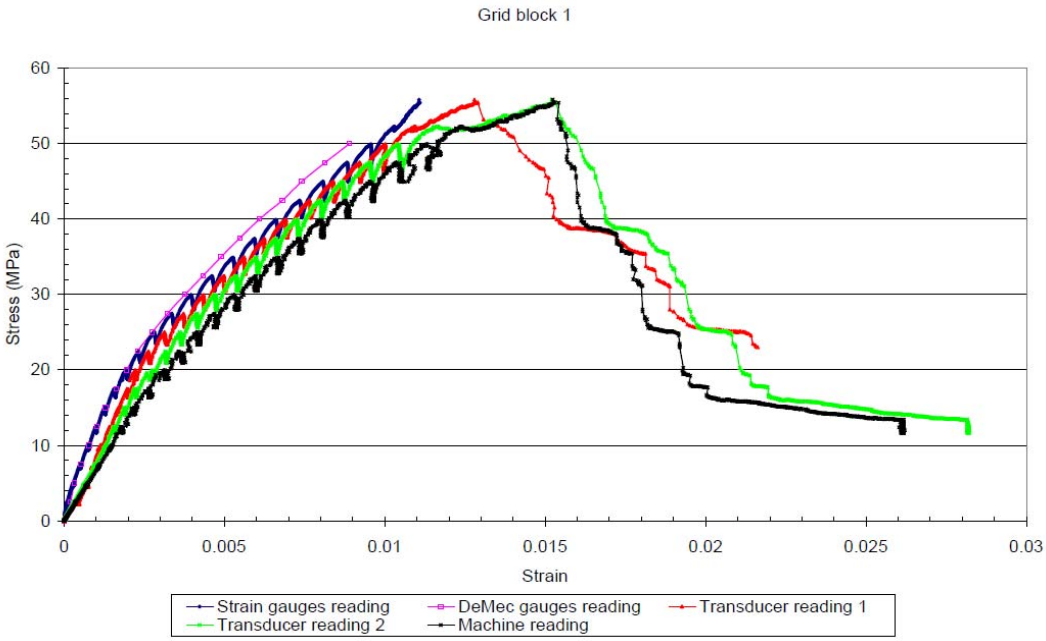

Figure 6.8 – Compressive stress vs. strain plot of the concrete-filled grating block 1

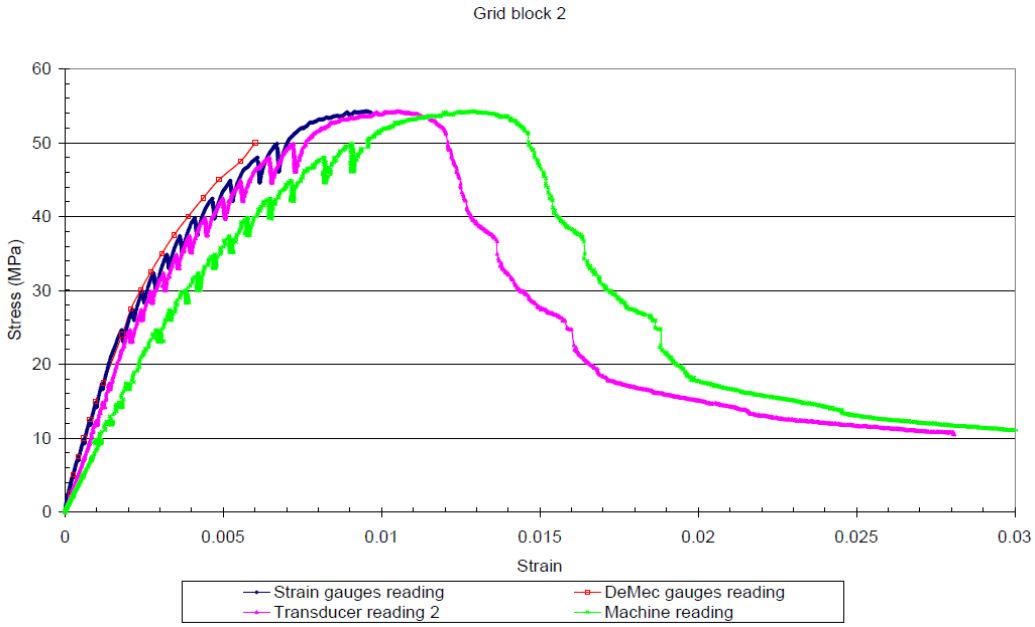

Figure 6.9 – Compressive stress vs. strain plot of the concrete-filled grating block 2

Figures 6.8 and 6.9 show the stress versus strain plots measured by the DeMec gauges, electrical resistance strain gauges, the transducers and the load-testing machine. Due to experimental error, it is not possible to obtain the Transducer reading 1. It is evident that the DeMec readings matched well with the strain gauge readings. However, both methods of measurement were unable to capture the post peak behaviour, and the whole stress versus strain plot including the post peak region, is crucial to establishing whether the grating can

introduce ductility into the concrete. It is clear that there exists a discrepancy between the load-testing machine reading and the transducer reading. Stress versus strain plots of unconfined concrete block 1 and 2 are shown in Figures 6.10 and 6.11, the DeMec reading matched well with the transducer reading in the concrete block specimens. However, there was still a difference between the transducer reading and the load-testing machine reading. Based on the initial linear-elastic stress versus strain relationship in Figure 6.11, the compressive modulus of unconfined concrete block 2 was calculated to be 18.1 GPa from the transducer reading, but only 9.24 GPa from the machine reading for a C30 concrete mix. As suggested in Eurocode 2 (BS EN1992-1-1, 2004), the compressive modulus of the concrete should be around 30 GPa for a C30 concrete mix based on a concrete cylinder test. It seems that the elastic modulus of concrete calculated from the machine reading (9.24 GPa) is significantly lower than the target value. Therefore, the value determined from transducer reading (18.1 GPa) seems more reasonable although, still significantly lower than expected and is selected for calculation of the compressive modulus and stress versus strain response for the concrete-filled grating block. Based on the transducer readings, the longitudinal compressive modulus was established as 7.57 GPa for concrete-filled grating block 1 at a cube strength of 22 MPa and 11.6 GPa for concrete-filled grating block 2 at a cube strength of 34 MPa.

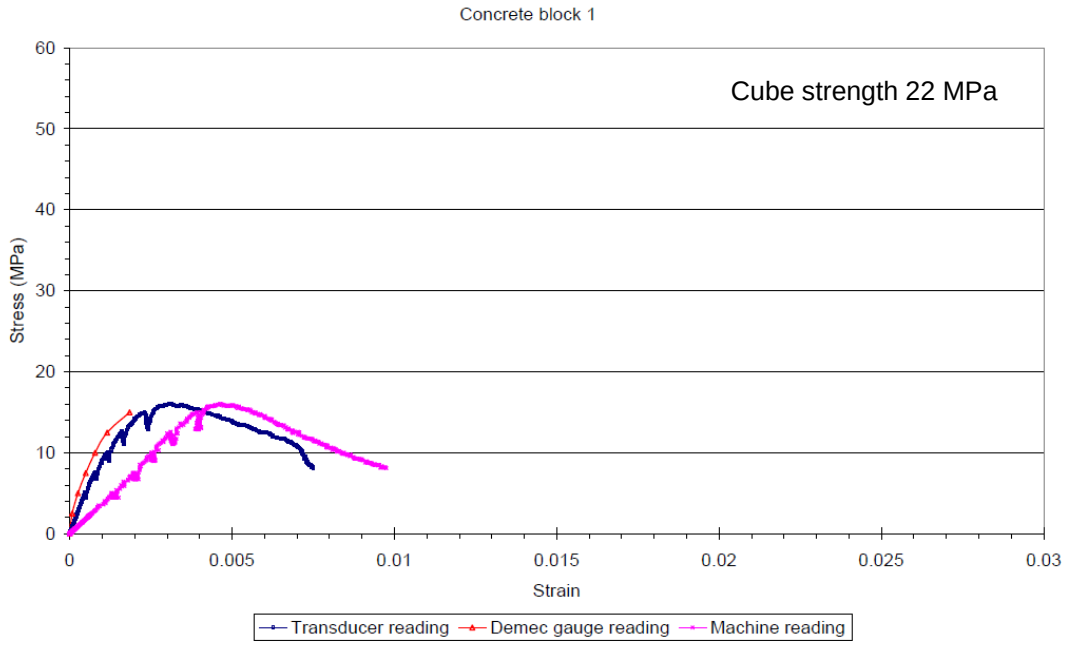

Figure 6.10 – Stress vs. strain plot of the concrete block 1

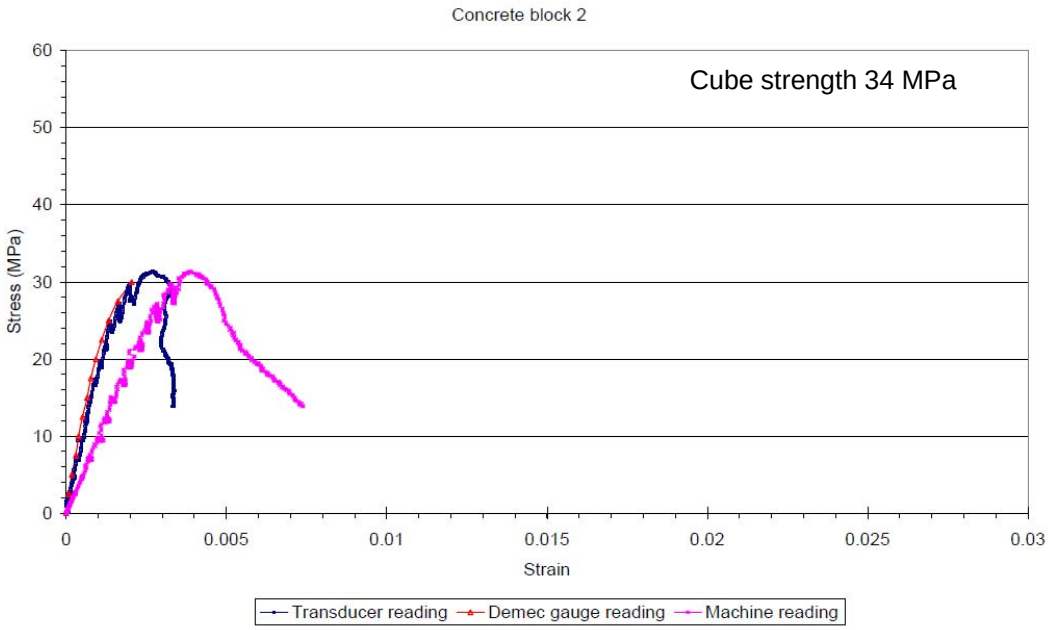

Figure 6.11 – Stress vs. strain plot of the concrete block 2

6.4 Comparisons between the Concrete-Filled Grating Block and Unconfined Concrete Block

Figures 6.12 and 6.13 compare stress versus strain plots between the concrete-filled grating block specimens and unconfined concrete block specimens based on the transducer readings. As shown in Figure 6.12, the concrete-filled grating block 1 led to a 246% increase in the ultimate compressive stress, and a 186% increase in strain capacity compared to identical sized unconfined concrete block 1. As shown in Figure 6.13, the concrete-filled grating block 2 led to a 69% increase in ultimate compressive stress, and a 400% increase in strain capacity compared to unconfined concrete block 2.

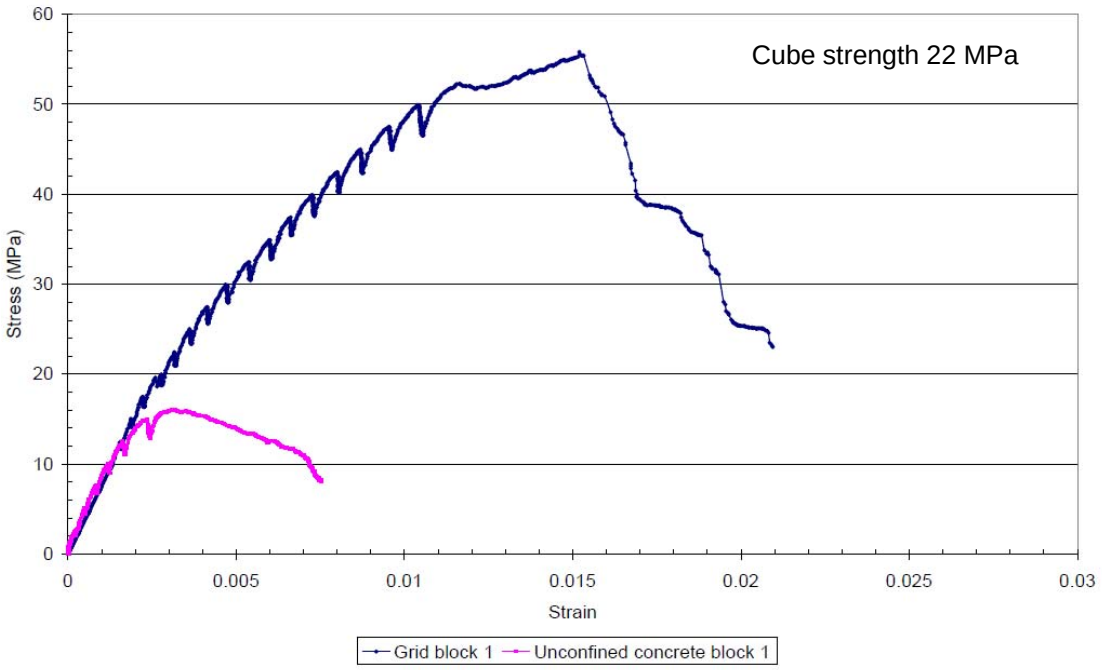

Figure 6.12 – Comparison between the concrete-filled grating block 1 and unconfined concrete block 1

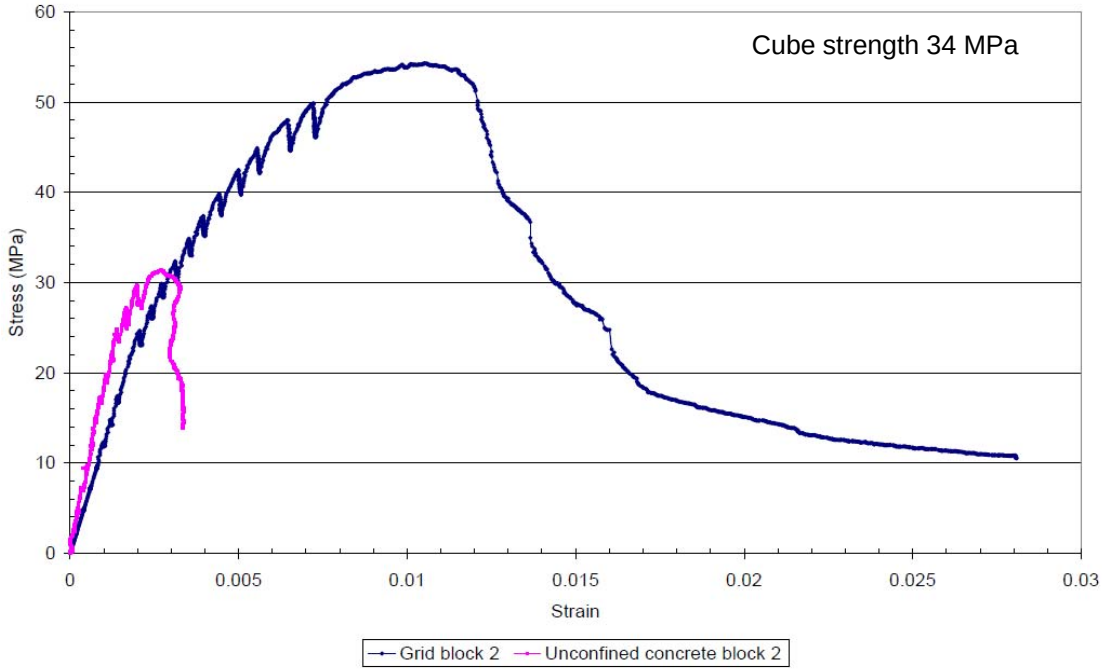

Figure 6.13 – Comparison between the concrete-filled grating block 2 and unconfined concrete block 2

By comparing Figures 6.12 and 6.13, the peak stresses of the concrete-filled grating specimens were 56 MPa for grating block 1 and 54 MPa for grating block 2. It is found that the concrete strength has minor effect on the peak strength of the concrete-filled gratings, but a significant impact on their modulus of elasticity.

As can be seen from Figures 6.12 and 6.13, the axial rigidity of concrete block 1 ($E_c A_c$) in elastic region is similar comparing with that of the concrete-filled grating block 1 ($E_{total} A_{total}$). As the axial rigidity of the concrete-filled grating is a combination of axial rigidity of the concrete and grating, this indicated that the axial rigidity of concrete at cube strength of 22 MPa is similar to that of grating ($E_f A_f$). However, the axial rigidity of concrete block 2 in elastic region is relative stiffer than that of the concrete-filled grating block 2. This difference might be caused by the relative stiffness of FRP grating and concrete. As suggested in Eurocode 2 (BS EN1992-1-1, 2004), a higher strength of concrete can lead to a higher elastic modulus of concrete, resulting in a higher axial rigidity of concrete. Therefore, for a relative higher concrete strength of 34 MPa in concrete block 2, the axial rigidity of concrete ($E_c A_c$) is higher than that of grating ($E_f A_f$). The relative low axial rigidity of the grating ($E_f A_f$) led to a lower axial rigidity of the concrete-filled grating ($E_{total} A_{total}$).

6.5 Summary

This chapter presented an experimental investigation on the feasibility of using GFRP grating as confinement for concrete to enhance strength and strain capacity at peak compressive stress. The amount of strain energy that the material can 'store' has greatly increased. This is indeed the key benefit of the hybrid material system. The investigation was conducted through two sets of concrete block compression tests. From both sets of tests, the concrete-filled grating blocks led to a dramatic increase in the ultimate strength and strain capacity compared with unconfined concrete blocks. The failure strain of the concrete-filled grating specimens was extremely high (approximately 0.02 for the concrete-filled grating block 1 and 0.015 for the concrete-filled grating block 2) compared to the typical concrete failure strain of 0.0035 (BS 8110, 1997). However, its post peak behaviour remained brittle. Therefore, relying on concrete crushing to impart ductility to the system is not feasible. Whilst the brittle failure is undesirable, this increase in strain capacity offers particular benefits, as illustrated in Figure 6.14. Assuming the neutral axis of the composite section is at the grating/box-section interface, by increasing strain capacity from 0.0035 to 0.007 through the confinement by the grating, this extra strain capacity

in the concrete allows the FRP in tension to reach a higher strain capacity of 0.007 to 0.014, which utilises FRP to a greater-extent.

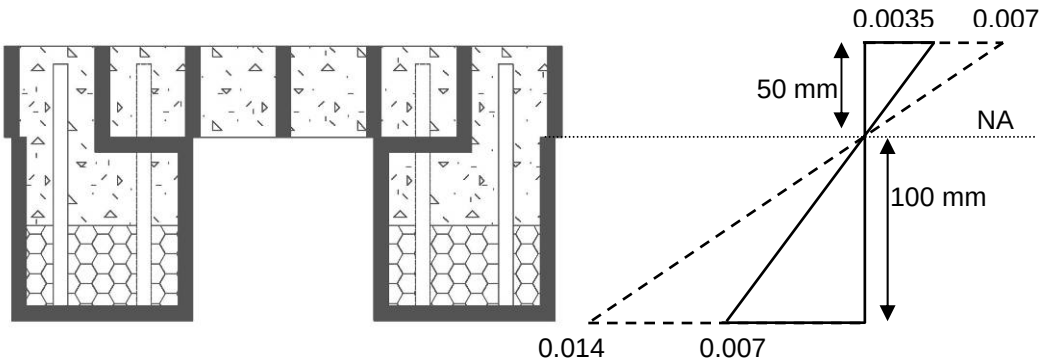

Figure 6.14 – The effect of having extra strain capacity in the concrete to the overall strain profile (solid line indicates a typical strain profile of FRP reinforced concrete member, and dash line indicates a strain profile with extra strain capacity in the concrete)

The stress versus strain response of the concrete-filled grating block is used in the Chapter 9 for sectional analysis of FRP-concrete hybrid formwork system. The investigation on the proposed shear connectors to provide a controlled longitudinal shear failure, resulting in a ductile failure manner, will be investigated through full-scale slab tests.

Chapter 7 Experimental Investigation of Permanent Participating GFRP Formwork for Concrete Floor Slabs

7.1 Introduction

Chapter 5 demonstrated a potential means of achieving ductility using GFRP dowels embedded into concrete at the grating/concrete interface, confirming feasibility through push-out tests. Chapter 6 demonstrated that a concrete-filled grating block can provide a significant increase in ultimate strength and strain capacity compared with an unconfined concrete block. However, the failure of the concrete-filled grating block was still brittle. Therefore, the prospect of relying on concrete crushing to introduce ductility is not feasible. This chapter details an experimental investigation into a complete prototype system at full-scale to determine whether sufficient ductility from a controlled longitudinal shear failure provided by the proposed shear connector can be achieved. Various dowel spacings, which influence the degree of composite action, are investigated for their performance under five-point bending, simulating both representative moment and shear envelopes. The details of these slab specimens and their test results are presented in Sections 7.2 to 7.4.

7.2 Experimental Programme

Based on the findings of component tests and shear bond tests, six slab tests were designed and tested under five-point bending. A description of the FRP-concrete hybrid formwork system and the material properties of each component are presented next.

7.2.1 Description of the FRP-concrete hybrid formwork system

The prototype slab specimens were composed of two 3 m long GFRP box sections (100 x 100 x 8 mm) adhesively bonded to 300 mm wide, 50 mm deep and 3 m long moulded GFRP grating using Araldite 2015. Each specimen has a length of 3000 mm, a width of 300 mm, and a depth of 150 mm. A schematic cross-section drawing of the cross section of the slab specimen is shown in Figure 7.1. Both components were connected at a variable spacing using 132 mm long sand-coated GFRP dowels (diameter 10 mm) with an embedment length of 88 mm into the concrete, as shown in Figure 7.1. Holes of 38 mm

diameter in the top flange of the box sections allowed the GFRP dowels to be inserted into the 44 mm thick foam blocks and allowed the concrete to fill the remaining 40 mm of the box section. Once the concrete had been cured, the top half of the GFRP dowels were anchored in the concrete-filled lattice of the grating, since the grating was completely filled with concrete. The bottom half of the GFRP dowels were embedded in the partially concrete-filled GFRP box sections (40 mm deep embedment in concrete). The composite action between the grating and box sections during the concrete casting initially relied on the adhesive bond provided by the epoxy adhesive. After placement of the concrete, the GFRP dowels and concrete studs which formed around these 38 mm holes acted compositely to resist longitudinal shear at the grating/box-section interface. This composite section was designed in order to fulfill the requirements for stiffness at the serviceability limit state and strength at the ultimate limit state. Different dimensions of pultruded box sections were considered in order to ensure that the neutral axis of the composite section was located at the grating/box-section interface. The box sections were fully utilised in tension and the concrete-filled grating were fully utilised in compression.

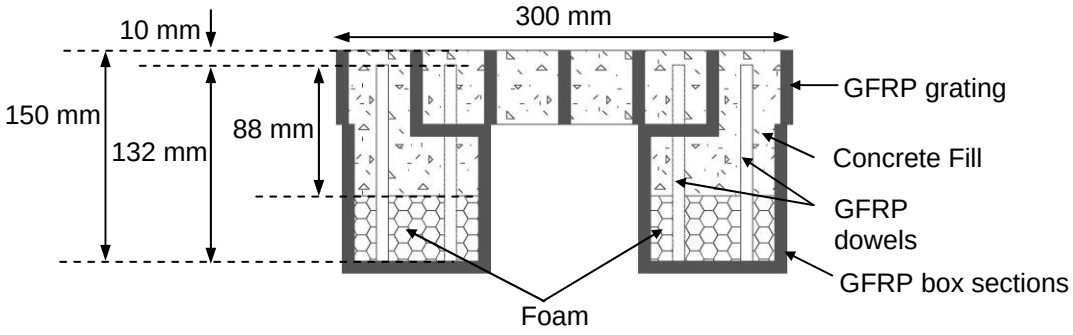

Figure 7.1 – The cross section of the FRP-concrete hybrid formwork system

7.2.2 Materials

Self-compacting concrete, along with pultruded GFRP box sections, GFRP dowels, foam blocks, and moulded GFRP gratings of the type shown in Figure 7.2 were used in this study. The following sections provide a detailed description of the different materials.

Figure 7.2 – GFRP dowels, moulded GFRP gratings, foam blocks, and GFRP box sections. (From left to right)

Pultruded GFRP box section

Commercially available 6 m long GFRP pultruded box sections of 100 x 100 x 8 mm were supplied by Fibreline Composites, Denmark, for the tension region. The box section had an average longitudinal tensile strength of 355 MPa and a longitudinal tensile modulus of 32.1 GPa, as shown in Table 7.1. These values were obtained from coupon tests undertaken according to BS EN ISO 527-5 (2009), as discussed in Chapter 4. These sections were each cut to a length of 3 m to fabricate the formwork.

Table 7.1 – Summary of coupon tensile test results

Tensile properties	*T*- thickness (mm)	*W*- width (mm)	*L*- total length (mm)	L_o- distance between grips(mm)	E_L- elastic modulus (GPa)	Failure mode	Failure stress (MPa)	Failure strain (%)
Top_1	7.8	25.1	302	150	31.3	Tab failure	N/a	N/a
Top_2	7.9	25.4	301	151	32.1	Tab failure	N/a	N/a
Bot_1	8.5	25.5	301	150	33.2	Tab failure	N/a	N/a
Bot_2	8.5	25.4	301	151	32.6	Tab failure	N/a	N/a
WA_1	8.2	25.2	300	150	32.4	Splitting of fibres	357	1.10
WA_2	8.2	25.2	301	151	31.5	Splitting of fibres	345	1.09
WB_1	8.0	25.4	301	151	31.8	Splitting of fibres	351	1.10
WB_2	7.9	25.7	300	150	32.2	Splitting of fibres	368	1.13
Average					32.1		355	1.10

Moulded GFRP grating

Commercially available panels of moulded GFRP grating (50 x 50 mm grid size) were cut into 300 x 3000 mm strips for fabrication of the formwork. The grating was 50 mm deep and has 35-40% fibre content by weight. Compressive strength

and compressive modulus of 243 MPa and 24.3 GPa, respectively, in the longitudinal direction, were obtained from compression coupon tests according to BS EN ISO 14126 (1999), as discussed in Chapter 4.

Pultruded GFRP bar

Aslan 100 GFRP pultruded rebar of 10 mm diameter, composed of E-glass fibres at minimum 70% fibre content by weight and vinylester resin, were supplied by Hughes Brothers and were used as GFRP dowels. Based on the values obtained from the manufacturer's data sheet, the GFRP bars had an ultimate tensile strength and modulus of elasticity of 760 MPa and 40.8 GPa, respectively. The shear strength and maximum bond strength were 152 MPa and 11.6 MPa, respectively, specified in the manufacturer's data sheet (Hughes Brothers Inc, 2010).

Epoxy adhesives

A two-component epoxy paste adhesive, Araldite 2015 (manufactured by Huntsman Advanced Materials), was used to bond the grating to the box sections to form a stay-in-place structural formwork for concrete. It had a mortar-like texture with a relative high viscosity, and ideal for bonding the FRP components. From the manufacturer's technical data sheet, bond strength was determined by testing specimens made by lap-jointing 114 x 25 x 1.6 mm strips with a joint area of 12.5 x 25 mm. The average lap shear strength of GFRP-GFRP joints was determined as 9 MPa (Huntsman Advanced Materials, 2010).

Polyethylene foam block

Foam blocks were used to create a void in the box sections in the tension zone. As discussed in Chapter 5, forming a void reduces the use of concrete in the tension zone. It is clear from the push-out test results of Chapter 5 that there is no difference in residual strength between fully concrete-filled specimens and partially concrete-filled specimens. The foam blocking was introduced to remove unnecessary concrete mass in the box sections. The secondary function of the foam in the box sections was to provide support for the GFRP dowels before the concrete was cast.

Self-compacting concrete

Due to manufacturer constraints, the maximum grid size of the grating provided by Fiberline composites was 50 x 50 mm, which is currently the maximum grid size which can be provided in the composites industry. During the concrete flow trial tests, it was found to be difficult for normal concrete (aggregate size up to 20 mm) to fill the box sections through the 38 mm diameter holes, which had been drilled into the box sections. In order to solve this construction issue, Self-Compacting Concrete (SCC) was used to improve flowability and for ease of casting. SCC is an innovative cementitious material that does not require vibration for placing and compaction. It is able to flow under its own weight, completely filling the formwork and achieving full compaction, even in the presence of congested reinforcement (The European Concrete Platform, 2005). In the SCC mix design, the maximum aggregate size for the first three of the total of six slab specimens, S_1 to S_3, was 10 mm. The water-cement ratio was 0.42. Three 100 mm concrete cubes were taken from each batch of concrete. The concrete mix design for specimens S_1 to S_3 is given in Table 7.2.

Table 7.2 – Concrete mix design for specimens S_1 to S_3

Concrete mix C50	kg/m^3 for 1 m^3 of concrete
Water	190
Portland-fly ash cement	450
Fine sand (0.15-0.25 mm)	150
Coarse sand (0.2-4 mm)	800
Aggregate (4-10 mm)	800
ADFLOW-EXTRA superplasticiser	6 l/m^3 (1.3% of mass of concrete)

For specimens S_1 to S_3, the concrete compressive strength was determined from three cube tests ranged from 46.5 MPa to 52.3 MPa with an average of 49.0 MPa at the time of slab testing. This is given in Table 7.3. Super-plasticiser ADOFLOW-EXTRA was used in order to make the mix self-flowing, allowing the concrete to easily fill the holes without excessive compaction. However, in reality, during casting there was visual evidence of concrete segregation and bleeding, indicating that ADOFLOW-EXTRA greatly accelerated the curing process, resulting in quick hardening of the concrete, which led to blocking of holes. Consequently, there were voids formed in the concrete fill inside the box sections, causing insufficient bonded embedment of GFRP dowels in the box sections.

Table 7.3 – Concrete strength for specimens S_1 to S_3

Specimens	Cube strength at the time of slab testing (MPa)
S_1	49.1
	51.0
	46.5
S_2	48.6
	49.4
	52.3
S_3	48.2
	47.5
	48.7

For the remaining three specimens S_4 to S_6, super-plasticiser GLENIUM 123 was used, and the dosage was minimised in order to avoid excessive bleeding of the concrete. As seen in Table 7.4, the maximum aggregate size was reduced to 6 mm to avoid blocking of the holes. Estimation of flowability and workability of SCC was verified by slump flow tests, in which the spread diameter of the mix is measured. For SCC, the flow diameter should exceed 600 mm (Kim *et al*, 1998). In order to achieve this spread, the water-cement ratio was increased from 0.42 to 0.60. The concrete slump spread diameter for the mixing in Table 7.4 was 640 mm. This can be seen in Figure 7.3. The design concrete strength for slab specimens S_4 to S_6 was reduced to 30 MPa, as C30 is a typical concrete strength grade in building construction. The concrete compressive strength was determined from five cube tests ranged from 25.5 MPa to 32.1 MPa with an average of 28.2 MPa at the time of slab testing. This is given in Table 7.5.

Table 7.4 – Concrete mix design for specimens S_4 to S_6

Concrete mix C30	kg/m^3 for 1 m^3 of concrete
Water	300
Portland-fly ash cement	500
Fine sand (0.15-0.25 mm)	351
Coarse sand (0.2-4 mm)	413
Aggregate (2-6 mm)	825
GLENIUM 123 superplasticiser	2.14 l/m^3 (0.43% of mass of concrete)
Slump spread diameter	640 mm

Table 7.5 – Concrete strength for specimens S_4 to S_6

Specimens	Cube strength at the time of slab testing (MPa)
S_4	25.7
	25.5
	26.1
	26.7
	25.8
S_5	27.2
	25.9
	27.9
	27.2
	27.0
S_6	31.2
	32.1
	31.2
	32.1
	31.8

Figure 7.3 – Concrete slump flow test

7.2.3 Design concept of full-scale test specimens

Loading schemes

All slab specimens were tested using a five-point bending set-up. Although buildings are generally designed for uniformly distributed loads, it is not necessarily the worst case and point loads should also be considered. Therefore, the point load envelope was chosen to simulate the worst case scenario in building construction. It defines the extreme boundary values of bending moment and shear force along the beam due to critical placements of design live loading. The bending moment envelope, which is caused by a point load 'Q' moving along the span from one support to the other, was plotted in order to investigate the behaviour of specimens due to flexural failure, as shown in Figure 7.4. The shear force envelope, which is also caused by the same load, was plotted in order to investigate the behaviour of specimens due to longitudinal shear failure, as the longitudinal shear force is directly related to the

vertical shear force. Both schemes were designed to verify the concepts that the controlled concrete crushing and/or progressive longitudinal shear failure can provide ductility to the overall system. The two types of loading schemes were chosen – Type A and Type B. Schematic drawings for both set-ups are shown in Figure 7.4.

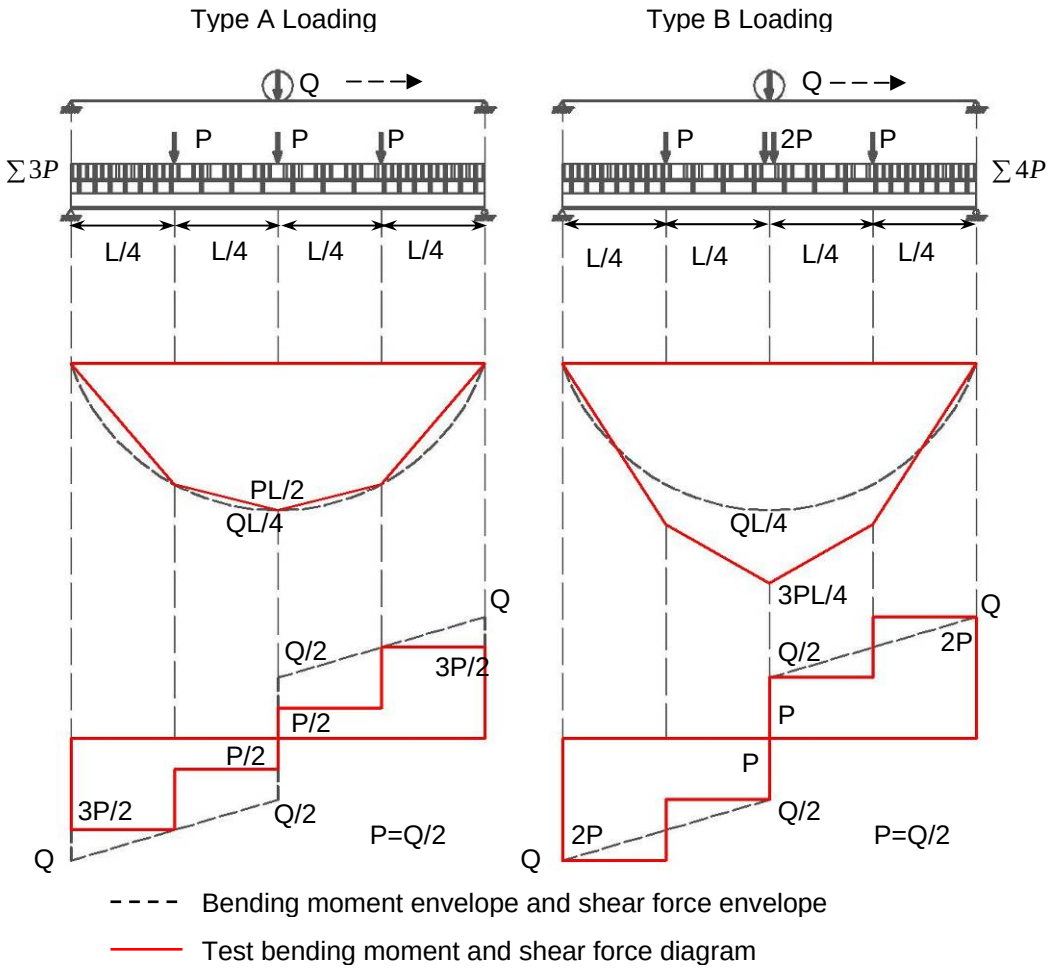

Figure 7.4 – Type A loading and Type B loading schemes

Type A loading

Specimens S_1 and S_6 were tested under three equal point loads, P, acting at the quarter span, mid-span and three-quarter span, as illustrated in Figure 7.4. This loading configuration was chosen to simulate approximately the bending moment envelope. The bending moment at each quarter span point and at mid-span of the Type A loading correlated well with that of the bending moment envelope. However, the shear force diagram under the Type A loading did not

match well with the vertical shear force envelope, with a significant underestimation of vertical shear force.

Type B loading

Type B loading was also chosen to better simulate the vertical shear force envelope. Specimens S_2, S_3, S_4, and S_5 were tested under three point loads P, 2P, and P, with the 2P at mid-span. In contrast to Type A loading, the mid-span loading (2P) is twice of magnitude as much as the loading at each of the quarter span points (P), as illustrated in Figure 7.4. The vertical shear demand under Type B loading correlated well with the vertical shear force envelope, with an exact match at mid-span and at the end support. Therefore, it was selected as an approximate simulation of the vertical shear force envelope. However, the bending moment diagram under Type B loading did not match closely with the bending moment envelope. Thus, it was not suitable for simulating the bending moment envelope.

Non-uniform distribution of shear connectors

When specimens are subject to several point loads, it is potentially inefficient to use a uniform distribution of shear connectors right across the entire span. Therefore, linear-elastic shear flow was used as a guideline to concentrate the connectors in areas of highest shear force demand. The longitudinal shear flow q may be found if the shear force V is known, from:

$$q = \frac{VA_c \bar{y}}{I} \tag{7.1}$$

where $\bar{y}$ is the distance between the centroid of the concrete-filled grating component and the centroid of the transformed composite beam (transformed to the concrete-filled grating), V is the vertical shear force, A_c is the cross sectional area of the concrete-filled grating component and I is the second moment of area of the transformed composite section.

As can be seen from Figure 7.4, under Type B loading, the vertical shear force between the support and the quarter-span is twice of magnitude as much as that between the quarter-span and the mid-span. Thus, a non-uniformly distributed shear connection has been adopted in order to ensure that all shear connectors

are able to reach full 'plastic' capacity. This is one of the important assumptions made in the subsequent elastic-plastic analyses in Chapter 9. The layouts of holes for forming shear connectors in specimens S_1 to S_6 are shown in Figure 7.5. Table 7.6 summarises the distribution of shear connectors along the span in specimens S_1 to S_6.

Figure 7.5 – Layout of 'zig-zag' pattern holes on top flange of box sections in specimens S_1 to S_6

Design parameters

Table 7.6 – Distribution of shear connectors along the span in specimens S_1 to S_6

Specimens	No. of FRP dowels (0<x<L/4)	No. of concrete studs (0<x<L/4)	No. of FRP dowels (L/4<x<L/2)	No. of concrete studs (L/4<x<L/2)	Loading scheme
S_1	30	30	8	8	P,P,P
S_2	14	14	8	8	P,2P,P
S_3	8	8	4	4	P,2P,P
S_4	8	8	4	4	P,2P,P
S_5	8	30	4	28	P,2P,P
S_6	8	8	4	4	P,P,P

A key objective of the slab tests was to verify the concept of relying on the post-yield characteristics of the proposed shear connector to provide ductility to the overall system. A total of six slab specimens were prepared and tested in two groups. The first group contained specimens S_1, S_2 and S_3, and the second group contained specimens S_4, S_5 and S_6. Table 7.6 provides a summary of the details of the slab specimens. The first group of specimens was designed with differing spacings of shear connectors at the grating/box-section interface in an attempt to determine the optimum number of shear connectors in order to achieve adequate ductile behaviour. The number of shear connectors was designed in proportion to the longitudinal shear required, and non-uniformly distributed along the span. Specimen S_1 was designed with the highest number

(76) of shear connectors, representing the highest longitudinal shear resistance, followed by S_2 and S_3. After testing specimens S_1 to S_3, three specimens were cut from the mid-span to examine the concrete-fill condition. It was found that there was poor concrete placement in the box sections across all three specimens. Therefore, three more tests were repeated following the design of specimen S_3, as it exhibited similarly ductile behaviour to that of specimens S_1 and S_2, with the lowest number (24) of shear connectors. Specimens S_4 and S_6 were designed to have an identical number of shear connectors as that in specimen S_3. Specimens S_4 and S_6 were tested using different loading schemes. Specimen S_5 was designed to have an identical number of GFRP dowels to specimen S_3, but with a much higher number (88) of circular holes without dowels cut into the top flange of the box sections to improve concrete flow into the box sections. Specimen S_5 allowed comparison with specimens S_4 and S_6 in order to quantify the contribution of having more concrete studs, but the same number of GFRP dowels, to the overall failure behaviour of the composite system. Schematic drawings of the dowel positions in the six specimens are given in Figure 7.6.

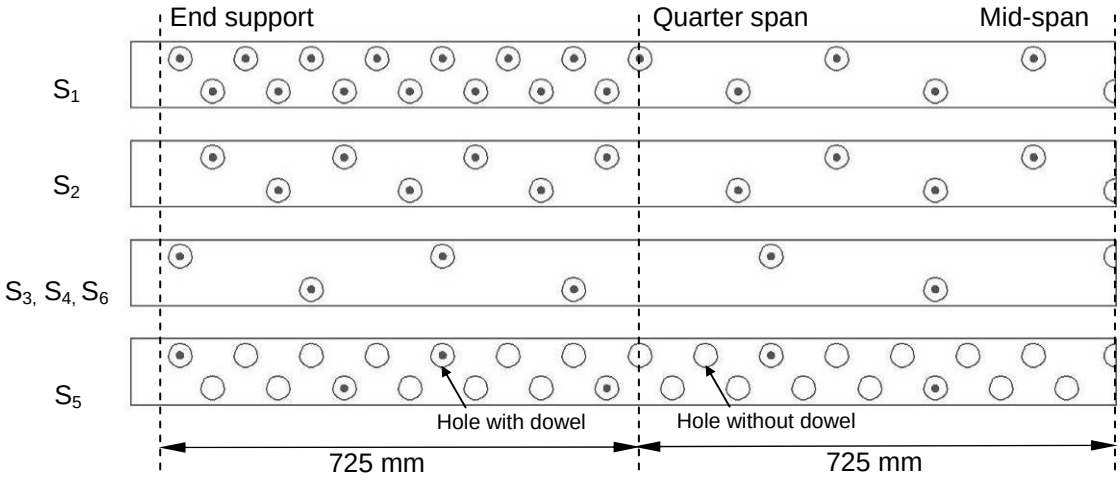

Figure 7.6 – Distribution of holes with and without dowels in specimens S_1 to S_6

7.2.4 Fabrication of test specimens

GFRP box sections and gratings were cut to size and their surfaces were cleaned thoroughly using acetone. The first step of the construction process was to mark the positions where holes were required to be drilled into the box sections. This was achieved by laying down the grating on top of the box sections and marking the positions of the holes on the upper flanges with a marking pen. Then, holes were drilled into the top flange of the box sections

using a 38 mm circular hole cutter, as shown in Figure 7.7(a). In specimens S_4 to S_6, several 8 mm holes were drilled through the top flanges between adjacent 38 mm holes. As shown in Figure 7.7(b), they were added to improve concrete flow, by letting trapped air out, and to allow the filling condition inside the box sections to be checked. The following step was to fabricate the formwork by adhering the grating to the top of two box sections spaced 100 mm apart. This was achieved by applying a thin layer of the mortar-like Araldite 2015 epoxy adhesive to the bond surfaces (see Figure 7.7(c)) and lightly clamping the two units together. Curing of adhesive bond lasted 24 hours. As there was a 100 mm gap underneath the grating between the two box sections, a 100 mm wide timber strip, as shown in Figure 7.7(d), was cut to size and fitted into this gap, and then suspended underneath the bottom surface of the grating using steel wires to stop wet concrete passing through the middle gap. Once the adhesive was fully cured, 84 x 44 mm (width x depth) rectangular foam blocks were cut to size and inserted into the box sections, as shown in Figure 7.7(e). Shear connectors were created by inserting 132 mm long GFRP dowels into the 38 mm circular holes, which were then pushed fully into the 44 mm deep foam block. All dowels were installed such that they protruded 88 mm from the top surface of the foam block, which were embedded in concrete later, as shown in Figures 7.7(e) and (f). Thus, an equal length of embedment (40 mm) was achieved in both the concrete-filled grating and the partially-concrete-filled box sections. This was desirable to prevent the creation of a weak link in either the grating or in the box sections. The shear-critical end zones of the specimens (300 mm in length) were fully filled with concrete in order to avoid end crushing at the supports.

Figure 7.7 – Fabrication procedure of the formwork

In specimens S_4 to S_6, concrete flow trial tests were conducted before the actual casting, in order to make sure the mix could flow appropriately. Figure 7.8(a) shows the 40 mm gap inside the box section was completely filled with concrete, using the concrete mix design as shown in Table 7.4. As shown in Figure 7.8(b), it was also found that the concrete overflowed through the 8 mm inspection holes, further indicating good concrete-fill inside the box sections.

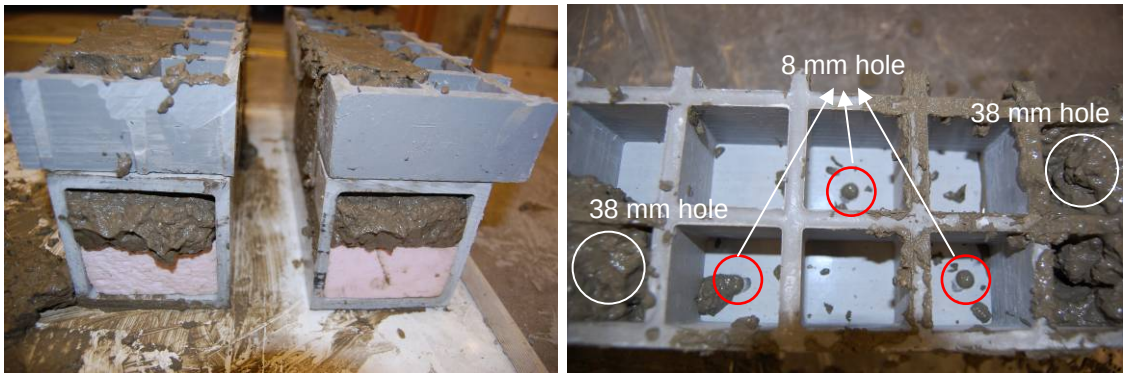

(a) (b)

Figure 7.8 – Concrete trial tests

After fabrication of the formwork, timber stops were mounted at each end in order to retain the concrete inside the box sections as shown in Figure 7.9. The formwork was then suspended on end supports, to reflect a real unpropped casting situation, and the concrete was cast. The surface was finished, and the specimens were cured for 28 days.

Figure 7.9 – Formworks were suspended during concrete casting

7.2.5 Immediate deflection during and after concrete casting

Prior to the casting of specimens S_1 to S_3, displacement transducers were installed at mid-span underneath the box sections to track the immediate deflection during the construction stage, as shown in Figure 7.10. Eurocode 4 (Part 1.1–Design of Composite Steel and Concrete Structures) states that the deflection of the permanent formwork after completion of concreting should not exceed 1/300 of the span, which is 9.7 mm vertical deflection for a 2.9 m span. It would seem reasonable to apply similar design requirements to this FRP formwork system. The immediate mid-span deflections following casting of specimens S_1 to S_3 were less than 2 mm, as shown in the deflection against time plot in Figure 7.11. The theoretical immediate deflection of the glue GFRP

section under its self weight and wet concrete is calculated to be 1.05 mm, determined from Eq. (7.1):

$$\delta = \frac{5wl^4}{384EI} \tag{7.1}$$

where w is the self weight of the glued GFRP section and wet concrete, and l is the span of the GFRP section, EI is the flexural rigidity of the GFRP section. As the glued GFRP section having different longitudinal moduli in the parts of the cross section, the flexural rigidity is calculated using the transformed section approach.

It was found that the measured immediate deflection in Figure 7.11 matched well with the theoretical value. Additional construction load was simulated by one person standing on top of the formwork for specimen S_2. This additional loading is represented in Figure 7.11 by a sudden increase in the deflection at mid-span of 1 mm, followed by recovery to its original deflection as the loading was removed from the formwork. This construction-sequence loading demonstrated that the proposed system satisfies deflection limits for composite construction under unpropped conditions.

Figure 7.10 – Test set-up for measuring the immediate mid-span vertical deflection of the glued GFRP section

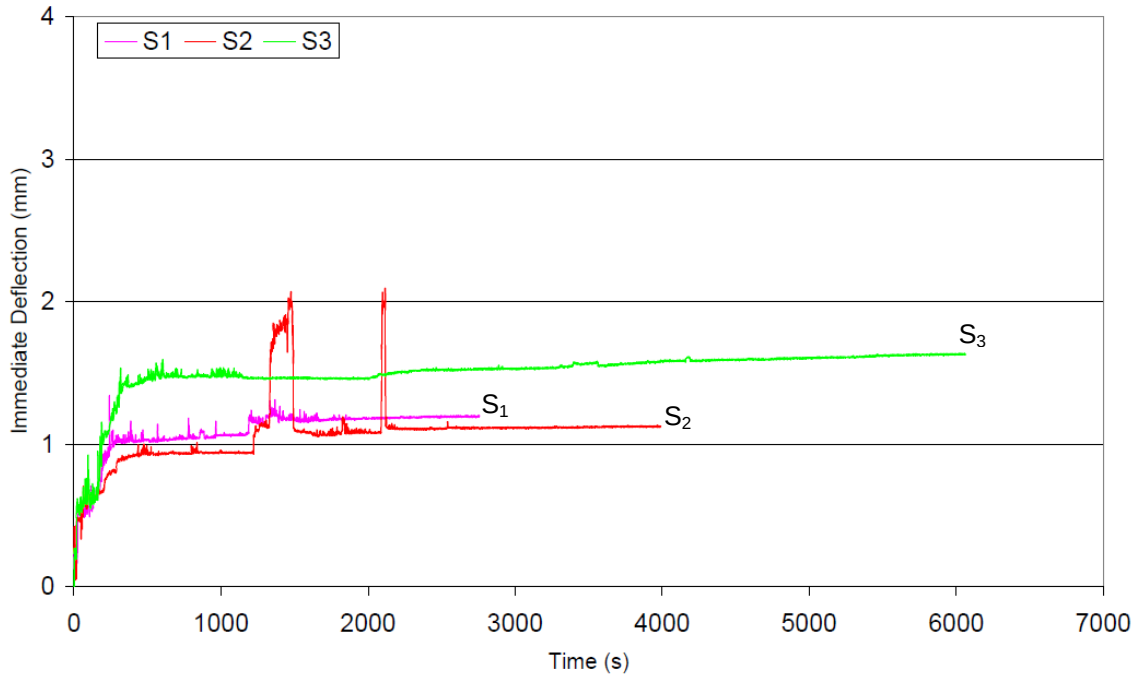

Figure 7.11 – Immediate mid-span vertical deflection during and after concrete casting

7.2.6 Test set-up and instrumentation

Each specimen was tested using a five-point bending set-up over a span of 2900 mm, with 725 mm spacing between each loading point. The end support conditions were one roller support and one pin support. Photographs of this set-up are shown in Figure 7.12. Specimens S_1 and S_6 were tested under three equal point loads (referred to as Type A) using a load increment of 2 kN. Only one pump was used to control these three jacks in order to make sure that three equal loads were applied. Specimens S_2, S_3, S_4 and S_5 were tested under three point loads (referred to as Type B) with the mid-span loading twice the load at each of the quarter points. Two pumps were used to control the two load types separately to ensure that the load imposed by the central jack was twice that at each of the quarter points. Thus, the load was applied using a load increment of 2 kN in the two jacks located at each of the quarter points, and a load increment of 4 kN in the mid-span jack. Steel plates of 300 x 100 x 10 mm (length x width x thickness) were present between specimens and pin plates to act as a load spreader to prevent local crushing.

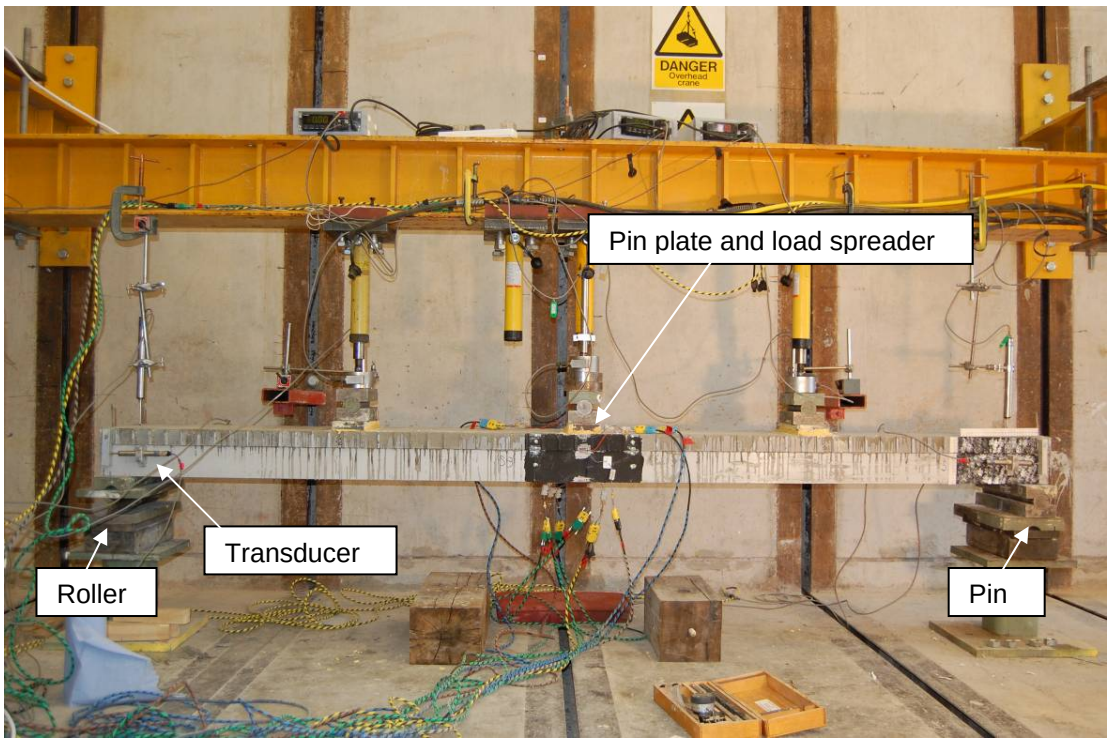

(a) Test set-up for specimens S_1 to S_3

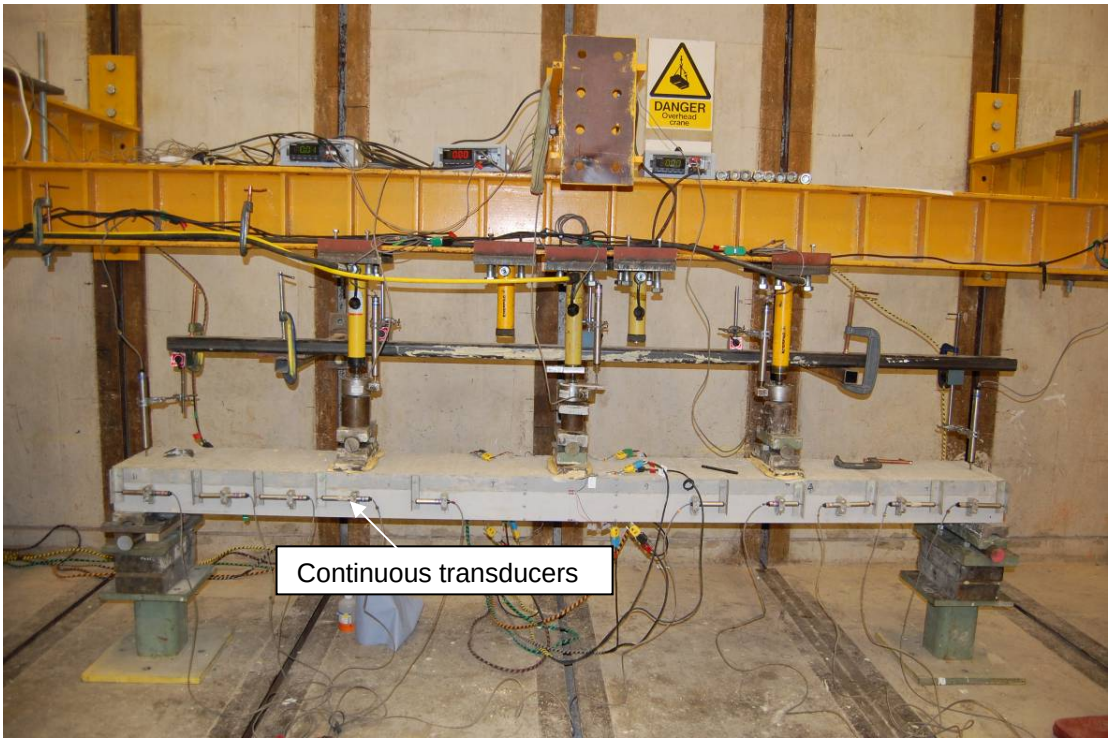

(b) Test set-up for specimens S_4 to S_6

Figure 7.12 – Five-point bending set-up

LVDTs (Linear Variable Differential Transducers) were used to monitor mid-span vertical deflection, as well as the relative end slip between the concrete-filled grating and the GFRP box sections. In specimens S_1 to S_3, end slips between

the grating and box sections were recorded by installing two pairs of transducers at both ends of the box sections, as seen in Figure 7.12(a). In specimens S_4 to S_6, a total number of ten LVDTs were installed at, almost, every dowel position along the grating/box-section interface on the front side (except the one closest to mid-span due to a lack of space to install the transducers). These displacement measurements can be seen in Figure 7.12(b). Their purpose was to record the relative slip continuously along the grating/box-section interface. Strains were monitored using 10 mm electrical resistance strain gauges FLA-10-11 (Tokyo Sokki Kenkyujo) and 300 mm DeMec gauges installed at mid-span on both sides of each specimen. On each side, a total of five electrical resistance strain gauges were placed in the longitudinal direction at just below the top surface of the grating, above the grating/box-section interface, below the grating/box-section interface, at the bottom corner of the box sections and on the bottom surface of the box sections, as shown in Figure 7.13(a). A total of six pairs of DeMec gauges (gauge length is 300 mm) were installed at these locations: just below the top surface of the grating, centre of the grating, above the grating/box-section interface, below the grating/box-section interface, centre of the box sections and bottom corner of the box sections, as shown in Figure 7.13(b). The purpose of applying both gauges in this particular regime was to monitor the strains, top and bottom, of the concrete-filled grating and of each box section, and to capture the strains at failure. By capturing the strain reading at each designated location, the strain profile before and after longitudinal shear failure at maximum bending moment could be plotted, and compared in order to understand the failure behaviour of this composite system. Loading interval for taking the DeMec gauge readings was set to be 4 kN increments for specimen S_1 and 2 kN increments for specimens S_2 and S_3, since specimen S_1 had been designed to fail at a higher load.

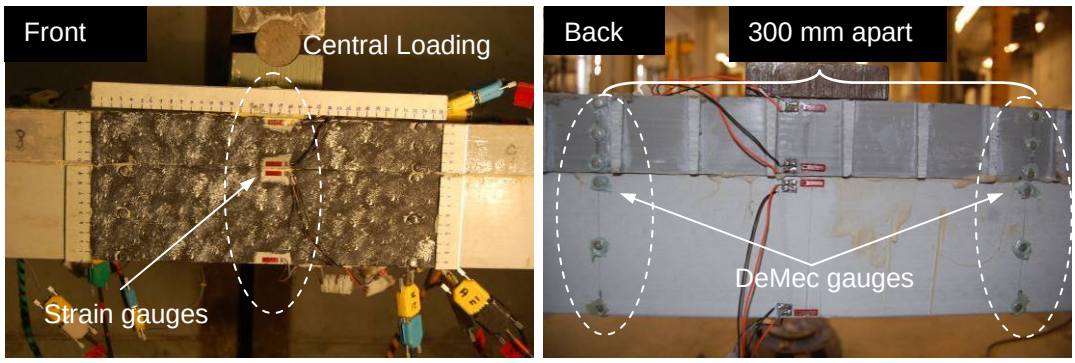

(a) Positioning of strain gauges (b) Positioning of DeMec gauges

Figure 7.13 – Positioning of strain gauges and DeMec gauges

7.3 Results of the Experimental Programme

A summary of test results for each specimen, including the load at which debonding occurs, peak load and mid-span vertical deflection at ultimate failure, are provided in Table 7.7. The total load versus mid-span deflection plots are shown for specimens S_1-S_3 in Figure 7.14 and for specimens S_4 to S_6 in Figure 7.15. Similarly, Figures 7.18 to 7.29 show the total load versus relative end-slip responses and total load versus mid-span deflection responses for each of the specimens S_1 to S_6.

Table 7.7 – Summary of slab test results

Slab specimens	Mean cube strength of concrete (MPa)	Load at which debonding occurs (kN)	peak load (kN)	Mid-span vertical deflection at ultimate failure (mm)
S_1	48.9	135	167	171
S_2	50.1	75	100	145
S_3	48.1	61	82	137
S_4	25.9	48	112	148
S_5	27.1	89	113	161
S_6	31.7	54	138	173

7.3.1 Load versus deflection responses of specimens S_1 to S_6

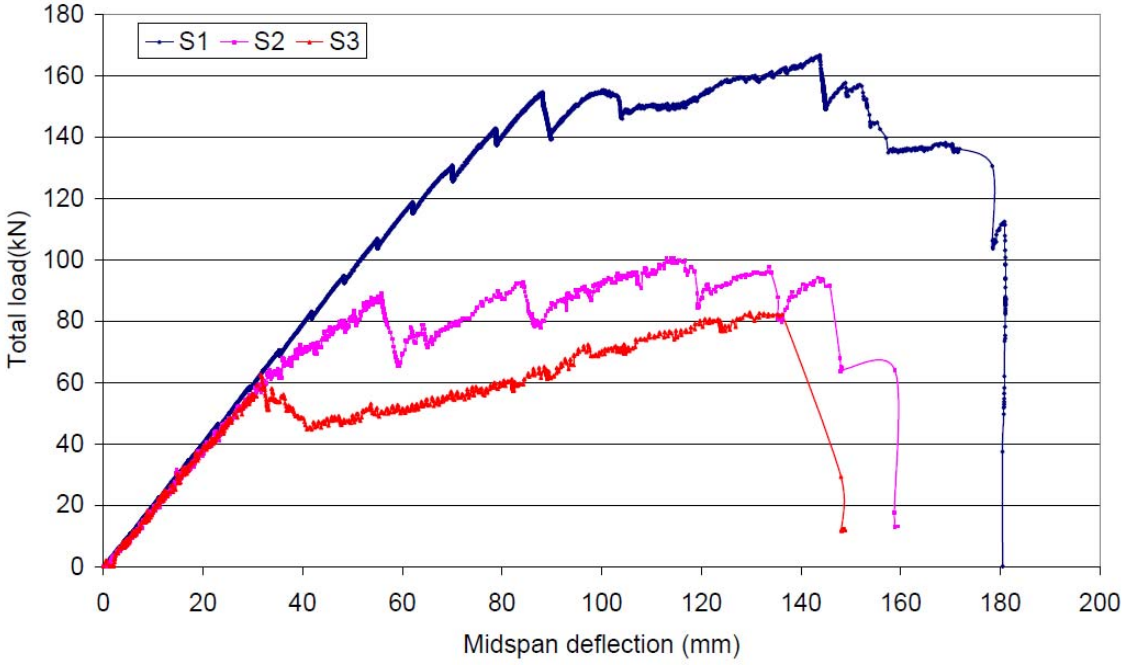

Figure 7.14 – Total load versus midspan deflection for specimens S_1, S_2 and S_3

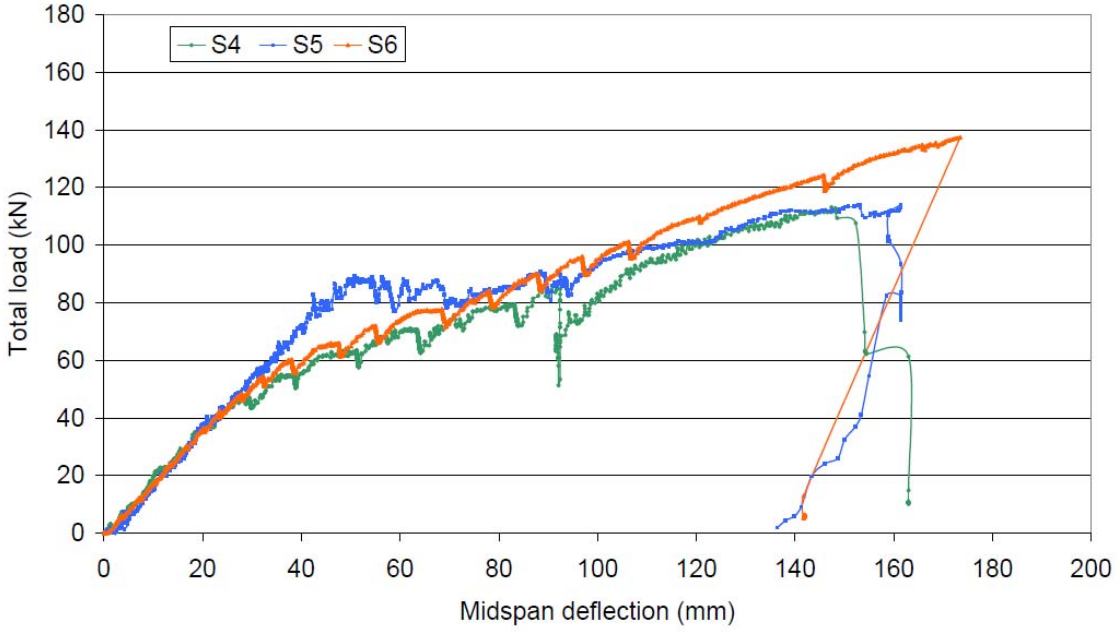

Figure 7.15 – Total load versus midspan deflection for specimens S_4, S_5 and S_6

Specimens S_1 to S_3 were cast on the same day as the first group and were load tested after 28 days. The mean concrete strengths determined from cube testing at the time of the slab tests ranged from 48.1 MPa to 50.1 MPa with a small difference of 4%, as seen in Table 7.7. Therefore, the results are directly comparable. As can be seen in Figure 7.14, all three specimens behaved in an

approximately linearly elastic fashion to the initial peak load, followed by a small drop in load capacity, and then carried on increasing in load response up to the second peak until final brittle failure occurred due to local buckling of the box sections at a deflection in excess of the depth of the member. The final failure occurred in the pultruded box sections in which the top flange separated from the webs at their junctions, followed immediately by in-plane buckling of unrestrained webs. The load capacity dropped almost to zero after the final failure.

Specimens S_4 to S_6 were cast on the same day as the second group and were load tested after 28 days. As can be seen in Figure 7.15, they behaved in a linearly elastic fashion prior to debonding failure, followed by exhibiting an increasing load response at a reduced slope up to the second peak. This transition from elastic to a softening response did not involve a significant drop in load at any point, in contrast to specimens S_1 to S_3.

This significant drop in load capacity after the initial peak in specimens S_1 to S_3 was probably caused by the fact that there were air voids in the concrete like a fist size in the box sections in the central region. These voids were discovered after cutting the three specimens at mid-span with a circular saw to examine the concrete-fill conditions. It was clear that the moulded GFRP grating was completely filled with concrete, as seen in Figure 7.16(a). However, the concrete-fill condition in the GFRP box section was poor, particularly between mid-span and quarter span, where there were fewer holes to allow the concrete to flow into the box sections. As mentioned earlier, in Section 7.2.2, there was evidence of concrete segregation and bleeding for specimens S_1 to S_3, resulting in blocking of holes. Consequently, large voids formed in the concrete-fill inside the box section of specimens S_1 to S_3, as seen in Figures 7.16(b) to 7.16(d). Due to the presence of large air voids, the dowels were not anchored properly on both sides of the grating/box-section interface, and as a result dowelling could not contribute fully to resisting the longitudinal shear force. Dowel action could not be fully mobilised within the void regions, causing a reduction in longitudinal shear resistance. This could explain why specimens S_1 to S_3 exhibited a significant drop in load capacity temporarily after the initial peak. As discussed in Section 7.2.4, in the subsequent tests of specimens S_4 to S_6, a series of 8 mm

diameter inspection holes were drilled through the top flange between adjacent 38 mm circular holes to improve concrete flow by letting trapped air out and to allow the filling condition of the concrete inside the box sections to be checked. During concrete casting, it was found that the concrete overflowed from these 8 mm inspection holes, indicating an acceptable concrete fill inside the box sections. This construction issue was solved by having a much higher number of circular holes cut into the top flange of the box sections in specimen S_5, as mentioned earlier in Section 7.2.3. The good quality of concrete-fill condition inside the box sections is shown in Figures 7.17(a) to 7.17(d). It is clear that there were no air voids in the concrete fill in specimens S_4 to S_6.

(a) Specimen S_3

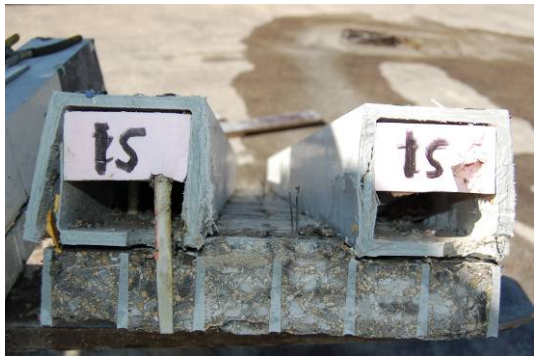

(b) Specimen S_1

(c) Specimen S_2

(d) Specimen S_3

Figure 7.16 – Poor concrete placement observed in specimens S_1 to S_3

(a) Specimen S_4

(b) Specimen S_5

(c) Specimen S_5 (d) Specimen S_6

Figure 7.17 – Good concrete placement observed in specimens S_4 to S_6

It was unknown whether the adhesive bond at the grating/box-section failed at the same time as the concrete studs when initial longitudinal shear failure occurred. This is because the concrete studs were invisible from the outside. The strength of the adhesive bond is difficult to calculate as the bond area between the grating and box section was small due to the hollow nature of the grating. However, no separation between the grating and box sections during the concrete casting stage indicated that the adhesive bond was sufficient enough to maintain full interaction between the two components under the weight of wet concrete and simulated construction load, which satisfied its main function. Final failure of specimens S_4 to S_6 was, again, caused by the local buckling of the box sections in a very brittle and sudden manner.

7.3.2 Comparisons between load versus slip responses and load versus deflection responses of specimens S_1 to S_6

As can be seen from Figure 7.18, up to the load at which debonding occurs, no slip was encountered. After initial bond slip, the end slip significantly increased, indicating that longitudinal shear failure had occurred locally. It was also found that slip did not develop evenly and simultaneously at each end of specimen, but rather that it developed in a discrete manner. The load at initial bond slip in Figure 7.18 was within the range between 135 kN and 155 kN. The load at which debonding occurs for specimen S_1 is 135 kN, as shown in Figure 7.19, correlating well to the values in that range. This close agreement demonstrates that the onset of the inelastic response was due to the onset of the longitudinal shear failure. It is clear that the end slip for the two box sections at the roller support in specimen S_1 was 11 mm and 14 mm respectively at final failure,

referred to as ‘roller 1’ and ‘roller 2’. However, the end slip of one box section at the pin support was 6 mm at final failure, referred to as ‘pin 2’, while there was no visible slip for the other box section, indicating no bond failure occurred in this vicinity, referred to as ‘pin 1’.

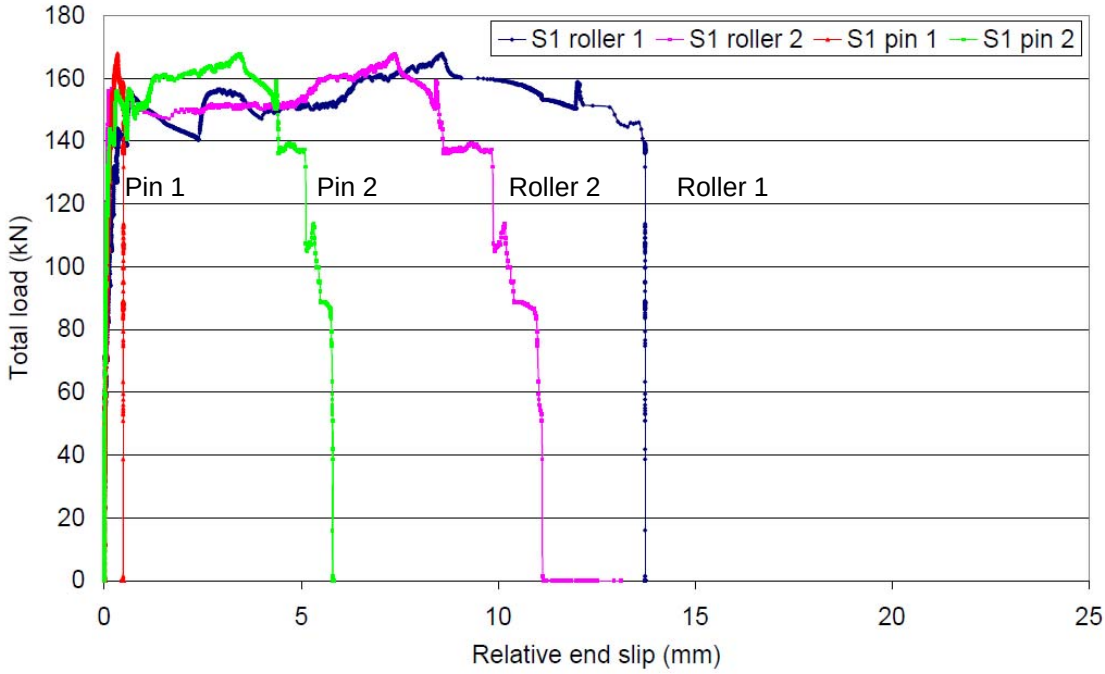

Figure 7.18 – Total load versus relative end-slip for specimen S_1

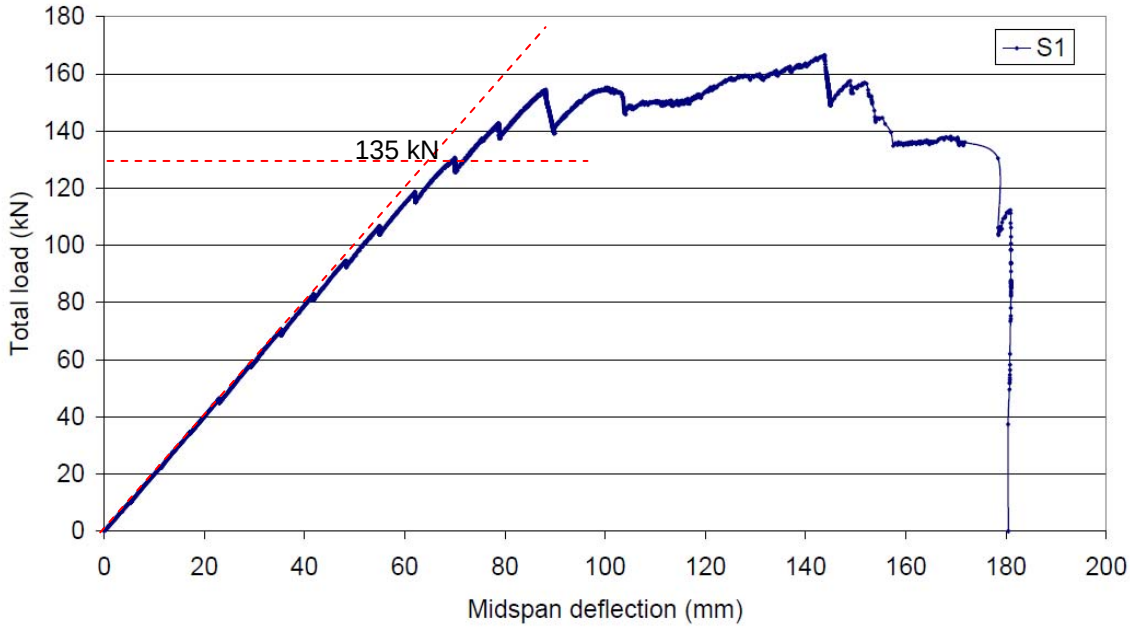

Figure 7.19 – Total load versus midspan deflection for specimen S_1

Figure 7.20 shows the load for specimen S_2 at initial bond slip was within the range between 65 kN and 92 kN, indicating that longitudinal shear failure at each end of the specimen occurred at a different load. The elastic limit at 75 kN in

Figure 7.21 was within that range. As can be seen from Figure 7.20, the end slip for the two box sections at the pin support in specimen S_2 was 13 mm and 5 mm respectively at final failure. The end slip of one box section at the roller support was 11 mm, and there was no visible slip for the other box section at the roller support.

Figure 7.20 – Total load versus relative end-slip for specimen S_2

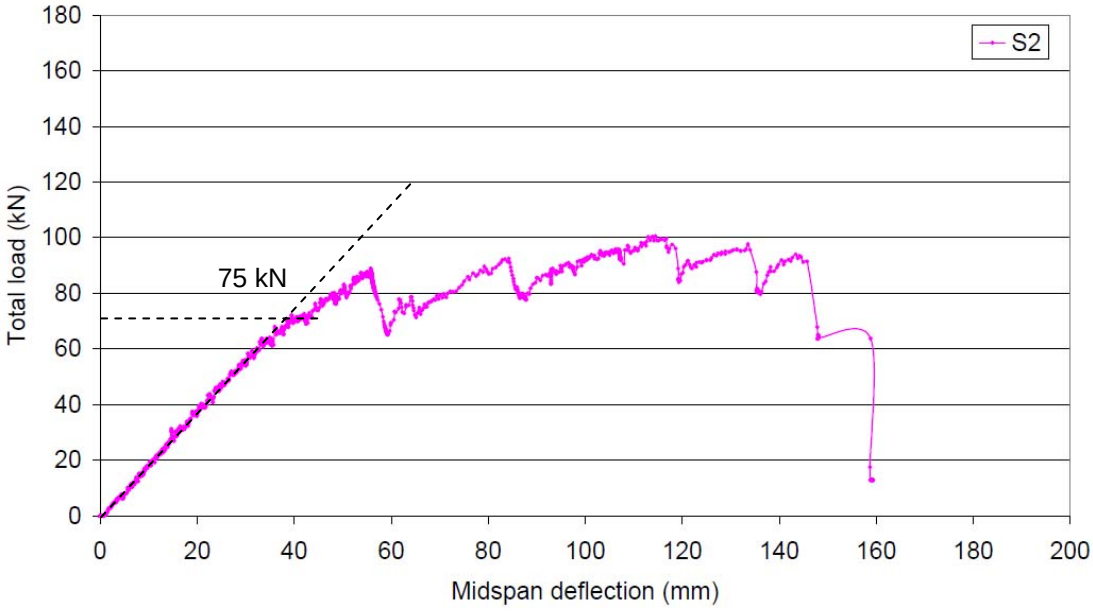

Figure 7.21 – Total load versus midspan deflection for specimen S_2

Figure 7.22 shows the load for specimen S_3, at initial bond slip to be 61 kN, which fits well with the linear elastic limit of 61 kN in Figure 7.23. The average end slip for the two box sections at the roller support was 19 mm at final failure. However, there was no visible slip at the pin support.

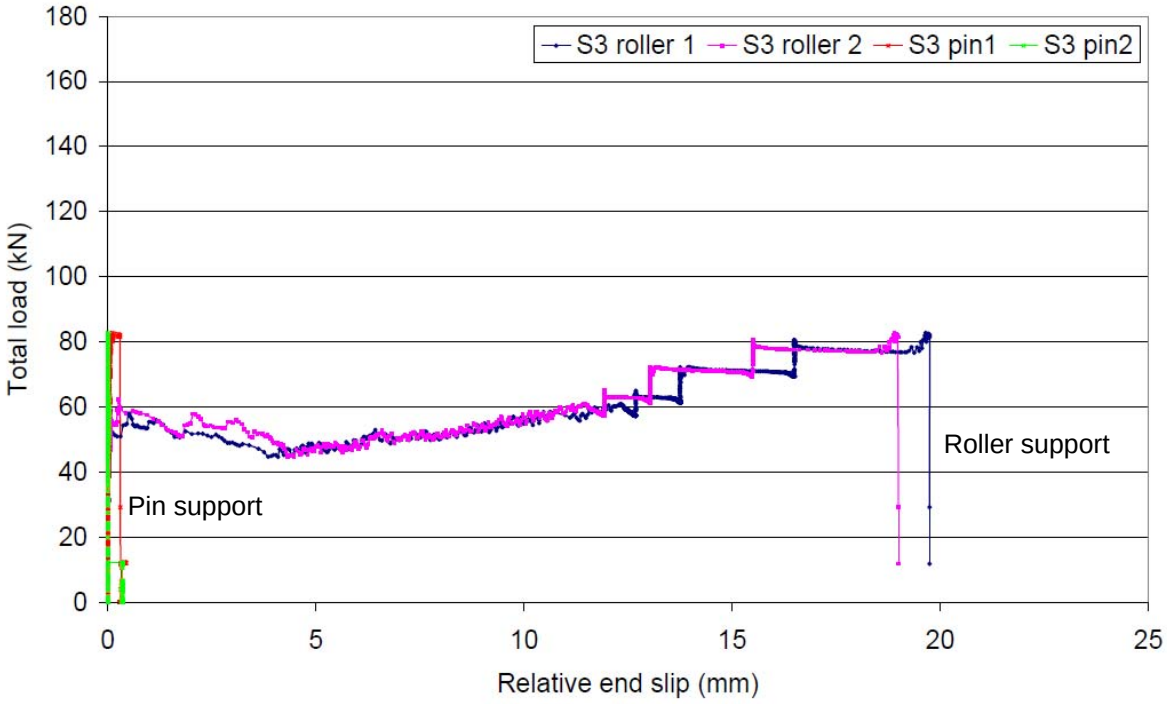

Figure 7.22 – Total load versus relative end-slip for specimen S_3

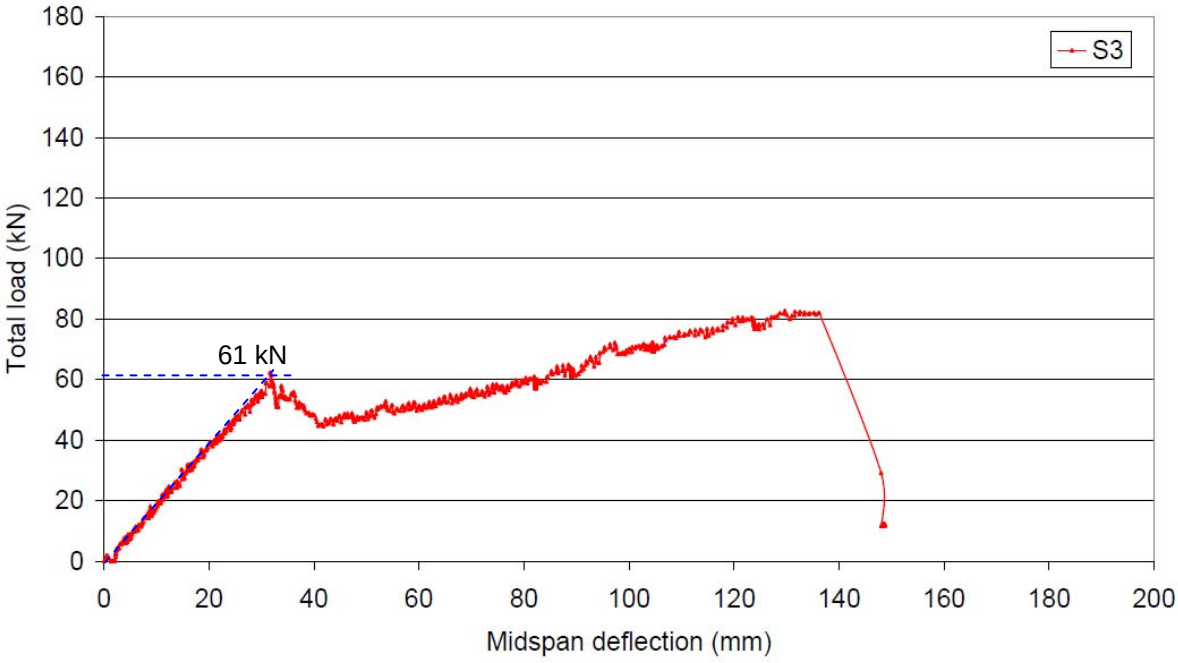

Figure 7.23 – Total load versus midspan deflection for specimen S_3

As can be seen from Figure 7.24, the initial bond slip in specimen S_4 primarily occurred at 48 kN with only one exception in one box section at the pin support, referred to as 'pin 2'. This matched well with the elastic limit of 48 kN in Figure 7.24. The end slips along the grating/box-section interface were distributed more evenly at each end of specimen S_4, with an average end slip of 7 mm at the roller support and 13 mm at the pin support when final failure occurred.

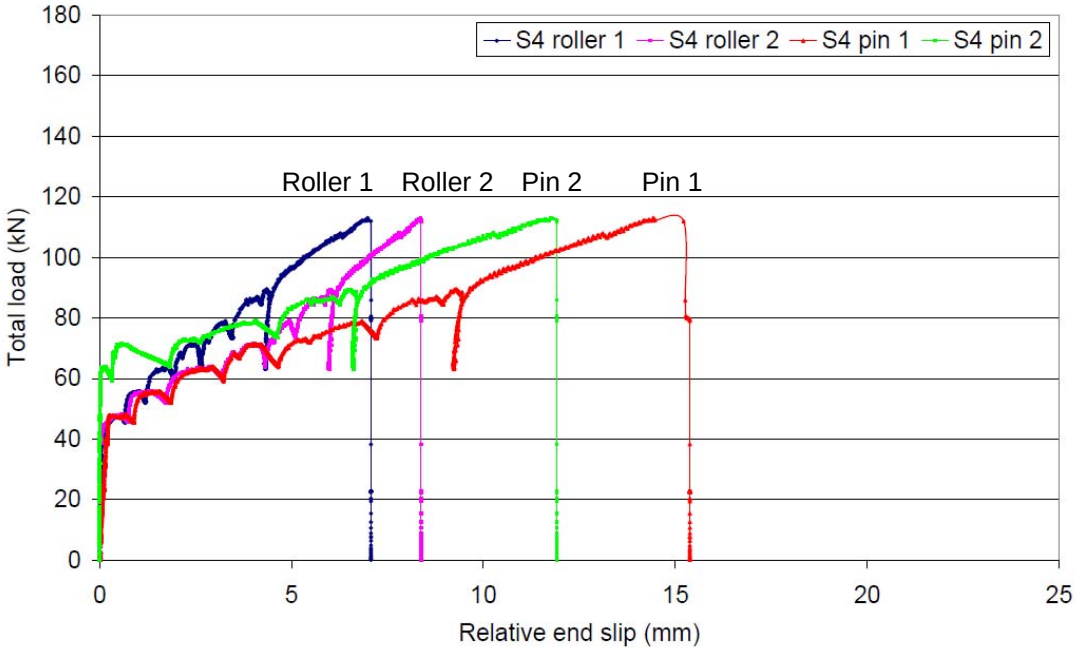

Figure 7.24 – Total load versus relative end-slip for specimen S_4

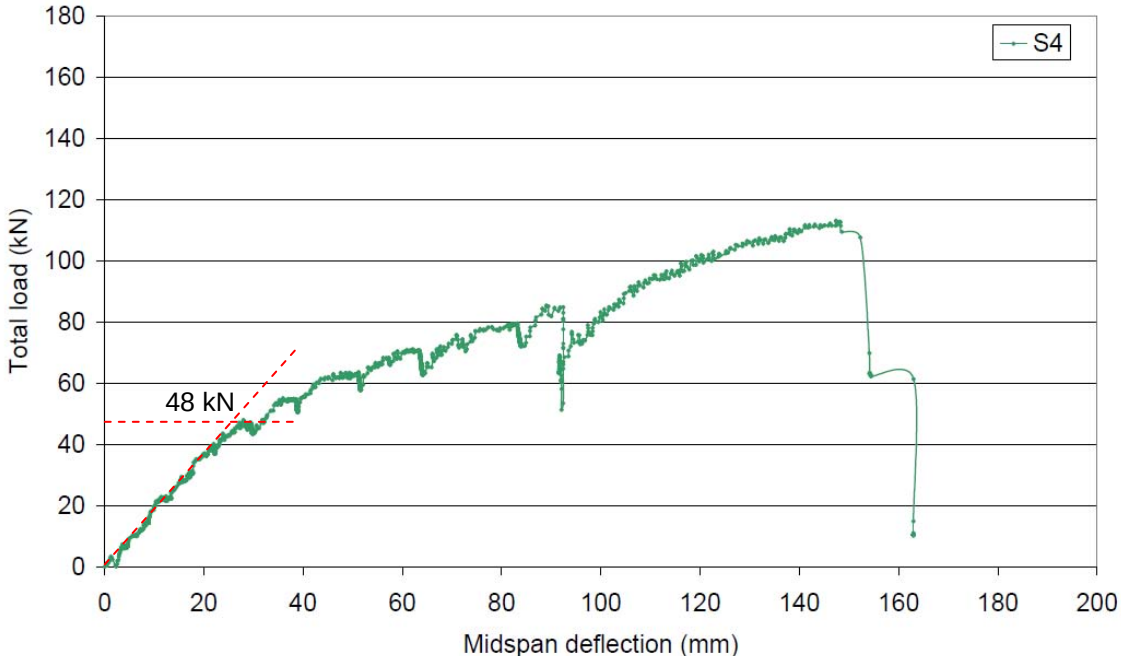

Figure 7.25 – Total load versus midspan deflection for specimen S_4

For specimen S_5, as shown in Figure 7.26, the initial bond slip occurred at 89 kN at each end. This matched well with the elastic limit of 89 kN in Figure 7.27. The average end slip for the two box sections was 15 mm at the roller support, and 9 mm at the pin support at final failure.

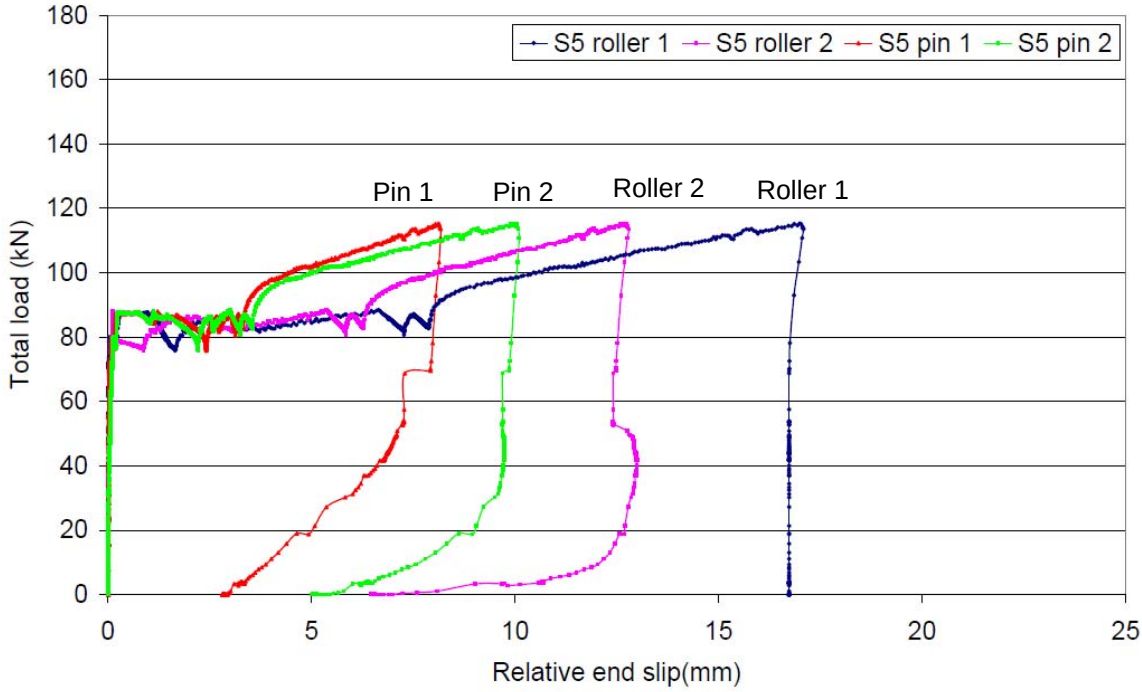

Figure 7.26 – Total load versus relative end-slip for specimen S_5

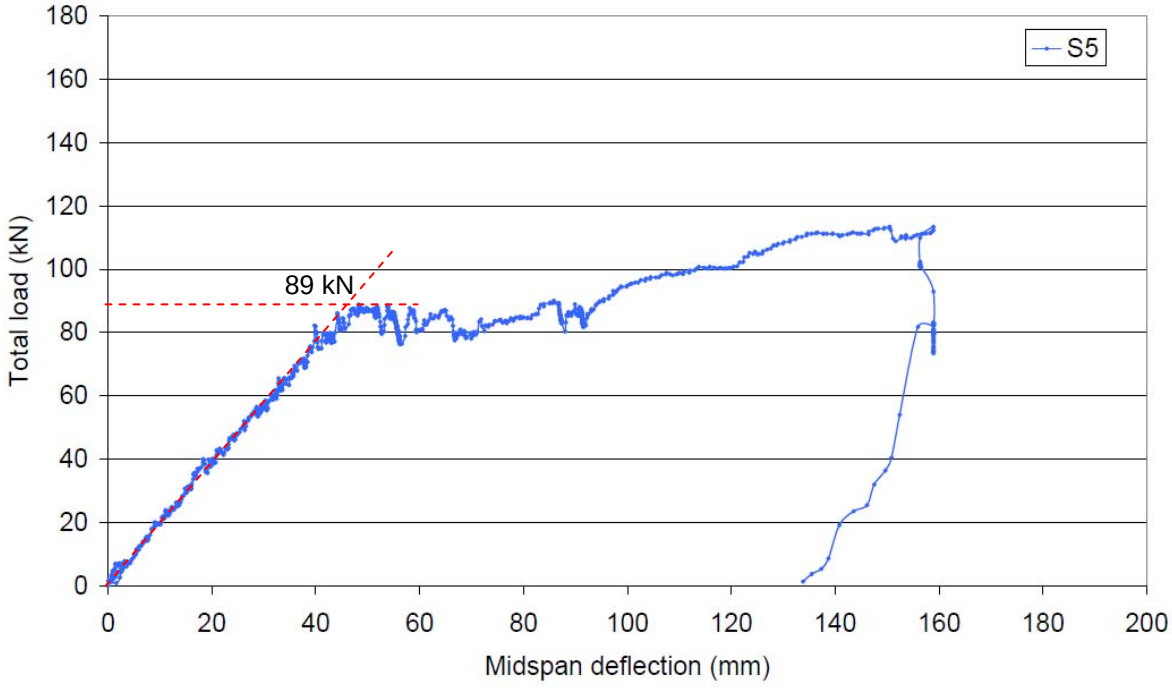

Figure 7.27 – Total load versus midspan deflection for specimen S_5

For specimen S_6, as shown in Figure 7.28, the initial bond slip occurred within the range between 42 kN and 65 kN. The elastic limit of 54 kN in Figure 7.29 was also within that range. The average end slip at the grating/box-section interface was 10 mm at the roller support and 14 mm at the pin support at final failure.

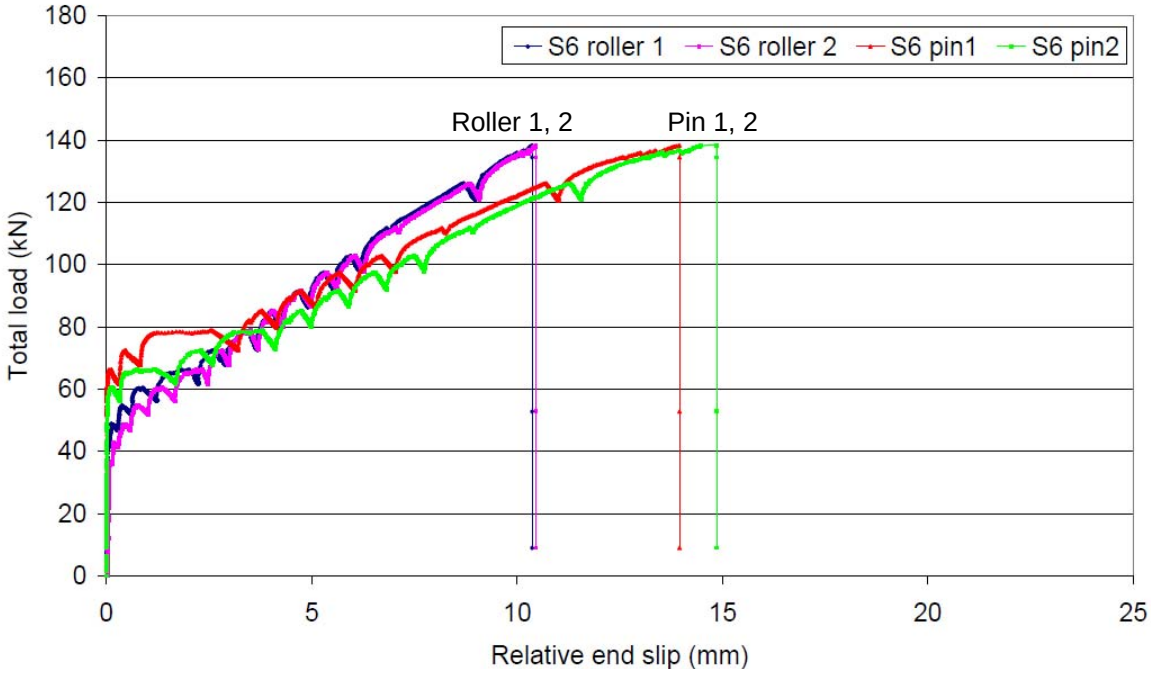

Figure 7.28 – Total load versus relative end-slip for specimen S_6

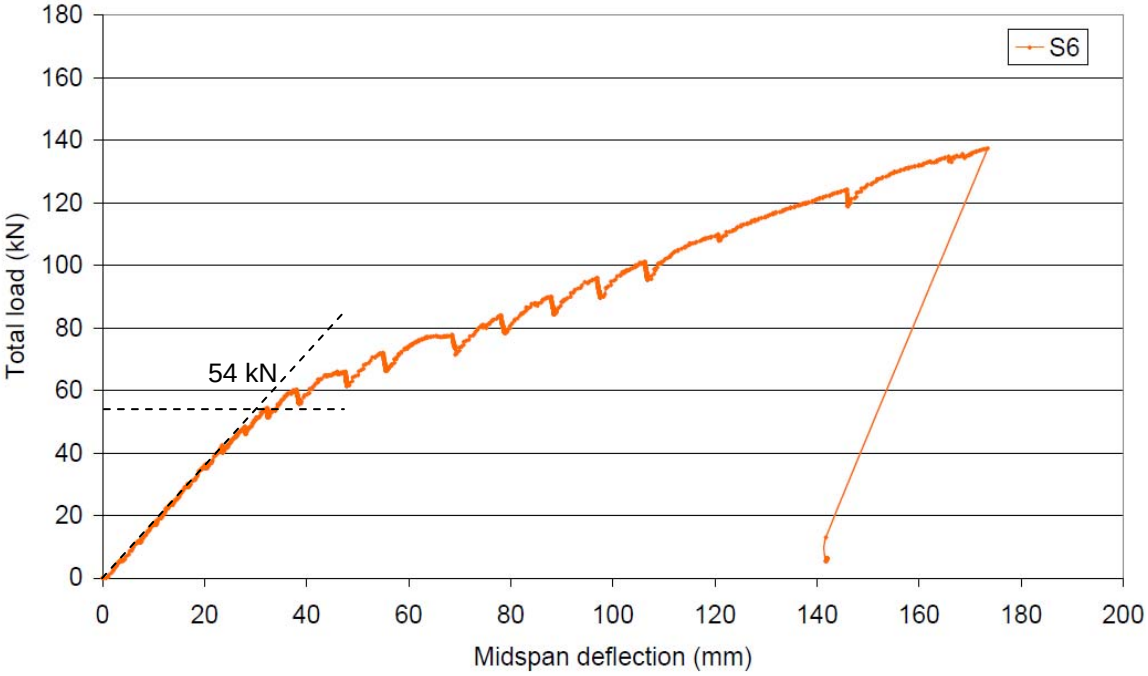

Figure 7.29 – Total load versus midspan deflection for specimen S_6

Summary of load versus slip responses

To summarise, the total load versus relative end-slip responses and total load versus midspan deflection responses for specimens S_1-S_6, shown in Figures 7.18 to 7.29, indicate that the average slip at failure at each end was in the range between 7 and 12 mm. Bond failure along the grating/box-section interface at each end occurred in a discrete manner. The load at initial bond slip in total load versus relative end-slip plots matched well with the load at the elastic limit in total load versus midspan deflection plots. Table 7.6 summarises, at final failure, the average end-slip at the grating/box-section interface for specimens S_1 to S_6. The load versus slip response of similar shear connectors determined from push-out tests, described in Section 5.3.4, is shown in Figure 7.30. The slip before fracturing of GFRP dowels was within the range 10 to 12 mm. This close agreement in slip capacity when compared with the present full-scale tests indicates that the shear connectors, particularly near to both ends, seem to have reached their full 'plastic' capacity. There is some evidence of fracture and delamination of GFRP dowels due to longitudinal shear at the grating/box-section interface, as shown in Figures 7.31 (a) and (b).

Table 7.8 – Average slip at the grating/box-section interface at final failure

Specimen	Slip at the roller support Roller 1/Roller 2 (mm)	Slip at the pin support Pin 1/Pin 2 (mm)	Average slip at each end at failure (mm)
S_1	11/14	6/0	8
S_2	11/0	13/5	7
S_3	19/20	0/0	10
S_4	7/8	14/12	10.5
S_5	17/13	8/10	12
S_6	10/10	14/15	12

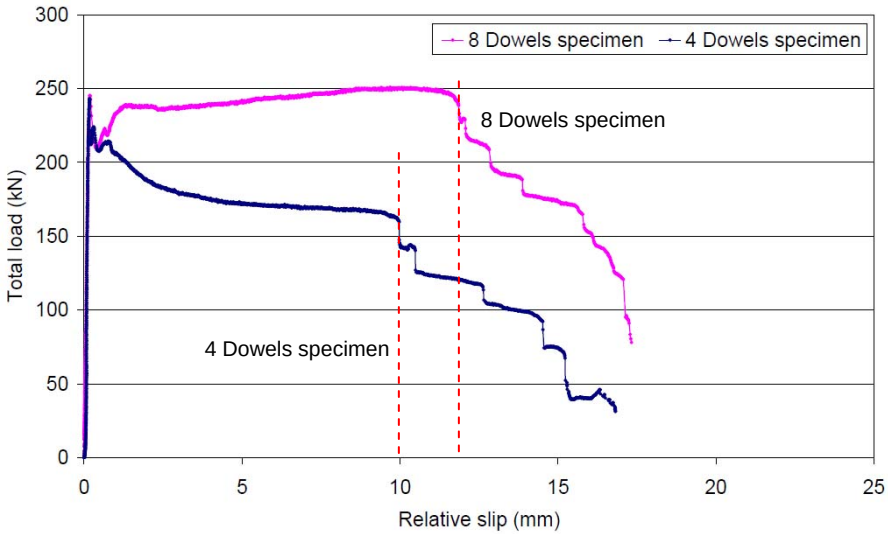

Figure 7.30 – Total load versus relative slip for push-out specimens

(a) Fracture of dowels near the ends (b) Fibre delamination (mid-span region)

Figure 7.31 – Typical failure of GFRP dowels at the grating/box-section interface in specimen S_5

In specimens S_4 to S_6 the slips at the grating/box-section interface were measured continuously at each dowel position and, more importantly, between the end span and the quarter span. Plots with increasing load are given in Figures 7.32 to 7.34. It should be noted in Figures 7.32 to 7.34 that the load increment is the total load. The relative slips between the grating and box section within the end quarter spans (up to 725 mm from the end) were fairly uniform. There was little or no slip in specimens before cracking occurred for initial longitudinal shear failure. As can be seen in Figures 7.32 to 7.34, the '0 mm' point on the horizontal axis is defined as 'roller 1', while the '3000 mm' point on the horizontal axis is defined as 'pin 1'. It is clear for specimen S_4 that the first visible slip occurred at 48 kN on 'roller 1' side and 56 kN on 'pin 1' side, particularly between end support and quarter span, as shown in Figure 7.32. As shown in Figure 7.33, the first visible slip occurred at 88 kN at both ends for specimen S_5. As shown in Figure 7.34, the first visible slip occurred at 48 kN on the 'roller 1' side and 60 kN on the 'pin 1' side, particularly between end support and quarter span, for specimen S_6.

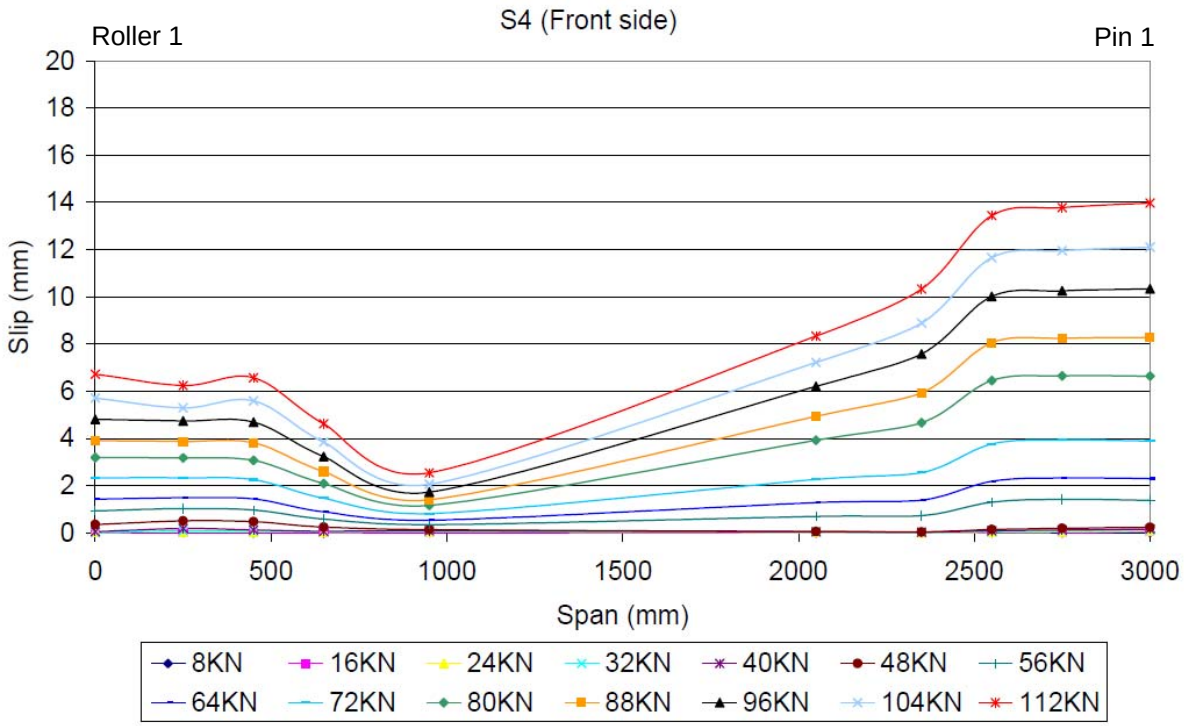

Figure 7.32 – Slips at each dowel position along the grating/box-section interface in specimen S_4

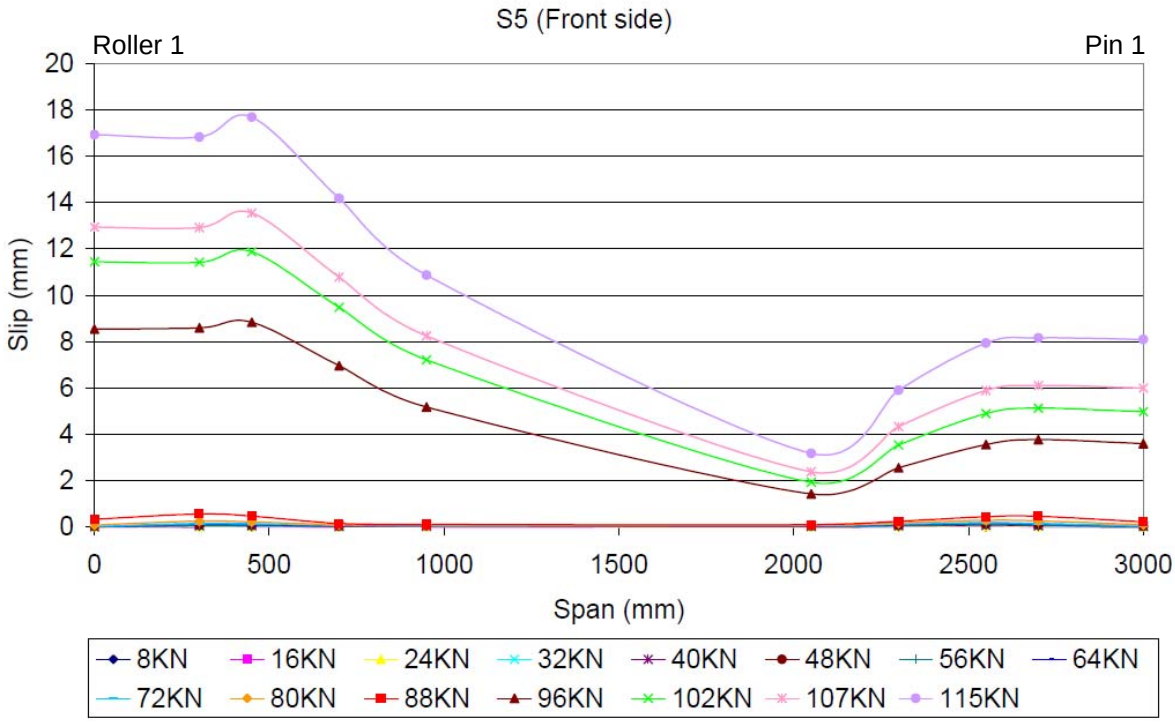

Figure 7.33 – Slips at each dowel position along the grating/box-section interface in specimen S_5

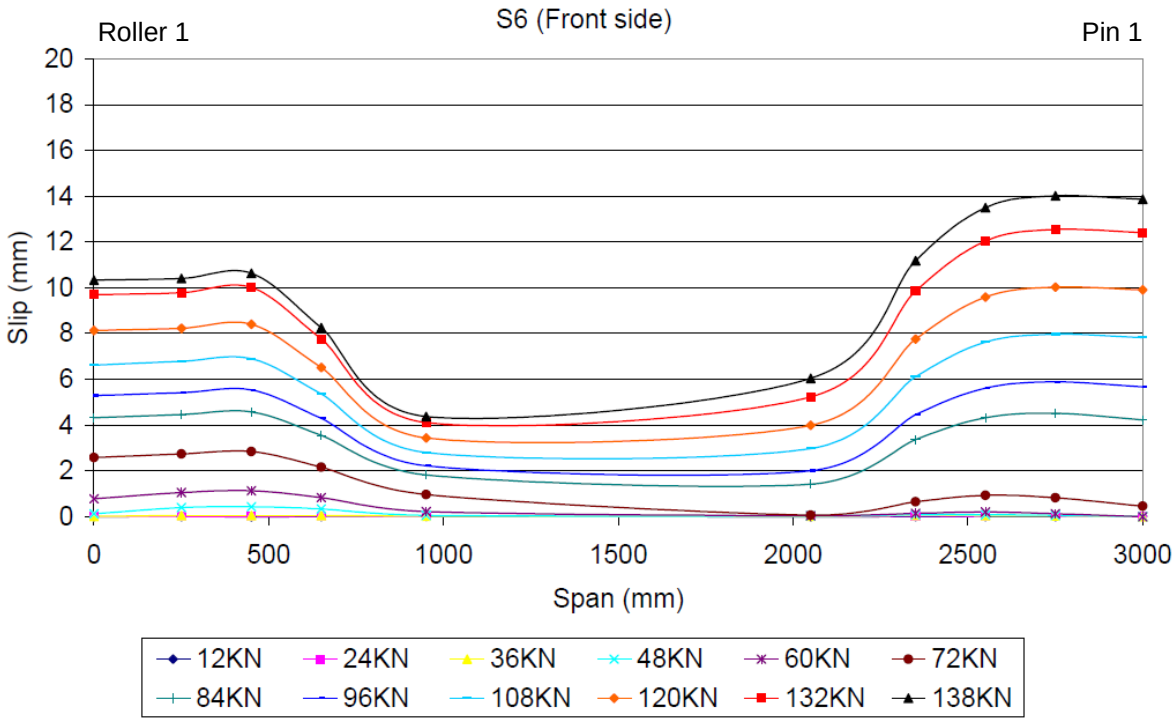

Figure 7.34 – Slips at each dowel position along the grating/box-section interface in specimen S_6

7.4 Summary

This chapter has provided details of an experimental investigation into concrete slab specimens, fabricated using commercially-available moulded GFRP grating adhesively bonded to two pultruded GFRP box sections as a SIP formwork for concrete. A total of six one-way spanning slab specimens were designed and statically tested under five-point bending. The feasibility of using GFRP dowels embedded into concrete to achieve ductility was investigated from these slab tests. The salient experimental results have been presented. In Chapter 8 test results will be discussed and compared to investigate the effects of each parameter contributing to the ductility of the whole FRP-concrete hybrid system.

Chapter 8 Discussion of Experimental Results

8.1 Introduction

Chapter 7 presented details of the experimental program in which the six slab specimens S_1 to S_6 were fabricated using moulded GFRP grating adhesively bonded onto pultruded GFRP box sections forming stay-in-place structural formwork for concrete slabs. Shear connection between the concrete-filled grating and box sections was achieved using GFRP dowels embedded in the concrete. Experimental results in terms of total load versus mid-span deflection responses and total load versus relative end-slip responses were presented.

Using the experimental results presented in Chapter 7, comparisons are made between the six specimens with regard to flexural behaviour, failure mode, effects of the different loading schemes and ductility. Measured strain profiles at the maximum moment region are also discussed, with respect to the gradual loss of composite action.

8.2 Comparisons amongst Specimens S_1 to S_3

The total load versus mid-span deflection plots for S_1 to S_3 are compared in Figure 8.1. The number and positioning of dowels are shown in Figure 8.2. The initial response of all the slab specimens was elastic, producing a stable, relatively linear relationship between load and deflection. This linear relationship indicates fully composite behaviour prior to reaching the initial peak load. It is evident from Figure 8.1, prior to the initial peak load, that the stiffnesses of the three specimens are fairly similar. This is logical, because all specimens had the same cross-sectional configurations, and therefore exhibit the same stiffness while behaving compositely.

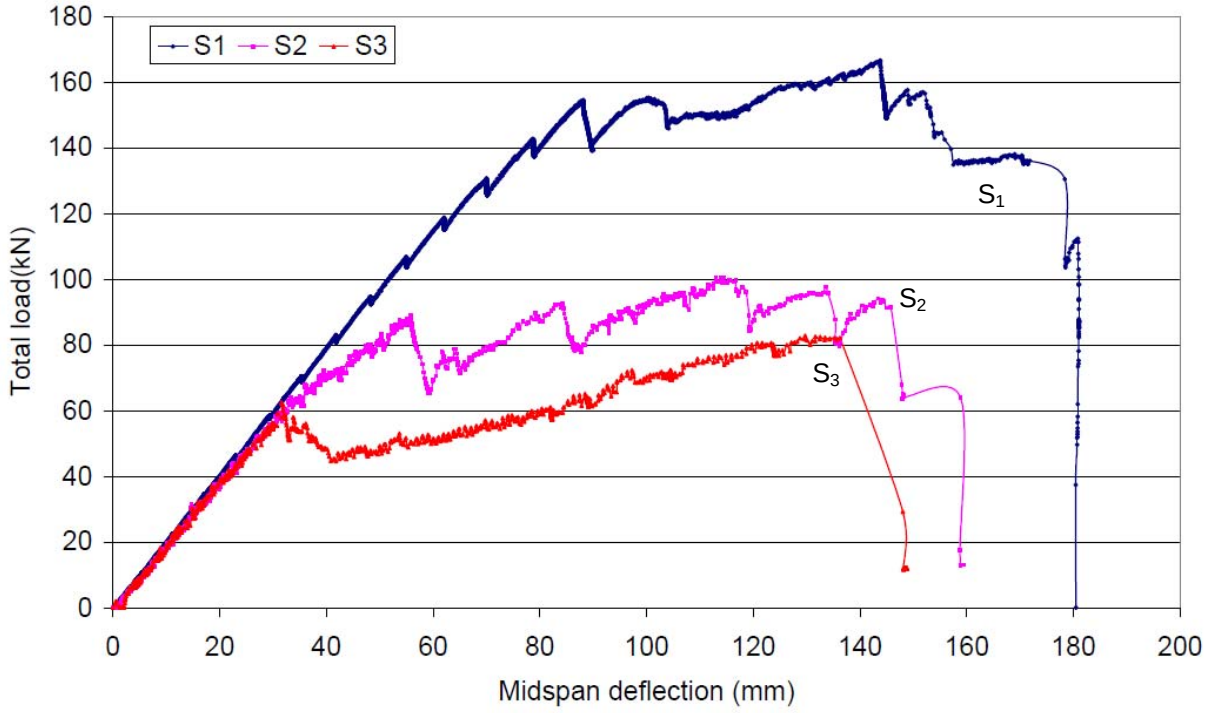

Figure 8.1 – Total load versus midspan deflection for specimens S_1, S_2 and S_3

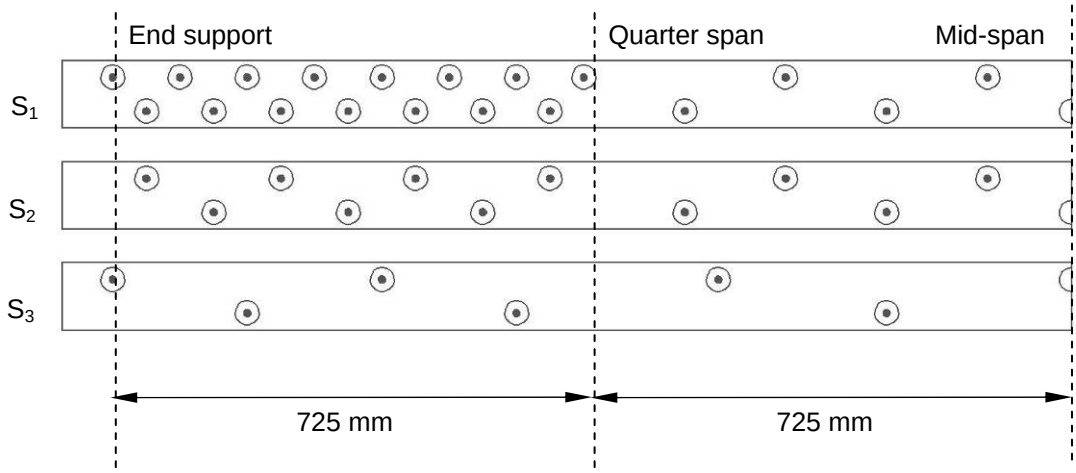

Figure 8.2 – Positioning of dowels in Specimens S_1, S_2 and S_3

Figure 8.3 shows a typical total load versus relative end-slip plot of specimen S_3, which could be considered to be typical for this specimens group. None of the three members exhibited any horizontal slip at the grating/box-section interface prior to reaching the initial peak load, indicating that all specimens behaved monolithically. It is to be noted that the initial peak load is determined by the mechanical bond at the concrete/FRP interface provided by the GFRP dowels embedded in the concrete studs and the adhesive bond at the glued FRP/FRP interface. Thus, even though the adhesive FRP/FRP bond is the same for all three specimens S_1 to S_3, the number of shear connectors (concrete studs

combined with GFRP dowels) was reduced in specimens S_1 to S_3. Experimental results shows S_1 achieved the highest initial peak load, followed by S_2 and S_3. This demonstrated that the initial peak load is governed by the combination of the concrete studs and GFRP dowels, since the primary function of adhesive bond is to provide composite action between the grating and box section during the construction stage.

The initial failure signifying the end of the linear response was likely to have been caused by a failure of the adhesive bond and cracking of the concrete, leaving only GFRP dowels responsible for resisting longitudinal shear at the concrete/FRP interface. It is logical that the shear connection provided by the GFRP dowels alone would result in a reduced stiffness for the slab specimens because it solely relies on shear and tensile resistance of GFRP dowels, coupled with the post-cracked restrained shear resistance of the concrete-to-concrete interface. After the initial peak load of 61 kN, as evident in Figure 8.3, although there was no visible end-slip observed at the pin support, the relative end-slip for S_3 at the grating/box-section interface at the roller support significantly increased, indicating that composite action had been compromised. Beyond this initial peak load, all three specimens S_1 to S_3, exhibited a slight drop in load capacity, followed by an increasing load response, at a reduced stiffness, until the final failure occurred, which in all cases was higher than the initial peak. This observation is confirmed by test results plotted in Figure 8.1.

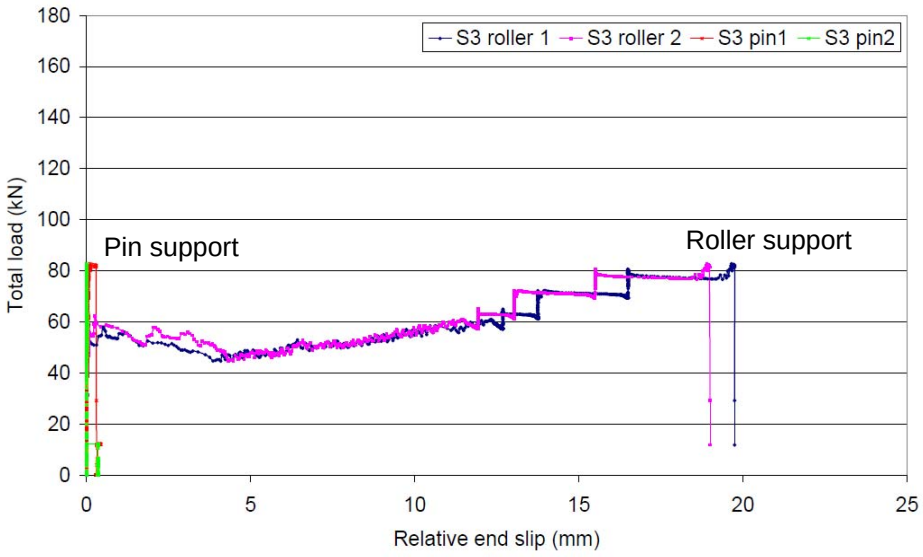

Figure 8.3 – Total load versus relative end-slip for specimen S_3

Following significant deflection in excess of the depth of the member, the test specimens showed a sudden, dramatic loss of load which ended the tests. This sudden loss of load was the result of the separation of the top flange and the webs at the upper corners of the cross-section, immediately followed by the local buckling of the webs of the pultruded box section, as shown in Figure 8.4(a). This local loss of stiffness consequently changed the deflected shape, and introduced sharp curvatures in the central-region underneath the loading head. Local fibre breakage and delamination in the webs of the box section were apparent, as can be seen in Figure 8.4(b). This damage appeared simultaneously with the separation of the top flange and the webs, and was present in both webs of the box section. The damage was a result of the local lateral deflection of both webs. The lateral deflection introduced local bending curvatures, and was facilitated by the separation of the webs from the top flange.

(a) Specimen S_1 (b) Specimen S_3

Figure 8.4 – Typical failure of local buckling of box sections

Table 8.1 summarises the slab test results. Specimens S_2 and S_3 were directly comparable as both specimens were tested under the same loading scheme (Type B loading). The number of shear connectors in specimen S_3 was 55% of that in specimen S_2, leading to the initial peak load being reduced to 69% of that in specimen S_2, and the final peak load being reduced to 86% of that in specimen S_2. This indicated that although the initial peak load is governed by the number of shear connectors, there is not a 100% increase in the initial peak load by doubling the number of shear connectors. The final failure due to local buckling of box section indicated that the ultimate strength was not directly related to the number of shear connectors. However, certainly by adding more shear connectors, the initial peak load and the ultimate failure load were both

enhanced. A higher degree of interaction between the grating and box sections was maintained following the initial peak when more shear connectors were present, leading to a higher failure load. S_1 to S_3 exhibited a ductile post peak behaviour, giving sufficient warning prior to the final failure.

Table 8.1 – Summary of slab test results

Slab specimens	Load schemes	Cube strength of concrete (MPa)	No. of concrete studs (half span)	No. of GFRP dowels (half span)	Load at which debonding occurs (kN)	Peak load (kN)	Ultimate failure load (kN)	Deflection at ultimate failure (mm)
S_1	A	48.9	38	38	135	167	138	171
S_2	B	50.1	22	22	75	100	95	145
S_3	B	48.1	12	12	61	82	82	137
S_4	B	25.9	12	12	48	112	112	148
S_5	B	27.1	58	12	89	113	113	161
S_6	A	31.7	12	12	54	138	138	173

8.3 Comparisons between Specimens S_3 and S_4

Following the evaluation of the test results for S_1 to S_3, specimens S_4 and S_6 were designed and tested to validate the test data by following the design of S_3. It was necessary to validate the behaviour of specimen S_3 as it showed a ductile behaviour with the lowest number of shear connectors. More importantly, the ultimate load capacity of S_3 (82 kN) was the closest to the service load capacity (20 kN), calculated based on a service load deflection limit of $\delta = span/250$ (11.6 mm), making most efficient use of materials (Johnson, 1993). Specimens S_3 and S_4 were designed to have an identical number of shear connectors and both were tested in Type B loading (simulating the required shear envelope). Therefore both test results are directly comparable and their load against mid-span deflection plots are given in Figure 8.5.

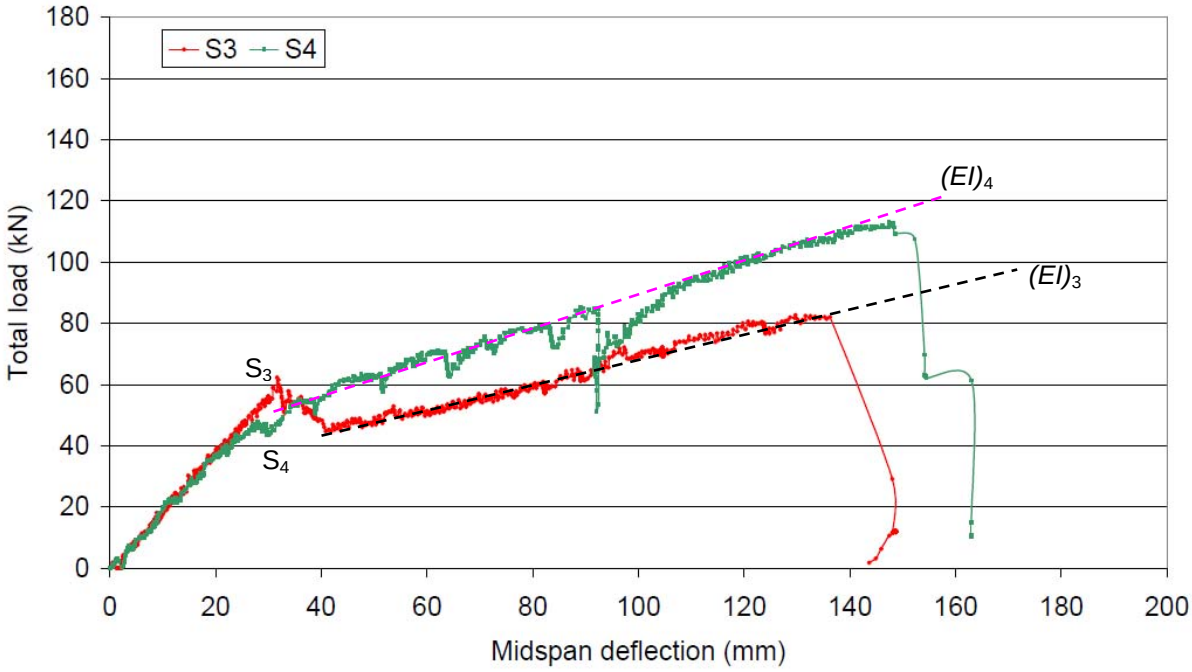

Figure 8.5 – Total load versus midspan deflection for specimens S_3 and S_4

Figure 8.5 shows that the initial stiffness of specimens S_3 and S_4 is identical. The initial peak load of specimen S_4 is slightly lower compared with that of specimen S_3, which might be due to the fact that the concrete strength in specimen S_4 was lower by 46% than that in S_3, as shown in Table 8.1, causing a reduction in contribution of mechanical bond provided by concrete studs. Therefore, the following simple analysis was carried out to verify whether the difference in concrete strength corresponds to the reduction in initial peak load. The longitudinal shear strength, τ_{Rd}, at the grating/box-section interface is calculated to be 1.3 N/mm^2 in specimens S_3 corresponding to the peak load of 61 kN, and 1 N/mm^2 in specimen S_4 corresponding to the peak load of 48 kN. The difference in longitudinal shear strength at the initial peak between two specimens is 0.3 N/mm^2. The shear strength of concrete can be calculated using the Eurocode 2 Part 1.1 for the Design of Concrete Structures. Results are given in Table 8.2. It is clear that the shear strength of concrete is directly related to the compressive strength of concrete, and the difference in shear strength of concrete (without safety factor) between specimens S_3 and S_4 is 0.25 N/mm^2, which matched well with the difference in longitudinal shear strength at the initial peak between two specimens. This finding indicates that the variation of concrete strength is likely to be the main cause to the difference of the initial peak load between specimens

S_3 and S_4, and the concrete studs play an important role in resisting the longitudinal shear during the elastic phase.

Table 8.2 – Comparison of shear strength of concrete in specimen S_3 and S_4

Specimen	S_3	S_4
Cube strength (N/mm^2) f_{cube}	48.1	25.9
Characteristic compressive strength f_{ck} (N/mm^2)	40	20
Mean tensile strength f_{ctm} (N/mm^2)	3.5	2.2
Lower characteristic tensile strength $f_{ctk0.05}$ (N/mm^2)	2.5	1.5
Shear strength τ_{Rd} without safety factor	0.63	0.38
Shear strength τ_{Rd} with safety factor	0.41	0.26
Notes $f_{ctm} = 0.3(f_{ck})^{0.67}$, $f_{ctk0.05} = 0.7 f_{ctm}$, $\tau_{Rd} = (0.25 f_{ctk0.05})/\gamma_c$ and γ_c=1.5 (BS EN 1992-1-1, 2004)		

It can also be seen from Figure 8.5 that S_3 exhibited a sudden drop in load capacity of 18 kN immediately after the initial peak, whereas S_4 exhibited a more gradual transition to reducted stiffness without any drop in load bearing capacity. The sudden reduction with S_3 was due to the large air voids present in the concrete (within the box sections), and as a result some of the dowels could not contribute fully to resisting the longitudinal shear force. Therefore, dowel action and concrete shear friction was not fully mobilised within the voided regions, causing a reduction in longitudinal shear resistance and a significant increase in slip. The reduction in stiffness after the initial peak strength is a direct result of the degradation of composite action between the concrete-filled grating and box sections. This was clearly reflected in the slip measurements at the grating/box-section interface (see Figure 8.6) that slip evolved after the initial peak. As discussed in Chapter 7, a number of 8 mm inspection holes were drilled into the top flange of box sections between adjacent holes in S_4 to S_6, to improve concrete flow. No air voids were observed in specimen S_4, and existence of continuous concrete material explains why there was no load capacity reduction after the initial peak. Furthermore, the ultimate failure capacity of specimen S_3 (82 kN) is also lower than that of specimen S_4 (112 kN), this is also caused by the fact that some of the dowels in specimen S_3 did not fully resist the shear due to voids in the concrete-fill. As shown in Figure 8.5,

after the elastic limit, there is a softening phase which represented by changing of stiffness in specimen S_4. The residual stiffness of specimen S_4, indicated by $(EI)_4$, is slightly higher than that in specimen S_3, indicated by $(EI)_3$. This is probably because that the shear connectors in specimen S_4 acted more efficiently to resist the longitudinal shear than that of specimen S_3. This indicated that specimen S_4 maintained a higher degree of partial interaction than specimen S_3.

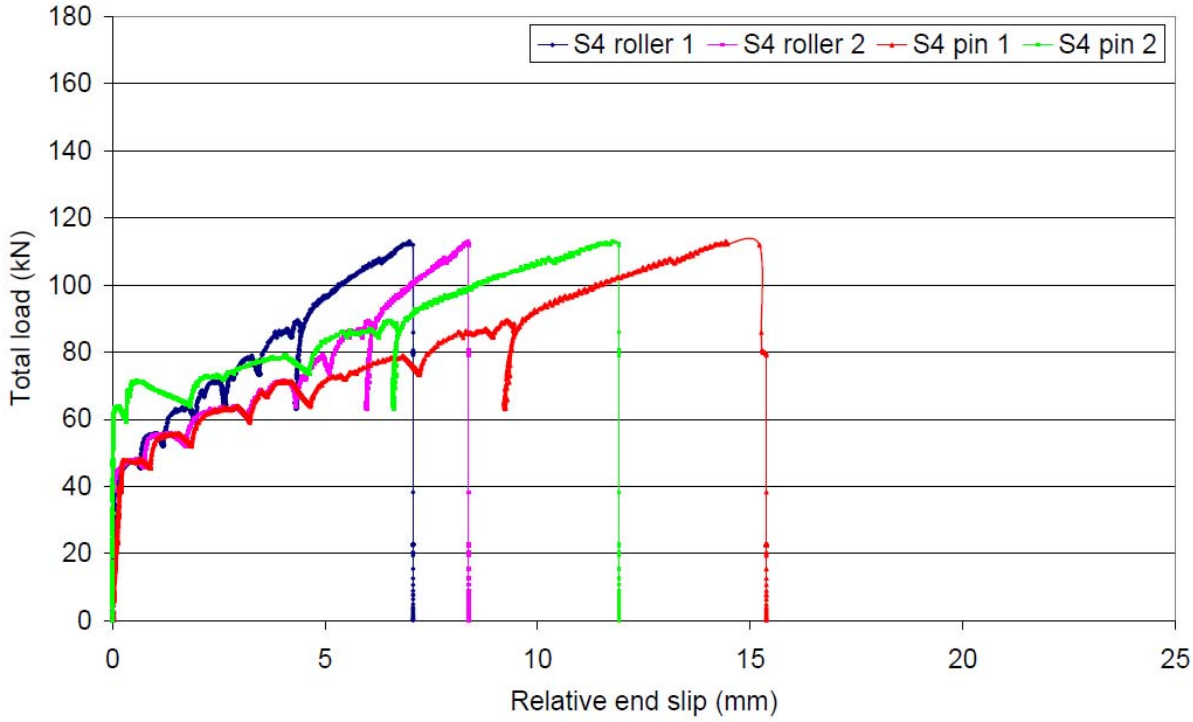

Figure 8.6 – Total load versus relative end-slip for specimen S_4

8.4 Comparisons amongst Specimens S_4 to S_6

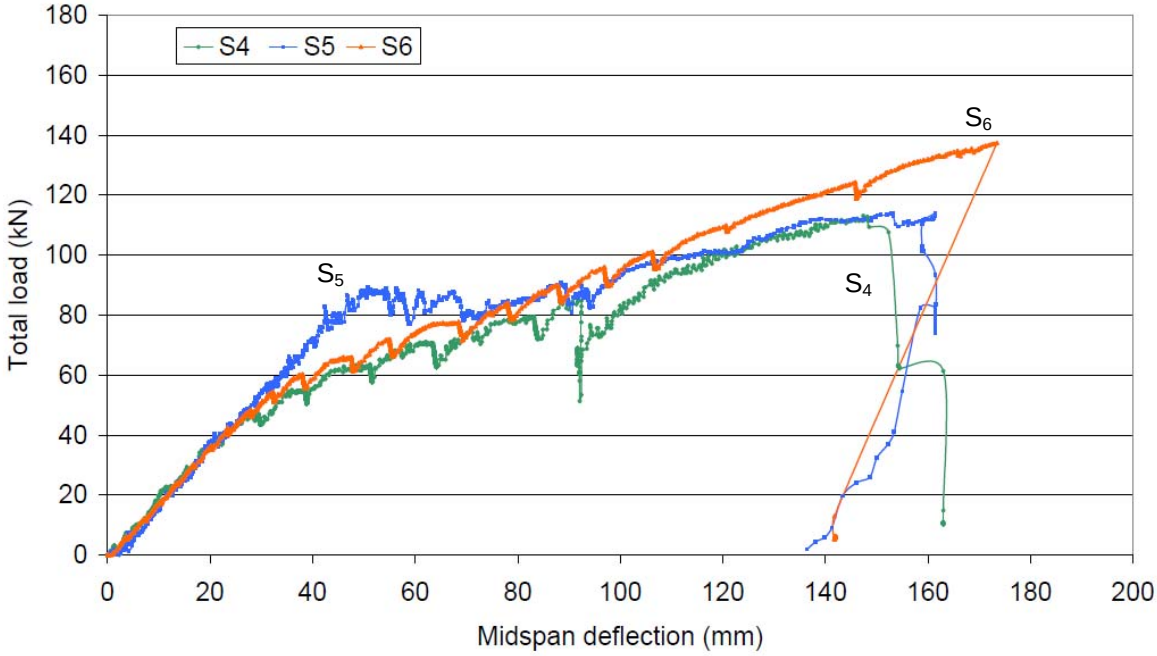

Figure 8.7 – Total load versus midspan deflection for specimens S_4 to S_6

The total load versus midspan deflection plots for specimens S_4 to S_6 are presented in Figure 8.7. S_4 and S_6 were identical with regards to the number of GFRP dowels, although S_4 was tested under Type B loading (shear envelope) and S_6 was tested under Type A loading (moment envelope). Specimen S_5 had an identical number of GFRP dowels as the other two in this group of three but with additional 46 concrete studs, and tested under Type B loading. It is evident that the stiffnesses of specimens S_4-S_6 were similar prior to the initial peak load. It is logical that S_5 achieved the highest initial peak load, as the mechanical bond in S_5 was enhanced by having additional concrete studs.

After the initial peak, S_4 and S_6 carried on increasing their load capacity at a similar stiffness without a drop in load capacity until they reached final failure. This was because only GFRP dowels contributed to resisting the longitudinal shear after initial failure and the number of GFRP dowels were the same for S_4 and S_6, giving rise to similar post elastic behaviour. After the initial peak S_5 exhibited a relative flat response (at least for 40 mm deflection), followed by an increase in stiffness similar to S_4 until reaching the final failure. This further indicates that only the GFRP dowels were resisting the longitudinal shear once

the concrete studs failed in shear, since S_4 and S_5 had the same number of GFRP dowels and both tested under Type B loading.

The effect of having additional concrete studs can be seen by comparing S_5 and S_4 (Type B loading). As can be seen from the test results listed in Table 8.1, there was an increase of 74% in initial peak load capacity by increasing the number of concrete studs from 12 (S_4) to 58 (S_5). As discussed earlier in Section 8.2, the initial peak load was seen to be dependent on the combination of concrete studs and GFRP dowels. Specimen S_5 had the same number of GFRP dowels as specimen S_4 but 3.8 times more concrete studs, it is logical that the initial peak load in S_5 was enhanced by having the additional concrete studs. More importantly, the construction issues with regard to the voids observed in the concrete-filled box sections in specimens S_1 to S_3 was solved by introducing more circular holes into the top flange of the box sections, some of which had no dowels, allowing for improved concrete flow into the box sections. It was also found that the concrete casting time for specimen S_5 was significantly reduced by 50% when compared with that of specimens S_4 and S_6. As described earlier in Chapter 7, it was found that the quality of concrete-fill in the specimens S_4-S_6 was significantly improved with no presence of air voids. Therefore, it seems clear that specimen S_5 is most optimised design by trial and error process in terms of ease of construction from the construction point of view. It also shows the potential for flexibility in positioning the dowels, meaning that the dowel locations can be altered to fit different loading requirements.

S_4 to S_6 failed due to local FRP buckling as a result of the separation between the webs and the compression flange at the upper corners of the box sections. As seen from the plots in Figure 8.7, the behaviour is ductile with specimens failing at a similar maximum vertical deflection to the range of 148 to 172 mm.

8.5 Comparisons between Type A Loading and Type B Loading

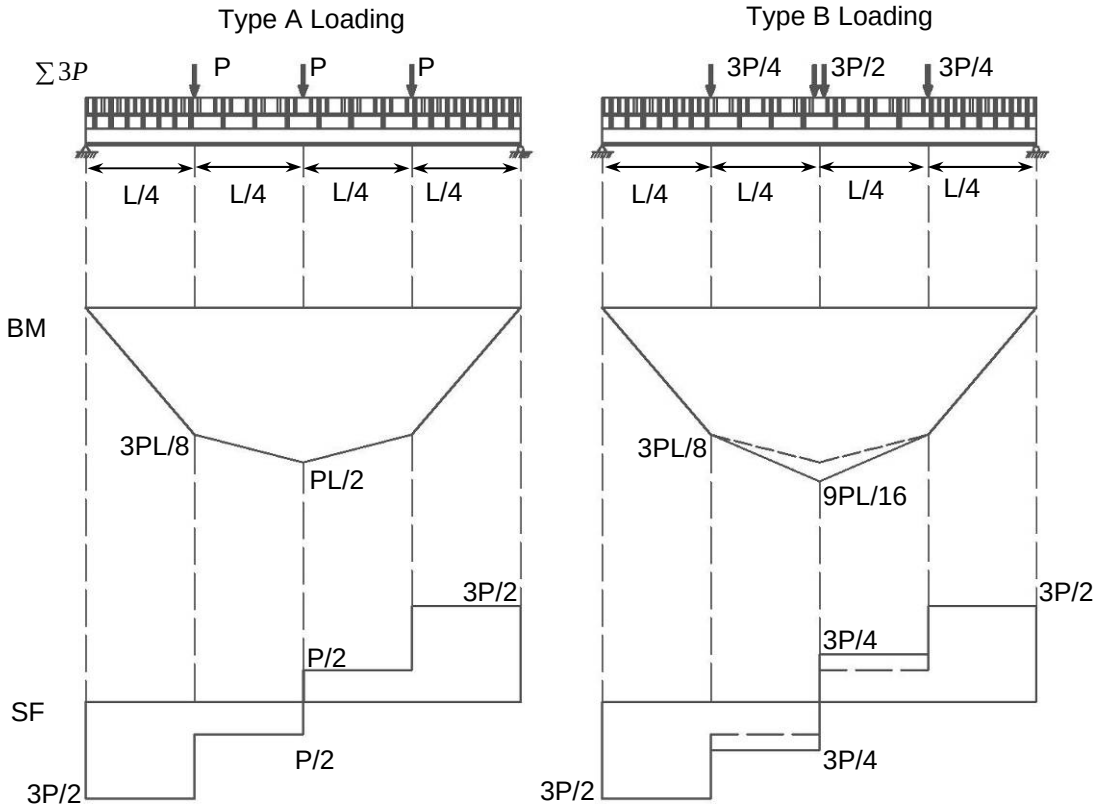

Figure 8.8 – Comparison of bending moment diagram and shear force diagram under Type A and Type B loading

Figure 8.8 shows the bending moment and shear force diagrams under Type A and Type B loading. In the right-sided figure the dash lines indicate the moment and shear diagrams with Type A loading for comparison. For a given amount of total load '3P', although there is 50% difference in the shear demand between the quarter span and mid-span between Type A and Type B loading, the shear demand within the end quarter span under Type A loading is identical with that under the Type B loading. It should be noted that the shear demand towards the end supports appear to be more critical for the onset of longitudinal shear failure. In addition, the maximum moment at mid-span for Type B loading is 12.5% higher than that from Type A loading. Specimens S_4 and S_6 were designed with the same number of shear connectors, representing the identical longitudinal shear resistance. This comparison finds that the moment at onset of longitudinal shear failure under Type B will, for the same total load, be 12.5% higher than Type A.

Figure 8.9 shows the moment versus deflection plots for S_4 and S_6. The moment at initial bond slip of S_4 is almost the same as that for S_6, which does not support the proposed explanation that the longitudinal shear governs. However, the onset of longitudinal debonding is very sensitive to the bond strength and localized stress, so this discrepancy does not necessarily invalidate the theory. It was also found from Figure 8.9 that deflection at failure in specimen S_6 (173 mm) was 16.9% higher than that of specimen S_4 (148 mm). This might be because specimen S_4 (under Type B) was tested under a 12.5% higher moment at mid-span than specimen S_6 (under Type A), resulting in a larger curvature for a given amount of total load. This might explain why specimen S_4 failed in a smaller deflection than specimen S_6.

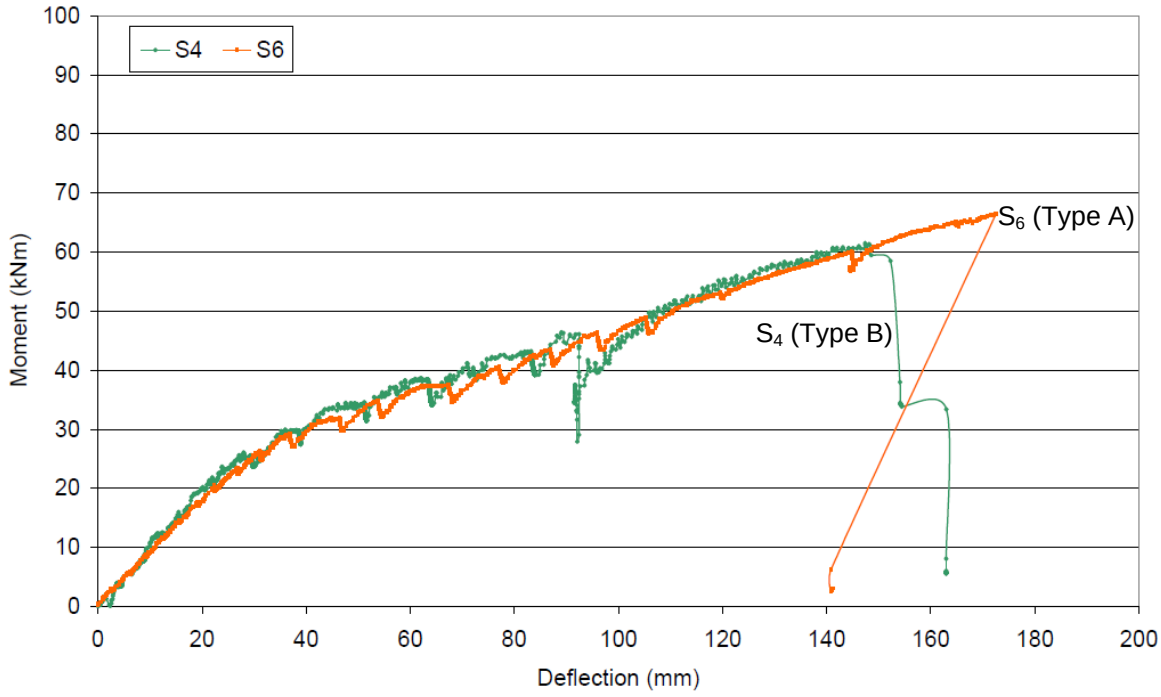

Figure 8.9 – Moment versus deflection plot for specimens S_4 and S_6

8.6 Failure Mode

8.6.1 Tension failure and compression failure

Table 8.3 reports the compressive strain measured using electrical resistance strain gauges, on the top side of the concrete-filled grating at ultimate failure. It should be noted that the front side is referred to as 'side a', and the back side is referred to as 'side b'. As shown in Figure 6.13, the ultimate strain capacity in the stress versus strain plot of the concrete-filled grating determined from the concrete block test was 0.015, for a concrete strength of 34 MPa. At ultimate

failure the maximum compressive strains of the concrete-filled grating measured in specimens S_1 to S_6 at failure were < 0.007, as illustrated in stress versus strain plot of the concrete-filled grating block discussed in Chapter 6. Compared with a typical failure strain of the unconfined concrete (ε_c=0.0035), the concrete is found to be confined by the grating, indicated by the additional strain capacity gained (up to 100% increase). However, it was also found that there was no evidence of crushing of the concrete-filled grating in any specimen. This indicates that there is no ductility provided by the concrete-filled grating in compression, with all the ductility coming from progressive failure of the longitudinal shear interface. The presence of GFRP dowels is therefore essential at the grating/box-section interface to ensure that the longitudinal shear failure occurs in a ductile manner.

Table 8.3 – Maximum strain at the top side of the concrete-filled grating (negative indicates compressive)

Specimens	Side a	Side b	
	Maximum strain	Maximum strain	Average
S_1	-0.0053	-0.0040	-0.0047
S_2	-0.0043	-0.0055	-0.0049
S_3	-0.0031	-0.0026	-0.0057
S_4	-0.0054	-0.0062	-0.0058
S_5	-0.0062	-0.0070	-0.0066
S_6	-0.0054	-0.0039	-0.0047

Table 8.4 shows the tensile strains at the bottom of the GFRP box sections at ultimate failure in specimens S_1 to S_6. As can be seen from Table 4.2, the average ultimate tensile strain capacity of the GFRP box section determined from coupon tests is 0.011. With the exception of specimen S_1, it can be seen that the maximum strains measured in the bottom flange of GFRP box sections at failure are below coupon measurement. In both specimens S_2 and S_3, the box sections did not develop full tensile strength, as the ultimate strains in the bottom flanges were 0.83 and 0.78 respectively. In specimens S_4 to S_6, the ultimate strains in the bottom flange of the box sections were approaching 0.011, suggesting that these configurations had probably been close to tension rupture when the local buckling failure occurred. This matched well with the evidence that tension failure of the box sections was not encountered in any specimen, although the box sections were clearly approaching their tensile limit when ultimate failure occurred. As discussed in Chapter 6, the extra strain capacity of

the concrete in the compression zone allowed the box sections in tension to approach their ultimate tensile strain, representing more efficient use of materials.

Table 8.4 – Maximum strain at the bottom flange of GFRP box sections (positive means tensile)

Specimens	Side a	Side b	
	Maximum strain	Maximum strain	Average
S_1	0.0160	0.0090	0.0125
S_2	0.0079	0.0087	0.0083
S_3	0.0079	0.0078	0.0078
S_4	0.0098	0.0090	0.0094
S_5	0.0090	0.0103	0.0097
S_6	0.0102	0.0094	0.0098

8.6.2 The web-flange separation failure mode

The cause of final failure in this study was the separation of the compression flange and the webs at the upper corners of the box section, leading to 'local buckling failure'. This mode is seen in Figures 8.10 and 8.11. This phenomena of local buckling failure in thin-walled, box-section pultruded composite beams caused by the large curvature has been observed in several previous pieces of research (Mottram, 1991; Palmer *et al*, 1998; Charoenphan *et al*, 2004; Bank *et al*, 1999). As can be seen in Table 8.1, the maximum deflection at failure was between 137 mm and 173 mm with a 26% variation across six tests. It seems that this local buckling failure was caused largely by a specific curvature in the box section, indicating that this type of failure is likely to have been governed by curvature, rather than by load.

The failure mode of the slab specimens is shown in Figures 8.10(a) to (f) for S_1 to S_3 and 8.11(a) to (f) for S_4 to S_6. Pairs of photographs were taken on either side of the section at different locations, where the local buckling occurred. These photographs were captured in the mid-span regions in most cases (S_1, S_2, S_4, and S_5) and between the mid-span and the quarter span regions (S_3 and S_6) at the location of the local buckling failure. Longitudinal cracks grew at the upper corner of box section to a considerable length in the range of 200 mm to 400 mm beneath the central load jack, as shown for S_1 (side b), S_2 (side a), S_3 (both sides a and b), S_4 (side b) and S_6 (both sides a and b). As a result, the top compressive flange and both webs became detached in a sudden manner. This detachment of compressive flange allowed both webs to buckle outward significantly, associated with an acoustic emission 'snap'. However, this was not

the case for faces of the box sections as shown in S_1 (side a), S_2 (side b), S_4 (side a) and S_5 (both sides a and b), the longitudinal cracks did not grow so large (< 50 mm) and both webs did not buckle as much. A vertical crack initiated and propagated in the webs in most cases with the exception of specimen S_1 (side b), S_3 (side a) and specimen S_4 (side b), where the longitudinal cracks grew to a significant length in excess of 300 mm. This line of rupture was either directly under the central load jack or from the central span to quarter span between two load jacks.

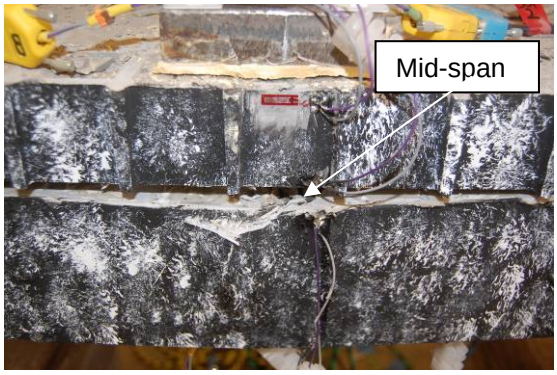

(a) Specimen S_1 (side a)

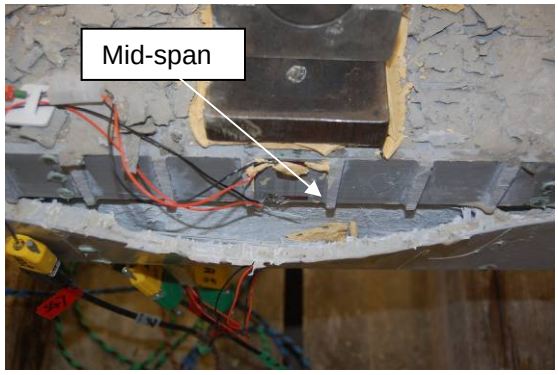

(b) Specimen S_1 (side b)

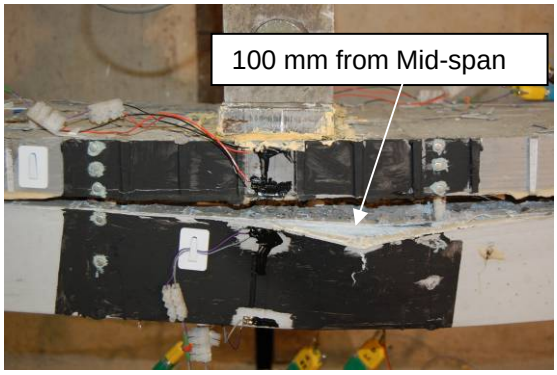

(c) Specimen S_2 (side a)

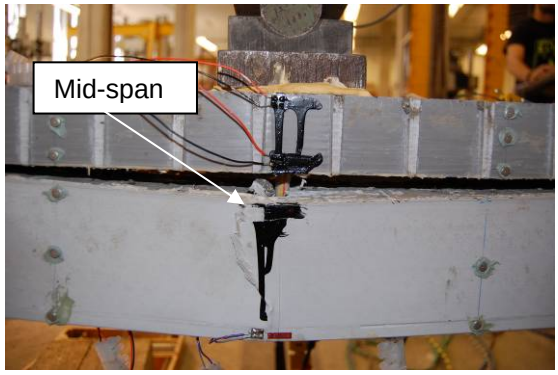

(d) Specimen S_2 (side b)

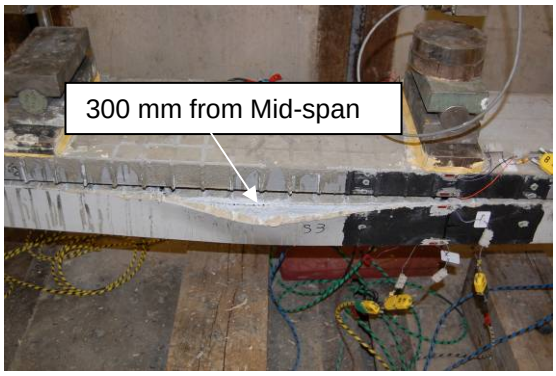

(e) Specimen S_3 (side a)

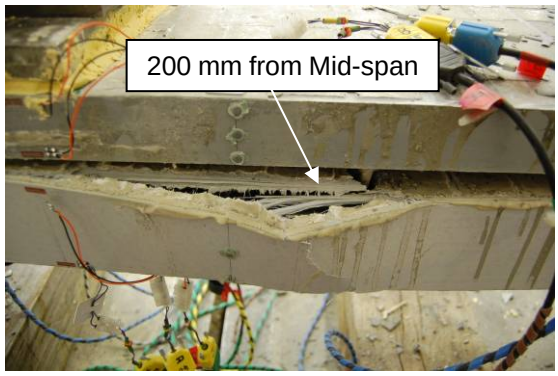

(f) Specimen S_3 (side b)

Figure 8.10 – Failure locations for specimens S_1-S_3

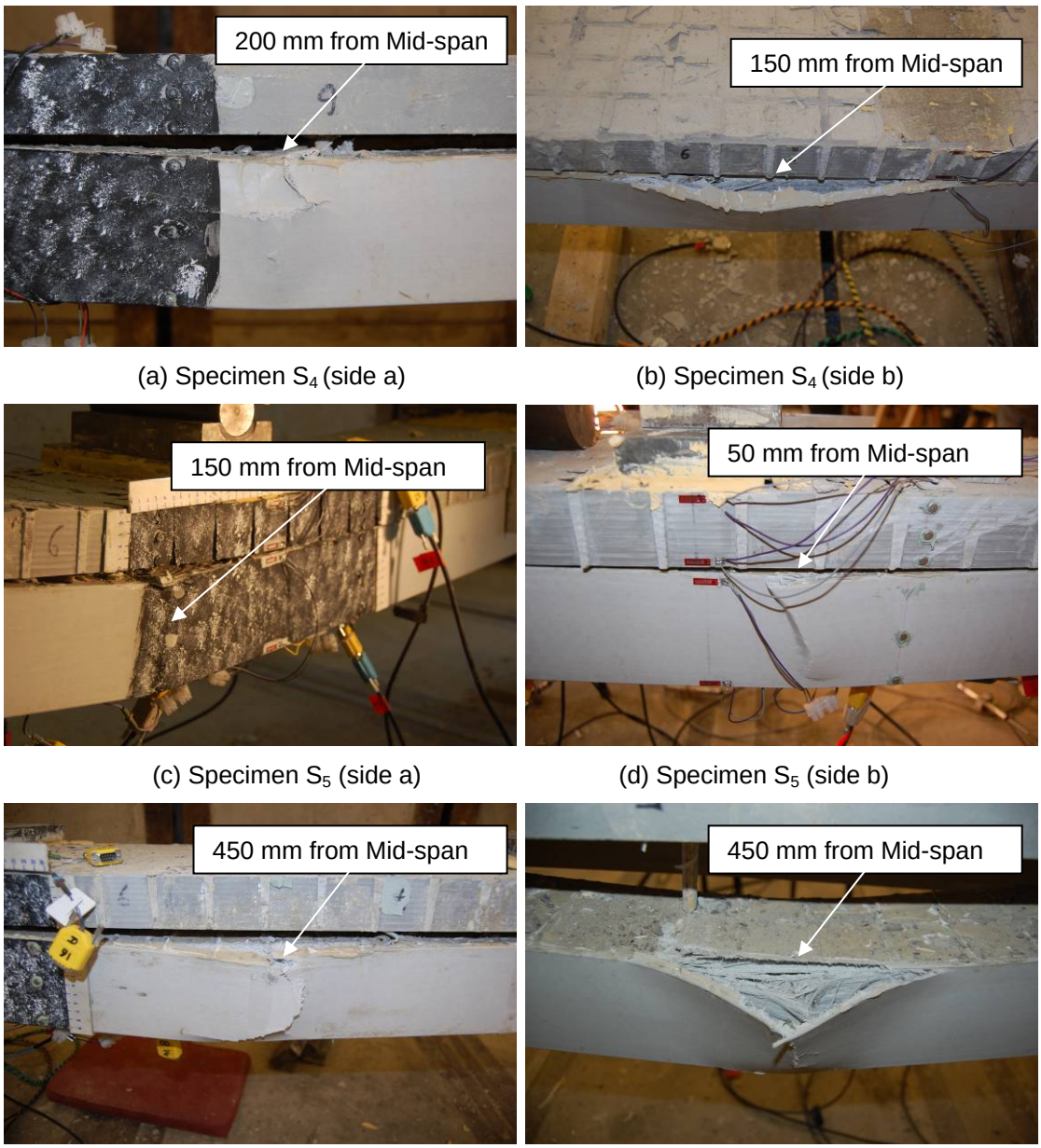

(a) Specimen S_4 (side a) (b) Specimen S_4 (side b)

(c) Specimen S_5 (side a) (d) Specimen S_5 (side b)

(e) Specimen S_6 (side a) (f) Specimen S_6 (side b)

Figure 8.11 – Failure locations for specimen S_4-S_6

Following testing, the failed specimens were cut through at mid-span in order to examine the damage to the compression flange of the box section. As shown in Figure 8.12 it can be seen clearly that there are longitudinal cracks in the top flange at the web-flange junctions, providing evidence of tensile separation failure between the webs and flanges. In some cases such as specimens S_3 and S_6, as shown in Figures 8.12(b) and (d), additional longitudinal cracks propagated between adjacent circular holes. This might be caused by high transverse tensile strain at the web-flange junctions when the compression flange of box section was compressed. To check whether the actual transverse

tensile strain in the top flange exceeds the allowable transverse tensile strain, the following simple analysis (ignoring plate coupling) was carried out. If this is the case, longitudinal splitting of fibres in the top flange would be inevitable. The major Possion's ratio of the box section is given by the equation:

$$\nu_L = \frac{\varepsilon_T}{\varepsilon_L} \tag{8.1}$$

where ε_T is the transverse tensile strain, ε_L is the longitudinal compressive strain in the fibre direction, ν_L is the Major Poisson's ratio of the box section.

The maximum longitudinal compressive strain ε_L is found to be 0.0132 in specimen S_5 across all six specimens, as shown in Table 8.5. The Major Possion's ratio of box section ν_L is 0.23, given by the manufacturer's design data. The transverse tensile strain is calculated to be 0.003, using Eq. (8.1). The actual transverse tensile stress is given by the equation:

$$\sigma_T = E_T \varepsilon_T \tag{8.2}$$

where E_T is the modulus of elasticity of the box section in the transverse direction, which is 8.5 GPa, determined from the manufacturer's design data (Fibreline composites, 2003)

The actual transverse tensile stress is calculated to be 25.5 MPa, using Eq. (8.2). This value is only half of the value of the allowable transverse tensile stress of 50 MPa, given from manufacturer's design data. This demonstrates that the transverse tensile strain at failure in the top flange is insufficient to cause the longitudinal splitting of the fibre at the top flange-web junctions.

(a) Specimen S_2

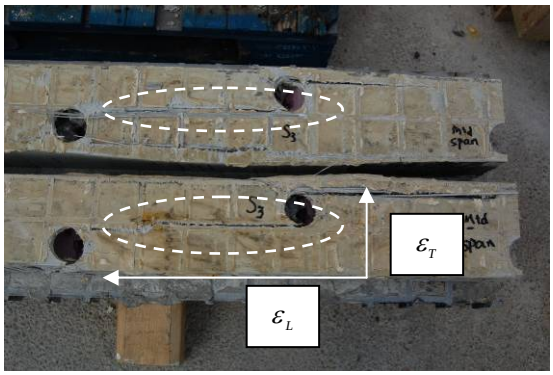

(b) Specimen S_3

(c) Specimen S_4

(d) Specimen S_6

Figure 8.12 – Longitudinal cracks initiated at the web-top flange junction

Table 8.5 – Strain measured at the top flange-web junctions at failure (negative means compressive)

Specimen	Side a		Side b	
	Buckling location	Maximum strain at top corner of box section 'A' at mid-span	Buckling location	Maximum strain at top corner of box section 'B' at mid-span
S_1	Mid-span	-*	Mid-span	-0.0092
S_2	100 mm from mid-span	-0.0083	Mid-span	-0.0059
S_3	300 mm from mid-span	-0.0059	200 mm from mid-span	-0.0063
S_4	200 mm from mid-span	-0.0057	150 mm from mid-span	-0.0083
S_5	150 mm from mid-span	-0.0132	50 mm from mid-span	-0.0034
S_6	450 mm from mid-span	-0.0037	450 mm from mid-span	-0.0052
Note * indicates the strain gauges failed before local buckling failure.				

As can be seen in Table 8.5 there are large discrepancies in the strains measured at the top flange-web junctions at failure across the six specimens. This is at least partially because the electrical resistance strain gauges were only installed at mid-span underneath the central load jack, and the gauge length was short, only being 10 mm. However, in most cases, the web buckling failure positions were outside the region being monitored by strain gauges. Therefore, the strain measured at the mid-span might not represent the ultimate strain of the bucking failure, when the buckling failure did not occur at mid-span. As shown in Table 8.5 the strain readings in specimen S_3 and S_6 are relatively low compared with the rest of specimens. This might be due to the fact that the slip of specimen S_3 was only observed at the roller support with no visible slip at the

pin support, resulting in unsymmetrical composite action along the length of the specimen, as discussed earlier in Section 8.2. Therefore, the maximum local curvature in the box sections may not be at mid-span as illustrated in Figure 8.13. The unsymmetrical deflection profile indicates that the strain reading measured at the mid-span is lower than the maximum strain at buckling.

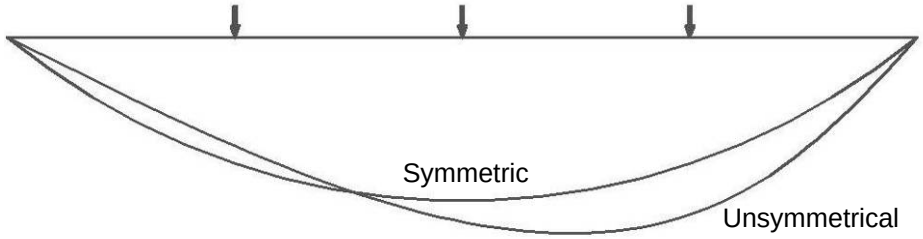

Figure 8.13 – Symmetric and unsymmetrical deflection profile

The vertical deflection profiles along the span for S_1 to S_6 were plotted in order to verify this proposal to explain the findings. As can be seen in Figure 8.14 it is clear that vertical deflection profiles of S_2 to S_6 are symmetric along the span. Vertical deflection profile of S_1 was excluded due to experimental error. Thus, the recorded symmetrical deflection profiles do not support the proposed explanation. Thus, the strain reading recorded at mid-span at failure give a measure for the maximum strain in the box sections.

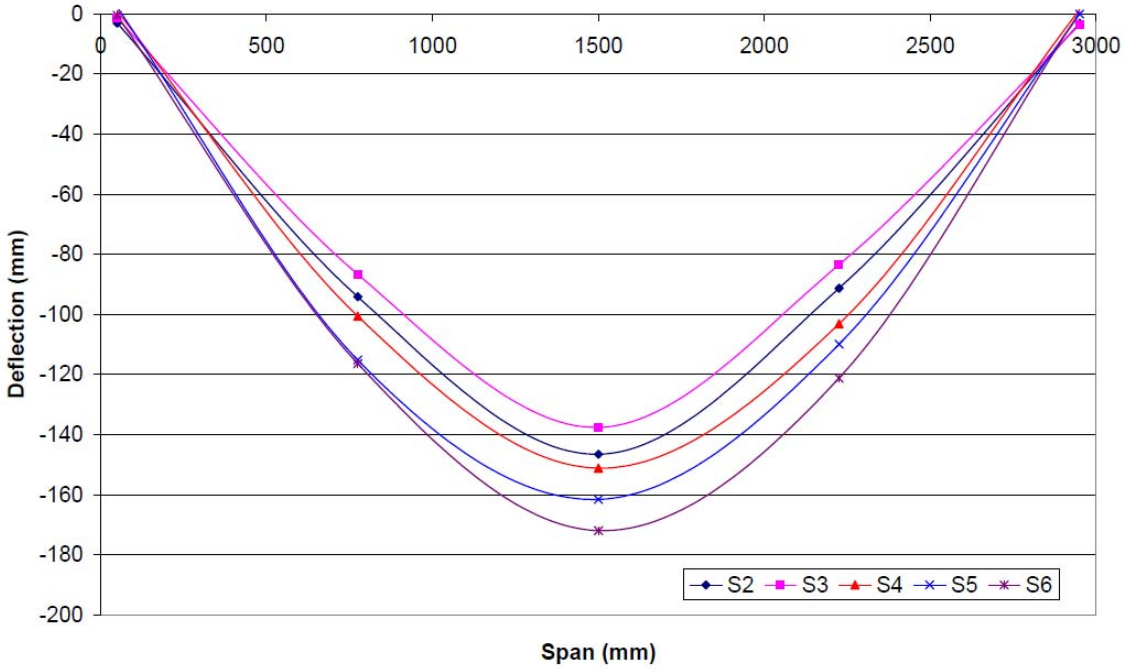

Figure 8.14 – Vertical deflection profiles along the span for specimens S_2 to S_6 at ultimate load.

Coupon tests show that the maximum compressive strain capacity of box section was between 0.0105 and 0.0129 with an average value of 0.011, as given in Table 4.4. It is clear that all the compression strains in Table 8.5 are below 0.011, with the one exception of S_5 (side a). This demonstrates that the maximum strain measured at the flange-web junction is insufficient to cause compressive material failure in specimens S_1, S_2, S_3, S_4 and S_6. One side of specimen S_5 (side a) indeed failed due to compression failure of the webs, as shown in Figure 8.11(e).

8.7 Strain Profiles in Maximum Moment Regions

As discussed in Chapter 7 two strain measuring techniques, namely electrical resistance strain gauges and DeMec gauges were used to record the strain at the top and bottom corner of the grating and box sections on both sides, which are referred to as 'side a' and 'side b' in the following strain profile plots. A typical strain profile at maximum bending moment (mid-span) for specimen S_4 recorded at every load increment were presented in Figures 8.15-8.19.

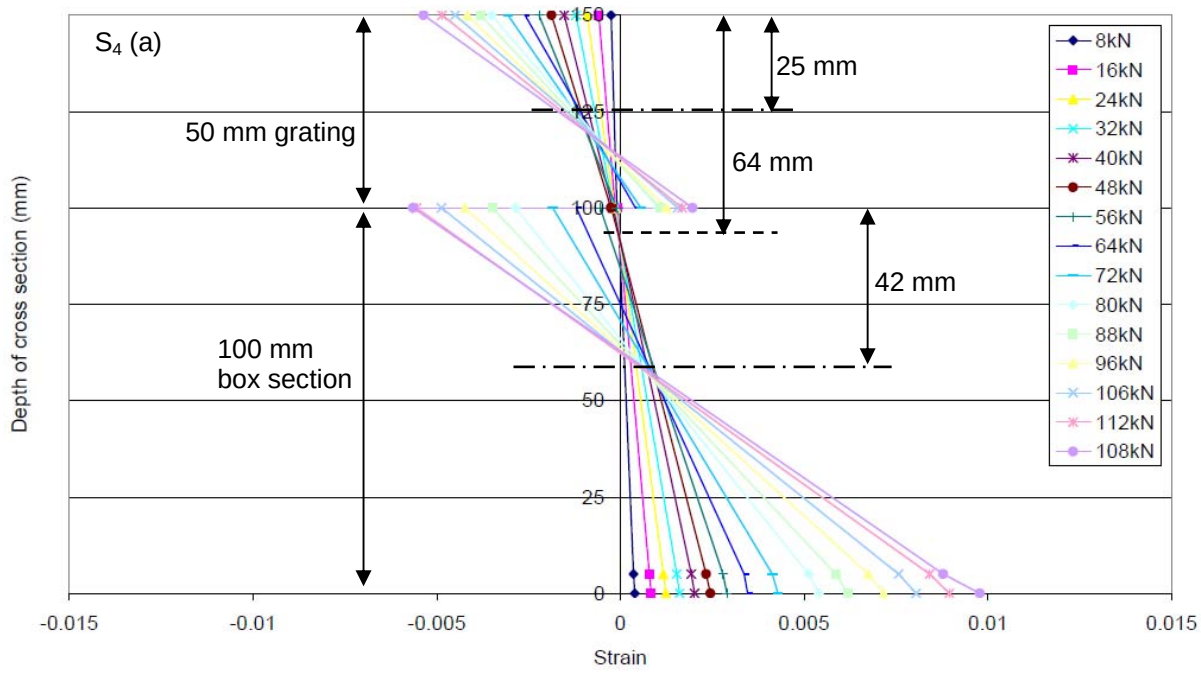

Figure 8.15 – Strain profile plotted from specimen S_4 side (a) electrical resistance strain gauge readings

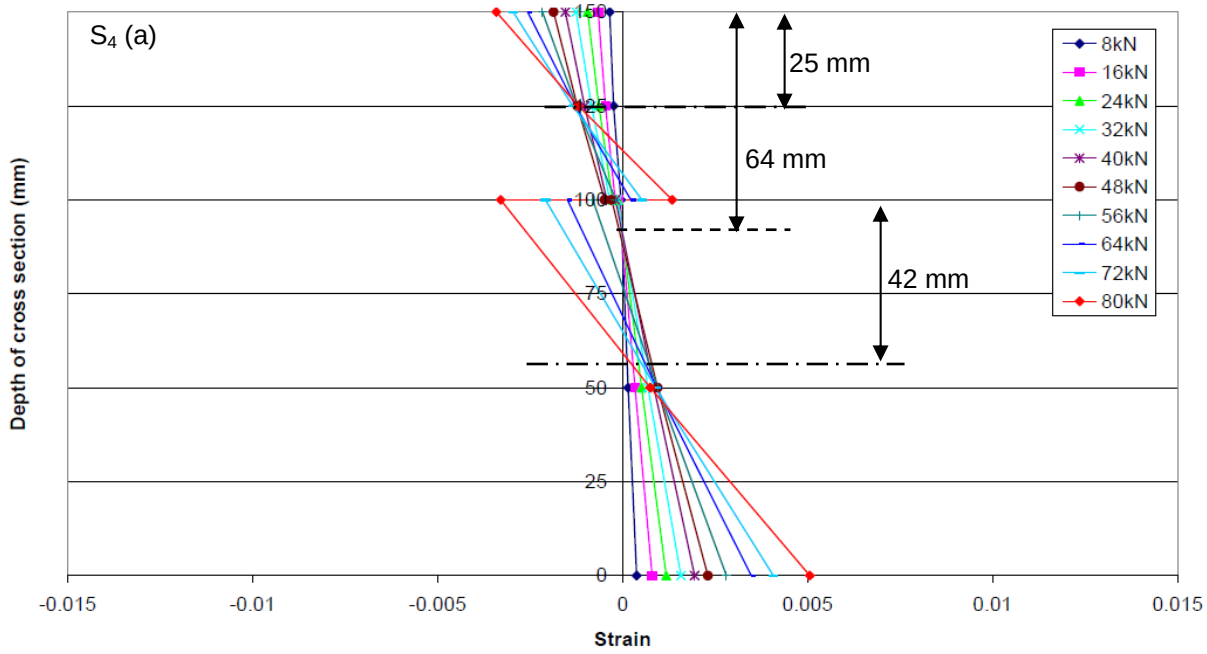

Figure 8.16 – Strain profile plotted from specimen S_4 side (a) DeMec gauge readings

As can be seen from Figures 8.15 and 8.16, the strain profile in specimen S_4 (side a) is continuous from top to soffit before 48 kN, representing full interaction between the concrete-filled grating and box sections up to this load, as illustrated in Figure 8.17(a). The theoretical neutral axis of transformed section was calculated to be 14 mm below the grating/box-section interface, the actual neutral axis was measured by both techniques matched with the analytical value, indicating that the concrete-filled grating was fully utilised in compression and that most of the box section, including both webs and the bottom flange were utilised in tension, with the top flange in a small amount of compression.

As the load increased beyond 56 kN, the strain profile splits into two separate strain profiles with independent neutral axes, indicating the loss of full interaction resulting from longitudinal shear failure occurred between 48 kN and 56 kN. This matches well with the evidence shown in the total load versus midspan deflection plot in Figure 8.5. At 48 kN, there was a reduction in stiffness as the deflection increased, indicating that the longitudinal shear failure occurred at 48 kN. This is also indicated in the total load versus relative end-slip plot (see Figure 8.6) by the presence of significant slip after 48 kN.

A small strain difference was shown at the grating/box-section interface between two separate strain profiles in Figures 8.15 and 8.16, indicating that there was

still a degree of partial interaction between the concrete-filled grating and box sections, as illustrated in Figure 8.17(b). This partial interaction between two components was provided by the shear connections from the GFRP dowels embedded within the concrete. After the concrete studs had failed in shear, these dowels resisted slip and hence ensured some levels of partial interaction at the grating/box-section interface.

As the load increases, the strain difference at the grating/box-section interface became larger. This is because partial interaction at the grating/box-section interface reduced as the GFRP dowels were sheared off. Consequently, the neutral axis in the grating gradually moved upwards, and the neutral axis in the box section gradually moved downwards. Both neutral axes were moving towards the components' centroids, leading to an increase in strain difference at the grating/box-section interface. This indicated that the interaction between the two components diminished over time and both acted largely as separate components towards the end of each test to sustain the load. The strain profiles progressing from 'full-interaction' to 'partial-interaction' and eventually approaching 'non-interaction' are illustrated, schematically, in Figure 8.17. When the concrete-filled grating and box sections act as separate components, as illustrated in Figure 8.17(c), the theoretical neutral axis of the concrete-filled grating should match with its own centroid, which is 25 mm below the top surface of the grating, since there is no evidence of cracking of concrete in the grating when the concrete is in tension. The effect of poor concrete-fill in the box sections in specimens S_1 to S_3 was ignored in calculating the neutral axis, thus the theoretical neutral axis of partially concrete-filled box sections is considered to be at the centroid of box sections, which is 50 mm below the grating/box-section interface. For good concrete-fill in the box sections in specimens S_4 to S_6, visual inspection of the failed specimens showed that there is no evidence of concrete crushing in the box sections. The theoretical neutral axis of the partially concrete-filled box sections is calculated using a transformed section approach, to be 42 mm below the grating/box-section interface. As shown in Figures 8.15 to 8.19, after the loss of full-interaction, the locations of individual neutral axis of the concrete-filled grating and box sections were within the boundary, defined by the theoretical neutral axes.

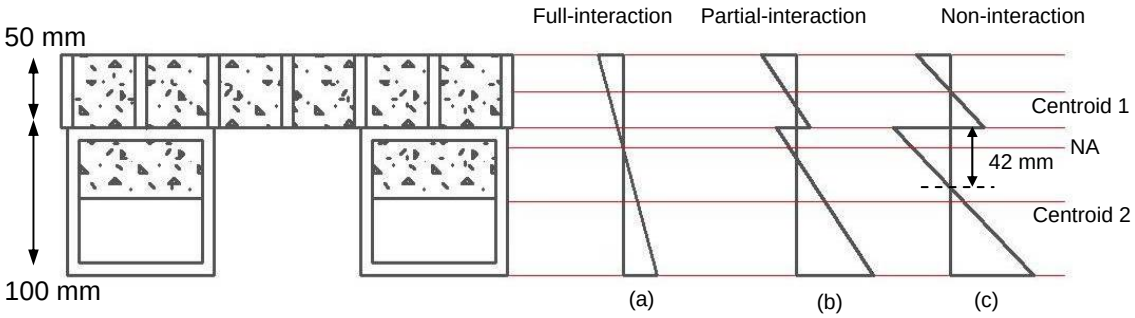

Figure 8.17 – Strain profile change at mid-span under increasing load (centroid 1 indicates the centroid of the concrete-filled grating, and centroid 2 indicates the centroid of the box sections)

Similar behaviour can be observed for 'side b' of specimen S_4, as can be seen in Figures 8.18 and 8.19, the strain profile through the depth of the composite section followed closely a linear distribution at loads below 48 kN, representing full interaction between the concrete-filled grating and box sections up to this load. As the load increased beyond 56 kN, the strain profile splits into two separate strain profiles, indicating that longitudinal shear failure occurred somewhere between 48 kN and 56 kN, with full interaction lost. This matches well with the evidence shown in the total load versus midspan deflection plot in Figure 8.5. Longitudinal shear failure occurred at about 48 kN for specimen S_4, represented by a change in stiffness as the deflection increased.

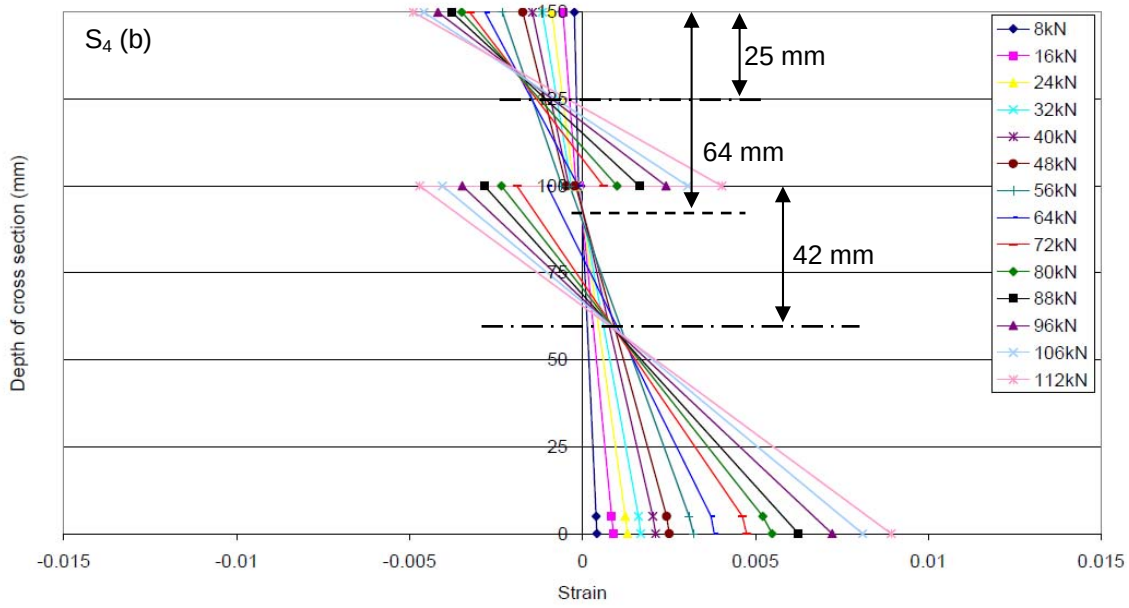

Figure 8.18 – Strain profile plotted from specimen S_4 (side b) electrical resistance strain gauge readings

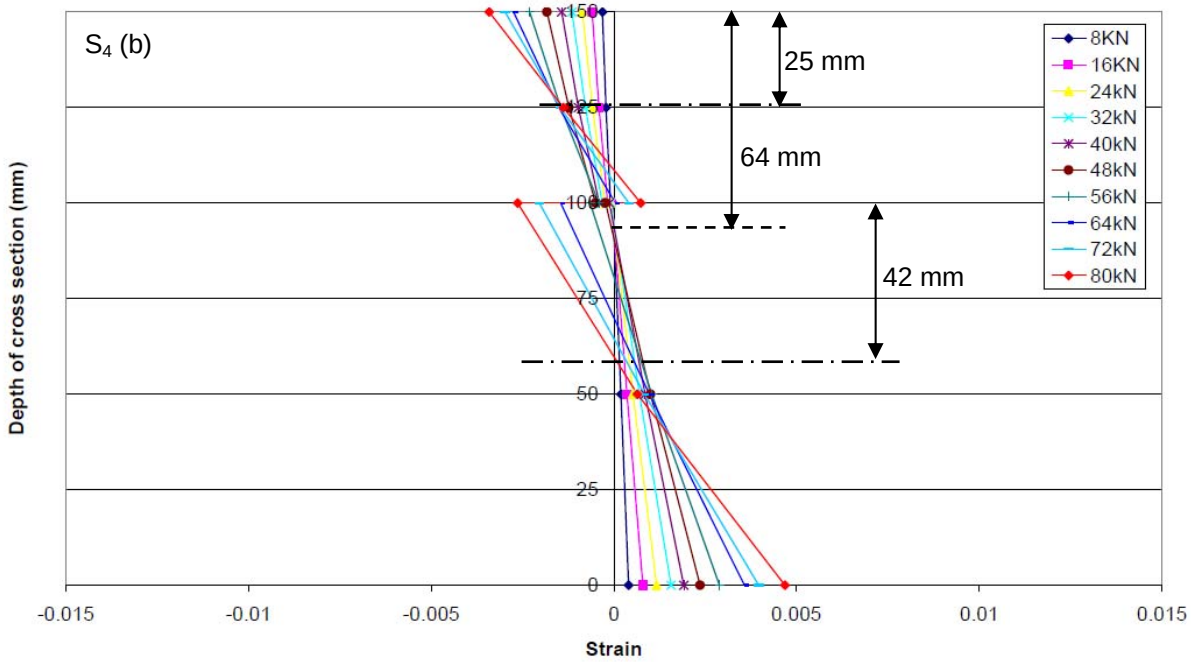

Figure 8.19 – Strain profile plotted from specimen S_4 (side b) DeMec gauges readings

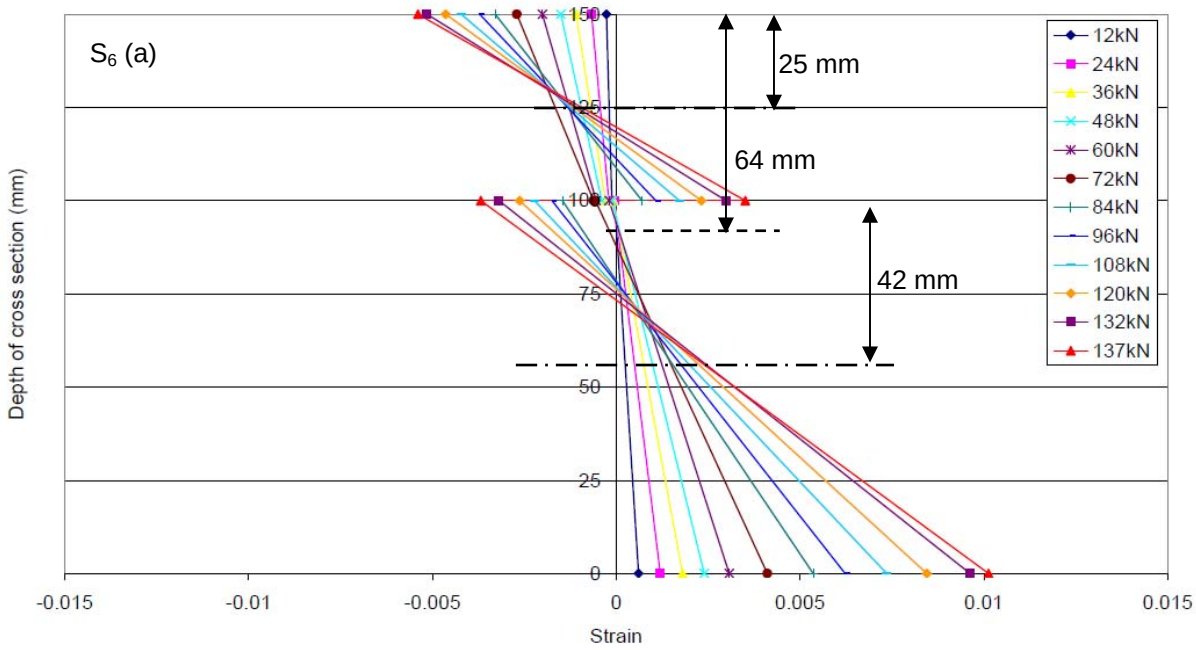

Figure 8.20 – Strain profile plotted from specimen S_6 (side a) electrical resistance strain gauge readings

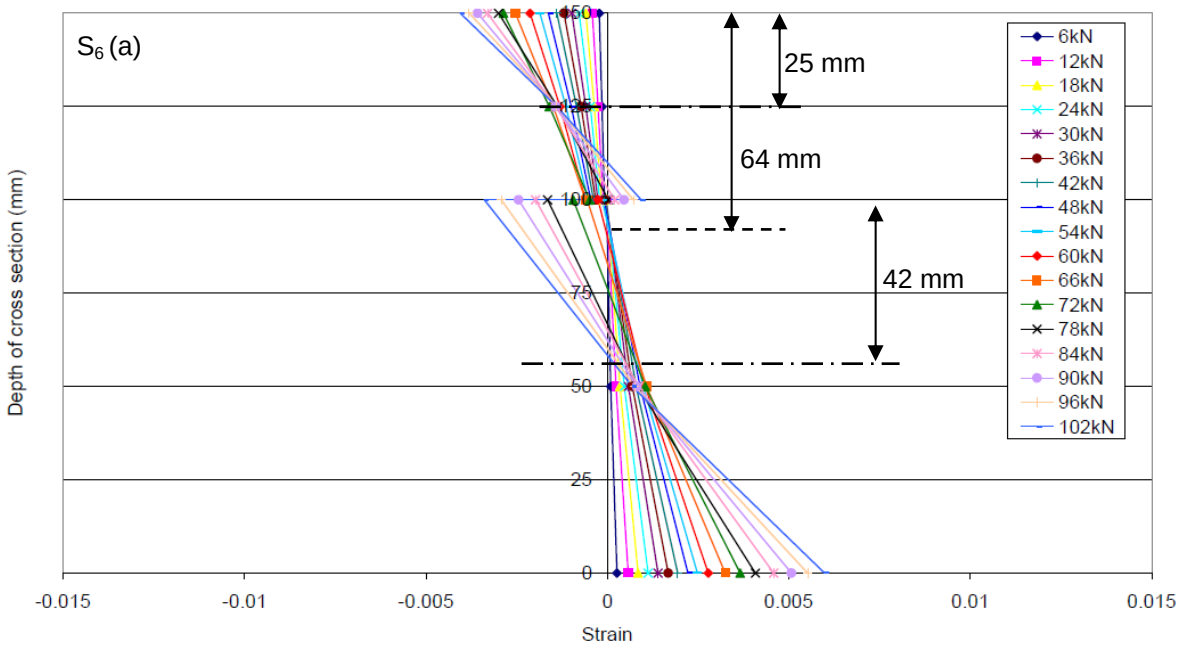

Figure 8.21 – Strain profile plotted from specimen S_6 (side a) DeMec gauges readings

Specimen S_6 showed similar behaviour, as can be seen in Figures 8.20 and 8.21, the strain profile in specimen S_6 (side a) measured by electrical resistance strain gauges is continuous from top to soffit before 72 kN, representing full interaction between the concrete-filled grating and box sections up to this load. As the load increased beyond 84 kN, the strain profile splits into two separate strain profiles, indicating that longitudinal shear failure occurred somewhere between 72 kN and 84 kN. Figure 8.19 shows that the strain profile in specimen S_6 (side a) measured by DeMec gauges is also continuous from top to soffit before 66kN, and the strain profiles splits into two separate strain profiles as the load increased beyond 72 kN, indicating that longitudinal shear failure occurred somewhere between 66 kN and 72 kN. This correlates well with the evidence shown in total load versus relative end-slip plot for specimen S_6 (see Figure 8.22). The longitudinal shear failure at both ends on 'side a' (referred to as 'roller 1' and 'pin 1') occurred at 50 kN and 66 kN, represented by a significant increase in slip.

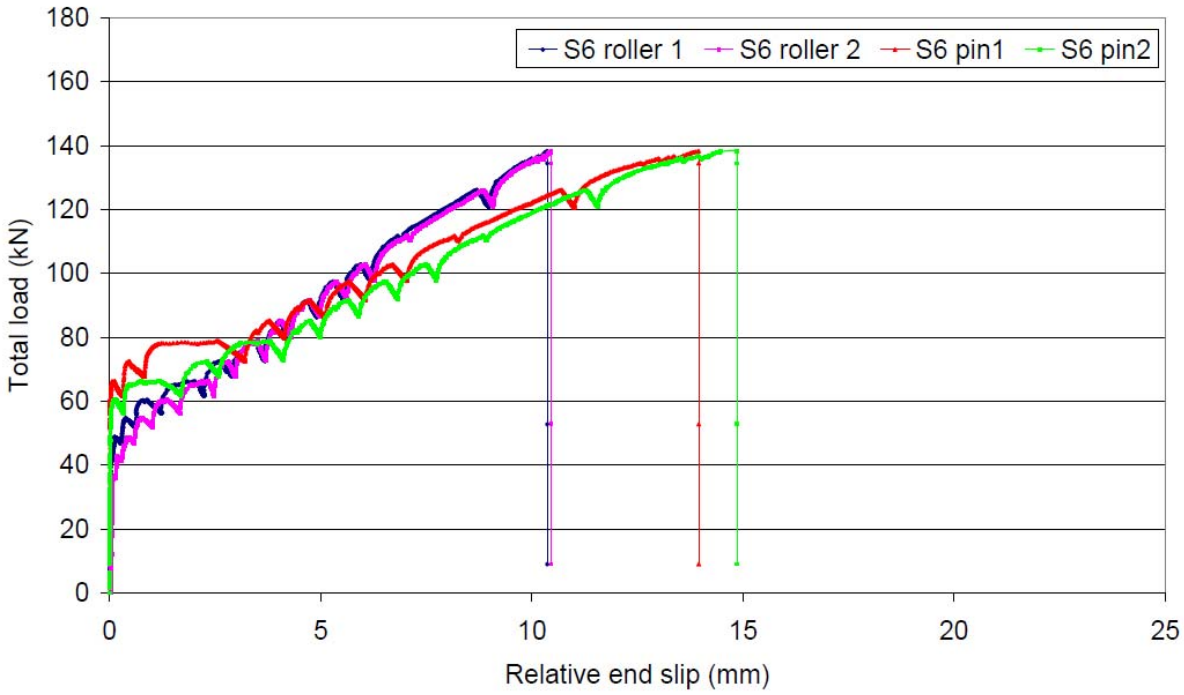

Figure 8.22 – Total load versus relative end-slip plot for specimen S_6

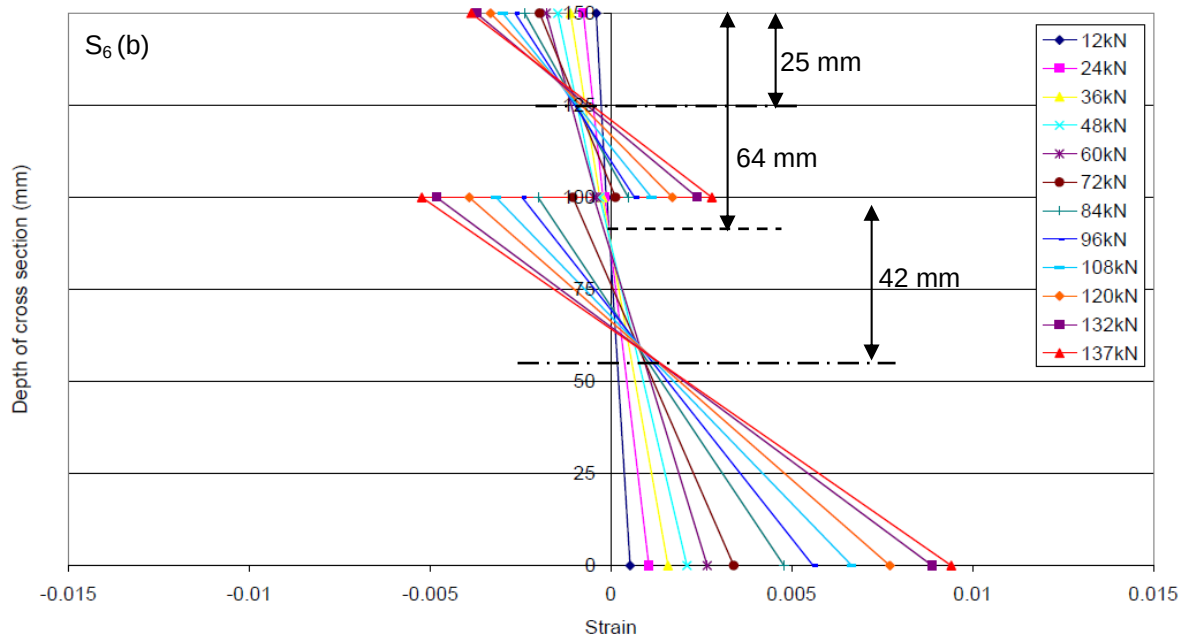

Figure 8.23 – Strain profile plotted from specimen S_6 (side b) electrical resistance strain gauge readings

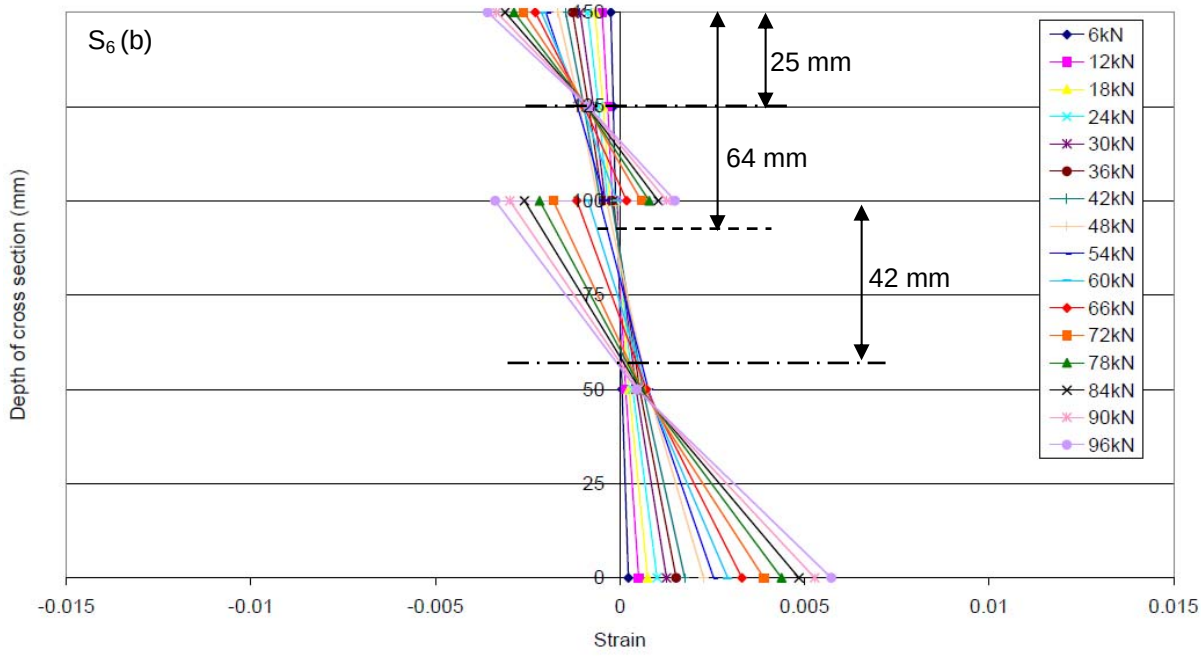

Figure 8.24 – Strain profile plotted from specimen S_6 (side b) DeMec gauge readings

As can be seen in Figures 8.23 and 8.24, the strain profile plotted from DeMec gauge readings in specimen S_6 (side b) is continuous from top to soffit before 54 kN, and the strain profiles splits in to two separate strain profile as the load increased beyond 60 kN, indicating that the longitudinal shear failure occurred somewhere between 54 kN and 60 kN. This correlates well with the evidence shown in total load versus relative end-slip plot for specimen S_6 (see Figure 8.22). The longitudinal shear failure at both ends on 'side b' (referred to as 'roller 2' and 'pin 2') occurred at 43 kN and 60 kN, represented by a significant increase of slip. This is also indicated in total load versus mid-span deflection plot for specimen S_6 (see Figure 8.7). The elastic phase terminated at 54 kN and there was a change in stiffness after this point, indicating that the longitudinal shear failure occurred.

To summarises, the typical progression of strain profiles in specimens S_4 and S_6 presented in Figures 8.18 to 8.24 demonstrated a gradual loss of composite action under increasing load. Similar behaviour was observed across all six specimens.

8.8 Ductile Behaviour of Specimens S_1 to S_6

Ductility of a structural member may be defined as its ability to sustain inelastic deformations prior to collapse, without a significant loss in strength (Mirmiran *et al*, 1998). In general, structures are designed to give reasonable warning before collapse, a ductile system displays sufficient warning of overload before catastrophic failure occurs. As discussed earlier in Chapter 3, FRP behaves purely linear-elastically to the ultimate failure, and concrete crushes in a rather brittle fashion, thus any failure associated with concrete crushing and FRP fracture is brittle and catastrophic. The results of push-out tests, as discussed in Chapter 5, demonstrated that the feasibility of achieving ductility from the longitudinal shear interface, this concept was further verified by full-scale slab tests. Six slab test results demonstrated that ductility did not come from the concrete-filled grating, although the concrete-filled grating behaved in a slightly non-linear fashion beyond the elastic phase. It was assumed that the concrete behaved linear-elastically up to the failure as a reasonable approximation. This is a crucial assumption made in the following analytical models. It also demonstrated that all the ductility was indeed provided by the progressive longitudinal shear failure along the grating/box-section interface. As shown in Figures 8.1 and 8.7, all slab specimens behaved linear-elastically under the service load (20 kN), calculated based on a service load deflection limit of $\delta = span/250$ (11.6 mm). As the load continued to increase until the imposed longitudinal shear exceeded the longitudinal shear resistance of the proposed shear connectors, it triggered the longitudinal shear failure at the grating/box-section interface, which ends the elastic phase. All specimens continued to carry the load at a reduced stiffness until a second peak was reached, immediately followed by the final failure. All slab specimens experienced a gradual loss of composite action between the concrete-filled grating and box section, progressing from ‘full-interaction’ before longitudinal shear failure, to ‘partial-interaction’ afterwards, and eventually approaching ‘non-interaction’ prior to the final failure. The behaviour of all specimens was ductile, with considerable warning before collapse.

8.9 Summary

This chapter has provided a discussion of the experimental results from the six slab tests. The following conclusions can be drawn from the results:

1. The proposed formwork showed great robustness during the construction stage.

2. All slab specimens behaved elastically and fully compositely until longitudinal shear failure occurred at the grating/box-section interface. After this, the specimens carried on resisting further load capacity at a reduced stiffness until a second peak was reached at final failure, due to local buckling of box sections. This local buckling failure is governed by a specific curvature. All specimens failed in a progressive manner, exhibiting reasonable ductility before approaching failure.

3. Comparison amongst specimens S_1 to S_3 showed that the initial peak load was governed by the combination of concrete studs and GFRP dowels. It also indicated certainly by adding more shear connectors, the initial peak load and the ultimate failure load were both enhanced.

4. Comparison amongst specimens S_4 to S_6 showed that the post elastic behaviour is solely dependent on the shear strength of GFRP dowels through dowel action at the grating/box-section interface and post-cracked restrained shear resistance from the concrete-to-concrete interface.

5. The design of specimen S_5 aimed to resolve the construction issue arising from poor concrete placement by introducing more holes to improve concrete flow. The initial peak load was enhanced by having additional concrete studs, and it also achieved a ductile failure.

6. The additional strain capacity (up to 100%) in the concrete from the confinement of the grating enabled box sections to reach a higher tensile strain capacity (up to 100%), indicating the efficient use of the materials.

7. The ductile behaviour of all slab specimens demonstrated that the feasibility of achieving ductility from the longitudinal shear interface through progressive longitudinal shear failure. The presence of GFRP dowels are essential at the

grating/box-section interface to ensure that the longitudinal shear failure occurs in a ductile manner.

8. For a given total load, the longitudinal shear demand within the end quarter span between Type A and Type B loading are identical, but the maximum moment at mid-span under Type B loading is 12.5% higher than that under Type A loading. This suggests that the moment at onset of longitudinal shear failure under Type B loading should be 12.5% higher than that under Type A loading. However, the moment versus deflection responses showed that the moment at onset of longitudinal shear failure of specimens S_4 and S_6 were similar, which did not support the proposed explanation.

9. Strain profiles at mid-span indicated that all slab specimens experienced a gradual loss of interaction between the concrete-filled grating and box section, progressing from ‘full-interaction’ before longitudinal shear failure, to ‘partial-interaction’ afterwards, and eventually approaching ‘non-interaction’ prior to the final failure.

To summarise, the slab testing results have demonstrated that the composite system behaved in a ductile manner prior to ultimate failure, through controlled debonding failure at the grating/box-section interface, and a robust interaction between FRP formwork and concrete was achieved. In Chapter 9, analytical models have been developed to predict the flexural behaviour of this composite system.

Chapter 9 Evaluation of Analytical Model by Comparison with Experimental Results

9.1 Introduction

Chapters 7 and 8 detail the experimental investigation into six slab specimens, referred to as specimens S_1 to S_6. It was found that all slabs behaved elastically until the initiation of longitudinal shear failure at the grating/box-section interface. After this, the load capacity of each specimen carried on increasing at a reduced stiffness to a peak load, before final failure occurred through compression flange/web separation of the box section, followed immediately by in-plane web buckling.

In this chapter, analytical models have been developed to predict the flexural behaviour of the slab specimens, designed with a ductile longitudinal shear failure criterion, and successfully verified by experimental results. This model has been divided into three stages. The first stage is a linear elastic analysis assuming the concrete-filled grating and box sections behave fully compositely until the onset of longitudinal shear failure. The analysis establishes a moment-curvature response of the section in the elastic phase, which is terminated at point A, governed by longitudinal shear failure, as illustrated in Figure 9.1(a). The second stage is an elastic-plastic analysis, assuming that all the shear connectors behave fully plastically throughout the length of the beam. The moment continues to increase, under reduced stiffness as the longitudinal interface allows partial interaction, eventually terminating at point B. Point B is governed by failure due to fracture of GFRP dowels after a certain amount of slip. All six slab test results indicated that the cause of final failure appeared to be web/flange separation, followed by local buckling of the box sections. This appears to be governed by curvature rather than load. Therefore, the final stage relies on a local buckling analysis of the box sections by assuming the box section consists of four identical orthotropic plates and failure is due to compression flange buckling. The deflection limits defined by curvature at buckling are plotted in the moment-deflection predictions. The final failure point C is given by the intersection of the deflection limit with the line AB. This approach should lead schematically to the final moment-deflection prediction plot shown in Figure 9.1(b).

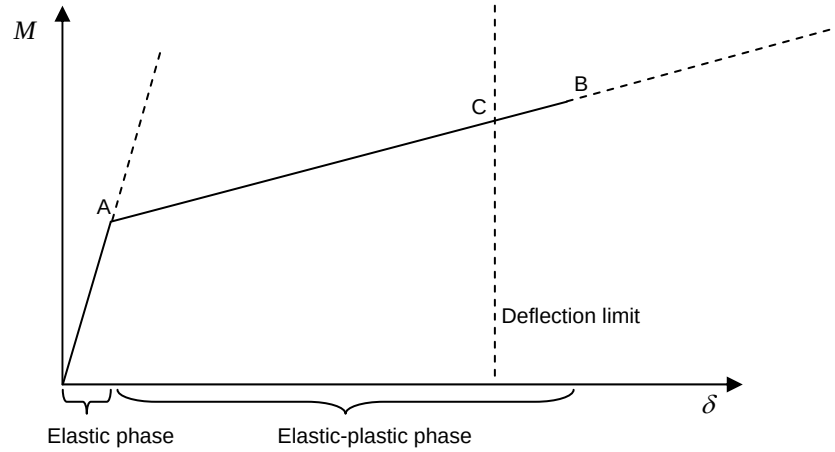

(a)

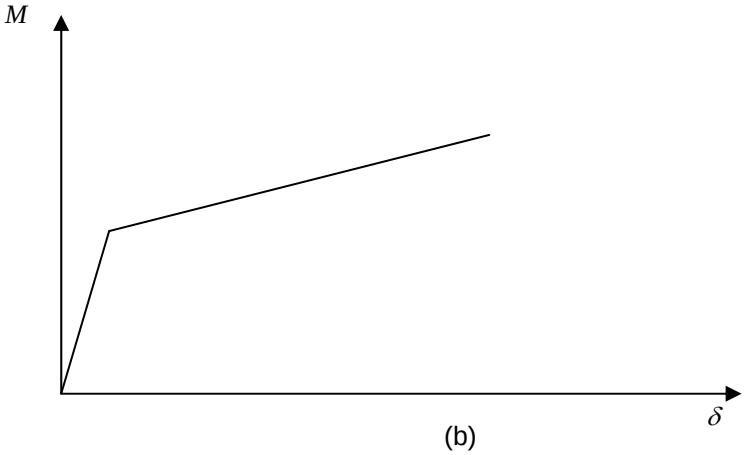

(b)

Figure 9.1 – Moment versus deflection prediction by the proposed analytical model

9.2 Description of Analytical Model for 'Elastic' Phase

9.2.1 The concrete-filled grating in compression

For concrete in compression, the stress-strain relationship determined from the concrete-filled grating compression test is shown in Figure 9.2. It was used to calculate the compressive force. As mentioned in Chapter 8, the maximum strain measured at the top surface of the concrete-filled grating of all slab specimens was 0.007, as shown in Table 9.1.

Table 9.1 – Maximum strain at the top surface of the concrete-filled grating (negative means compressive)

Specimens	Side a	Side b	
	Maximum strain	Maximum strain	Average
S_1	-0.0053	-0.0040	-0.0047
S_2	-0.0043	-0.0055	-0.0049
S_3	-0.0031	-0.0026	-0.0057
S_4	-0.0054	-0.0062	-0.0058
S_5	-0.0062	**-0.0070**	-0.0066
S_6	-0.0054	-0.0039	-0.0047

Figure 9.2 shows the stress-strain plot of the concrete-filled grating block, determined from axial compression tests reported in Chapter 6. The initial phase in Figure 9.2, up to the strain reading $\varepsilon_c = 0.010$, was selected and used for the stress-strain response of the concrete-filled grating for the calculation of compressive force. As shown in Figure 9.3, the stress-strain response up to $\varepsilon_c = 0.002$ is linear elastic. Beyond this point, the stress-strain response is non-linear. Therefore, the compressive force is calculated by taking account of the non-linearity of the concrete-filled grating. The initial modulus of elasticity of the concrete-filled grating is taken as 11.6 GPa, calculated from the gradient in the elastic phase (up to $\varepsilon_c = 0.002$) in the stress versus strain plot, as shown in Figure 9.3.

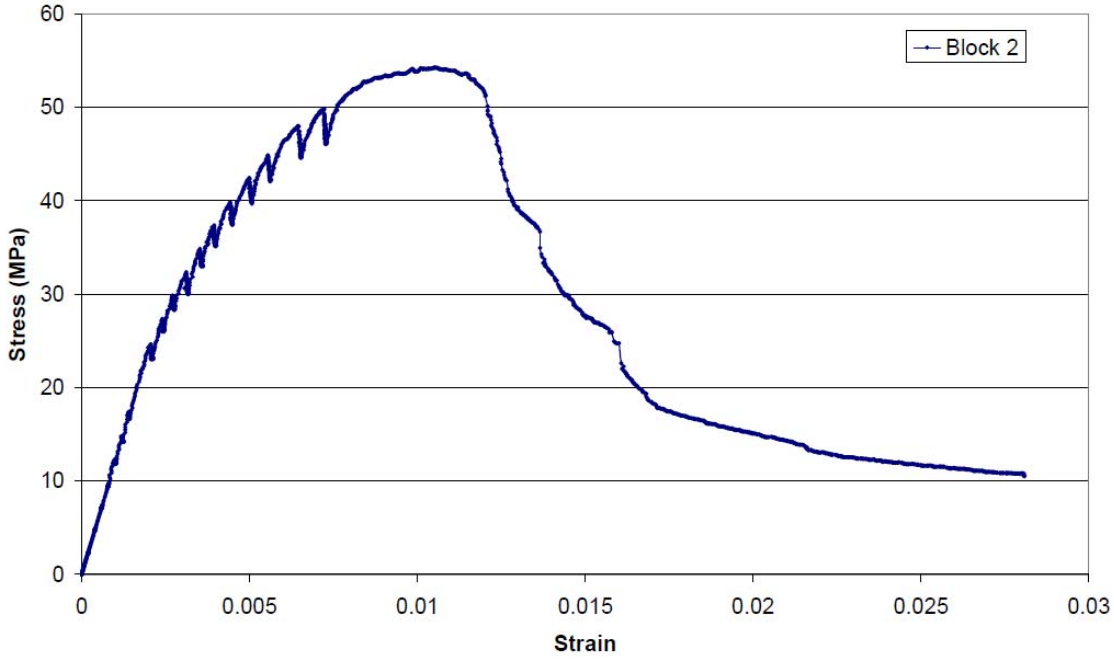

Figure 9.2 – Stress versus strain plot of the concrete-filled grating block (specimen 2)

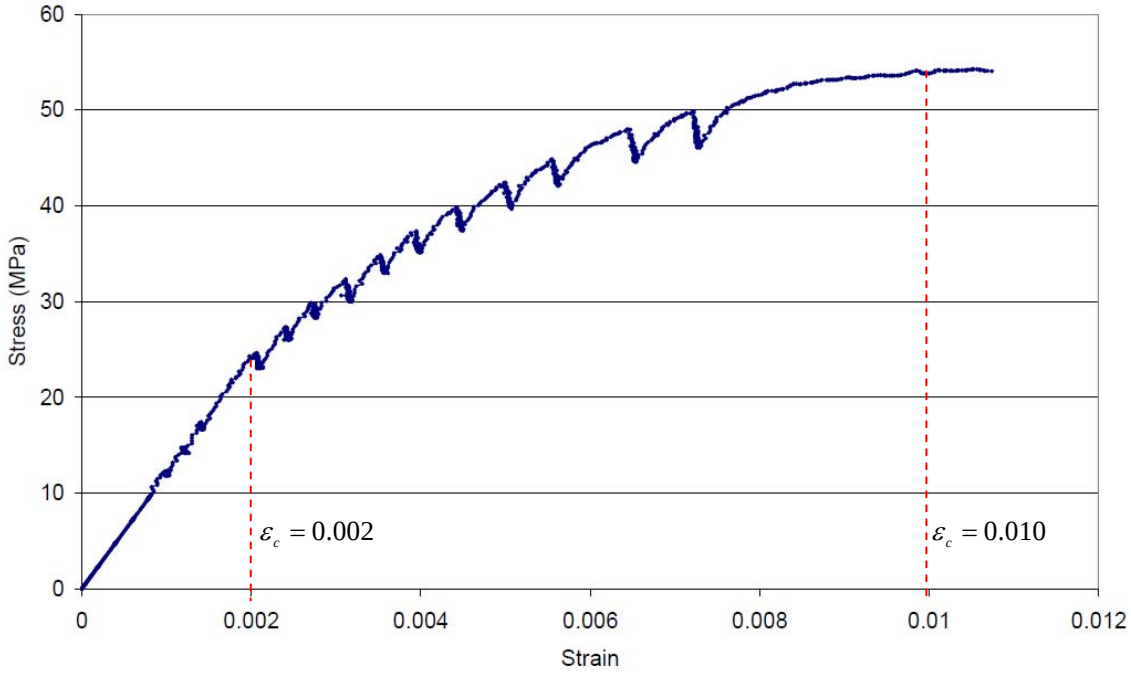

Figure 9.3 – Stress versus strain plot of the concrete-filled grating applied in the analysis

9.2.2 GFRP sections in tension or compression

For pultruded GFRP box sections in compression or tension, a linear stress-strain relationship is assumed. The compressive and tensile forces are calculated by treating the top flange, two webs and the bottom flange as three individual components. The force in each component is calculated separately using:

$$F_f = E_f \varepsilon_f A_f \tag{9.1}$$

where F_f is compressive or tensile force in each component, A_f is the cross sectional area of each component, and ε_f is the mean strain in each component, as the strain varies across the section.

The manufacturer has published some data pertaining to the mechanical properties. Also, characterisations of materials were discussed in Chapter 4, and reproduced in Table 9.2. As mentioned earlier, the properties given by the manufacturer can be assumed to be lower bound values. Properties determined by coupon tests are more realistic for the calculation of the tensile force in the analysis. Therefore, the elastic modulus of the pultruded GFRP box sections in the longitudinal direction is taken as 32.1 GPa, as determined from coupon tests.

Table 9.2 – Summary of coupon tensile test results

Tensile properties	*T*- thickness (mm)	*W*- width (mm)	*L*- total length (mm)	L_o- distance between grips (mm)	E_L- elastic modulus (GPa)	Failure mode	Failure stress (MPa)	Failure strain (%)
Top_1	7.8	25.1	302	150	31.3	Tab failure	N/a	N/a
Top_2	7.9	25.4	301	151	32.1	Tab failure	N/a	N/a
Bot_1	8.5	25.5	301	150	33.2	Tab failure	N/a	N/a
Bot_2	8.5	25.4	301	151	32.6	Tab failure	N/a	N/a
WA_1	8.2	25.2	300	150	32.4	Splitting of fibres	356	1.10
WA_2	8.2	25.2	301	151	31.5	Splitting of fibres	345	1.09
WB_1	8.0	25.4	301	151	31.8	Splitting of fibres	350	1.10
WB_2	7.9	25.7	300	150	32.2	Splitting of fibres	368	1.13
Average					32.1		355	1.10

9.2.3 Section geometry

As mentioned above, the modulus of elasticity of the concrete-filled grating and pultruded box section are taken as 11.6 GPa and 32.1 GPa. By applying a modular ratio of 2.77, the composite section can be transformed into an equivalent whole concrete-filled grating section. As the centroid of the transformed section is calculated to be 64 mm below the top surface of the grating, it is reasonable to assume that the neutral axis of the composite section matches with its centroid during the initial stage when the concrete and box sections are still showing full-interaction elastic. Figure 9.4 shows a typical strain profile plotted from the DeMec gauge readings of specimen S_4 (side a). The actual neutral axis in slab specimen S_4 was 64 mm below the top surface of the grating. This demonstrates that the assumption made on the neutral axis position correlates well with experimental results. The distance to the neutral axis, 64 mm below the top surface of the grating, indicated that the concrete-filled grating and the top flange of the box sections (8 mm thick) were in compression, and both webs and bottom flange were in tension.

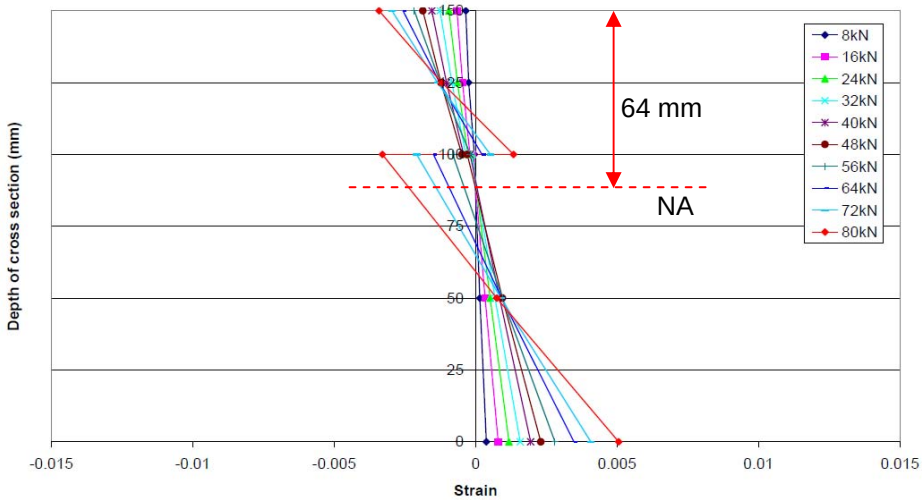

Figure 9.4 – Strain profile plotted from specimen S_4 (side a) DeMec gauge readings

9.2.4 Moment versus curvature response

Utilising the aforementioned constitutive relationships for the materials and geometric relationships for the cross-section, the method to establish the moment-curvature response of the composite slab is as follows:

Step 1: An initial strain of $\varepsilon_c = 0.0005$ is assumed at the top of the concrete-filled grating.

Step 2: The location of the neutral axis is then assumed in order to establish a complete strain profile assuming a linear strain distribution, where plain sections remain plane.

Step 3: Based on the stress-strain response of the concrete-filled grating, as described in Section 9.2.1, an equation representing the stress-strain relationship is derived from experimental results using a curve fit. Following that, a layered sectional approach is adopted, as shown in Figure 9.5. The cross-section of the concrete-filled grating is sliced into ten horizontal layers, each with an equal depth of 5 mm. The compressive force in the concrete-filled grating is determined from the overall area of concrete stress profile, which is the sum of the area of each layer. The tensile force in the box sections is determined by assuming a linear stress-strain relationship, as described in Section 9.2.2.

Step 4: If the compression and the tension force are not equal, then a new value of the neutral axis depth in step 2 is assumed by trial and error method and the process is repeated until equilibrium is satisfied.

Step 5: The sum of the moments generated by all forces from each component (M) is calculated and the corresponding curvature (ψ) is also calculated as the slope of the strain profile assumed at step 1. This provides one point on the moment-curvature response. The strain at the top of the grating is then increased with a strain increment of 0.0005 in step 1 and the process is repeated, to establish the full moment-curvature response.

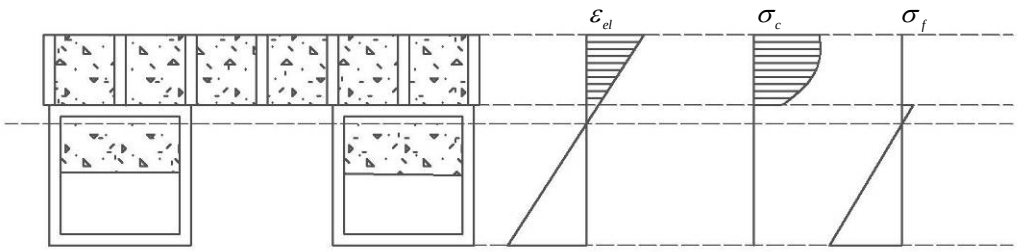

Figure 9.5 – Strain and stress distribution of slab specimens at 'elastic' phase

9.2.5 Moment versus deflection predictions

Once the moment-curvature $(M-\psi)$ response of a section is determined, it can be used to establish the moment-deflection $(M-\delta)$ response using a numerical integration approach. The concept to transform curvature into deflection is achieved by integrating curvature twice. In order to do so, an initial load is assumed, half of the span is divided in to several segments, each with a length of $\Delta d_x = 100mm$, and the bending moment experienced within each of these regions (M_i) is calculated in accordance with the loading schemes being used (either Type A or Type B loading). The data from the previously established moment-curvature response is then employed in order to determine the curvature in the member in each region (ψ_i). The product of the length of each region and the curvature value within that region ($\psi_i \text{x} \Delta d_x$) approximates the change in slope ($\Delta\theta_i$) of the member within that region. The summation of all of the $\Delta\theta_i$ values for each region between the mid-span and the support gives the total slope angle of the member (θ_i). The product of the length of each region and the average slope within that region ($\theta_i \text{x} \Delta d_x$) gives the change in deflection ($\Delta\nu_i$) of the member within that region. The summation of all of the $\Delta\nu_i$ values for each region between the mid-span and the support gives the total mid-span deflection of the member (δ). This entire process is repeated at various load

levels in order to establish the complete moment-deflection response of the member.

A simplified flow chart illustrating the procedure for establishing the moment-curvature response is provided in Figure 9.6. The results is given in Figure 9.7.

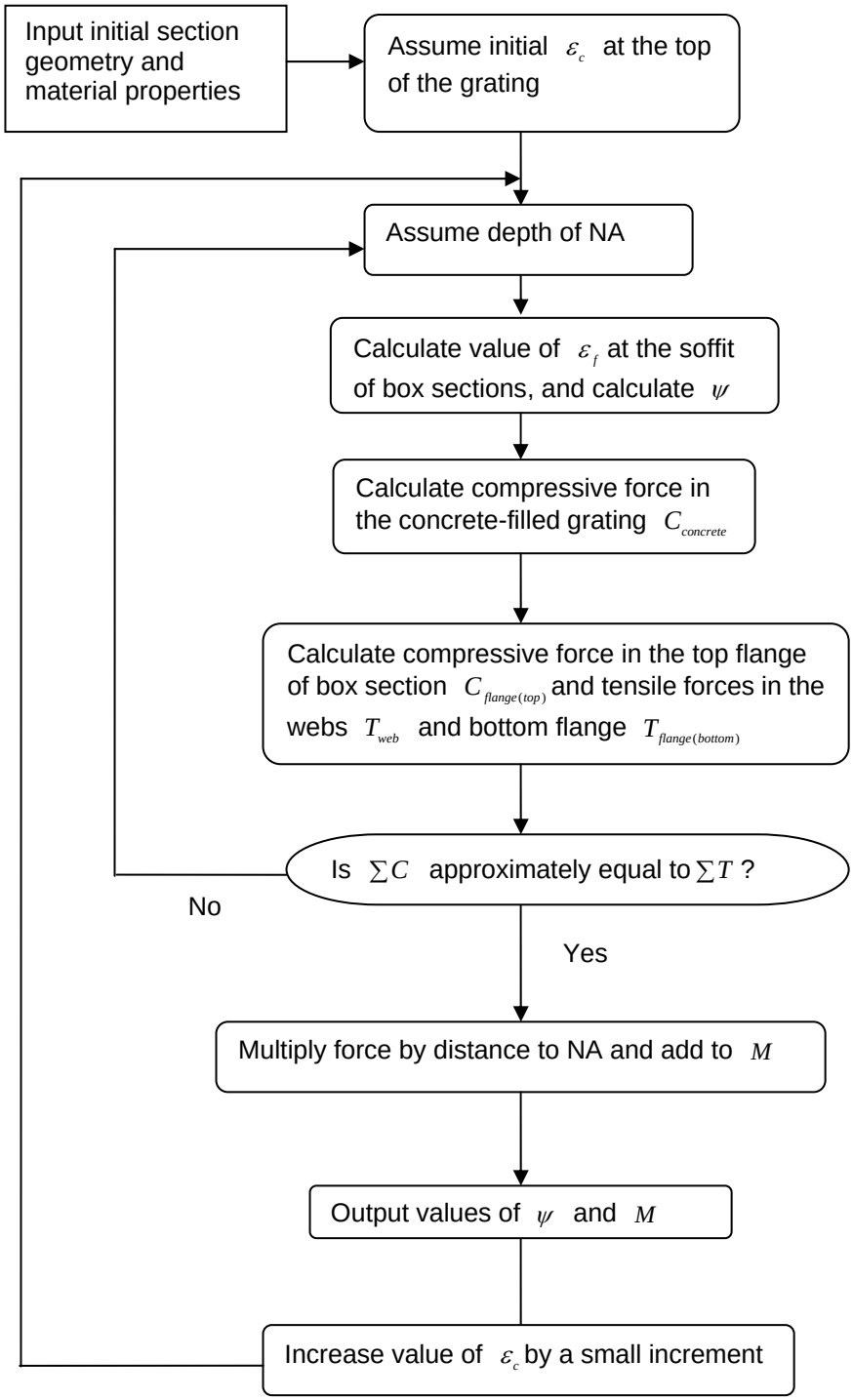

Figure 9.6 – Flow chart illustrating the method used for determining moment-curvature response

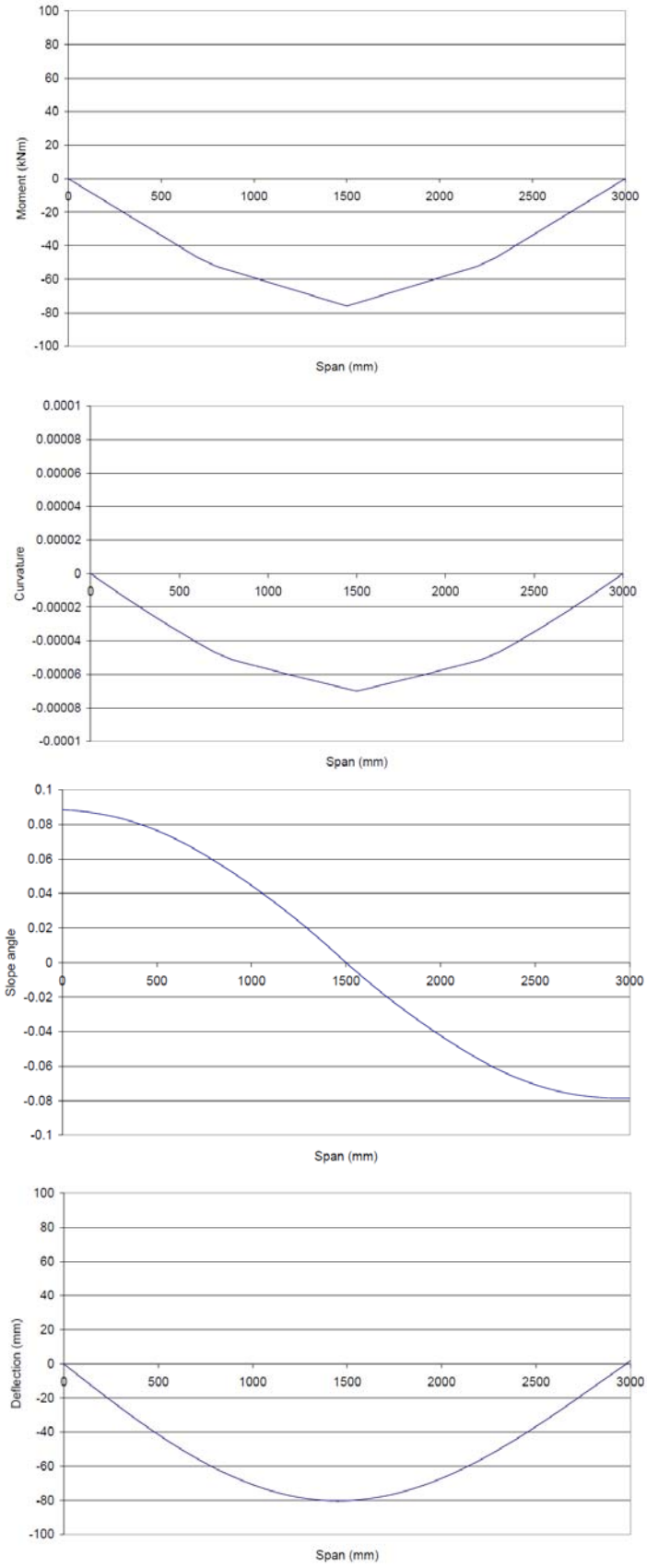

Figure 9.7 – Schematic of the process for determining moment versus deflection response

9.2.6 End of elastic phase

All specimens failed initially due to longitudinal shear, as was expected. Assuming linear elastic full interaction analysis, the longitudinal shear flow at any level in the section can be calculated using:

$$q_{imposed} = \frac{VQ}{I} = \frac{VA_c\bar{y}}{I} \tag{9.1}$$

where V is the vertical shear force experienced by the slab specimen at a given cross section, I is the second moment area of the section about its neutral axis, and Q is the first moment of area of the region above or below the elevation of interest, taken about the neutral axis of the cross-section of the composite section. It should be noted that both I and Q are transformed in accordance with the relative elastic moduli of the materials present in the sections, since the shear flow of interest is at the grating/box-section interface. $\bar{y}$ is taken as the distance between the centroid of the concrete-filled grating and the centroid of the transformed composite section (the whole section transformed with respect to the concrete-filled grating), and A_c is the cross sectional area of the concrete-filled grating. It should be noted that Eq. (9.1) is only valid if the section is elastic. Therefore, an assumption that the whole section is elastic is applied in order to apply Eq. (9.1).

The resistance to shear flow, $q_{resistance}$, is established from the measured load-slip response of concrete studs combined with GFRP dowels, determined from the push-out tests discussed in Chapter 5.

$$q_{resistance} = \frac{P_u N}{a} \tag{9.2}$$

where P_u is the peak strength provided by a single concrete stud with one GFRP dowel. N is the total number of shear connectors along the shear span a.

When the imposed longitudinal shear flow exceeds the resistance to shear flow, indicating the initiation of longitudinal shear failure, the end of the elastic phase is defined from Figure 5.19.

To conclude, the first stage of the model is an 'elastic' analysis. The assumption is made that the composite section behaves fully compositely at this stage with a linear-elastic behaviour of the GFRP box section and a slightly non-linear behaviour of the concrete-filled grating. The criterion limiting the capacity of this stage is the initiation of longitudinal shear failure. The termination point of this 'elastic' phase is established when the maximum shear flow imposed exceeds the shear flow resistance provided by the shear connectors, indicating that longitudinal shear failure has begun. Beyond this point, the stiffness of the specimens reduces, as full composite action is lost and the GFRP dowels begin to resist the shear plastically, leading to some degree of partial interaction at the grating/box-section interface. Consequently, an elastic-plastic analysis has been developed to predict the behaviour for the post 'elastic' phase, and this is presented in Section 9.3.

9.3 Description of Analytical Model for Post Elastic Phase

9.3.1 Oehlers' elastic-plastic analysis

Newmark *et al*. (1951) provided a classical linear elastic partial-interaction analysis of composite beams, however, it only deal with the serviceability limit state, as concrete and steel are all assumed to be elastic. Therefore, it is not suitable for ultimate-strength analysis (Oehlers *et al*, 1995). Oehlers and Sved (1995) developed an analytical approach for an idealised composite beam in which the steel and concrete components remain linear-elastic but the shear connector component (in their case a steel stud) is fully plastic. This procedure is developed for predicting connector fracture by extending Newmark's (1951) linear elastic work, considering the plasticity and the finite ductility of shear connectors. As a first assumption in Oehlers' analytical model, it is assumed here that all the shear connectors are fully 'plastic' throughout the length of the beam. A failure criterion of fracture of shear connectors due to excessive slip is then adopted. The elastic regions near mid-span are ignored, and hence all the shear connectors are fully loaded at their maximum strength P_u with the load-slip characteristic A-B-C defined in Figure 9.8. P_u indicates the peak strength of a single shear connector, S_i indicates the slip when the shear

connector reaches its full plastic capacity, and S_u indicates the ultimate slip at which fracture of the shear connectors occurs (Oehlers and Sved, 1995).

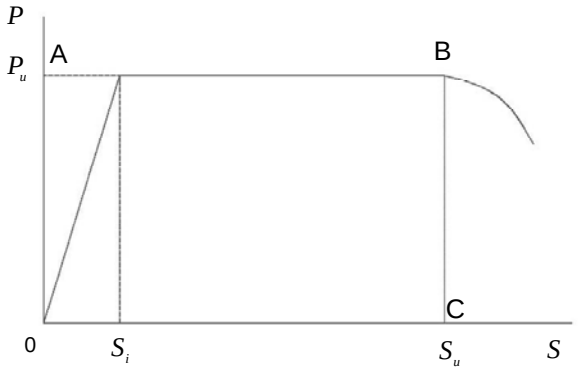

Figure 9.8 – Load versus slip response of steel stud shear connector (Oehlers and Sved, 1995)

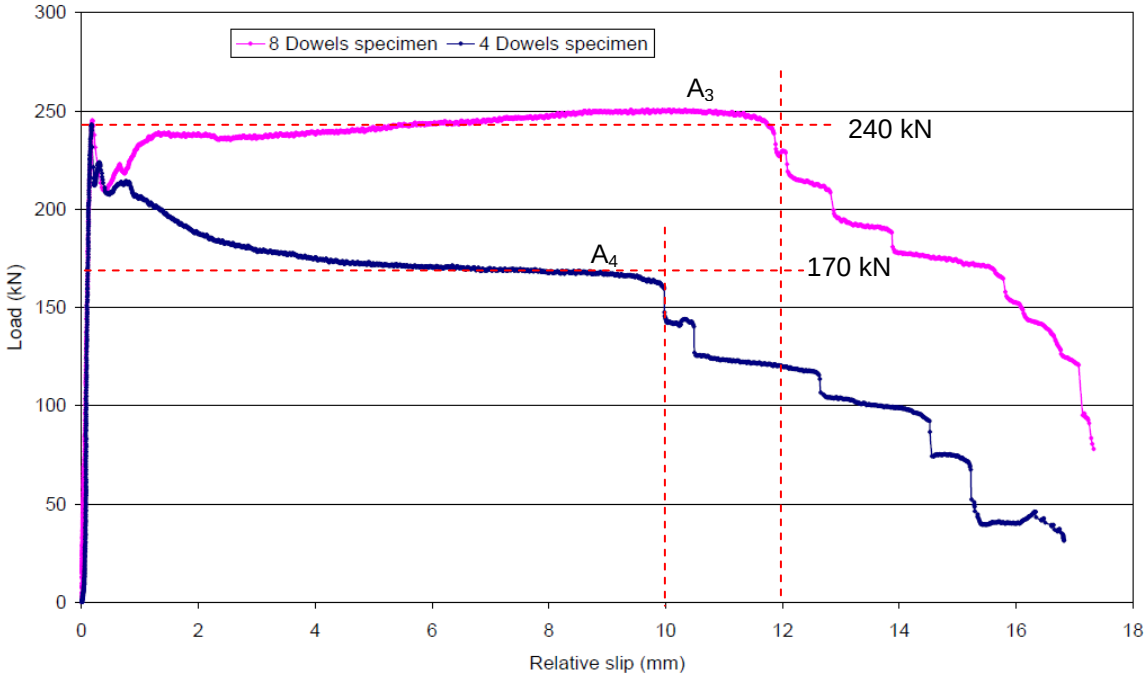

Figure 9.9 – Load versus slip responses of concrete studs combined with GFRP dowels

Figure 9.9 reproduces the load-slip response of concrete studs combined with GFRP dowels from the push-out tests of Chapter 5. The characteristics are similar to that of steel stud shear connectors (Oehlers and Sved, 1995). It is clear that the elastic phase ended at a small amount of slip, approximately 0.2 mm, in comparison with an ultimate slip at 10 mm and 12 mm. Therefore, it seems reasonable to assume a rigid plastic behaviour of such shear connectors. After initial bond slip, a residual strength is provided by the GFRP dowels,

indicated by a ‘plastic’ plateau in the load-slip response. Therefore, the load-slip response of concrete studs combined with GFRP dowels can be simplified in the form shown in Figure 9.8. The ultimate shear resistance is assumed to be identical to the residual load, even though the initial peak load in specimen A_4 (four dowels) was higher than its residual load. The shear resistance, P_u, for each shear connector can be calculated using:

$$P_u = \frac{F_{sh}}{N_{sh}} \tag{9.3}$$

where F_{sh} is the residual load determined from push-out testing. From Figure 9.9, F_{sh} is 240 kN for specimen A_3 and 170 kN for specimen A_4. N_{sh} is the number of shear connectors, and is 16 for A_3 and 8 for A_4.

According to this approach, the ultimate shear resistance of a single shear connector ranges between 15 kN (A_3) to 21 kN (A_4). It would therefore seem reasonable to use the lower bound value (15 kN) as the ultimate shear resistance of a single shear connector in the analysis. S_u is the ultimate slip of the shear connector before fracture occurs, determined, again, from the load-slip response in Figure 9.9, taken as 10 mm.

Once the load versus slip response of the proposed shear connectors has been developed, similar to that of steel stud shear connectors, the assumption for Oehlers’ analysis is applied to the GFRP-concrete composite system in this study. In order to apply Oehler’s analysis, the following assumptions are made. The GFRP box sections and concrete-filled grating are assumed to be linear-elastic throughout the length of the beam and the shear connectors are fully stressed throughout, where P_{sh} is the strength of the shear connectors along the shear span a being considered. These assumptions are shown diagrammatically in Figure 9.10.

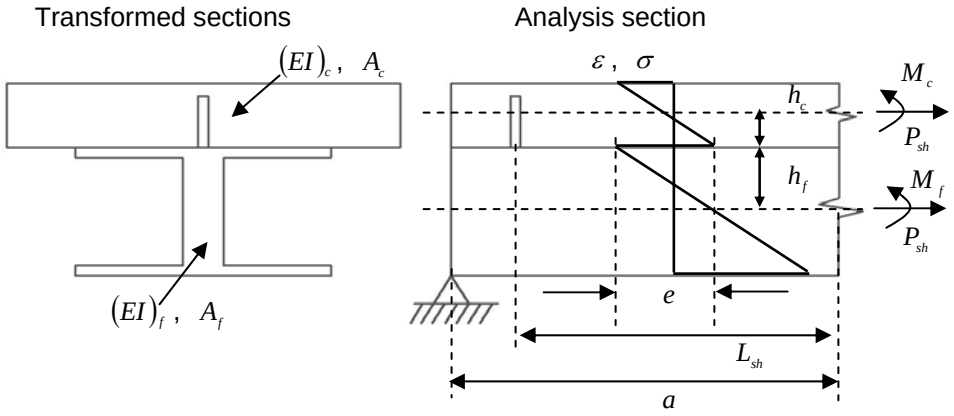

Figure 9.10 – Analysis of GFRP-Concrete composite slab

As is normal practice in concrete composite-beam analysis, it will be assumed that the connectors prevent vertical separation at the grating/box-section interface so that the curvatures in both elements are the same. Based on these assumptions, the following relationship is obtained:

$$\frac{M_c}{(EI)_c} = \frac{M_f}{(EI)_f} = \psi \tag{9.4}$$

where M_c is moment in the concrete-filled grating, M_f is moment in the GFRP box sections, $(EI)_c$ is flexural stiffness of the concrete-filled grating, $(EI)_f$ is flexural stiffness of GFRP box sections, and ψ is curvature of the composite slab specimen.

Furthermore, based on Newmark's linear elastic theory, the moment of resistance can be calculated by resolving the forces (see Figure 9.11) into 'non-interaction' components, and the balance of the forces at the neutral axes.

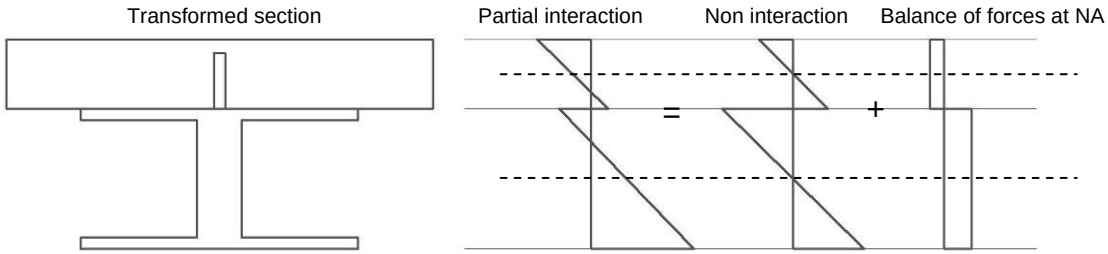

Figure 9.11 – Strain distribution for partial interaction

$$M = M_c + M_f + P_{sh}(h_c + h_f) \tag{9.5}$$

where h_c is distance from centroid of the concrete-filled grating to the grating/box-section interface (see Figure 9.10), h_f is distance from centroid of the GFRP box sections to the grating/box-section interface, and M is applied moment at the section. P_{sh} is balanced force at neutral axis.

Considering compatibility, the strain difference at the grating/box-section interface is given by:

$$e = \frac{ds}{dx} = (h_c\psi - \frac{P_{sh}}{(EA)_c}) + (h_f\psi - \frac{P_{sh}}{(EA)_f}) \tag{9.6}$$

where $(EA)_c$ is axial rigidity of the concrete-filled grating, and $(EA)_f$ is axial rigidity of the GFRP box sections. $\frac{ds}{dx}$ is the strain difference at the grating/box-section interface, where S (the slip) is defined as the displacement in the horizontal direction of a point at the grating soffit relative to the top flange of the box section.

Substituting Eq. (9.4) into Eq. (9.5) gives the following equation for curvature ψ:

$$\psi = \frac{M - P_{sh}(h_c + h_f)}{(EI)_c + (EI)_f} \tag{9.7}$$

Consider the case of a simply supported beam with a single connector in each shear span at a distance L_{sh} from the section being considered. This model is shown in Figure 9.10. The analysis section is chosen to coincide with the section of zero connector slip, which is at a distance a from the support. However, P_{sh} is now modelled as an equivalent force on a single connector, and hence the axial force on the slab is constant between the connector and the section being considered. Substituting Eq. (9.7) into Eq. (9.6) gives the following:

$$\frac{ds}{dx} = M \cdot \frac{(h_c + h_f)}{(EI)_c + (EI)_f} - P_{sh} \cdot \left[\frac{(h_c + h_f)^2}{(EI)_c + (EI)_f} + (\frac{1}{(EA)_c} + \frac{1}{(EA)_f}) \right] \tag{9.8}$$

Re-written, Eq. (9.8) is:

$$\frac{ds}{dx} = M \cdot C_1 - P_{sh} \cdot C_2 \tag{9.9}$$

where

$$C_1 = \frac{(h_c + h_f)}{(EI)_c + (EI)_f} \tag{9.9a}$$

$$C_2 = \frac{(h_c + h_f)^2}{(EI)_c + (EI)_f} + \left(\frac{1}{(EA)_c} + \frac{1}{(EA)_f} \right) \tag{9.9b}$$

C_1 and C_2 are therefore two coefficients, dependent on the geometry of the composite section and independent of x, the position along the beam.

Integrating from the supports (position of maximum slip) to the centre of the beam (position of zero slip) gives:

$$S = C_1 \int_0^{L/2} M dx - C_2 P_{sh} L_{sh} \tag{9.10}$$

where $L/2$ is the half-span length. The integral in Eq. (9.10) is the area under the moment diagram between the position of zero slip and where the slip is being calculated, which is at its maximum at the support. The first term in Eq. (9.10) is the slip when the beam has no shear connectors. In the second term, $C_2 P_{sh} L_{sh}$, the product $P_{sh} L_{sh}$ is the area of the longitudinal thrust diagram between the position of zero slip and where the slip is being calculated. The second term, $C_2 P_{sh} L_{sh}$, is the beneficial effect of the reduction in slip due to the residual resistance provided by the shear connectors (Ohelers and Sved, 1995).

9.3.2 Application of elastic-plastic analysis under five-point bending

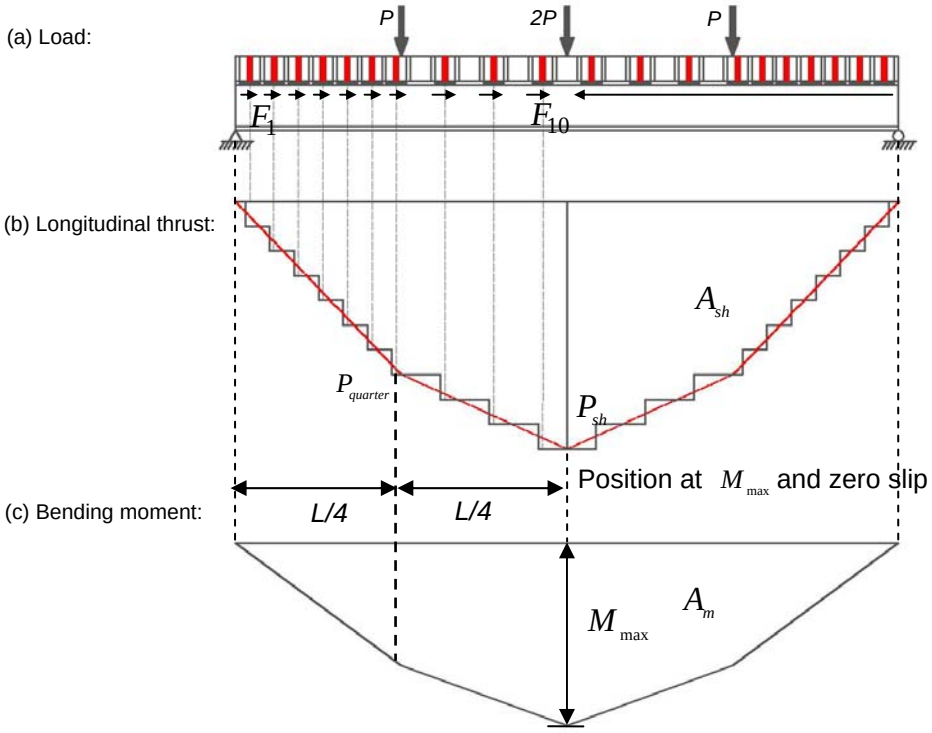

Figure 9.12 – Five point bending and variable connector distribution

Eq. (9.10) can be re-written in the following terms that apply to all loading configurations and shear-connector distributions:

$$S = A_m C_1 - A_{sh} C_2 \tag{9.11}$$

where A_m is the area of the moment diagram and A_{sh} is the area of the longitudinal thrust diagram.

The area-parameters A_m and A_{sh} in Eq. (9.11) are shown diagrammatically in Figure 9.12 for specimens S_2, S_3, S_4 and S_5 under Type B loading in this study.

Considering the case of a simply supported slab specimen of span L with a point load of $2P$ at mid-span, and a point load of P on each quarter span, the applied moment is given by the equation:

$$M_{\max} = \frac{3}{4} PL \tag{9.12}$$

This can be rearranged to give: $PL = \frac{4}{3} M_{\max}$ (9.13)

Integrating the moment diagram as shown in Figure 9.12, gives the following:

$$A_m = \int_0^{L/2} M dx = \frac{7}{32} PL^2 \tag{9.14}$$

Substituting Eq. (9.13) into Eq. (9.14):

$$A_m = \frac{7}{24} M_{\max} L \tag{9.15}$$

Based on the assumption that the shear connectors have reached their residual capacity, the connectors impose a thrust on the concrete component which is zero at the supports and accumulates along the length of the shear span, reaching a total thrust of P_{sh} at the position of the maximum bending moment. Considering the case of specimen S_2 with a non-uniform distribution of shear connectors, the longitudinal shear thrust between the end support and the quarter span, $P_{quarter}$,is calculated as the product of the residual strength of a single shear connector P_u (15 kN) with the 14 shear connectors between the end support and the quarter span in specimen S_2. The overall longitudinal shear thrust between the end support and the mid-span, P_{sh} , is calculated as the product of the residual strength of a single shear connector P_u (15 kN) with the 22 shear connectors between the end support and the mid-span in specimen S_2. Therefore, the area of the longitudinal shear thrust diagram from the end support to the mid-span, A_{sh} , is the sum of the area between the end support and the quarter span and the area between the quarter span and the mid-span, which is found to be :

$$A_{sh} = \frac{25}{88} P_{sh} L \tag{9.16}$$

Therefore, the maximum slip under Type B loading can be calculated by substituting Eq. (9.15) and Eq. (9.16) in to Eq. (9.11) and gives the following:

$$S = C_1 \frac{7}{24} M_{\max} L - C_2 \frac{25}{88} P_{sh} L \tag{9.17}$$

Given the limit on slip which causes fracture of the shear connectors, as seen in Figure 9.9, Eq. (9.17) can be re-arranged to give the corresponding maximum moment:

$$M_{\max} = \frac{24}{7LC_1}(S + C_2 \frac{25}{88} P_{sh} L) \tag{9.18}$$

Using the same procedure as described above, for Type A loading, considering the case of specimen S_1, the maximum slip can be calculated by Eq. (9.11) and gives the following:

$$S = C_1 \frac{5}{16} M_{\max} L - C_2 \frac{147}{456} P_{sh} L \tag{9.19}$$

which can be re-arranged to give the following maximum moment, limited by maximum slip:

$$M_{\max} = \frac{16}{5LC_1}(S + C_2 \frac{147}{456} P_{sh} L) \tag{9.20}$$

Once the coefficients C_1 and C_2 are calculated, based on the sectional geometry of composite sections, the maximum moment due to fracture of shear connectors is given by Eq. (9.18) for Type B loading and Eq. (9.20) for Type A. When the maximum moment $M_{\max}$ and shear strength of shear connectors P_{sh} are calculated, the corresponding curvature ψ is calculated from Eq. (9.7). Therefore, a second termination point can be plotted when shear connectors reach their ultimate slip, which is considered to be failure of this elastic-plastic stage.

It should be noted that the analytical model in Section 9.3 was developed before the experiment work has been undertaken. It was found from experiments later that the final failure was caused by the local buckling of box sections prior to failure of shear connectors. Hence, a local buckling analysis of GFRP box sections was developed later to establish the actual failure point.

9.4 Description of Analytical Model for Local Buckling Analysis

9.4.1 Introduction

As reported in Chapter 8 local buckling of GFRP box sections was the governing failure mode for slab specimens observed in the experimental investigation. It appears that this local buckling failure was caused by curvature, rather than by load. Therefore, a deflection limit apparently defines the ultimate behaviour, which is convenient to apply analytically to prevent this sudden and catastrophic failure. Although there is uncertainty in the ultimate failure mode of slab specimens due to lack of understanding on this type failure, local buckling analysis appears to be a more reasonable approach to predict the ultimate failure. However, further work may lead to a more rational model for the observed behaviour which will allow a more definitive value for the ultimate load to be provided. Two buckling models were investigated to obtain this deflection limit. The first one was developed by Kollar (2003), referred to as Kollar's model. The second one was developed by Johnson (1985), referred to as Johnson's model. Descriptions of both models are discussed in sub-section 9.4.2 and 9.4.3:

9.4.2 Kollar's model

Before discussing Kollar's local buckling analysis, the material properties of pultruded GFRP profiles, which are the parameters of the analysis, are discussed. In structural engineering, the in-plane directions are identified as the longitudinal (L), transverse (T), and shear (LT) directions (Bank, 2006). The in-plane constitutive relationship for an orthotropic plate made of a laminate material is given as:

$$\begin{Bmatrix} \varepsilon_L \\ \varepsilon_T \\ \varepsilon_{LT} \end{Bmatrix} = \begin{bmatrix} \frac{1}{E_L} & -\frac{\nu_{LT}}{E_T} & 0 \\ -\frac{\nu_{TL}}{E_L} & 0 & 0 \\ 0 & 0 & \frac{1}{E_T} \end{bmatrix} \begin{Bmatrix} \bar{\sigma}_L \\ \bar{\sigma}_T \\ \bar{\sigma}_{LT} \end{Bmatrix} \tag{9.21}$$

where $\varepsilon_L, \varepsilon_T, \varepsilon_{LT}$ are the in-plane strains in the plate and $\bar{\sigma}_L, \bar{\sigma}_T, \bar{\sigma}_{LT}$ are the average in-plane stresses in the plate in the longitudinal (L), transverse (T), and shear (LT) directions, respectively.

Conventional pultruded GFRP profiles are especially susceptible to local buckling due to the low in-plane modulus and the inplane slenderness (width-to-thickness ratio) of the walls. It is because the strength-to-stiffness ratios of FRP are relatively bigger than for an isotropic material. Local buckling in compression flanges of beams has been demonstrated in numerous tests (e.g. Barbero *et al*., 1991; Bank *et al*., 1994; 1996), as previously discussed in Chapter 2.

Local buckling analysis of thin-walled profiles is generally performed by modeling the wall segments as orthotropic plates and by assuming that edges common to two or more plates remain straight. The buckling load can then be determined 'exactly' by assuming that all the wall segments buckle simultaneously and that the continuity conditions at the plate intersections are satisfied (Bulson, 1955). The buckling load can also be determined approximately by considering the wall segments as individual plates, which are elastically restrained by the adjacent walls (Bleich, 1952). An approximate method to obtain closed-formed equations for the buckling load, for free and rotationally restrained orthotropic plates, has been proposed by Kollar (2002). Kollar (2003) subsequently extended this work to give closed-form equations for buckling of many different thin-wall sections with orthotropic walls, using his equations together with existing equations in the literature for other boundary conditions. Kollar's closed form equation show very good agreement with finite element analyses and tests on conventional pultruded profiles, and reduce to well-known solutions in the literature for plates with special properties. Kollar's method has the ability to distinguish between flange buckling in beams subjected to transverse load (flexure) and flange buckling in columns subjected to axial loads (pure compression) since the web restraint is given as a function of the end conditions of the restraining plate, following the procedure presented by Bleich (1952). Kollar's method also allows the user to determine, a priori, whether flange buckling or web buckling controls the design based on the slenderness ratios of the flange and web of the sections. Kollar has presented

results for doubly symmetric I- and box-shaped profiles and singly symmetric single-leg-angle-, channel-, and Z-shaped sections (Bank, 2006).

To use Kollar's method, first the buckling stresses of the walls (compression flange and webs) are found, assuming that they are simply supported at their restrained edges. These buckling stresses are then used to determine whether the compression flange or webs buckle first, and the coefficient of edge restraint for the critical wall determined by taking account of the rotational stiffness of the junction. The final solution for the buckling stress for the restrained wall is then given by a closed-form equation that includes the coefficient of edge restraint, ζ, of the critical wall. More details on the derivation of equations are presented in Kollar (2002, 2003). Two types of simply supported walls for pultruded box sections are needed for the first part of the solution.

1. To determine the critical stress in the flange of a box section. It is assumed that the flange is simply supported along both edges under uniform compressive stress. It is given in terms of the flexural rigidities of the flange as

$$(\sigma_{ss}^{ss})_f = \frac{2\pi^2}{t_f b_f^2}(\sqrt{D_L D_T} + D_{LT} + 2D_s) \tag{9.22}$$

where, t_f is the flange thickness, b_f is the width of box section, D_L, D_T , D_{LT}, and D_S are the longitudinal, transverse, coupling, and shear flexural rigidity of the orthotropic plate (the equivalents of EI per unit width for a beam), which are given by:

$$D_L = \frac{E_L t_p^3}{12(1-\nu_L \nu_T)} \tag{9.23a}$$

$$D_T = \frac{E_T t_p^3}{12(1-\nu_L \nu_T)} \tag{9.23b}$$

$$D_{LT} = \frac{\nu_T E_L t_p^3}{12(1-\nu_L \nu_T)} = \frac{\nu_L E_T t_p^3}{12(1-\nu_L \nu_T)} \tag{9.23c}$$

$$D_S = \frac{G_{LT} t_p^3}{12} \tag{9.23d}$$

where E_L is the longitudinal modulus of an orthotropic plate, E_T is the transverse modulus of an orthotropic plate, ν_L is the major Poisson ratio, and ν_T is the minor Poisson ratio, G_{LT} is the in-plane shear modulus.

The flexural rigidities relate the plate bending moments (per unit length) to the plate curvatures and are measured in units of force times length. In classical texts on orthotropic plate behaviour, the equations of state are written in terms of plate flexural rigidities (e.g., Timoshenko and Woinowsky-krieger, 1959), and this notation is often used in analytical equations for pultruded profiles (Bank, 2006).

The length of the buckle half-wavelength for this mode is given by:

$$(a_{ss}^{ss})_f = b_f \sqrt[4]{\frac{E_L}{E_T}} \tag{9.24}$$

2. To determine the critical stress in the web of a box section, it is assumed that the web is simply supported along both edges under linearly varying compressive stress. It is given in terms of the flexural rigidities of the web as:

$$(\sigma_{ss}^{ss})_w = \frac{\pi^2}{t_w d_w^{\,2}}(13.9\sqrt{D_L D_T} + 11.1 D_{LT} + 22.2 D_s) \tag{9.25}$$

where t_w is the thickness of the web and d_w is the depth of the web. The length of the buckle half-wavelength for this mode is given by:

$$(a_{ss}^{ss})_f = 0.707 d_w \sqrt[4]{\frac{E_L}{E_T}} \tag{9.26}$$

As a first step, the compression flange and webs are considered to be simply supported and the critical buckling stress for each wall segment is calculated using Eq. (9.22) and (9.25) respectively. However, in reality, these walls are rotationally restrained by adjacent wall segments. Therefore, a non-dimensional coefficient known as the coefficient of restraint (Bleich, 1952), ζ, is defined to account for the combined effect of the rotational stiffness of the junction itself and the plate geometric and mechanical properties on the critical buckling stress. It is defined as:

$$\zeta = \frac{D_T}{kL_T} \tag{9.27}$$

where k is the rotational stiffness of the junction between the walls, and L_T and D_T are the width and flexural rigidity of the plate perpendicular to the edge being restrained (i.e., in the transverse direction of the orthotropic plate, hence the subscript T).

The next step is to determine whether it is the compression flange or webs which buckle first by comparing the critical strain in these wall segments. The wall segment with the lowest critical strain is considered further, because the wall segment (web or compression flange) in which the axial strain is the lowest is most susceptible to buckling. Then, the critical buckling stress of the wall segment is calculated by treating it as a plate rotationally restrained by the adjoining wall segments.

If $(\sigma_{ss}^{ss})_f/(E_L)_f < (\sigma_{ss}^{ss})_w/(E_L)_w$, the compression flange will buckle before one of the webs. For a box section, the compression flange is restrained by two webs, one on either longitudinal edge of the flange. The spring constant, which depends on the adjacent (restraining) wall segment, is given as

$$k_{box-flange} = \frac{4(D_T)_w}{d_w}\left[1 - \frac{(\sigma_{ss}^{ss})_f (E_L)_w}{(\sigma_{ss}^{ss})_w (E_L)_f}\right] \tag{9.28}$$

The local buckling stress for the rotationally restrained flange is given in terms of the properties of the flange as

$$\sigma_{cr}^{local,box-flange} = \frac{\pi^2}{b_f^{\,2} t_f}\left[2\sqrt{(D_L D_T)(1 + 4.139\xi_{box-flange})} + (D_{LT} + 2D_s)(2 + 0.62\xi_{box-flange}^{\,2})\right] \tag{9.29}$$

where $$\xi_{box-flange} = \frac{1}{1+10\zeta_{box-flange}} = \frac{1}{1+10[(D)_T / k_{box-flange} b_f]} \tag{9.30}$$

The critical bending moment for compression flange buckling for a homogeneous box section for bending about the major axis is given as

$$M_{cr}^{local,box-flange} = \sigma_{cr}^{local,box-flange} \frac{2I_x}{d} \tag{9.31}$$

The buckle half-wavelength, a, for this case is given in terms of the properties of the flange as (Kollar and Springer, 2003)

$$a_{box-flange} = b_f \sqrt[4]{\left(\frac{1}{1+4.139\xi_{box-flange}}\right)\frac{D_L}{D_T}} \tag{9.32}$$

If $(\sigma_{ss}^{ss})_f/(E_L)_f > (\sigma_{ss}^{ss})_w/(E_L)_w$, the webs will buckle before the flange. A closed-form expression to predict the buckling stress of the web when restrained by the compression and tension flanges and loaded with a linearly varying axial stress is not currently available in the literature. Equation (9.25), for a web simply supported on its two edges, can be used as a conservative approximation (i.e. $(\sigma_{ss})_w = \sigma_{cr}^{local,box-web}$). For conventional pultruded GFRP square box sections, the flange will buckle before the web. Only in the case of rectangular box sections with large depth-to-width ratios (>2) will the web possibly buckle before the flange (Bank *et al*, 2006).

The critical bending moment for local web buckling for a homogeneous box section bent about the major axis is given as

$$M_{cr}^{local,box-web} = \sigma_{cr}^{local,box-web}\frac{2I_x}{d-2t_f} \tag{9.33}$$

Presented in Table 9.3 are typical mechanical properties for the 100 x 100 x 8 mm box section. The longitudinal elastic modulus (E_L) is found to be 32.1 GPa, determined from the coupon tests, as coupon test data is more appropriate to use than manufacturer's design data. However, due to limitations in testing machinery, coupon test results for determining material properties in other directions are not available. Manufacturer's design data was, therefore, used for transverse, shear elastic modulus and Poisson ratios in the analysis. Table 9.4 gives the calculation using Kollar's model.

Table 9.3 – Typical material properties for pultruded GFRP box sections

Description	Symbol	Value
Longitudinal modulus (MPa)	E_L	32100
Transverse modulus (MPa)	E_T	8500
Shear modulus (MPa)	G_{LT}	3000
Major Poisson's ratio	ν_L	0.23
Minor Poisson's ratio	ν_T	0.09
Plate thickness (mm)	t	8
Box section width (mm)	b	100
Box section depth (mm)	d	100
Span of the slab specimen (mm)	L	2900
Tensile strength (N/mm^2)	$\sigma_{t_{\max}}$	355

Table 9.4 – Data for Kollar's buckling analysis by Eqs. (9.22) to (9.35)

Description	Symbol	Value	Equation
Longitudinal flexural rigidity (Nmm)	D_L	1.40x10^6	(9.23a)
Transverse flexural rigidity (Nmm)	D_T	3.70x10^5	(9.23b)
Coupling flexural rigidity (Nmm)	D_{LT}	1.26x10^5	(9.23c)
Shear flexural rigidity (Nmm)	D_s	1.28x10^5	(9.23d)
Critical stress of flange (simply supported) (MPa)	$\left(\sigma_{ss}^{ss}\right)_f$	321	(9.22)
Critical stress of web (simply supported) (MPa)	$\left(\sigma_{ss}^{ss}\right)_w$	2076	(9.25)
Critical stress (flange)/Elastic Modulus (flange)	$\left(\sigma_{ss}^{ss}\right)_f / \left(E_L\right)_f$	0.010	-
Critical stress (web)/Elastic Modulus (web)	$\left(\sigma_{ss}^{ss}\right)_w / \left(E_L\right)_w$	0.065	-
The spring constant	$k_{box-flange}$	1.36x10^4	(9.28)
Coefficient of edge restraint	$\xi_{box-flange}$	0.253	(9.30)
Critical buckling stress of flange (MPa)	$\sigma_{cr}^{local,box-flange}$	414	(9.29)
Critical buckling moment of flange (kNm)	$M_{cr}^{local,box-flange}$	69.5	(9.31)
Mid-span deflection for Type A loading at buckling (mm)	δ_A	196	(9.34)
Mid-span deflection for Type B loading at buckling (mm)	δ_B	183	(9.35)

In Table 9.4, the flexural rigidities D_L, D_T, D_{LT}, and D_S are calculated from Eqs. (9.23a) to (9.23d) based on the material properties given in Table 9.3. The critical buckling stress for the compression flange and webs are calculated from Eqs. (9.22) and (9.25). Then, the critical strain in the compression flange and webs are determined from the critical buckling stress divided by their longitudinal elastic modulus. It is found that the critical strain in the compression flange (0.010) is significantly lower than that in the webs (0.065), indicating that the compression flange will buckle first. The critical buckling stress of the compression flange, rotationally restrained by the webs, was calculated to be

414 MPa, determined from Eq. (9.29). The critical buckling moment (M_{cr}) of the compression flange is calculated to be 69.5 kNm for two box sections, determined from Eq. (9.31), as shown in Table 9.4. As mentioned in Chapter 8, it appears that the local buckling failure was governed by curvature, rather than by load. It appears to be more convenient to convert the critical buckling moment into a deflection limit, which varies with each particular load condition (either Type A or Type B loading).

For Type A loading (moment envelope), assuming fully elastic behaviour of the GFRP sections, the mid-span deflection at buckling is given by:

$$\delta = \frac{20PL^3}{384E_L I_{box\,section}} \tag{9.34}$$

$$P = \frac{2M_{cr}}{L}$$

where P is the point load acting on each quarter span and mid-span, M_{cr} is the critical buckling moment of the compression flange of the box section, E_L is the longitudinal modulus of elasticity of the box section, I_{box} is second moment area of a box section, and L is the span of the slab specimen.

For Type B loading (shear force envelope), assuming fully elastic behaviour of the GFRP sections, the mid-span deflection at buckling is given by:

$$\delta = \frac{28PL^3}{384E_L I_{box\,section}} \tag{9.35}$$

$$P = \frac{4M_{cr}}{3L}$$

The mid-span deflection of slab specimen at buckling is calculated to be 196 mm for Type A loading, and 183 mm for Type B Loading, determined from Eqs. (9.34) and (9.35) respectively, as shown in Table 9.4. Comparisons between the predictions using Kollar's model and the experimental data are discussed in Section 9.5.

9.4.3 Johnson's model

Johnson analysed the failure of fibre reinforced polymer box beams under transverse loads, and developed a simplified analysis method for determining critical bending moments, shear forces and transverse loads for box beams (Johnson, 1985). Later on, Mottram (1991) tested twenty-three specimens to failure in three-point loading, and evaluated the ability of Johnson's analysis to predict the failure load of pultruded box sections. He concluded that for long-span specimens with a span-to-depths ratio above 17.7, Johnson's analysis can predict the ultimate load at failure accurately, providing that a modification is made for specimens with a thick wall thickness (6 mm). However, for short-span specimens with a span-to-depth ratio below 11.9, the analysis is inappropriate because the mode of failure is not in one of the modes assumed in Johnson's analysis (Mottram, 1991). Johnson's simplified buckling analysis is based on the assumption that an FRP box beam is composed of four identical material panels which have orthotropic in-plane material properties and are oriented in the beam such that the stiffness orthotropic axis is parallel with the beam axis. The material of the wall panels is assumed to be perfectly elastic to failure. The beam is simply supported at its ends and loaded by a central load of magnitude P. It spans a length L. The beam has a hollow square cross-section with outer side wall length b and is assumed to have thin walls of uniform thickness t. It is further assumed that the elastic failure of the beam in bending is in any one of five distinct global modes and there is no interaction between the five modes. These failure modes are: compression face buckling; tensile material rupture; compression material rupture; shear material rupture; and shear buckling of the side walls (Mottram, 1991). Applying these assumptions and linear elastic theory it can be shown that predicted ultimate loads in the box beam corresponding to failure in bending P_B and shear P_s are as follows:

$$P_B = \left(\frac{16b^2t}{3L}\right)\varphi\sigma_{\max} \tag{9.36}$$

and,

$$P_S = \frac{8}{3}bt\gamma\tau_{\max} \tag{9.37}$$

In Eq. (9.36) σ_{max} is the material failure stress in either tension $\sigma_{t_{max}}$ or compression $\sigma_{c_{max}}$. The thin-walled compression buckling coefficient, φ, is defined by

$$\varphi = \frac{1}{3}\pi^2 K_1 \left(\frac{t}{b}\right)^2 \left(\frac{E_L}{(1-\nu_L \nu_T)\sigma_{max}}\right) \tag{9.38}$$

where

$$K_1 = \frac{1}{2}\left[\left(\frac{D_T}{D_L}\right)^{0.5} + \left(\frac{D_O}{D_L}\right)\right] \tag{9.39}$$

is an anisotropy factor which depends on the elastic moduli of the wall material.

In Eq. (9.39) D_L, D_T, D_o are the orthotropic plate flexural rigidities. They are defined in terms of the orthotropic elastic constants and wall thickness by:

$$D_L = \frac{E_L t^3}{(1-\nu_L \nu_T)}, D_T = \frac{E_T t^3}{(1-\nu_L \nu_T)} \quad \text{and} \quad D_O = \frac{\nu_T E_L t^3}{(1-\nu_L \nu_T)} + \frac{G_{LT} t^3}{12} \tag{9.40}$$

In the derivation of Eq. (9.38) it is assumed that the edge restraint is simply supported. If the edge restraint approximates to the clamped condition, Eq. (9.38) must be multiplied by 1.75. If, for a specific box profile, φ<1, from Eq. (9.38), bending failure is controlled by compression buckling of the top flange, and Eq. (9.36) gives the ultimate load in bending P_B. When φ>1, the failure in bending is controlled by material strength, and P_B is then given by Eq. (9.36), with φ set to 1.

In Eq. (9.37), τ_{max} is the shear strength of the side wall material. The thin-walled shear buckling coefficient, γ, is defined by

$$\gamma = 6.6 K_2 \left(\frac{t}{b}\right)^2 \left(\frac{E_L}{(1-\nu_L \nu_T)\tau_{max}}\right) \tag{9.41}$$

where

$$K_2 = \left(\frac{D_T}{D_L}\right)^{0.5} \left(\frac{D_O}{D_L}\right)^{0.5} f(\delta) \tag{9.42}$$

δ is given by $\delta = \frac{(D_L D_T)^{0.5}}{D_O}$, and the function $f(\delta)$ is defined as,

$$f(\delta) = \delta^{0.5}(0.62 + \frac{0.38}{\delta}), \delta > 1$$

$$f(\delta) = 0.89 + 0.04\delta + 0.07\delta^2, \delta > 1 \qquad (9.43)$$

In the derivation of Eq. (9.41) the long edges are assumed to be simply supported. If these edge restraints approximate to the clamped condition, Eq. (9.41) for γ must be multiplied by 1.68. If, for a specific box profile, γ<1, from Eq. (9.41), shear failure is controlled by shear buckling of the side walls and Eq. (9.37) gives the shear failure load. When γ>1, the failure in shear is controlled by material strength. P_s is then given by Eq. (9.37), with γ set to 1.

It should be noted that Eqs. (9.36) and (9.37) are derived based on the case of a central point loaded box beam in three-point bending. More details of the derivation of these equations are presented in Johnson (1985). For a beam with length L, simply supported ends, and subjected to a central point load P, the maximum bending moment, M_{cr}, is given by

$$M_{cr} = \frac{P_B L}{4} \qquad (9.44)$$

Table 9.5 – Data for Johnson's local buckling analysis by Eqs. (9.34) to (9.45)

Description	Symbol	Value	Equation
Longitudinal flexural rigidity (Nmm)	D_L	16.8x10^6	(9.40)
Transverse flexural rigidity (Nmm)	D_T	4.44x10^6	(9.40)
Coupling flexural rigidity (Nmm)	D_o	1.64x10^6	(9.40)
Anisotropy factor	K_1	0.306	(9.39)
Buckling coefficient	φ	0.590	(9.38)
Critical buckling load of flange (kN)	P_B	31.1	(9.36)
Critical buckling moment of flange (kNm)	M_{cr}	22.5	(9.44)
Critical buckling stress of flange (MPa)	σ_f	268	(9.45)
Mid-span deflection for type A loading at buckling	δ_A	147	(9.34)
Mid-span deflection for type B loading at buckling	δ_B	137	(9.35)

As can be seen in Table 9.5, the flexural rigidity D_L, D_T and D_o were calculated using Eq.(9.40) based on the material properties given in Table 9.3. The buckling coefficient was calculated to be 0.59 from Eq. (9.38), which is less than

1. Therefore, the failure in bending is controlled by local buckling of the compression flange. The critical buckling load for the compression flange was calculated from Eq. (9.36) to be 31kN. The critical buckling moment for the compression flange was calculated to be 22.5 kNm for each box section, determined from Eq. (9.44). For Type A loading condition, using Eq. (9.34), the critical buckling moment was converted into the mid-span deflection of the specimen at buckling, was calculated to be 147 mm. For Type B loading condition, using Eq. (9.35), the mid-span deflection was calculated to be 137 mm, as shown in Table 9.5. The agreement between the prediction using Johnson's model and experimental data are compared in Section 9.5.

As described in Section 9.4.2, the pultruded GFRP box sections are assumed to consist of four identical orthotropic plates and each wall segment is assumed to be perfectly elastic to failure. This is a key assumption made in Kollar's and Johnson's model. In Kollar's model, the compression flange, which is susceptible to local buckling, is considered to be rotationally restrained by the adjacent webs, and a coefficient of edge restraint is introduced by taking account of the rotation stiffness at the junctions. The critical buckling stress of the flange is calculated to be 414 MPa. However, in Johnson's model, the edge condition of the buckling plate is considered to be simply supported with no edge restraint. The critical stress in the flange at buckling is calculated to be 268 MPa using the follow equation:

$$\sigma_f = \frac{M_{cr}\,\bar{y}}{I} \tag{9.45}$$

Johnson's prediction is 35.3% below Kollar's prediction. While by comparing the critical buckling stress of the flange, where the edge condition is simply-supported, Johnson's prediction (268MPa) is 16.5% below Kollar's prediction (321 MPa). Evaluations of two buckling modes by comparison with experimental results are discussed in the following sections.

9.5 Validation of Analytical Model

9.5.1 Comparison between experimental results and predictions

The aforementioned three-stage analytical model has been developed to predict the full behaviour of slab specimens. The analytical model begins with a linear-elastic analysis to predict the moment at which debonding occurs, followed by an elastic-plastic analysis to predict the moment when shear connectors fracture after a certain amount of slip. Failure is governed by a deflection limit calculated using two different buckling analyses. One is based on Kollar's model, referred to as 'deflection criterion K', and the other based on Johnson's model, referred to as 'deflection criterion J'.

Figure 9.13 shows a moment-deflection response of the analytical prediction against experiment result for specimen S_4. Linear-elastic analysis predicts the elastic behaviour up to the elastic limit, defined by 'point A' in Figure 9.13. Based on Oehler's elastic-plastic analysis, the second termination point is established by assuming a fixed amount of longitudinal shear resistance, provided by the GFRP dowels coupled with the post-cracked restrained shear resistance of the concrete-to-concrete interface, with a failure criterion defined by fracture of shear connectors after a certain amount of slip. The limitation of this model is that it only predicts a failure point, defined by 'point B' in Figure 9.13. The actual behaviour between point A and B is unknown, and a linear response is assumed between these points. It can be seen from Figure 9.13 that point B significantly overestimates the failure moment when compared against experimental results. This is because the final failure, in reality, was caused by local buckling of the box sections, rather than by fracture of shear connectors, as assumed in the model. As mentioned earlier, deflection defined by curvature is the governing factor for buckling failure. Two deflection criteria K and J were incorporated into the analytical model. The intersection between line AB and deflection criterion K is referred to as 'point C', and intersection between line AB and deflection criterion J is referred to as 'point D'.

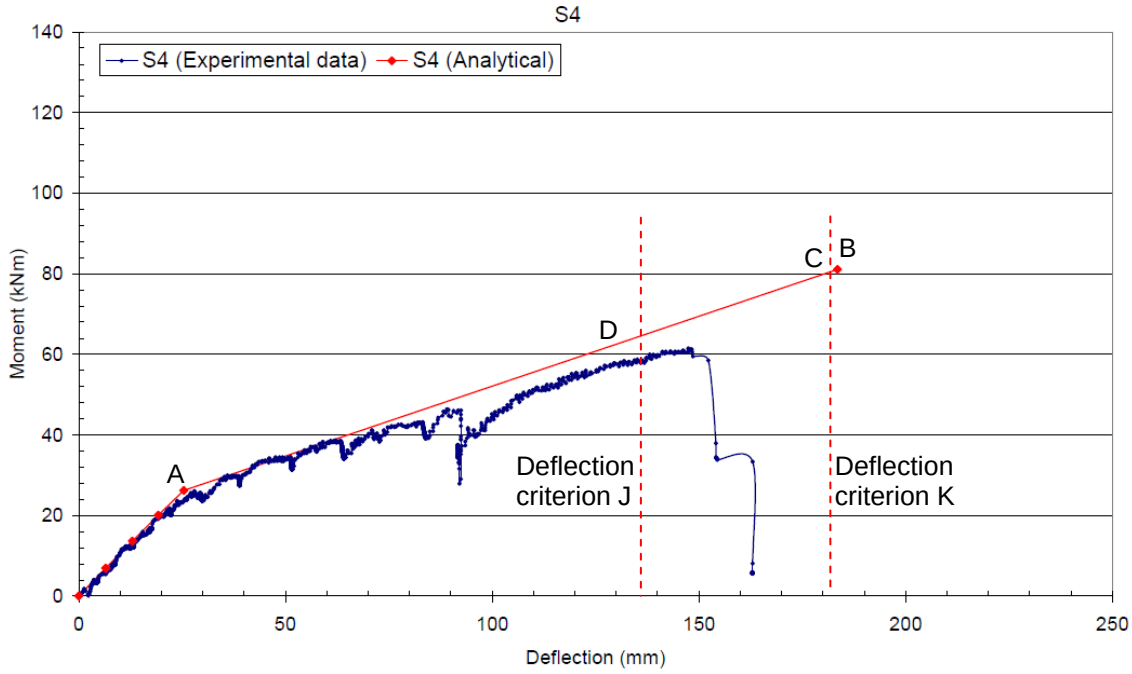

Figure 9.13 – Experimental result versus analytical prediction plot (specimen S_4)

The experimental moment-deflection responses and analytical predictions for the six specimens are compared in Figures 9.14 to 9.19. For specimens S_1 to S_3, in Figures 9.14 to 9.16 it can be seen that the first termination point predicted by 'elastic' analysis, assuming a failure criterion due to longitudinal shear failure at the grating/box-section interface, matches well with the moment at the onset of debonding failure in the moment-deflection responses, although the moment at the onset of debonding failure is underestimated by 23.5% in specimen S_3. This might be caused by the assumption made in the simplified load-slip response of shear connectors (see Figure 9.8). In the model, the ultimate shear strength of the shear connectors was assumed to be equal to their residual strength, maintained until failure. However, it can be seen from Figure 9.9 that there was a significant peak prior to the drop off to 70 kN post peak residual strength in specimen A_4. This may explain why the 'elastic' analysis slightly underestimates the moment at the onset of debonding failure of specimen S_3.

It is evident from Figures 9.14 to 9.16 that deflection criterion K tends to overestimate deflection at final failure by 14 percent for specimen S_1, 23 percent for specimen S_2, and 34 percent for specimen S_3. However, deflection criterion J tends to underestimate deflection at final failure by 14 percent for specimen S_1, 7 percent for specimen S_2, and 0 percent for specimen S_3. Therefore, deflection

criterion J seems more reliable, and, generally, conservative compared with deflection criterion K. The discrepancy with regard to final failure moment between the analytical prediction and the experimental results is attributed to an assumption made in the elastic-plastic analysis that all the GFRP dowels contribute to the longitudinal shear resistance at the grating/box-section interface. It was however found that some of the GFRP dowels did not contribute fully to resisting the longitudinal shear due to the poor concrete-fill in the box sections, as discussed in Chapter 8. This could explain why the slope of the line between points A and B is stiffer compared with the actual slope of experimental data in specimens S_1 to S_3. This is examined further in Section 9.5.2.

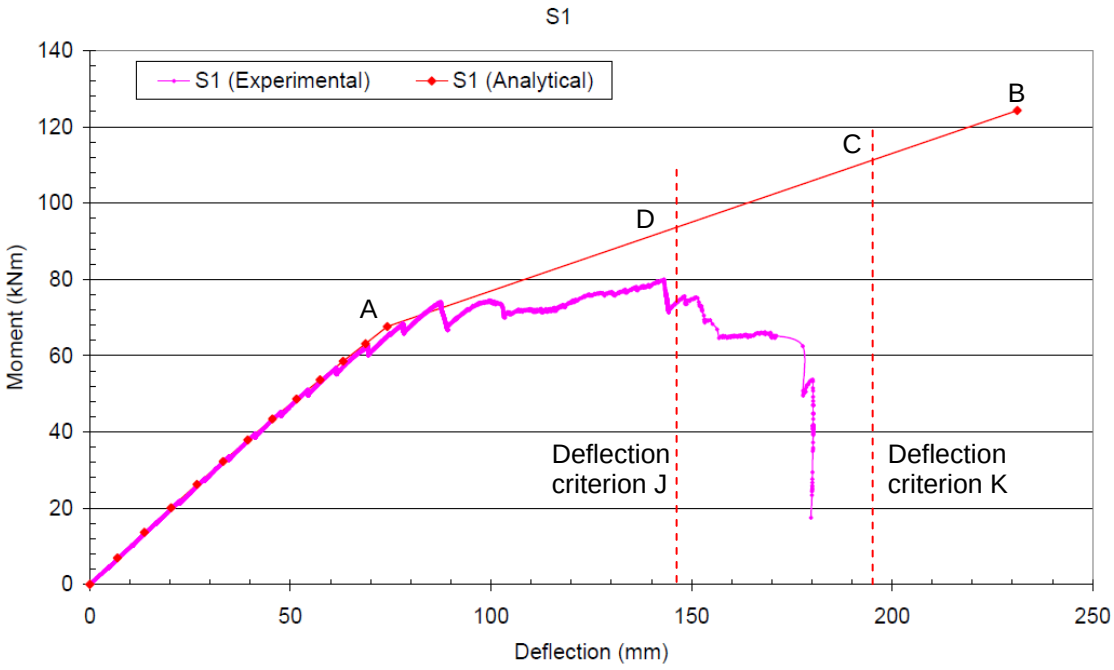

Figure 9.14 – Experimental versus predicted moment-deflection responses of Specimen S_1

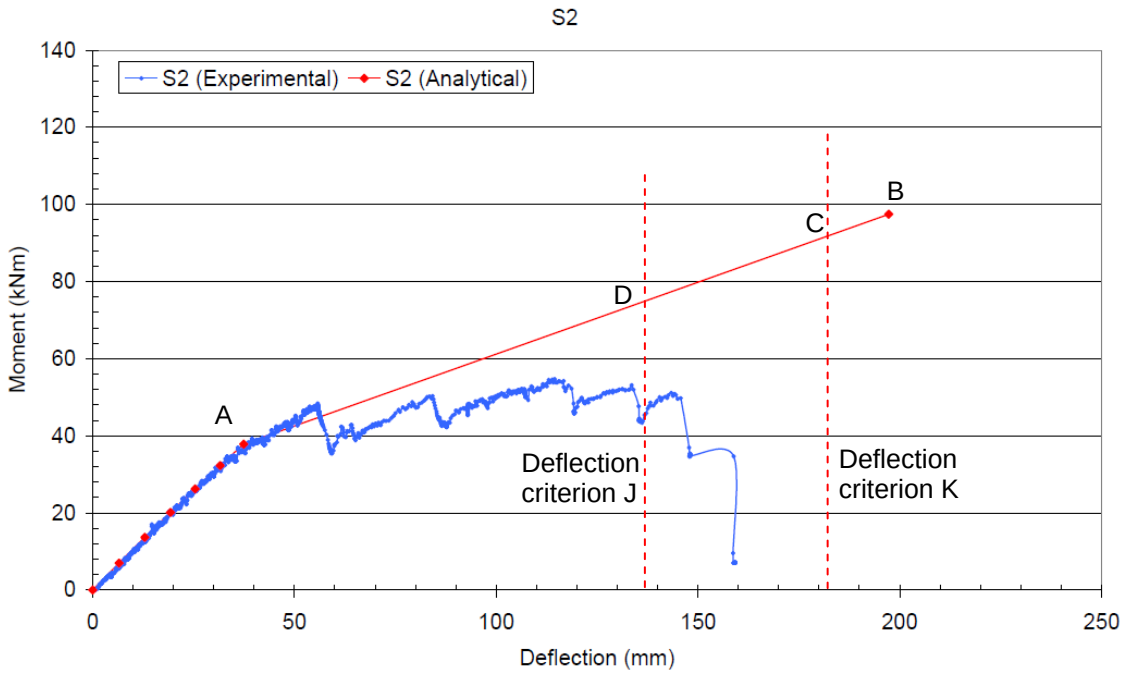

Figure 9.15 – Experimental versus predicted moment-deflection responses of Specimen S_2

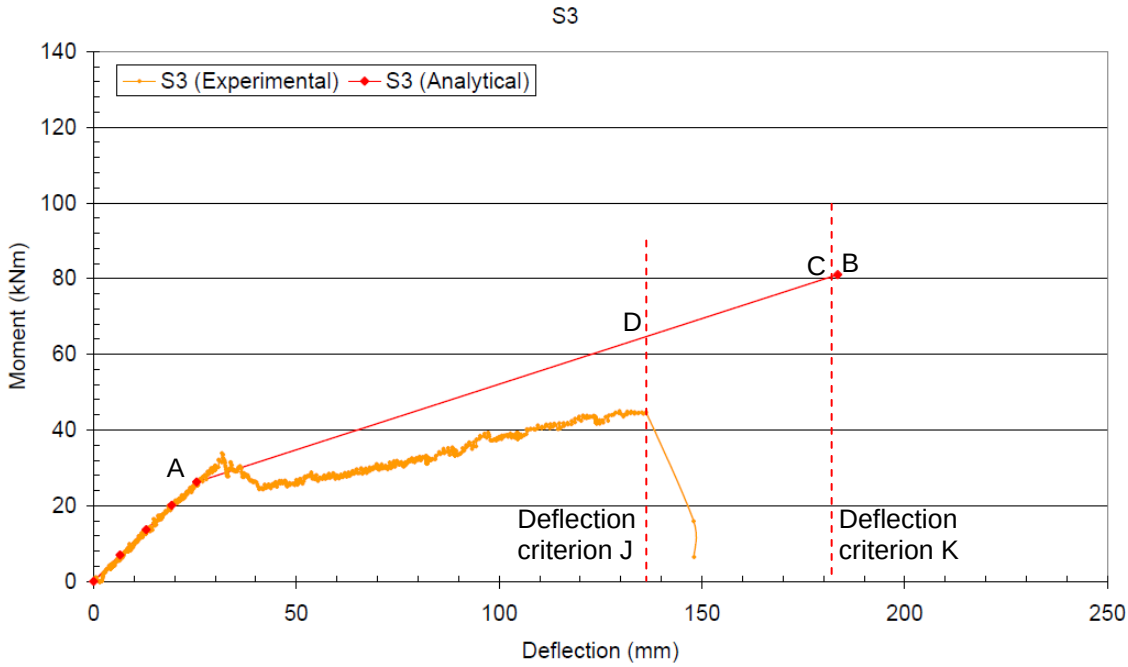

Figure 9.16 – Experimental versus predicted moment-deflection responses of Specimen S_3

Figures 9.17 and 9.18 show the experimental moment-deflection responses and the analytical predictions for specimens S_4 and S_6. The analytical model provides a good estimate of the moment at the elastic limit, and the reduced stiffness after the elastic limit, represented by line AB, correlates well with experimental results. It is clear that deflection criterion J underestimates deflection at final failure by 9 percent for specimen S_4, and 15 percent for specimen S_6. Deflection criterion K overestimated deflection by 22 percent for

specimen S_4 and 14 percent for specimen S_6. It is apparent that deflection criterion J from Johnson's model is more reliable than deflection predicted by Kollar's model. Deflection criterion J appears to be appropriate to use in the prediction of the vertical deflection for failure by local buckling.

Figure 9.19 shows the comparison between the moment-deflection response and the analytical prediction for specimen S_5. It is seen that the analytical prediction significantly overestimates the moment at the onset of debonding failure. This is because the load-slip model of shear connector, applied in the elastic analysis, was developed from the experimental results of specimens with one dowel in each concrete stud. However, this is not the case in specimen S_5, which has additional concrete studs without dowelling. A more relevant load-slip model for the shear connector, considering the effect of having additional concrete studs, can be obtained from the Hofbeck tests described in Chapter 5. This will be applied in the analytical model to give a more reasonable prediction in Section 9.5.3.

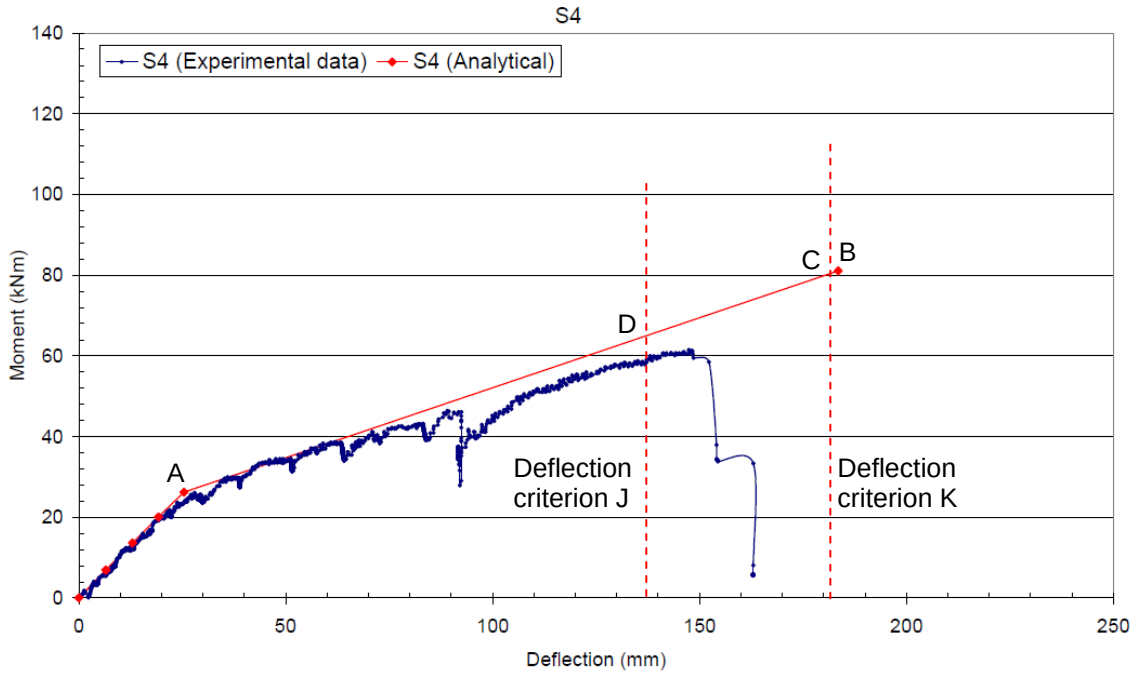

Figure 9.17 – Experimental versus predicted moment-deflection responses of Specimen S_4

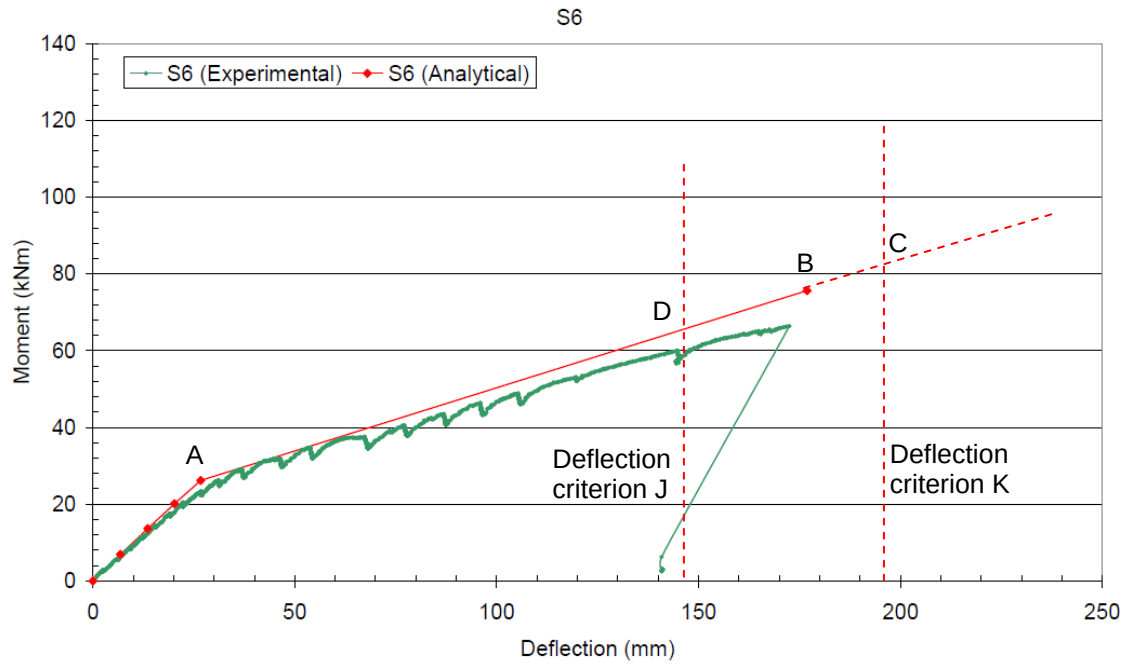

Figure 9.18 – Experimental versus predicted moment-deflection responses of Specimen S_6

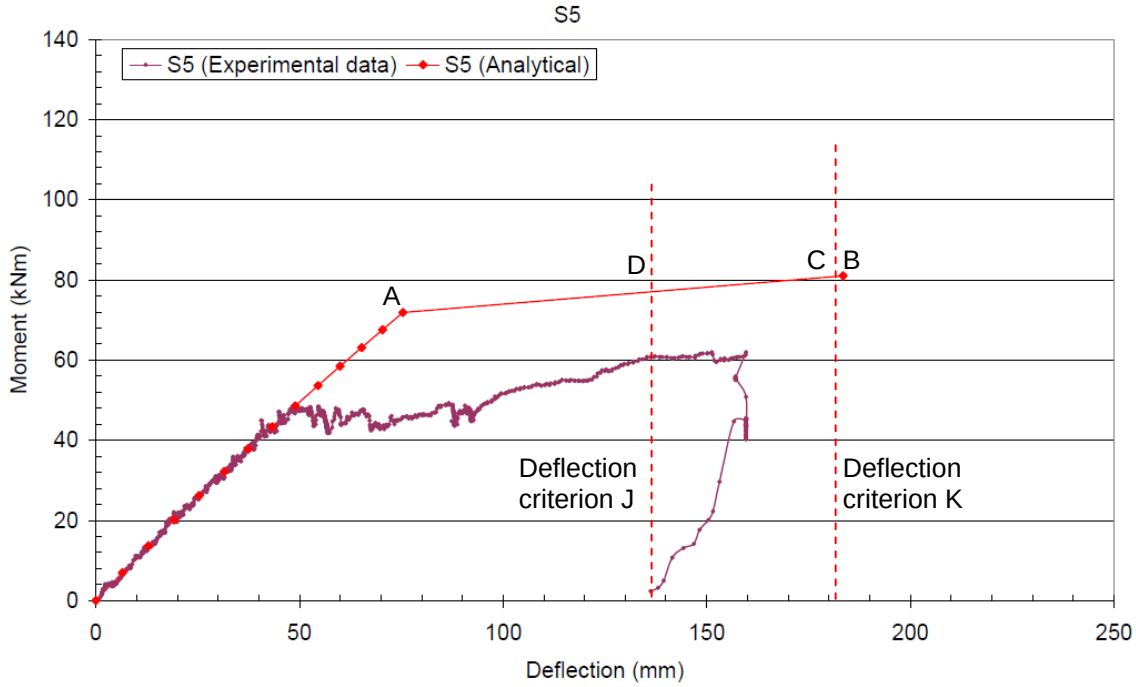

Figure 9.19 – Experimental versus predicted moment-deflection responses of Specimen S_5

9.5.2 Effect of reduced composite action

As discussed in sub-section 9.5.1, analytical predictions for specimens S_1 to S_3 did not fit well with experimental data beyond the elastic phase and tended to overestimate the ultimate moment at failure. This might have been caused by the assumption made in the model that all shear connectors were resisting the longitudinal shear, which was not the case in reality. This is because a number of dowels did not resist the shear due to poor concrete-fill in the box sections.

Therefore, to investigate this, the elastic-plastic model was modified by introducing an effective number of shear connectors, rather than using a total number of shear connectors. The GFRP dowels between the mid-span and the quarter span, referred to as 'region A' in Figure 9.20, are assumed not to resist the longitudinal shear effectively due to the poor concrete-fill in this region. In the modified model, the dowels in region A were considered to be non-effective, and only the dowels between the end support and the quarter span, referred to as 'region B', were taken into account in the analysis, with a reduced number of shear connectors working effectively. Therefore, an effective number of GFRP dowels is taken as 20 rather than 30 (total number of GFRP dowels at 'region B') in S_1, 7 rather than 14 in S_2, and 4 rather than 8 in S_3. It should be noted that this was a backward calculation. In the elastic-plastic analysis, the fixed amount of longitudinal shear resistance was calculated based on the effective number of shear connectors, leading to a drop in prediction of ultimate failure moment and its corresponding deflection. Predictions derived from the new analytical modelling assumption are compared with the experimental results in Figures 9.21 to 9.23. It is clear that moment-deflection responses predicted by the new model correlate better with the experimental results, validating the use of an effective number of shear connectors. This clearly indicates that the poor behaviour of these specimens S_1 to S_3 was indeed, mainly, due to the inadequate anchorage of the dowels. Furthermore, it is found that Johnson's model gives conservative estimates of the deflection at buckling failure compared to the experimental results.

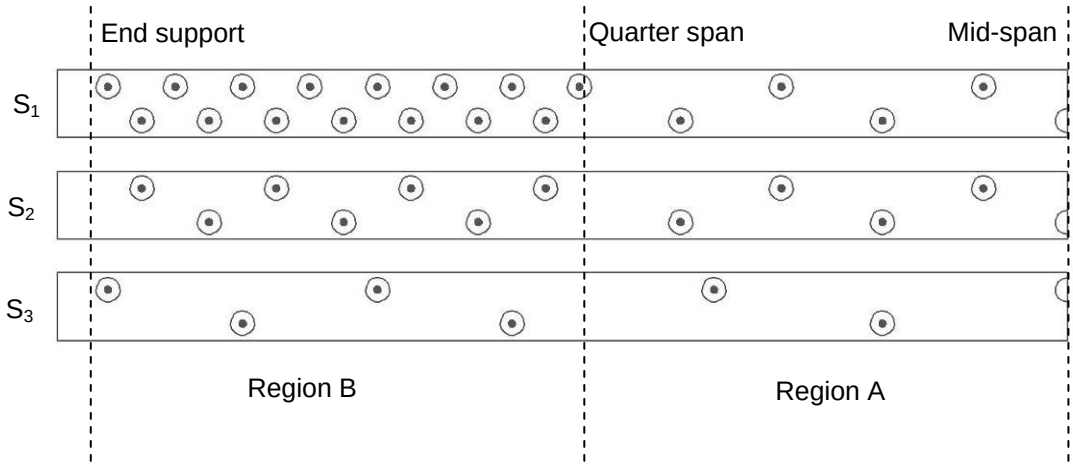

Figure 9.20 – Total number of GFRP dowels in specimens S_1 to S_3

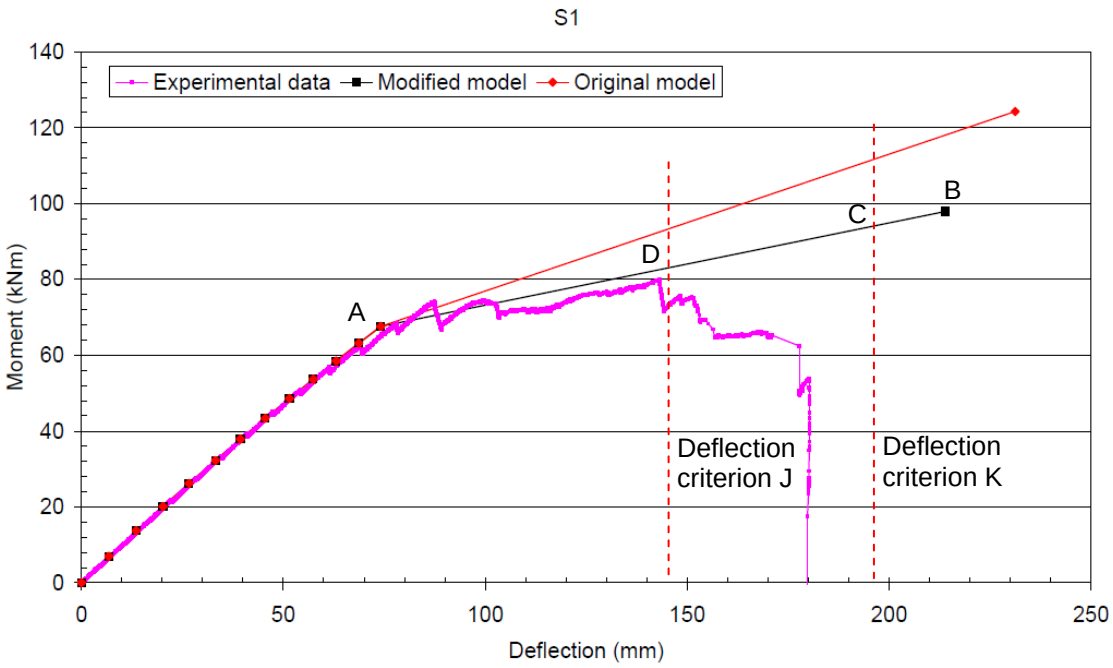

Figure 9.21 – Experimental versus predicted moment-deflection response of specimens S_1

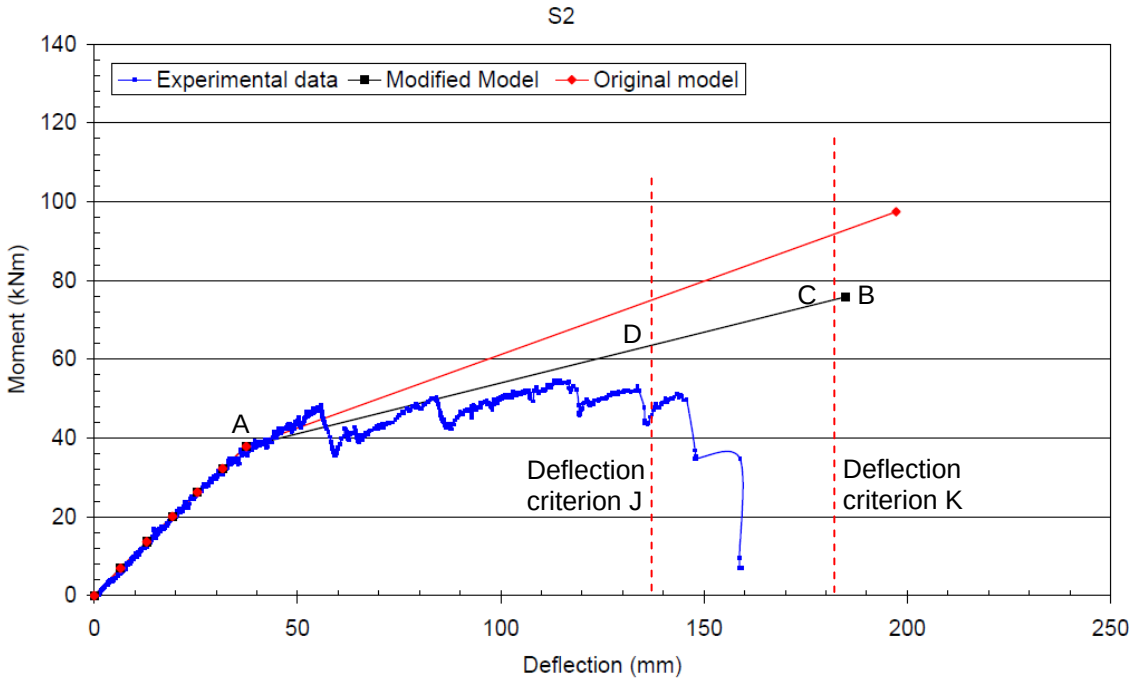

Figure 9.22 – Experimental versus predicted moment-deflection response of specimens S_2

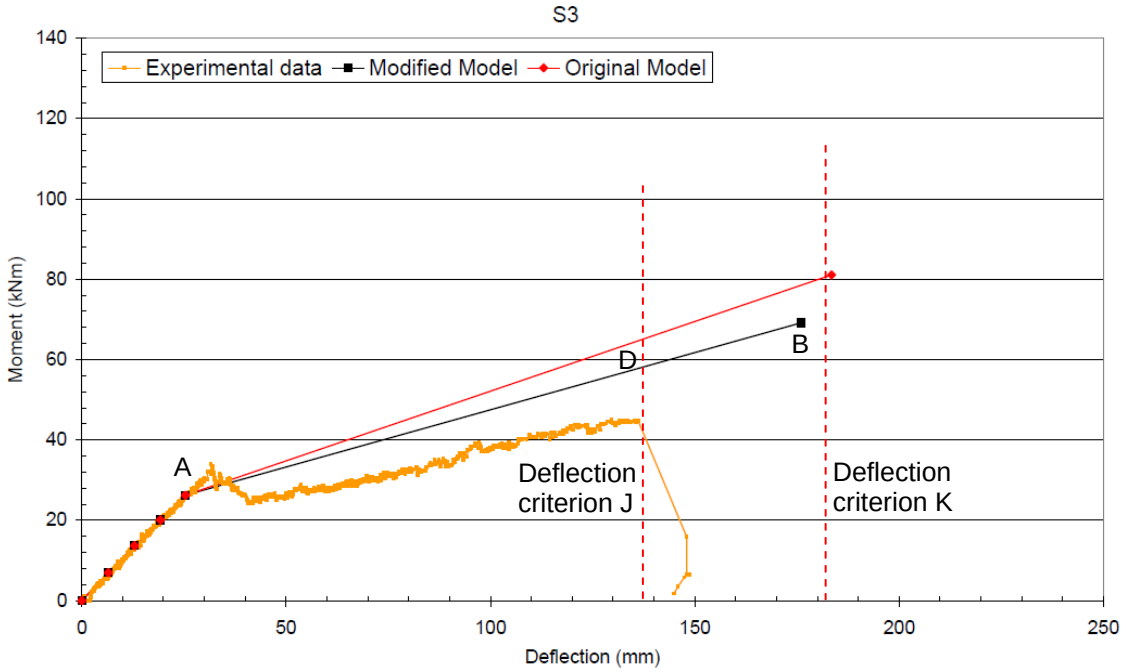

Figure 9.23 – Experimental versus predicted moment-deflection response of specimens S_3

9.5.3 Modification of analytical model for specimen S_5

As discussed in sub-section 9.5.1, the analytical prediction for S_5 significantly overestimated the moment, at the onset of debonding failure, by 50 percent. The load-slip response of concrete studs with dowels used in the original analytical model was determined from push-out test specimens based on the design of one GFRP dowel in each concrete stud. However, unlike other beam specimens, specimen S_5 had additional concrete studs without GFRP dowels. Therefore it is inappropriate to use the same load-slip response of the shear connector (one GFRP dowel in each concrete stud) in the analytical prediction for this specimen. An alternative load-slip response for a shear connector (one GFRP dowel in every fourth concrete stud) derived from the Hofbeck tests reported in Chapter 5, is reproduced in Figure 9.24. Hofbeck specimens H_1 and H_2 were designed with one GFRP dowel in every fourth concrete stud with a total of 24 concrete studs and 6 dowels. Specimen S_5 had a total of 15 concrete studs and 4 dowels between the end support and the quarter span in each box section. The arrangement of the dowels was not exactly the same between the Hofbeck specimens and specimen S_5, but the Hofbeck results provide a reasonable estimation for modelling purposes. It appears to be more suitable to incorporate the load-slip response of shear connectors derived from these Hofbeck tests, into a modified linear-elastic analysis. The Hofbeck test results indicated that the

elastic limit for H_1 and H_2 was 270 kN. Then, the maximum shear strength of a single shear connector (P_u), which primarily relies on concrete studs, is 11 kN. Therefore, in the elastic analysis of S_5, longitudinal shear resistance within the elastic range was calculated based on the assumption that the shear resistance of a single shear connector is 11 kN. Figure 9.25 shows the comparison between the experimental results and modified analytical prediction for S_5. The moment at the onset of debonding failure determined by the new model is 12.5% higher than the experimental moment, but the difference is much less compared with the difference (50%) between experimental moment and the original model. It is seen that deflection criterion J underestimates deflection at final failure by 14 percent, and deflection criterion K overestimates deflection at final failure by 14 percent. Deflection criterion J gives a conservative estimate of the deflection at buckling failure compared with deflection criterion K.

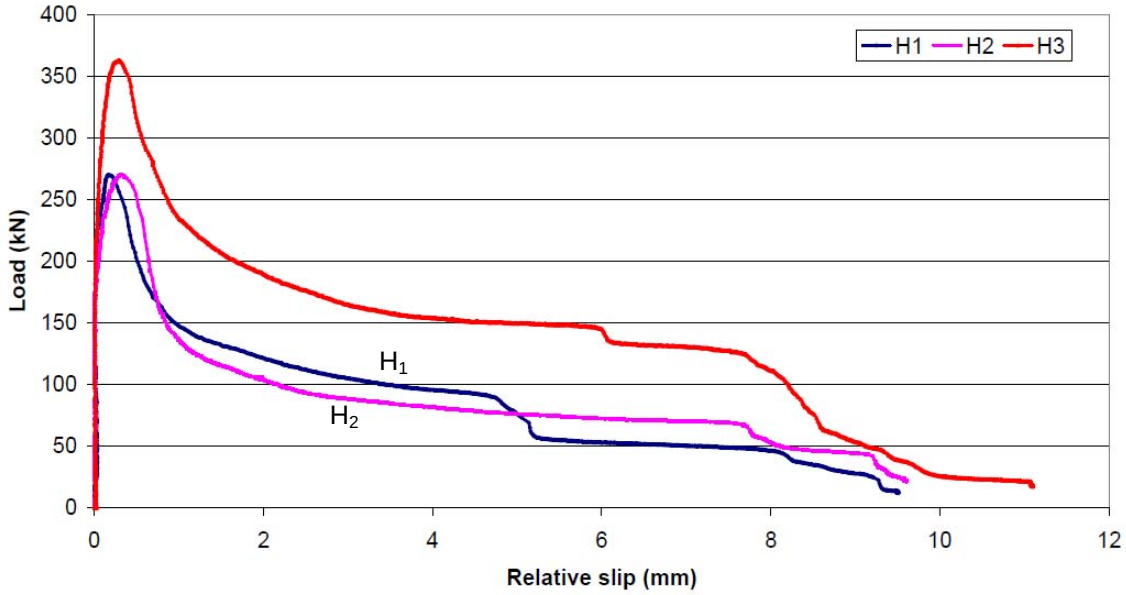

Figure 9.24 – Load versus relative slip plot of one dowel in every fourth concrete stud (H_1 and H_2 represent specimens with 6 dowels embedded in 24 concrete studs)

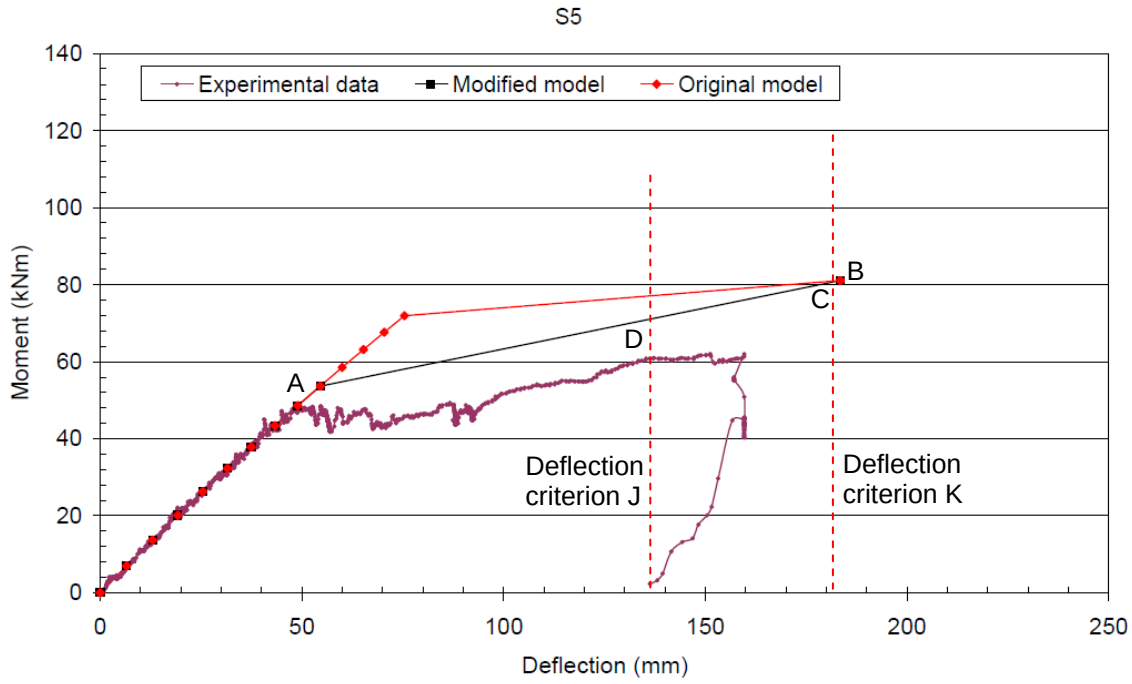

Figure 9.25 – Experimental versus predicted moment-deflection responses of specimens S_5

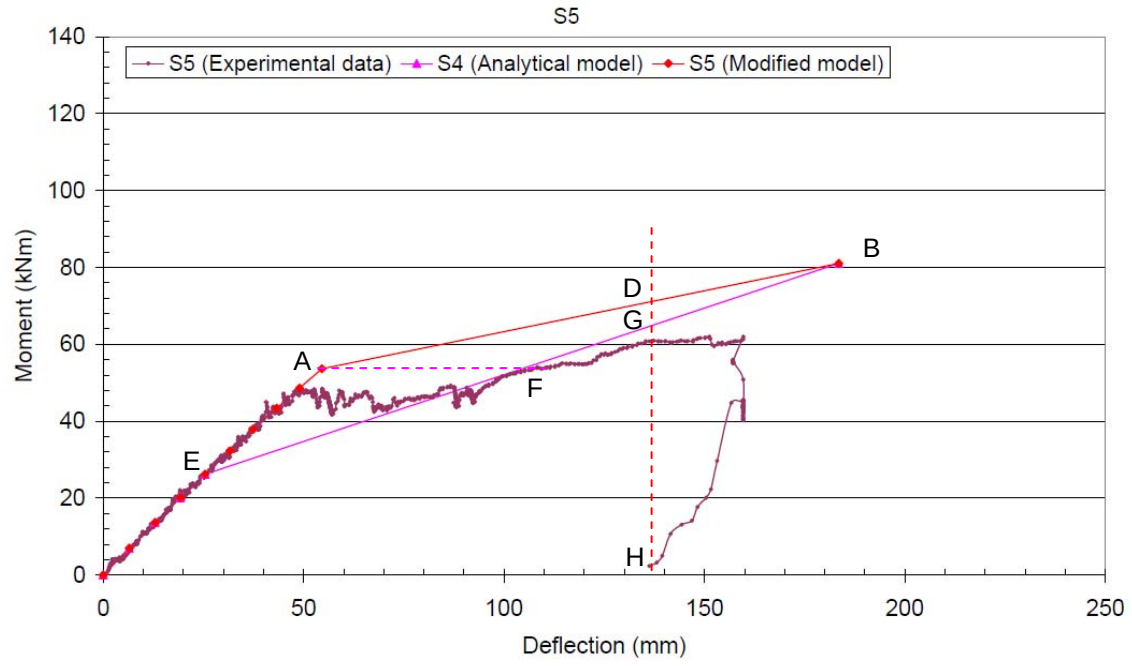

Figure 9.26 – Experimental result of specimen S_5 versus analytical predictions of S_5 and S_4

Figure 9.26 shows the comparison of the experimental moment-deflection response for S_5 with analytical predictions for S_4 and S_5. The analytical results for S_5 given by lines as A-D-H, fit reasonable well with the experimental moment-deflection curve. In addition, the analytical prediction for S_4 is given by line EG. The reason for incorporating this line is because it represents the moment at the onset of debonding failure, for a specimen having the same

number of GFRP dowels as S_5, but without the additional concrete studs. For specimen S_5, it appears that there is a flat transition zone once the moment exceeds the elastic limit at point A, represented by dashed line AF. After that, the moment continues to increase in moment-deflection response, represented by line FB, following the slope of line EB. It is logical that the slope of the experimental data for S_5, after point F, fits well with that of the prediction for S_4, since there are an identical number of GFRP dowels in the two slabs, and the residual strength is governed by the shear strength of GFRP dowels and concrete shear friction.

If an unloading and loading cycle were introduced in specimen S_5, the contribution of concrete studs in initial peak strength would be lost once there is cracking in the concrete at the grating/box-section interface. Therefore, in the second load cycle, point A will never be reached. Line EG, therefore, can give a conservative lower bound for specimen S_5. The additional concrete studs only solve the construction issue, however their contribution to strength cannot be relied on once the studs fail. Hence, in the design procedure, line EG should be used in order to make sure the design is safe.

9.6 Conclusions

This chapter has described a three-stage analytical model for predicting the flexural behaviour of six slab specimens, and the model shows fairly good agreement with the experimental results. The linear-elastic analysis accounts for the concrete-filled grating nonlinear behaviour in compression and assumes full composite action between the concrete-filled grating and box sections as evident from test results. The end of the elastic phase was determined due to longitudinal shear, and matches well with the experimental results. Subsequent elastic-plastic analysis fairly accurately predicted the flexural behaviour after the elastic phase. This was defined by the prediction of a second termination point due to fracture of shear connectors when they reached their ultimate slip. The straight line which links two termination points fits well with the experimental flexural behaviour after the elastic limit. Local buckling analysis developed by Johnson gives a critical buckling moment, and the corresponding deflection gives fairly good estimates of the deflection at buckling failure.

Chapter 10 Summary and Conclusions

10.1 Introduction

Moulded GFRP gratings adhesively bonded to pultruded GFRP box sections have excellent potential as stay-in-place structural participating formwork for concrete. There are a number of significant potential benefits offered by FRP formwork over existing products in the construction market, discussed as follows:

1. Rapid construction process and labour saving on site by eliminating any internal reinforcement and scaffoldings. The 'all-in-one' formwork can be prefabricated as a single unit in the factory, and be easily placed on-site by construction workers without the aid of heavy machinery.

2. Potential improvement in site safety due to the lightweight system. The formwork itself is relatively lightweight compared to pre-cast concrete slabs, and the relatively low weight-to-stiffness ratio of GFRP means that this weight is similar to the profiled steel decking.

3. Minimisation of the structural depth and reduction in the dead weight of the floor slab. Voids are introduced in the FRP formwork so that the vast majority of the concrete is only cast in the compression region.

4. Use of the best properties of the FRP and the concrete by virtue of their designated positions. The design allows the FRP to be fully utilised in tension and the concrete fully utilised in compression, with confinement enhancing capacity.

5. Elimination of any problems associated with corrosion that threatens many conventional profiled steel decking and pre-cast concrete slabs.

However, lack of ductility, resulting in the potential for sudden and brittle failure, is the primary concern regarding the use of FRP structural formwork in practice. The proposed FRP formwork system successfully solves the ductility issue by extracting ductility from the longitudinal shear interface between concrete and FRP formwork. A ductile behaviour has been achieved through progressive longitudinal shear failure. The following discusses the main findings from the

present experimental and analytical investigations, together with their significance.

10.2 Summary and Conclusions

10.2.1 Ductility at the longitudinal shear interface and compression zone

Chapter 5 provided details of an experimental investigation into the shear connector fabricated using pultruded GFRP dowels embedded in concrete studs at the FRP/concrete interface. A preliminary experimental investigation of using concrete studs as mechanical shear connectors showed that this shear connection exhibited linear-elastic behaviour up to failure with no ductility. However, the insertion of GFRP dowels cross the failure plane acting compositely with concrete studs, led to shear connection exhibiting an elastic-'plastic' behaviour before onset of failure. The residual strength, represented by a 'plastic' plateau, was provided by the presence of GFRP dowels and concrete shear friction. This demonstrated the feasibility of achieving ductility from the longitudinal shear interface between FRP and concrete through progressive shear failure. Chapter 6 presented an experimental investigation into using GFRP grating as confinement for concrete in the compression zone to provide ductility. Experimental results showed that the concrete blocks confined by the grating achieved a significant increase in ultimate strength and strain capacity compared with unconfined concrete blocks. However, its failure behaviour remained brittle. It is therefore not practical to utilise this enhanced strain capacity to introduce ductility into the overall system when used in a floor slab system. Nonetheless, this increased strain capacity in compression enables greater use of the FRP capacity in tension.

10.2.2 GFRP stay-in-place structural formwork for concrete slabs experimental investigation

Six slab specimens were fabricated using a moulded GFRP grating adhesively bonded to pultruded GFRP box sections, which was subsequently filled with concrete. The shear connection at the grating/box-section interface was achieved using GFRP dowels embedded in concrete studs. All specimens were tested in five-point bending schemes simulating representative moment and shear envelopes. In the first group of specimens S_1 to S_3, various dowel

spacings were investigated in order to examine whether ductility from longitudinal shear failure could be achieved, as well as to examine their performance under the influence of different degrees of composite action. It is clear from the total load versus mid-span deflection responses that all three specimens displayed adequate ductility. However, poor concrete placement occurred in the box sections of all three specimens. Subsequent analytical work has demonstrated that the poor behaviour of these specimens S_1 to S_3 was indeed due to the poor anchorage of the dowels in the concrete. For this reason, a second group of specimens S_4 to S_6 were tested in order to further examine the performance of the proposed FRP-concrete composite system and investigate whether the behaviour was ductile. Another important objective was to resolve the construction issue with regard to improving the concrete flow in the box sections. Based on the findings of all six slab tests, discussed in Chapters 7, 8 and 9, the following conclusions can be drawn:

1. As shown in load versus deflection responses, all slab specimens behaved elastically and fully compositely until longitudinal shear failure occurred at the grating/box-section interface. Following this, the load capacity of each specimen carried on increasing at a reduced stiffness until a second peak was reached at final failure, due to local buckling of the box sections. This indicated the proposed FRP-concrete composite slab achieved a ductile behaviour, giving sufficient warning before final failure. It demonstrated that progressive longitudinal shear failure did indeed provide reasonable ductility to the overall system.

2. Comparisons among load versus deflection responses in slab specimens S_1 to S_3 showed that, by adding more shear connectors, the initial peak load and the ultimate failure load were both enhanced. For specimens S_1 to S_3, each with the same adhesive bond properties at the FRP/FRP interface, it can be concluded that the initial peak load prior to longitudinal shear failure depended on the mechanical bond provided by the concrete studs combined with GFRP dowels.

3. Comparisons among load versus deflection responses in slab specimens S_4 to S_6 showed that once failure of the adhesive bond and cracking of concrete occurred, only the GFRP dowels were responsible for resisting longitudinal

shear. The residual strength was provided by dowel action of the GFRP dowels crossing the grating/box-section interface and by the post-cracked shear resistance at the concrete-to-concrete interface. Therefore, it can be concluded that the GFRP dowels are essential at the grating/box-section interface to ensure that longitudinal shear failure occurs in a ductile manner.

4. Load versus deflection responses for specimens S_1 to S_3 indicated that there was a small drop in load capacity initially beyond the elastic phase, followed by a softening response. This was caused by poor concrete placement in the box sections in specimens S_1 to S_3, leading to some of the dowels not contributing fully to resisting longitudinal shear. Load versus deflection responses for specimens S_4 to S_6 indicated that the transition from elastic to a softening response did not involve a significant drop in load capacity at any point until failure. This is because there was good concrete placement in the box sections for specimens S_4 to S_6, indicating that all the dowels fully contributed to resisting longitudinal shear. This explanation for the discrepancy of behaviour after the elastic limit has been verified by analytical work. This indicates that good concrete placement in the box sections is crucial to ensure the GFRP dowels resist the longitudinal shear effectively. It is a key assumption to ensure the analytical theory matches with experimental results.

5. Comparison between specimens S_6 (Type A loading) and S_4 (Type B loading) demonstrated how different loading conditions affect the behaviour of specimens. Both specimens were identical and designed for a longitudinal shear failure to occur prior to flexural failure. For a given total load, the longitudinal shear demands within the end quarter span between Type A and Type B loading were identical, but the maximum moment at mid-span under Type B loading was 12.5% higher than that under Type A loading. This suggests that the moment at onset of longitudinal shear failure under Type B loading should have been 12.5% higher than that under Type A loading. However, the moment versus deflection responses showed that the moment at the onset of longitudinal shear failure of S_4 and S_6 were similar. The similar flexural behaviour of specimens S_4 and S_6 demonstrated that different

loading conditions (Type A and Type B) had a minor effect on the behaviour of identical specimens.

6. Comparisons of load versus deflection responses between specimens S_4 and S_5 indicated that the initial peak load of specimen S_5 was enhanced by having additional concrete studs, and its behaviour remained ductile before final failure. The design of specimen S_5 successfully resolved the construction issue arising from poor concrete placement in the box sections by introducing more holes in the top flange of the box sections, in order to improve concrete flow.

7. The maximum strain readings of the concrete-filled grating measured in all slab specimens at failure were all below 0.007, and it was found that there was no evidence of crushing of the concrete-filled grating in any specimen. This indicates that the concrete in the compression zone with confinement provided little ductility to the overall system. Therefore, relying on concrete crushing to impart ductility is not practical. However, this enhanced strain in the concrete allowed the tensile strain in the box sections for all specimens to reach an average value of 0.0096, approaching its ultimate failure strain at 0.011, which indicates effective use of the materials. It can be concluded that the concrete with confinement in the compression zone allowed FRP tensile components to be utilised to a greater extent, with 100% gain in their tensile strain.

8. Initial failure of all specimens was caused by longitudinal shear failure. Strain profiles plotted from the strain readings indicated that all specimens experienced a transition from ‘full-interaction’ before longitudinal shear failure to ‘partial-interaction’ after longitudinal shear failure, eventually approaching to ‘non-interaction’ when the concrete-filled grating and box sections acted, effectively, as separate components before the final failure. At ‘full-interaction’ stage, the actual neutral axis of the composite section was measured to be 14 mm below the grating/box section interface, indicating the concrete-filled grating was fully utilised in compression and that most of the box section was ultilised in tension. The change from ‘full’ to ‘partial’ interaction demonstrated that the GFRP dowels were crucial to ensure levels

of partial interaction at the grating/box-section interface, preventing a sudden and brittle failure behaviour when the concrete studs failed in shear.

9. The cause of final failure was due to the separation of the compression flange and the webs at the upper corners of the box sections, followed by the immediate buckling of unrestrained webs. The maximum deflection of six specimens at failure ranged between 137 mm and 173 mm with a 26% variation, indicating that this type of failure is likely to be governed by a specific curvature, rather than by load.

10.2.3 GFRP stay-in-place structural formwork for concrete slabs: analytical investigation

A three-stage analytical model was developed to predict the flexural behavior of the six slab specimens. The end of the elastic phase, governed by longitudinal shear failure, was predicted by elastic analysis. Then, the post-elastic flexural behaviour was predicted by elastic-plastic analysis with an assumption made that failure was governed by fracture of the shear connectors. Eventually, a deflection limit at final failure was predicted by local buckling analysis. The model showed good agreement with experimental results. The following conclusions can be drawn:

1. The flexural behaviour before and after longitudinal shear failure, initial peak capacity and deflection at ultimate failure of the GFRP-concrete composite slab specimens studied in this investigation can be modeled fairly accurately using the proposed three-stage model. It should be noted that the concrete-filled grating and box sections behaved linear-elastically at every stage. This was a key assumption to ensure the whole analysis was valid.

2. During the elastic phase, the concrete-filled grating and box sections behaved fully compositely until the onset of longitudinal shear failure. Elastic analysis established a first termination point A, governed by the onset of longitudinal shear failure. In specimens S_1-S_6 (except specimen S_5), the ratio of GFRP dowels to concrete studs was 1:1. Based on push-out test results, a rigid plastic load versus slip model of such shear connector was developed and applied in an elastic analysis to predict point A. As specimen S_5 had additional concrete studs, the ratio of GFRP dowels to concrete studs was

1:4, so that the original load versus slip model was not applicable to specimen S_5. Based on Hofbeck test results with a similar arrangement of shear connectors, a new load versus slip model of shear connector was developed and applied in an elastic analysis. The elastic analysis gave fairly good estimates of the moment at the elastic limit when compared with experimental results.

3. Beyond the elastic phase, assuming constant longitudinal shear resistance, elastic-plastic analysis predicted a second termination point B, governed by fracture of the shear connectors. For specimens S_4-S_6 with good concrete placement, the total number of shear connectors was incorporated in the analysis. The theory fitted well against flexural behaviour beyond the elastic phase. However, the elastic-plastic analysis tended to overestimate the ultimate moment at failure compared with the experimental results. This is because in reality the final failure was caused by local buckling of the box sections, rather than by fracture of the shear connectors, as assumed in the model.

4. The final stage of this model considered local buckling of the box sections. Both Kollar's (2003) and Johnson's (1985) buckling modes were investigated to obtain a deflection limit which would define ultimate failure, verified against experimental results. In Johnson's model, the edge condition of the buckling plate was considered to be simply supported with no edge restraint. However, in Kollar's model, the buckling plate was considered to be rotationally restrained by the adjacent walls. In comparison with experimental results, Johnson's model gave fairly accurate, and generally conservative, estimates of the deflection at buckling failure. However, Kollar's model tended to overestimate the deflection at ultimate failure due to the different assumption made concerning the edge condition of the buckling plate.

These important findings demonstrated the feasibility of developing a practical means to design an FRP-concrete composite slab system, exhibiting a ductile behaviour up to the ultimate failure, through a controlled progressive longitudinal shear failure.

10.3 Recommendations for Future Work

This study has illustrated that the use of GFRP sections as stay-in-place structural participating formwork for concrete flexural members is quite promising, and indeed this technology should be researched further. It is important that the following aspects are studied prior to implementation of the technologies discussed in this thesis:

1. The proposed GFRP-concrete composite system should be further assessed under loading-unloading cycles in order to investigate how energy is dissipated through longitudinal shear failure. An energy based method could be adopted to quantify the energy dissipation, in order to compare the ductility of the proposed GFRP-concrete composite system with conventional steel-reinforced concrete members.

2. The bond mechanism at the grating/box-section interface should be further investigated, in order to quantify how the different bond mechanisms, including epoxy adhesive, concrete studs and GFRP dowels contribute to longitudinal shear capacity.

3. The long-term performance of the proposed GFRP-concrete composite system should be assessed in terms of creep and fatigue, since both FRP and concrete are indeed susceptible to creep and fatigue, which might cause serviceability issues.

4. The performance of the proposed system under fire should be investigated.

5. Due to the low stiffness of GFRP profiles compared with steel, serviceability limit state (SLS) governs the design of this proposed FRP-concrete composite system, rather than the ultimate limit state (ULS). Conventional steel-reinforced concrete members are designed initially to fulfill the strength requirement at ULS, and further checked to satisfy the SLS requirements. Normally, steel-reinforced concrete members which meet the ULS requirements also satisfy the SLS requirements. However, it should be noted from Figure 10.1 that the design service load A, which is governed by a deflection limit of $L/250$, is significantly below the load at onset of longitudinal shear failure. This indicates that the design ultimate load (factored load A) is still well within the elastic range in load versus deflection response, which

does not make best use of the post elastic behaviour. As illustrated in Figure 10.1, if the difference between the service load and the load at the end of the elastic phase could be minimised, represented by service load B, potentially by increasing the stiffness of the overall system without increasing the longitudinal shear resistance of shear connection, then the system would be very attractive. The factored load B would then be located within the post elastic range. Thus, ductility through progressive longitudinal shear failure could be utilised. For this reason, potential means to overcome this serviceability issue need to be investigated.

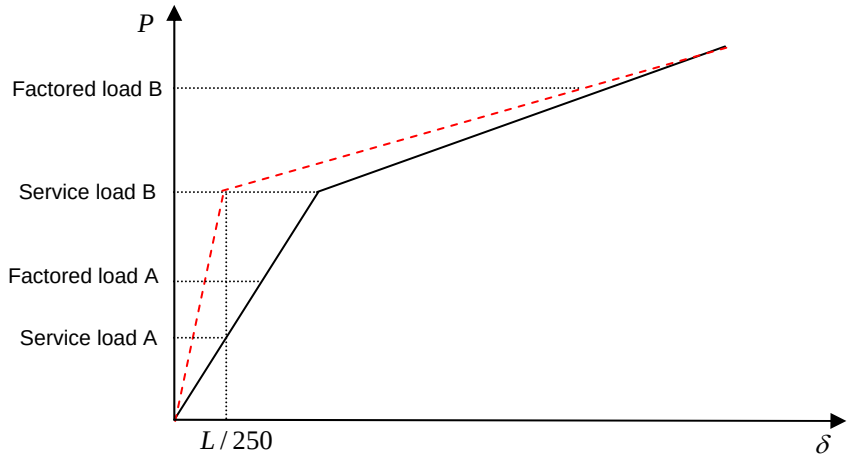

Figure 10.1 – Comparison of ultimate load in design and experiments.

While this work has shown that the proposed composite system performs quite well, the study also highlighted some aspects of the technology that require further refinement, as well as some other potential applications of the technology that may be developed. Key topics requiring further work are listed below:

1. This study was focused only on GFRP-concrete composite members in uniaxial bending. It is recommended that this technology be further developed for applications that generate biaxial bending conditions. In order to utilise the bi-directional properties of the compression component, with a proper modification in the tension component by inserting GFRP reinforcement in the transverse direction, the GFRP formwork could be developed into a two-way spanning system.

2. This proposed GFRP-concrete composite system was designed and tested over a span of 3 m for the convenience of laboratory testing. However, the

potential for this system to be applied to longer spans (5 or 6 m) should be investigated in future.

References

Araldite 2015 structural adhesives technical data sheet (2010). Huntsman Advanced Materials, Switzerland. web content. Sourced from: http:// www.huntsman.com/advanced_materials.

ADOFLOW-EXTRA data sheet (2010). Superplasticiser for concrete and mortar, Adomost Building Chemicals Limited, Essex, UK. web content. Sourced from: http:// www.adomast.co.uk.

Aslan 100 Fibreglass Rebar (2010). Hughes and Brothers, Inc. Seward, Nebraska, U.S. web content. Sourced from: http:// www.hughesbros.com.

Bakis, C. E., Bank, L. C., Brown, V. L., Cosenza, E., Davalos, J. F., Lesko, J. J., et al. (2002). Fiber-reinforced polymer composites for construction-state-of-the-art review. *Journal of Composites for Construction, 6*(2), 73-87.

Bank, L. C. (2006). Composites for construction: structural design with FRP materials. John Wiley&Sons, New York.

Bank, L. C., Gentry, T. R., and Nadipelli, M. (1996). Local buckling of pultruded FRP beams - analysis and design. *Journal of Reinforced Plastics and Composites, 15*, 283-294.

Bank, L. C., Nadipelli, M., and Gentry, T. R. (1993). *Local buckling and failure of pultruded fiber-reinforced plastic beams.* Paper presented at the Proceedings of the 1993 ASME Winter Annual Meeting, November 28, 1993 - December 3, 1993, New Orleans, LA, USA.

Bank, L. C., Nadipelli, M., and Gentry, T. R. (1994). Local buckling and failure of pultruded fiber-reinforced plastic beams. *Journal of Engineering Materials and Technology, Transactions of the ASME, 116*, 233-237.

Bank, L. C., Nadipelli, M., Gentry, T. R., and Yin, J. S. (1994). *Local buckling of pultruded FRP beams: theory and experiment.* Paper presented at the Proceedings of the Structures Congress '94, April 24, 1994 - April 28, 1994, Atlanta, GA, USA.

Bank, L. C., Oliva, M. G., Bae, H. U., Barker, J. W., and Yoo, S. W. (2007). Pultruded FRP plank as formwork and reinforcement for concrete members. *Advances in Structural Engineering, 10*(5), 525-535.

Bank, L. C., Oliva, M. G., Bae, H. U., and Bindrich, B. V. (2010). Hybrid concrete and pultruded-plank slabs for highway and pedestrian bridges. *Construction and Building Materials, 24*(4), 552-558.

Bank, L. C., Oliva, M. G., Russell, J. S., Dieter, D. A., Dietsche, J. S., Hill, R. A., et al. (2003). *Details and specifications for a bridge deck with FRP formwork, grid and rebar*.

Bank, L. C., Oliva, M. G., Russell, J. S., Jacobson, D. A., Conachen, M., Nelson, B., et al. (2006). Double-layer prefabricated FRP grids for rapid bridge deck construction: case study. *Journal of Composites for Construction, 10*(3), 204-212.

Bank, L. C., and Yin, J. (1996). Buckling of orthotropic plates with free and rotationally restrained unloaded edges. *Thin-Walled Structures, 24*, 83-96.

Bank, L. C., and Yin, J. (1999). Failure of web-flange junction in postbuckled pultruded I-beams. *Journal of Composites for Construction, 3*(4), 177-184.

Beales, C., Ives, D. A., (1990). *TRRL Research Report 254-The Behaviour of Permanent Formwork*. Bridges Division, Structures Group, Transport and Road Research Laboratory, Crowthrone, UK.

Beeby, A., and Narayanan, R. (1995). Designers' guide to EN 1992-1-1 and EN 1992-1-2. Eurocode 2: design of concrete structures: general rules and rules for buildings. Thomas Telford Services Ltd.

Berg, A. C., Bank, L. C., Oliva, M. G., and Russell, J. S. (2006). Construction and cost analysis of an FRP reinforced concrete bridge deck. *Construction and Building Materials, 20*(8), 515-526.

Birkeland, P. W., and Birkeland, H. W. (1966). *Connections in precast concrete construction*.

Bisby, L. A., Green, M. F., and Kodur, V. K. R. (2005). Response to fire of concrete structures that incorporate FRP. *Progress in Structural Engineering and Materials, 7*, 136-149.

Bleich, F. (1952). Buckling of metal structures. *McGraw-Hill, New York.*

BSI, B. S. 8110-1:(1997), Structural use of concrete–Part 1: Code of practice for design and construction.

BS EN 1992-1-1. (2004). Design of concrete structures. General rules and rules for buildings.

BS EN 13706-2. (2002). Reinforced plastics composites. Specifications for pultruded profiles. Method of test and general requirements. British Standards Institution.

BS EN ISO 527-4. (1997). Plastics - Determination of tensile properties, Part 4: Test conditions for isotropic and orthotropic fibre-reinforced plastic composites.

BSEN ISO 14126. (1999). Fibre-reinforced plastic composites - Determination of compressive properties in the in-plane direction.

BS EN ISO 527-5. (2009). Plastics - Determination of tensile properties, Part 5: Test conditions for unidirectional fibre-reinforced plastic composites.

Bulson, P. S., (1955). *Local instability problems of light alloy struts*. The Aluminium Development Association, New York.

Burgoyne, C., Leung, H. Y. (2007). Model for concrete confined by aramid FRP. FRPRCS-8, Univeristy of Patras, Patras, Greece, July 16-18.

Canning, L., Hollaway, L., Thorne, A. M. (1999). An investigation of the composite action of an FRP/concrete prismatic beam. *Construction and Building Materials, 13*(8), 417-426.

Carreira, D. J., and Chu, K. H. (1985). Stress-strain relationship for plain concrete in compression.

Charoenphan, S., Bank, L. C., and Plesha, M. E. (2004). Progressive tearing failure in pultruded composite material tubes. *Composite Structures, 63*, 45-52.

Deskovic, N., Meier, U., and Triantafillou, T. C. (1995). Innovative design of FRP combined with concrete - long-term behaviour. *Journal of Structural Engineering, ASCE, 121*(7), 1079-1089.

Deskovic, N., Triantafillou, T. C., and Meier, U. (1995). Innovative design of FRP design of FRP combined with concrete - short-term behaviour. *Journal of Structural Engineering, ASCE, 121*(7), 1069-1078.

Dieter, D., Dietsche, J., Bank, L., Oliva, M., and Russell, J. (2002). Concrete Bridge Decks Constructed with Fiber-Reinforced Polymer Stay-in-Place Forms and Grid Reinforcing. *Transportation Research Record, Journal of the Transportation Research Board, 1814*(-1), 219-226.

Fib, Bulletin 14. (2001). Externally Bonded FRP Reinforcement for RC structures, Federation Internationale Du Beton, Lausanne, Switzerland, 130pp

Fam, A., and Honickman, H. (2010). Built-up hybrid composite box girders fabricated and tested in flexure. *Engineering Structures, 32*(4), 1028-1037.

Fam, A., Manda, S., and Rizkalla, S. (2005). Rectangular filament-wound glass fiber reinforced polymer tubes filled with concrete under flexural and axial loading: Analytical modeling. *Journal of Composites for Construction, 9*(1), 34-43.

Fam, A., Schnerch, D., and Rizkalla, S. (2005). Rectangular filament-wound glass fiber reinforced polymer tubes filled with concrete under flexural and axial loading: Experimental investigation. *Journal of Composites for Construction, 9*(1), 25-33.

Fam, A., and Skutezky, T. (2006). Composite T-beams using reduced-scale rectangular FRP tubes and concrete slabs. *Journal of Composites for Construction, 10*(2), 172-181.

Fam, A. Z., and Rizkalla, S. H. (2001). Behavior of axially loaded concrete-filled circular fiber-reinforced polymer tubes. *ACI Structural Journal, 98*(3), 280-289.

Fam, A. Z., Schnerch, D. A., and Rizkalla, S. H. (2003). Rectangular FRP tubes filled with concrete for beam and column applications.

Fardis, M. N., and Khalili, H. (1981). Concrete encased in Fiberglass-reinforced plastic. *Journal of the American Concrete Institute, 78*(6), 440-446.

Fardis, M. N., and Khalili, H. H. (1982). FRP-encased concrete as a structural material. *Magazine of Concrete Research, 34*(121), 191-202.

Fiberline Composite Design Manual. (2003). Fiberline Composites, Denmark. web content. sourced from: http://www.fiberline.com.

Green, M. F., Bnichou, N., Kodur, V. R., and Bisby, L. A. (2007). *Design guidelines for fire resistance of FRP strengthened concrete structures*, Patras, Greece.

Glenium 123 Data sheet (2011). super plasticising admixture, BASF plc, Cheshire, UK. web content. sourced from: http://www.basf-cc.co.uk.

Hall, J. E. and Mottram, J. T. (1998). Combined FRP Reinforcement and Permanent Formwork for Concrete Members. *Journal of Composites for Construction, 2*(2), 78-89.

Honickman, H., and Fam, A. (2009). Investigating a Structural Form System for Concrete Girders Using Commercially Available GFRP Sheet-Pile Sections. *Journal of Composites for Construction, 13*(5), 455-465.

Honickman, H., Nelson, M., and Fam, A. (2009). Investigation into the Bond of Glass Fiber-Reinforced Polymer Stay-in-Place Structural Forms to Concrete for Decking Applications. *Transportation Research Record*(2131), 134-144.

Honickman, H. N. (2008). Pultruded GFRP sections as stay-in-place structural open formwork for concrete slabs and girders. Department of Civil Engineering, Queen's University, Canada.

Hulatt, J., Hollaway, L., and Thorne, A. (2003). The use of advanced polymer composites to form an economic structural unit. *Construction and Building Materials, 17*(1), 55-68.

Ibell, T., Darby, A., and Denton, S. (2009). Research issues related to the appropriate use of FRP in concrete structures. *Construction and Building Materials, 23*(4), 1521-1528.

Ibell, T., and Darby, A. (2007). Advanced composites in construction. Department of Architecture and Civil Engineering, University of Bath, Bath, UK.

Johnson, A. F. (1985). *Simplified buckling analysis for RP beams and columns*. The first European Conference on Composite Materials, Bordeaux, 541-549.

Johnson, R. P., and Anderson, D. (1993). Designers' guide to EN 1994-1-1: Eurocode 4: design of composite steel and concrete structures. General rules and rules for buildings. Thomas Telford Services Ltd.

Keller, T., Schaumann, E., and Vallee, T. (2007). Flexural behavior of a hybrid FRP and lightweight concrete sandwich bridge deck. *Composites Part A-Applied Science and Manufacturing, 38*(3), 879-889.

Keller, T., and Vallee, T. (2004). Adhesively bonded lap joints from pultruded GFRP profiles. Part I: stress-strain analysis and failure modes. *Composites Part B-Engineering, 36*(4), 331-340.

Kim, G. B., Pilakoutas, K., and Waldron, P. (2008a). Development of thin FRP reinforced GFRC permanent formwork systems. *Construction and Building Materials, 22*(11), 2250-2259.

Kim, G. B., Pilakoutas, K., and Waldron, P. (2008b). Thin FRP/GFRC structural elements. *Cement and Concrete Composites, 30*(2), 122-137.

Kim, J. (1998). Material Properties of Self-Flowing Concrete. *J. Mater. Civ. Eng., 10*(4), 244.

Kollar, L. P. (2002). Buckling of Unidirectionally Loaded Composite Plates with One Free and One Rotationally Restrained Unloaded Edge. *J. Struct. Eng., 128*(9), 1202.

Kollar, L. P. (2002). Discussion of "Local buckling of composite FRP shapes by discrete plate analysis" by Pizhong Qiao, Julio F. Davalos, and Jialai Wang. *Journal of Structural Engineering-ASCE, 128*(8), 1091-1093.

Kollar, L. P. (2003). Local buckling of fiber reinforced plastic composite structural members with open and closed cross sections. *Journal of Structural Engineering-ASCE, 129*(11), 1503-1513.

Kollar, L. P. (2005). Closure to "Local buckling of fiber reinforced plastic composite structural members with open and closed cross sections" by Laszlo P. Kollar. *Journal of Structural Engineering-ASCE, 131*(5), 853-853.

Kollar, L. P., and Springer, G. S. (2003). *Mechanics of composite structures*. Cambridge University Press.

Kuennen, T. (2006). Transportation officials weigh SIP bridge forms, laud FRP design. *Transportation Research Board*.

Larralde, J. (1992). Feasibility of FRP moulded grating-concrete composites for one-way slab systems.

Lawson, R. M., and Leskela, M. (1996). Slim floor construction. *Structural engineering international, 6*(2), 122-126.

Leung, H. Y., and Burgoyne, C. J. (2005). Uniaxial stress-strain relationship of spirally confined concrete. *ACI materials journal, 102*(6), 445.

Li, T., Feng, P., and Ye, L. (2006). Experimental study on FRP-concrete hybrid beams.

Lopez-Anido, R., Bendidi, R., GangaRao, H. V. S., and Al-Megdad, M. (1996). *Local buckling experiments on pultruded composite beams.* Paper presented at the Proceedings of the 1996

4th Materials Engineering Conference. Part 2 (of 2), November 10, 1996 - November 14, 1996, Washington, DC, USA.

Mirmiran, A., and Shahawy, M. (1996). New concrete-filled hollow FRP composite column. *Composites Part B: Engineering, 27*, 263-268.

Mirmiran, A., Shahawy, M., and Beitleman, T. (2001). Slenderness limit for hybrid FRP-concrete columns. *Journal of Composites for Construction, 5*(1), 26-34.

Mirmiran, A., Shahawy, M., El Khoury, C., and Naguib, W. (2000). Large beam-column tests on concrete-filled composite tubes. *ACI Structural Journal, 97*(2), 268-276.

Mirmiran, A., Shahawy, M., and Samaan, M. (1999). Strength and ductility of hybrid FRP-concrete beam-columns. *Journal of Structural Engineering-ASCE, 125*(10), 1085-1093.

Mottram, J. T. (1991). Evaluation of design analysis for pultruded fibre-reinforced polymeric box beams. *Structural Engineer London, 69*, 211-220.

Mottram, J. T. (2005). Discussion of "Local buckling of fiber reinforced plastic composite structural members with open and closed cross sections" by Laszlo P. Kollar. *Journal of Structural Engineering-ASCE, 131*(5), 851-853.

Naaman, A. E., and Jeong, S. M. (1995). Structural ductility of concrete beams prestressed with FRP tendons. 379-384.

Newmark, N. M., Siess, C. P., and Viest, I. M. (1951). Tests and analysis of composite beams with incomplete interaction. *Proc. Soc. Exp. Stress Anal, 9*(1), 75-92.

Oehlers, D. J., and Bradford, M. A. (1999). Elementary behaviour of composite steel and concrete structural members. Butterworth-Heinemann.

Oehlers, D. J., and Sved, G. (1995). Composite beams with limited-slip-capacity shear connectors. *Journal of Structural Engineering-ASCE, 121*(6), 932-938.

Ominia wideslab permanent formwork technical guidance note (2011). Hanson Heielberg Cement Group. web content. sourced from: http:// www.omnidec.co.uk.

Palmer, D. W., Bank, L. C., and Gentry, T. R. (1998). Progressive tearing failure of pultruded composite box beams: experiment and simulation. *Composites Science and Technology, 58*(8), 1353-1359.

Qiao, P. H., and Zou, G. P. (2002). Local buckling of elastically restrained fiber-reinforced plastic plates and its application to box sections. *Journal of Engineering Mechanics-ASCE, 128*(12), 1324-1330.

Qiao, P. Z., Davalos, J. F., and Wang, J. L. (2001). Local buckling of composite FRP shapes by discrete plate analysis. *Journal of Structural Engineering-ASCE, 127*(3), 245-255.

Qiao, P. Z., Davalos, J. F., and Wang, J. L. (2002). Closure to "Local buckling of composite FRP shapes by discrete plate analysis" by Pizhong Qiao, Julio F. Davalos, and Jialai Wang. *Journal of Structural Engineering-ASCE, 128*(8), 1093-1093.

Ringelstetter, T., Bank, L., Oliva, M., Russell, J., Matta, F., and Nanni, A. (2006). Cost-Effective, Structural Stay-in-Place Formwork System of Fiber - Reinforced Polymer for Accelerated and Durable Bridge Deck Construction. *Transportation Research Record: Journal of the Transportation Research Board, 1976*(-1), 183-189.

Ralph, T. C., and Denton, S. R. (2004). Participating FRP Formwork - Feasibility study, Highways Agency Framework Arrangement 2/353, Parsons Brinckerhoff Ltd, Bristol.

Samaan, M., Mirmiran, A., and Shahawy, M. (1998). Model of concrete confined by fiber composites. *Journal of Structural Engineering-ASCE, 124*(9), 1025-1031.

Schaumann, E., Vallee, T., and Keller, T. (2008). Direct load transmission in hybrid FRP and lightweight concrete sandwich bridge deck. *Composites Part A-Applied Science and Manufacturing, 39*(3), 478-487.

Seible, F. (1996). *Advanced composites materials for bridges in the 21st century*. Proceeding of the First International Conference on Composites in Infrastructure (ICCI 96), Tuscon, Arizona, Jan., 17-30.

Sims, G. D., Johnson, A. F., and Hill, R. D. (1987). Mechanical and Structural-properties of a GRP pultruded section. *Composite Structures, 8*(3), 173-187.

Take, W. A. (2003). The influence of seasonal moisture cycles on clay slopes. University of Cambridge.

Tarjan, G., Sapkas, A., and Kollar, L. P. (2010). Local Web Buckling of Composite (FRP) Beams. *Journal of Reinforced Plastics and Composites, 29*(10), 1451-1462.

Timoshenko, S., Woinowsky-Krieger, S., and Woinowsky, S. (1959). *Theory of plates and shells* (Vol. 2). McGraw-Hill, New York.

Timoshenko, S. P., and Gere, J. M. (1961). Theory of elastic stability. McGraw-Hill, New York.

The European Guidelines for self-compacting concrete. (2005). The European Concrete Platform. web content. sourced from: http://www.europeanconcrete.eu.

Wrigley, R. (2001). *Permanent formwork in construction*. Construction Industry Research and Information Association (CIRIA). UK.

Yam, L. C. P. (1981). *Design of composite steel-concrete structures*. Surrey University Press. (Guildford, Surrey).